Gamma-ray Spectroscopy of Neutron Deficient Pr and Nd Nuclei

Thesis submitted in accordance with the requirements of
the University of Liverpool for the degree of Doctor of Philosophy

by

David Charles Bruce Watson

Oliver Lodge Laboratory

September 1989

Abstract

Transitions have been identified and decay schemes deduced for highly neutron deficient light rare earth nuclei using coincident γ-ray and recoil mass spectroscopy. Likely configurations for decay sequences are proposed on the basis of systematics and observed properties. The results are discussed in terms of the cranked shell and particle-rotor model and a comparison is made with predictions from calculations made within the Woods-Saxon potential. Many questions regarding the data remain unsolved and it is hoped that further work, both experimental and theoretical, will be carried out on the nuclei in this challenging region.

Acknowledgments

The research for this work was carried out during the period 1985–9. I wish to acknowledge Professors C.E. Johnson and E. Gabathuler for providing the opportunity to carry out the work, Dr A.N. James for his supervision and the Science and Engineering Research Council for financial support.

I am grateful to Dr. K.L. Ying for weaning me onto the subject and his boundless cheer in the darkest hours at Daresbury and Dr. D.J.G. Love for help when all around was failing. I am indebted to Dr. R. Wyss for providing the TRS and bandhead calculations presented in this work as well as assistance in the interpretation of the data.

On the technical side, many thanks go to Dr. J.R. Cresswell, Dr. T.P. Morrison, Dr. R.M. Lovely and Ms. J.A. Sampson for their computer support (and biscuits in one case!), Christine Brookes for her tender nursing of the detectors, Bob Darlington and Joe Reynolds for the targets and the N.S.F. crews and support staff at Daresbury for keeping all on an even keel.

Many thanks also to the proof readers; Dave Love , Thaamon Mullins, Janet Sampson, Neil Rowley and Arthur James, and Ruth for sticking the cattle prod in at the final stages. I owe a great debt or even a pint to you all!!

Finally, thanks to my parents for all their encouragement over the years and the odd bob or two when SERC were not so forthcoming!!

Contents

1 Nuclear Phenomena 1

1.1 Introduction 1
1.2 Compound Nucleus Formation 2
1.3 Decay of the Compound Nucleus 2
1.4 General Features Observed in Level Schemes 4
1.5 Rotational Behaviour in Nuclei 5
1.6 Rotational Properties of Bands 6
1.7 Band Crossing 7
1.8 Transition Strengths 8

2 The Theoretical Nucleus 11

2.1 Introduction 11
2.2 Macroscopic models 11
2.2.1 The Liquid Drop Model 11
2.2.2 The Collective Model 13
2.3 Microscopic Models 14
2.3.1 The nuclear problem 14
2.3.2 Shell Models 14
2.3.3 The Nilsson Model 15
2.3.4 The Woods-Saxon Potential 19
2.3.5 The Cranking Concept 21
2.3.6 Pairing Correlations 22
2.3.7 Quasiparticles 24
2.3.8 CHFB Theory 26
2.3.9 The Cranked Shell Model 27
2.4 Macroscopic–Microscopic Methods 29
2.4.1 The Shell Correction Method 29
2.4.2 Energy Surfaces 30
2.4.3 Cranked Macroscopic-Microscopic calculations 31

3 Apparatus and Techniques 44

3.1 Introduction 44
3.2 Techniques 44
3.2.1 Coincident Spectroscopy 44

3.2.2 The Doppler Shift Attenuation Method 45
3.2.3 Angular Correlation and Distribution 46
3.3 The Recoil Separator 47
3.3.1 Why use the Recoil Separator? 47
3.3.2 General Description 47
3.3.3 Target Chamber 49
3.3.4 Crossed Field Devices 49
3.3.5 Sextupoles 50
3.3.6 Dipole Sector Magnet 50
3.3.7 Detection System 51
3.3.8 Control System 53
3.4 Gamma-ray detection 56
3.4.1 Basic Principles 56
3.4.2 Compton Suppression 58
3.4.3 Detector Arrays 58
3.5 Data Collection 61
3.5.1 Data Acquisition 61
3.5.2 Array Electronics 61
3.5.3 RS Electronics 62
3.6 Choice of Beam and Target 63
3.7 Data Analysis 65
3.7.1 Terminology 65
3.7.2 $\gamma - \gamma$ Data analysis 67
3.7.3 Recoil Separator Data analysis 68

4 Experimental Results **75**
4.1 General Comments on the Data 75
4.2 ^{129}Pr 81
4.2.1 Bands 1,2 and 3 86
4.2.2 Bands 4 and 5 93
4.2.3 Bands 6 and 7 97
4.2.4 Band 8 100
4.3 ^{128}Pr 102
4.4 ^{129}Nd 109
4.4.1 Bands 1 and 2 113
4.4.2 Bands 3 and 4 115
4.4.3 Band 5 117
4.4.4 Band 6 119
4.5 ^{131}Nd 121
4.5.1 Bands 1 and 2 125
4.5.2 Bands 3 and 4 127
4.5.3 Band 5 129
4.5.4 Band 6 131

5 Interpretation and Discussion **133**
5.1 Comparison with CSM predictions 133
5.1.1 CSM calculations 133
5.1.2 The Reference Concept 138
5.1.3 Routhian Plots 140
5.1.4 Alignment Diagrams 140
5.2 Systematics of neighbouring nuclei 141
5.2.1 Even-A Nd Nuclides (Z=60:$^{128-136}$Nd) 143
5.2.2 Odd-A Pr Nuclides (Z=59:$^{131-137}$Pr) 143
5.2.3 Odd-A Nd Nuclides (Z=60:$^{133-137}$Nd) 144
5.2.4 Even Pr Nuclides (Z=59:$^{130-134}$Pr) 146
5.3 ^{129}Pr 148
5.4 ^{131}Nd 155
5.5 ^{129}Nd 159
5.6 ^{128}Pr 161

6 Summary **166**

Chapter 1

Nuclear Phenomena

1.1 Introduction

It is the intention of this introductory chapter to survey the production of nuclei in states of high angular momentum and the properties of the subsequent decay of such states as accessed by discrete line nuclear spectroscopy. With recent accelerator and detector developments excited states can be produced and observed in nuclei with increasing angular momentum and decreasing cross section. The nuclei discussed in this work were populated via compound nucleus formation near to the proton drip line and are thus at the current limits of 'observability'. There are several reasons for studying these nuclei:

- Nuclear models in general require an input of parameters fitted over a broad region from which the detailed behaviour of nuclei can be calculated. More specifically, energy levels produced by the Nilsson or other single particle models depend critically upon the shape of the potential in which they are generated. A fit of the observed levels over a wide range of nuclei fixes the parameterisation of the potential. Thus it is important to study the nuclei at the extremes of stability.

- The nuclei in the region around N=70,Z=70 have long been predicted [MPS63] to be deformed in their ground states. The A$\sim$130 light rare earth nuclei are the closest experimentally accessible nuclei to this region and should thus show the transition to increasing deformation as the neutron number is decreased by virtue of the collective properties observed. The varying shape also permits the effect of increasing deformation on the single particle spectrum to be examined.

- At N$\sim$70, Z$\sim$60 the protons and neutrons occupy the same shells so that any proton neutron interaction should be maximal and the effects most obvious.

- Both protons and neutrons occupy high j orbitals so the interplay between

the collective and single particle behaviour of the nucleus via the Coriolis force should be apparent.

- Recent observation of highly deformed states has generated much theoretical and experimental interest regarding configurations upon which these structures are based and the definition of the N,Z region in which they are observed

- Other recent observations are consistent with triaxial and oblate shapes and thus probe a different degree of freedom of the nucleus.

1.2 Compound Nucleus Formation

In order to form a compound nuclear system the beam energy must generally be sufficient to overcome the Coulomb barrier [1] between target and projectile nuclei given by

$$V_{CB} = \frac{1.44 Z_t Z_p}{1.16(A_t^{1/3} + A_p^{1/3} + 2)} \frac{A_t + A_p}{A_t} \quad \text{MeV}$$

in the lab frame. Z_t, Z_p and A_t, A_p are the target and projectile atomic numbers and mass respectively. The compound system rapidly equilibrates, distributing its energy amongst all degrees of freedom and losing all projectile/target identity. Pre-equilibrium processes are not important in the temperature regions accessed here. For high Z or low A nuclear fission will be the most rapid decay mode if the fission barrier is approached. Fission is the factor limiting the maximum angular momentum that may be brought into the system; this ceiling is at a maximum at $A \sim 135$ and so is not important here.

The simple classical model of colliding black charged spheres may be used to estimate the reaction cross section as

$$\sigma = \pi(R_p + R_t)^2(1 - V_{CB}/E_p(cm))$$

and the maximum angular momentum brought into the system as

$$l_{max} \approx (R_p + R_t)[2\mu\{E_p(cm) - V_{CB}\}]^{1/2}\hbar^{-1}$$

The actual cross section and maximum angular momentum is lower than this since the higher angular momentum components of the cross section correspond to direct reactions rather than compound nucleus formation.

1.3 Decay of the Compound Nucleus

The initial excitation energy of the compound system is

$$E^* = E_p(cm) + Q$$

[1] sub-Coulomb barrier fusion does occur due to quantal effects not considered in this simple classical discussion

where $E_p(cm)$ is the centre of mass energy of the projectile and Q the reaction Q-value. The nucleus then decays via emission of particles whilst the excitation energy satisfies

$$E_i - E_f + Q_\nu \geq \frac{\hbar^2 l(l+1)}{2\mu_\nu R_\nu^2} + \frac{Z_\nu(Z - Z_\nu)e^2}{R_\nu} \tag{1.1}$$

where E_i and E_f are the excitation energies of the system before and after emission of particle ν with charge Z_ν, relative orbital angular momentum l , effective radius R_ν and reaction Q-value Q_ν.

The Coulomb term in (1.1) usually means that cooling by neutron evaporation dominates. For the compound nuclei considered here the Q-values for charged particle emission are high due to the proximity of the proton drip line so charged particle channels compete strongly. The nuclear species formed after the particle evaporation is termed an evaporation residue. If the formation of each evaporation residue is considered in the excitation energy v angular momentum plane then it is found that the residues are populated with a distribution of angular momentum and excitation energy known as the 'entry region'. The extent of this region is determined by the compound nuclear reaction cross section as a function of input angular momentum and the spread in kinetic energy of the evaporated particles. The maximum angular momentum at any excitation for a particular nucleus is delineated by the 'yrast' line, ie the envelope of states with minimum excitation for all angular momenta. The population of such residues can be estimated using statistical codes. The results of such calculations are unreliable in the highly neutron deficient regions considered here due to uncertainties in the input parameters for the codes. Predictions from the Cascade [Pu77] statistical model code using default input parameters are shown in Table 1.1.

^{74}Se(^{58}Ni@300 MeV					^{76}Se(^{58}Ni@300 MeV					
	La	Ce	Pr	Nd		La	Ce	Pr	Nd	Pm
123	9				125	10	2			
124					126					
125	22	28			127	5	44	1		
126		83	5		128		49	22		
127		2	1		129		8	5		
128		74	77	1	130		13	80	25	
129			60	15	131			34	45	2

Table 1.1: Predictions of the relative cross sections of formation for the compound nuclear reactions used to populate the nuclei discussed in this work.

The centrifugal term in 1.1 favours the emission of particles with a large reduced mass μ_ν. This and the Coulomb term particularly favour α-particle emis-

sion which may still be energetically possible below the proton/neutron emission threshold (~8MeV).It is generally desirable to produce the nucleus of interest by a 'clean' reaction with few competing reaction channels. In the very light rare earth region this is not possible and the reaction intensity is fragmented into many channels making the resulting data correspondingly 'dirtier'.

Below the particle evaporation threshold nuclear decay proceeds via three types of gamma ray emission [GG67]:

1. the statistical cascade removing excitation energy but little angular momentum via high energy dipole(E1) transitions.

2. the 'collective cascade' which removes angular momentum via collective stretched E2 transitions. The distribution of these transitions over many bands prevents the resolution of dicrete transitions.

3. dicrete transitions between yrast and near yrast [2] states.

The first two types of decay contribute to the unresolved background region in which discrete transitions are observed. It is the latter type of γ transitions with which this work is concerned.

1.4 General Features Observed in Level Schemes

The first general feature to note in nuclear spectra is that even-even nuclei show very few levels [3] below about 1 MeV , whilst odd-even and odd-odd nuclei show appreciable level density below this excitation. This provides evidence for the special stability of paired nucleons, the gap in even-even nuclei representing the energy required to break nucleonic pairs. A more complete discussion of this feature is postponed until Chapter 2. In the case of odd (odd) nuclei the last nucleon(s) is(are) unpaired and free to occupy various nuclear energy levels. Thus the excitation energy spectra for an odd (odd) nucleus is more complex than that of an even-even nucleus. Secondly, the excitation energy spectrum may be classified as either 'collective' (exhibiting bands of levels with smoothly varying excitation and angular momentum) or 'single particle' (exhibiting levels with erratically varying excitation energy and angular momentum). The spectrum of a nucleus may change between collective and single particle behaviour depending upon the spin and excitation energy region considered. The states populated in the neutron deficient light rare earths via compound nuclear reactions are of collective nature and only such behaviour will subsequently be considered. Besides regularity, collective behaviour is characterized by enhanced transition

[2] the next lowest states are termed 'yrare'.

[3] those levels that do appear within this 'energy gap' can be ascribed to collective excitations, ie rotational and vibrational bands.

strength. The collectivity of states may be interpreted in terms of a dynamic nuclear shape; either vibration of the nuclear shape, or in the case of statically deformed nuclei, (as the A$\sim$130 light rare earths are expected to be), rotation of the nucleus. The spectrum in such a case is characterized in terms of a mass parameter i.e. stiffness or inertia. Since the decay patterns observed in the light rare earth region appear approximately rotational the discussion will be limited to collective rotations.

1.5 Rotational Behaviour in Nuclei

Rotational behaviour is characterised by de-excitation through enhanced transitions between states which can be classified into bands with regular energy spacings. The bands may be modelled as collective rotations of a deformed nucleus based on particular intrinsic states characterised by K. If axial symmetry of the nucleus is assumed then rotation is implied around an axis perpendicular to the symmetry axis and the projection of the angular momentum (K) onto the symmetry axis is conserved. For even-even nuclei the pairing force (see Section 2.3.6) aligns nucleons into I=0 pairs so at low spins even-even nuclei have no angular momentum projection. A consideration of such an axially symmetric system [BM75] under the operation ($R_2(\pi)$) of rotation through π around the rotational axis leads to constraints on the total angular momentum that can be carried by states in a band of given K. For K=0, bands are only permitted to possess odd or even I according to the value of $r = (-1)^I$:

$$I = 0, 2, 4, \ldots \quad r = +1; \qquad I = 1, 3, 5, \ldots \quad r = -1$$

Odd-A nuclei may be considered as an appropriate even-even core with a coupled odd nucleon in which case K is determined by the projection of the angular momentum of the odd nucleon (K=Ω) and in the case of odd-odd nuclei K is determined by the projection of the angular momentum of the two odd coupled nucleons. The question as to how the angular momenta of the last two nucleons are coupled was tackled in [GM58] where it is proposed that in deformed nuclei the band head spin (and K) is given by

$$\begin{aligned} I &= \Omega_p + \Omega_n \quad ; \Omega_p = \Lambda_p \pm \tfrac{1}{2}\,,\ \Omega_n = \Lambda_n \pm \tfrac{1}{2} \\ I &= \mid \Omega_p - \Omega_n \mid \quad ; \Omega_p = \Lambda_p \pm \tfrac{1}{2}\,,\ \Omega_n = \Lambda_n \mp \tfrac{1}{2} \end{aligned} \tag{1.2}$$

which is equivalent to applying the coupling rule that the nucleons align the spin components of their angular momenta Σ_p and Σ_n (the notation used refers to the asymptotic Nilsson labels for single particle levels as discussed in section 2.3.3). For bands with K>0 there exist two degenerate intrinsic states with projections $\pm$K but invariance with respect to $R_2(\pi)$ implies that only one rotational state can be formed from these states for each value of I resulting in a sequence of states with angular momentum:

$$I = K, K+1, K+2, \ldots$$

The wave function for these states is a sum of two terms such that the matrix elements have an interference term with a sign dependent upon the signature defined as

$$\sigma = (-1)^{I+K}$$

This quantity differentiates between two classes of states within a band of states with the same intrinsic K value.

1.6 Rotational Properties of Bands

In order to discuss collective rotations it is customary to introduce the concepts of rotational frequency and moment of inertia. For a classical rotor the energy is given as a function of angular momentum by

$$E = \frac{1}{2} I\omega \quad ; \quad I = \omega\mathcal{J} \tag{1.3}$$

where ω is the rotational frequency and $\mathcal{J}$ the moment of inertia of the rotor. The rotational frequency ω can be rewritten for a rigid rotor as

$$\omega = \frac{dE}{dI} \tag{1.4}$$

which is the form of the Lagrangian multiplier ω encountered in cranking calculations. Hence, to facilitate comparison, data is often presented in terms of ω, in a suitably discretised form, rather than I. Cranking codes are not generally 3-dimensional in the sense that cranking is performed around only one axis (conventionally referred to as the 1- or x-axis defined so that the angular momentum along the y- or 2-axis is zero) perpendicular to the nuclear symmetry axis (referred to as the 3- or z-axis). For the comparison to be meaningful we therefore wish to look at ω_x, the rate of change in excitation energy with respect to increase in angular momentum aligned along the x-axis, I_x:

$$\omega_x(I) \approx \left(\frac{\Delta E}{\Delta I_x}\right)_I \approx \frac{E(I+1) - E(I-1)}{\sqrt{(I+1)(I+2) - K^2} - \sqrt{I(I-1) - K^2}}$$

where K is the projection of the angular momentum on the symmetry axis. This discrete approximation is correct to second order in ΔI. Note the rotational frequency defined is that for a (possibly imaginary) intermediate state of spin I within a $\Delta I = 2$ sequence to avoid problems associated with signature splitting. For an even-even state K=0 at low spins due to the pairing of nucleons into I=0 doublets but for odd and odd-odd systems K may be very significant depending upon how the particles are coupled. Bandhead spins can be implied from the Nilsson diagram and from systematics in the absence of a direct measurement. It is generally assumed that K remains constant within a band (unless an interaction is observed with another band) with increasing angular momentum; this is an assumption made out of necessity since the spin projection in a band is not a

direct experimental observable. Some idea of the likely K of a band may be obtained from its properties e.g. transition strengths and signature splitting. Note that K is only well defined at $\omega = 0$ (at least in cranking models) after which states of different K mix. Fortunately K mixing is only crucial when I_x does not greatly depend on K i.e. configurations involving low-Ω orbitals (and hence low-K states) or at high spins ($I \gg K$).

Two moments of inertia are commonly defined experimentally to investigate deviation of a nuclear rotor from perfect behaviour. These are

$$\text{(kinematic)} \quad \mathcal{J}^{(1)} = \frac{I}{\omega} \tag{1.5}$$

$$\text{(dynamic)} \quad \mathcal{J}^{(2)} = \frac{dI}{d\omega} = \mathcal{J}^{(1)} + \omega \frac{d\mathcal{J}^{(1)}}{d\omega} \tag{1.6}$$

For a perfect rotor $\mathcal{J}^{(1)} = \mathcal{J}^{(2)}$ but for a real nucleus the two are often very different and neither necessarily approach any constant value. For a series of $\Delta I = 2$ transitions in a rotational sequence the above moments of inertia are defined as:

$$\mathcal{J}^{(1)} = \frac{\hbar^2}{2E_\gamma}(4I - 2) \tag{1.7}$$

$$\mathcal{J}^{(2)} = \frac{4\hbar^2}{\Delta E_\gamma} \tag{1.8}$$

The $\mathcal{J}^{(2)}$ moment of inertia has the advantage that it can be defined even when the absolute spins are not known in a band.

1.7 Band Crossing

If experimental rotational states are plotted in an E_{ex} v I plane then they will usually be seen to follow a parabola (in an idealised rotational nucleus at least!) at low spins and then an abrupt change will take place. The change is highlighted even more strongly if the equivalent plot is made as a function of frequency. This behaviour can be understood if we consider a second rotational band at higher excitation initially but with a larger moment of inertia. At a certain angular momentum the second band becomes yrast. This phenomenon is termed 'band crossing' and is widely observed. The real nucleus is not as simple as this and the transition between the two bands takes place over a range of angular momenta or frequency. This is because the bands interact with each other; the sharper the crossing the weaker the interaction.

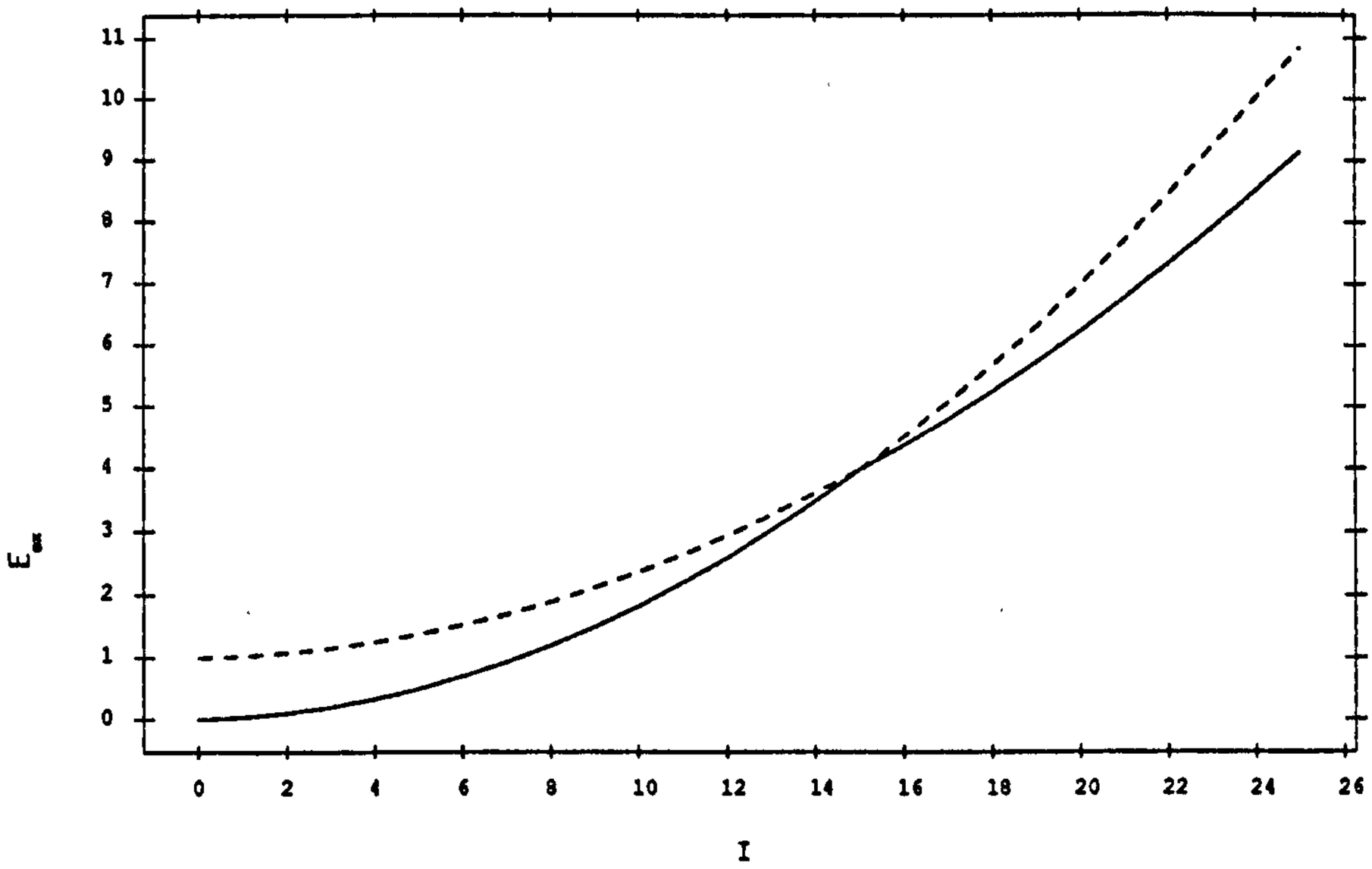

Figure 1.1: Pedagogical figure illustrating the band crossing between two (idealized) rotational bands at an initial relative excitation of 1 MeV . The moments of inertia for the bands are taken at 30 and 35 $\hbar^2$MeV $^{-1}$ which are realistic for the A=130 region.

1.8 Transition Strengths

The calculated matrix elements between states turn out to be highly sensitive to the admixtures of orbitals involved in the wavefunctions of states in any particular model. Thus the measurement of transition strengths between states provides a critical test of a model or assumptions made within a model. The total transition probability of a γ decay of multipolarity L is given by:

$$\lambda^{\gamma}(L\pi) = \frac{8\pi(L+1)}{L[(2L+1)!!]^2\hbar}\left(\frac{E_\gamma}{\hbar c}\right)^{2L+1} B(L\pi) \tag{1.9}$$

where the reduced transition probability $B(L\pi)$ is defined as:

$$B(L\pi) = \frac{1}{2j_i+1} |< j_f \parallel \mu(L\pi) \parallel j_i >|^2 \tag{1.10}$$

Direct determination of the reduced transition probability requires an accurate measurement of the lifetime and spin of the emitting state. Some information can be gleaned from branching ratios between decays from the same initial state, the ratio giving a measure of the relative transition probabilites but not the absolute values. In particular, for coupled rotational bands where both inter-band (i.e.

$\Delta J = 1$ transitions between states of opposite signature) and intra-band (i.e. $\Delta J = 2$ transitions between states of the same signature) transitions are observed the ratio

$$\frac{B(M1)}{B(E2)} = \frac{0.697}{1+\delta^2}\frac{E_\gamma(\Delta J=2)^5}{E_\gamma(\Delta J=1)^3}\frac{\lambda^\gamma(\Delta J=1)}{\lambda^\gamma(\Delta J=2)} \quad (\mu_N/eb)^2 \qquad (1.11)$$

can be determined from the relative transition intensities and energies. The energies in 1.11 and the constant is derivable by substitution into Equation 1.10. The mixing ratio δ is the ratio of the amplitude of the E2 J=1 component to the stretched M1 component in the $\Delta J = 1$ transition. This will generally be small and other admixtures of more exotic multipolarity in this and the $\Delta J = 2$ transition are known to be negligible. This quantity is of interest since the $B(M1)$ magnitude is largely determined by the free valence nucleons whilst the $B(E2)$ is directly dependent on the quadrupole deformation of the proton distribution.

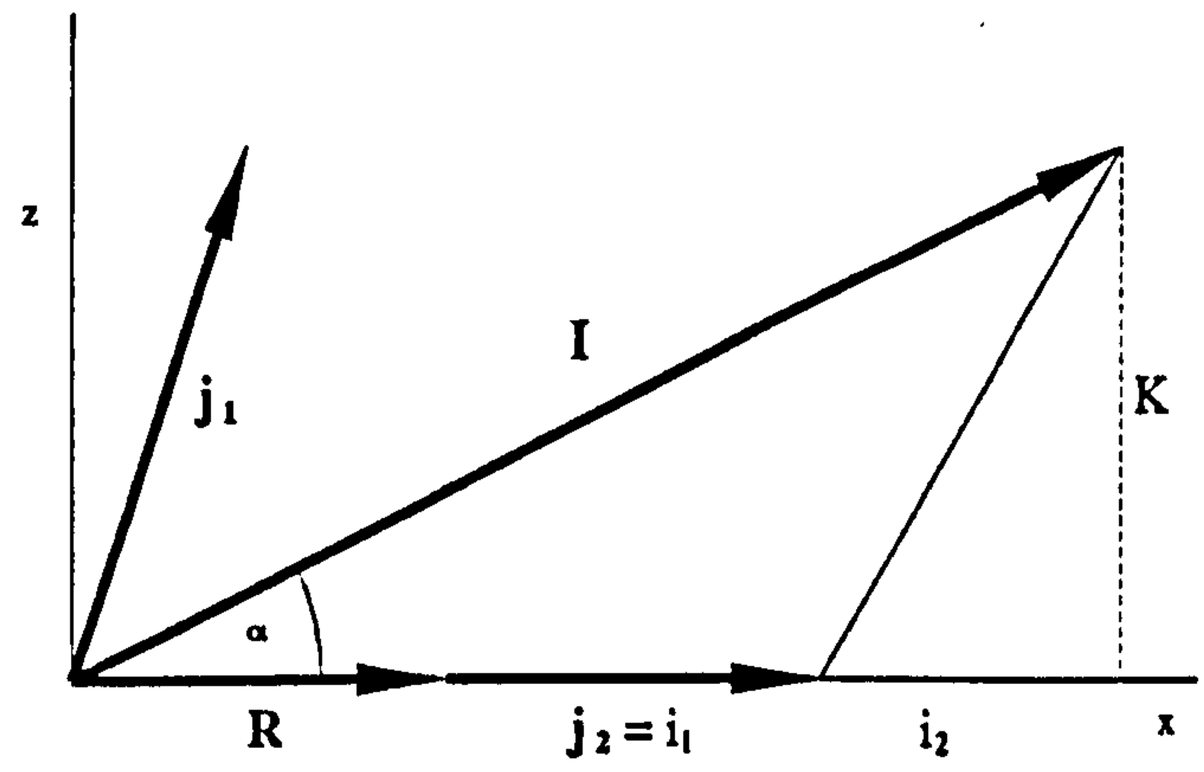

Figure 1.2: Coupling of quasiparticle and core rotational angular momenta to a state of total angular momentum I as envisaged semi-classically. i_1 and i_2 are the projections on the single nucleonic angular momenta onto the rotational (x) axis. The vectors for (1) FAL and (2) RAL quasiparticles are shown. DAL can be considered in a manner similar to the FAL case except that in this case $i_1 = 0$. The components of angular momentum perpendicular to I can be obtained by noting that $\sin\alpha = \frac{K}{I}$.

The magnetic properties of a single nucleon depend strongly upon the orientation of its angular momentum vector. Three different alignments are distinguished; Rotational ALignment (RAL) where the nucleonic angular momentum is aligned along the rotational axis and perpendicular to the symmetry axis, Deformation ALignment where the angular momentum is aligned along the symmetry

axis and Fermi ALignment where the angular momentum is aligned according to the level of the Fermi surface a particular nuclear shell. The three cases are well defined by semi-classical orbits and can be identified from the behaviour of quasiparticle levels in the cranked shell calculations discussed later. Donau and Frauendorf [DF82] propose a simple geometrical model to estimate the $B(M1)$ for a given quasiparticle configuration semi-classically. The magnetic moment (μ) can be expressed in terms of the rotational and single quasi-particle angular momenta as:

$$\mu = g_R \mathbf{R} + \sum g_\nu \mathbf{j}_\nu = g_R \mathbf{I} + \sum (g_\nu - g_R)\mathbf{j}_\nu \tag{1.12}$$

The g_R-factor is that associated with the collective (vacuum) configuration and may be estimated as Z/A whilst the g_ν-factors refer to those of the quasi-particles and, for a high-j intruder orbital, may be estimated by the single particle (Schmidt) values

$$g_{j_{s,p}} = g_l \pm \frac{(g_s - g_l)}{2l+1} \quad ; \quad j = l \pm \frac{1}{2} \tag{1.13}$$

Classically, $M1$ radiation is generated by the component of the magnetic moment perpendicular to the angular momentum ($\mu_\perp$). The $M1$ matrix element can thus be approximated geometrically as

$$\begin{aligned} < II \mid (M1) \mid II > &= \sqrt{\frac{3}{8\pi}}\mu_\perp \\ &\approx \sqrt{\frac{3}{8\pi}}\frac{K}{I}[(g_1 - g_R)(\sqrt{I^2 - K^2} - i_1) - (g_2 - g_R)i_2] \end{aligned} \tag{1.14}$$

where the quantities are as defined in Figure 1.2. If the degeneracy between the two signatures of a band is destroyed and a signature splitting $\Delta e'$ is introduced then a further motion corresponding semi-classically to an oscillation between states with $\pm K$ is introduced. This gives the B(M1) strength a signature depen-dance and the B(M1) must be multiplied by a factor $(1 \pm \frac{\Delta e'}{E})$ for transitions of energies $E_\gamma = \overline{E} \mp \Delta e'$.

Chapter 2

The Theoretical Nucleus

2.1 Introduction

Ideally one would like to understand all nuclear phenomena in terms of individual nucleonic interactions. This remains a distant ideal due to both the complexity of the problem and an incomplete knowledge of the internucleonic force. Thus attempts to describe the nucleus are inherently phenomenological since even the most microscopic of theories must rely on a model strong force. Other models tend to treat the nucleus classically to some extent. This chapter attempts to summarise some of the models pertinent to the study of deformed heavy nuclei. Much of the material covered is contained in standard texts, notably [RS80,Ro70,BM75] which have been relied upon heavily.

2.2 Macroscopic models

2.2.1 The Liquid Drop Model

The Liquid Drop Model (LDM) [We35] has its basis in the saturation of the nuclear force which allows one to conceive of an incompressible 'nuclear fluid'. The nuclear fluid is not, however, a direct classical analogue since the nucleons are on average separated by a distance (~2.4fm) greater than the distance at which the inter-nucleon force is minimal (~0.7fm) due to the Fermi nature of the statistics obeyed. The LDM reproduces bulk nuclear properties of closed shell nuclei well (e.g. binding energies) by considering the energy of the nucleus to be given in a form appropriate to a sharply defined liquid drop

$$\begin{aligned} E_{LDM} &= E_{volume} + E_{surface} + E_{coulomb} + E_{symmetry} + E_{odd-even} \\ &= -a_v A + a_s A^{2/3} + a_c Z^2 A^{-1/3} + a_y (N-Z)^2 A^{-1} - \delta(A) \end{aligned} \quad (2.15)$$

where the constants are fitted to known masses. The above formulation is applicable to a spherical drop. Equation 2.15 may be generalised by the inclusion of extra degrees of freedom corresponding to the nuclear shape. This manifests itself in a shape dependence of the surface and Coulomb terms. The term

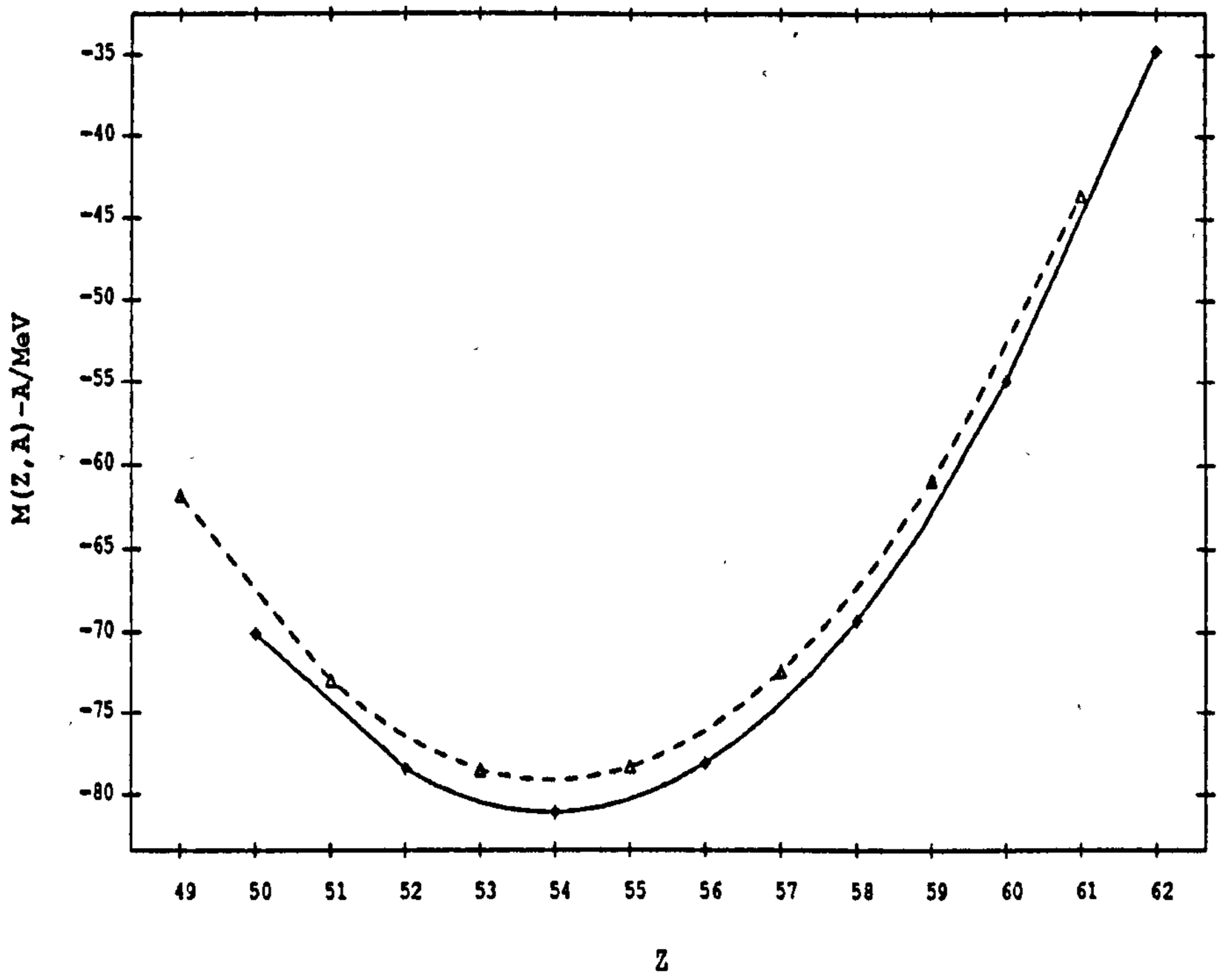

Figure 2.1: Mass excess for a set of A=128 isobars showing the pair gap. Note the nuclides discussed in this work are those corresponding to Z=59,60 and are unstable with respect to β^+ and electron capture decay. The nuclear masses are calculated using equation 2.15 and constants found in [Re72]. The energy difference between the even-even (solid) and odd-odd (dotted) isobars corresponds to approximately twice the pair gap discussed in section 2.3.6. The corresponding curve for odd-A nuclides shows no gap implying that the pairing strength is approximately the same for protons and neutrons.

$\delta(A)$ is usually parameterised as $a_p A^{-3/4}$ with $a_p = 0$ for odd-even nuclei and $a_p \pm$ constant for odd-odd and even-even nuclei respectively, and was included within the model on a purely empirical basis. $\delta(A)$ is known as the pairing energy and is microscopic in origin (see section 2.3.6). The model can be further refined by the admission of surface diffuseness (the Droplet model [MS69]). The LDM was extended [CPS74] by the inclusion of a rotational term in an attempt to predict the stability of the nucleus to fission resulting in the Rotating Liquid Drop Model (RLDM) where the energy is now determined by:

$$E_{RLDM}(\beta) = E_{LDM}(\beta) + E_{Rotation}(\beta) \quad ; E_{Rotation}(\beta) = \frac{\hbar^2 I^2}{2\mathcal{J}(\beta)} \tag{2.16}$$

where β denotes a set of shape parameters. Excitations can be predicted corresponding to $\beta-$ and $\gamma-$ shape vibrations. Generally the model is not very successful in predicting excited states unless the parameters are treated empirically (the Collective Model) and we must look to a more microscopic description. The fact that the LDM is so globally successful in its predictions of bulk properties where the microscopic theories generally fail (and are very computationally exhaustive) has ensured the continuing applicability of this model, particularly within the macroscopic-microscopic approach (see Section 2.4.1.)

2.2.2 The Collective Model

The shape of the nuclear liquid drop surface may be parameterised as

$$R(\theta,\phi) = R_o[1 + \alpha_{00} + \sum_{\lambda=1}^{\infty}\sum_{\mu=-\lambda}^{+\lambda} \alpha^*_{\lambda\mu} Y_{\lambda\mu}(\theta\phi)]$$

The term α_{00} is chosen to conserve the nuclear volume $V = \frac{4}{3}\pi R_0^3$ which expresses the incompressible nature of nuclear matter. Generally a very restricted set of λ is required to describe the nuclear shape; $\lambda = 1$ corresponds to a trivial translation for small deformations and some subset of $\lambda = 2,3,4$ is sufficient. By a rotation of the coordinate system into the body fixed coordinate system defined by the principal axes of the mass distribution of the drop the $\alpha_{\lambda\mu}$'s for $\lambda = 2,4$ can be defined in terms of the parameters β_2, β_4, γ and 3 Euler angles describing the rotation $\Omega = (\alpha,\beta,\gamma)$ [NR81]:

$$\begin{array}{rclrcl} \alpha_{20} & = & \beta_2\cos\gamma & \alpha_{40} & = & \frac{1}{6}\beta_4(5\cos^2\gamma+1) \\ \alpha_{22} = \alpha_{2-2} & = & \frac{-1}{\sqrt{2}}\beta_2\sin\gamma & \alpha_{42} = \alpha_{4-2} & = & \frac{-1}{12}\sqrt{30}\beta_4\sin^2\gamma \\ & & & \alpha_{44} = \alpha_{4-4} & = & \frac{1}{12}\sqrt{70}\beta_4\sin^2\gamma \end{array} \qquad (2.17)$$

where γ is defined according to the Lund convention [ALL76]. γ values that are multiples of $\pi/3$ correspond to axial shapes, those in between, triaxial shapes. In the static frame the interval $0 \le \gamma \le \pi/3$ is sufficient to describe the nuclear shape, whereas $0 \le \gamma \le \pi$ is needed to describe a shape rotating about a specific axis. One form of excitation of such a system is a dynamical shape oscillation (i.e. variation of the β or γ coordinate) and such states have been observed. The model of a liquid drop only permits the existence of spherical ground states. Shell effects can give rise to non-spherical stable ground states in which case rotational excitations can be described in terms of time dependent $\alpha_{\lambda,\mu}$ coefficients in the laboratory frame. Such a model leads to the Bohr Hamiltonian [Bo52]

$$T = \frac{1}{2}\sum_{k=1}^{3}\mathcal{J}_k\omega^2 + \frac{1}{2}B(\dot\beta^2 + \beta^2\dot\gamma^2)$$

with $\mathcal{J}_k = 4B\beta^2\sin^2(\gamma - \frac{2\pi}{3}k)$. The β and γ vibrations are coupled to the rotational energies by the dependence of the moments of inertia $\mathcal{J}_k$ on the deformations β,γ. We can see from such a Hamiltonian that nuclei may be visualised

as lying somewhere between the limits of a rotor and a vibrator. In the light rare earth region we are concerned with transitional nuclei and both modes are evident.

2.3 Microscopic Models

2.3.1 The nuclear problem

A reasonably full microscopic theory of the nucleus would entail the solution of the many body Schrodinger equation:

$$H\Psi = \{\sum_{i=1}^{A} \frac{-\hbar^2}{2m_i}\Delta_i + \sum_{i<j}^{A} \nu(i,j)\}\Psi = E\Psi \tag{2.18}$$

where Ψ is a function of A coordinate sets {i} ({$\mathbf{r},\sigma,\tau$} involving position, spin and isospin). Already this Hamiltonian represents a considerable simplification assuming only 2–body interactions [1] and a non-relativistic formulation [RS80] and yet the idea of a direct solution of such a problem is completely untenable. Hence we are 'simply forced to simplify the force' [Mo62].

2.3.2 Shell Models

The first major simplification that can be made is to replace the complex 2–body interaction $\nu(i,j)$ by an average central potential V(i). This has the great advantage that the eigenfunctions of

$$H\Psi = \{\sum_{i=1}^{A} \frac{-\hbar^2}{2m_i}\Delta_i + V(i)\}\Psi = E\Psi \tag{2.19}$$

now become anti-symmetrised products (Slater determinants) of the solutions to the single particle Hamiltonian

$$h_i\Phi = \{\frac{-\hbar^2}{2m_i}\Delta_i + V(i)\}\Phi = \varepsilon_i\Phi \tag{2.20}$$

and hence the approximation is termed the Independent Particle Model(IPM). The A levels lowest in energy are then considered to be occupied by particles and the remaining states by holes. Excitations to this ground state are made by exchanging particles and holes.

It is hoped that V(i) in such a model accounts on average for the 2–body (and possibly higher order) interactions; the extent to which this is true depends on the situation in question. If the potential V(i) introduced is spherically symmetric then we obtain the Spherical Shell Model(SSM) which has been successful in

[1] there is no *a priori* physical reasoning behind this; it is merely a reflection of the computational difficulties involved

its predictions for near-closed shell nuclei (i.e. V(i) gives matrix elements that are a reasonable approximation to those of $\nu(i,j)$). However the SSM fails to describe the collective behaviour (e.g. rotational bands, E2 strengths many times greater than the single particle estimates and low-lying 2^+ states) observed far from closed shells.

This failure lead Rainwater to introduce of the idea of deformed nuclei and the calculation of nuclear energy levels within a spheroidal nuclear potential [Ra50]. The shape and orientation of the average potential must now be considered as dynamical variables, variations in this field giving rise to collective nuclear motions. If we consider the nuclear wave function to be separable in the form

$$\Psi = \chi_{intrinsic} \cdot \Phi_{vibrational} \cdot \mathcal{D}_{rotational} \tag{2.21}$$

then we have the basis of the phenomenological Unified model which descibes the coupling of these modes. Implicit in the adoption of a mean field is the assumption that the field reflects internucleonic correlations mediated by some component of the nuclear force. Current thought seems to suggest that the p-n interaction is important in creating a deformed field [DNSW88,FP77].

Having calculated a set of basis states, we may now attempt to correct for the inadequacies of V(i) as an approximant to $\nu(i,j)$ in equation 2.18 by diagonalising the residual interaction

$$V_{residual} = \sum_{i<j} \nu(i,j) - \sum_{i} V(i) \tag{2.22}$$

within the basis of states obtained in 2.20. Different methods exist to treat different parts of the residual interaction. Each reflects a different component of the internucleonic force. Of particular pertinence to deformed nuclei is the short range pairing part of the residual interaction (see Section 2.3.6).

The replacement of the 2–body interaction by a potential leads to several problems associated with the breaking of symmetries present in the 'true' Hamiltonian (2.18). In particular the deformed mean field breaks rotational symmetry and destroys angular momentum conservation. The z-component of angular momentum is still retained as a good quantum number provided the deformation of the field is restricted to axial symmetry. Many of the more complex models attempt to restore these symmetries or improve upon the independent particle assumptions by accounting for the residual interactions within the basis provided by the IPM states. Deformed IPM results are usually presented in the form of level diagrams as functions of some shape parameter of the mean field (see Figures 2.2 and 2.3).

2.3.3 The Nilsson Model

Probably the most widely used phenomenological potential describing the average field in a deformed IPM framework is the Nilsson or Modified Harmonic Oscillator (MHO) potential. In its simplest form it assumes the density of the nucleus

to be ellipsoidal and the average potential to closely follow this shape due to the short range of the nuclear force compared to the average nuclear radius. The Hamiltonian may then be approximated to that of an anisotropic harmonic oscillator:

$$V_{osc} = \frac{-\hbar^2}{2m}\Delta + \frac{m}{2}(\omega_x^2 x^2 + \omega_y^2 y^2 + \omega_z^2 z^2) \tag{2.23}$$

Equation 2.23 is separable in x, y, z and the deformation is implicit in the fact that the oscillator frequency is inversely proportional to the dimensions of the half axes of the elliptical potential. In order to mimic the nuclear potential more accurately the oscillator is modified [Ni55]

$$h = V_{osc} + C\mathbf{l}.\mathbf{s} + D\mathbf{l}^2 \tag{2.24}$$

where l.s is the spin-orbit term [2] and the $\mathbf{l}^2$ term is introduced to correct for some of the deficiencies of the oscillator potential as an approximant to the actual nuclear potential. The latter term has the effect of depressing the high angular momentum states (one problem with the Nilsson model is in fact that it brings down some of the high j states too sharply) and imitating the level ordering of a more realistic potential; in some sense it 'squares off' the potential. The field deformation is introduced into the oscillator frequencies as [Sz83] [3]

$$\begin{aligned}
\omega_x^2 &= \omega_o^2(\varepsilon_2,\gamma)(1 + \frac{1}{3}\varepsilon_2\cos\gamma + \frac{1}{\sqrt{3}}\varepsilon_2\sin\gamma) \\
\omega_y^2 &= \omega_o^2(\varepsilon_2,\gamma)(1 + \frac{1}{3}\varepsilon_2\cos\gamma - \frac{1}{\sqrt{3}}\varepsilon_2\sin\gamma) \\
\omega_z^2 &= \omega_o^2(\varepsilon_2,\gamma)(1 - \frac{2}{3}\varepsilon_2\cos\gamma)
\end{aligned} \tag{2.25}$$

subject to the conservation of volume condition [LVH70]:

$$\omega_x\omega_y\omega_z = \mathring{\omega}_o^{\,3} = \text{constant}$$

where $\mathring{\omega}_o$ is a constant dependent only on A ($\hbar\,\mathring{\omega}_o \sim 41A^{\frac{1}{3}}$MeV). [4]

---

[2] an analogous term is obtained from a relativistic treatment of electrons in an atom. The l.s form is only correct for an isotropic potential , a more general form being $\frac{\hbar}{2mc}^2 \nabla V.(\sigma \wedge \mathbf{p})$. The inclusion of such a force is as a result of the overwhelming success of the $j-j$ coupling scheme in the SSM after the inclusion of an l.s term [Ma49]

[3] originally Nilsson used the shape parameter δ with the oscillator frequencies defined as :

$$\begin{aligned}
\omega_x^2 = \omega_y^2 = \omega_\perp^2 &= \omega_o^2(\delta)(1 + \frac{2}{3}\delta) \\
\omega_z^2 &= \omega_o^2(\delta)(1 - \frac{4}{3}\delta)
\end{aligned}$$

[4] such an expression leads to an r.m.s radius of the proton matter some 5-10% less than that of the neutron matter. Approximately equal proton and neutron radii can be obtained using the

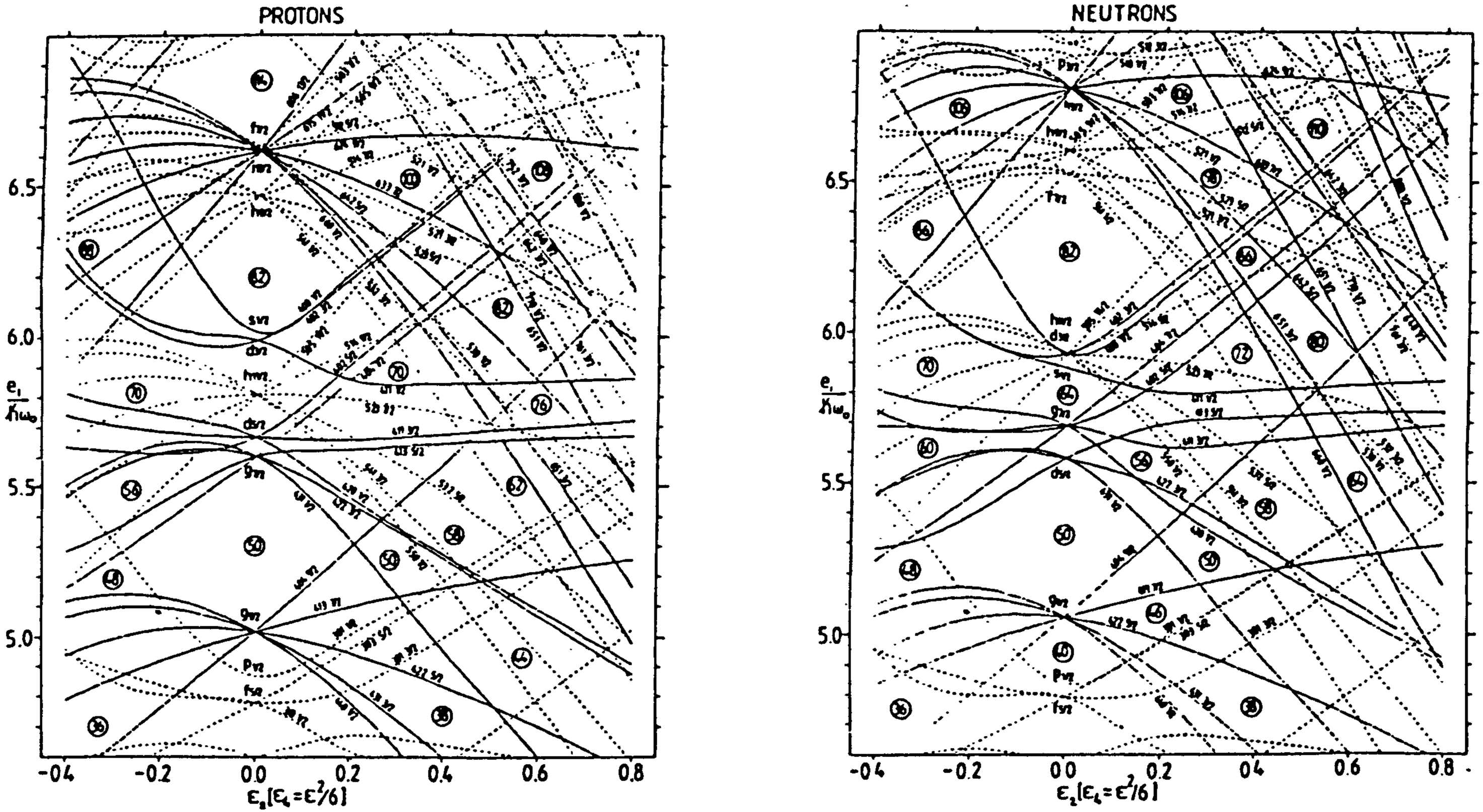

Figure 2.2: Single Particle levels calculated in the Nilsson Potential

Generally the MHO Hamiltonian is solved in a stretched cylindrical coordinate system $\xi = x\sqrt{m\omega_x/\hbar}$ etc, and $\rho^2 = \xi^2 + \zeta^2 + \eta^2$ in which V_{osc} becomes:

$$V_{osc} = \frac{1}{2}\hbar\omega_\circ(\rho^2 - \frac{2}{3}\varepsilon\rho^2 P_2(\cos\theta_t))$$

where $P_2(\cos\theta_t)$ is a Legendre polynomial as described in the stretched coordinate system. Such a transformation may be thought of as restoring the spherical symmetry of the problem and has the advantage that coupling between shell N and $N \pm 2$ [5] is made negligible. V_{osc} may be simply generalised by the addition of higher order terms to account for more exotic potential shapes. In particular a hexadecupole distortion (ε_4) is often included and the reflection asymmetric octupole term (ε_3) is of increasing interest in some regions. A more sophisticated MHO Hamiltonian is [NTS69]:

$$\begin{aligned} H &= \frac{1}{2}\hbar\omega_\circ(\varepsilon_2,\varepsilon_4)[-\Delta_\rho + \frac{2}{3}\varepsilon_2\frac{1}{2}(2\frac{\partial^2}{\partial\xi^2} - \frac{\partial^2}{\partial\zeta^2} - \frac{\partial^2}{\partial\eta^2}) + \rho^2 \\ &- \frac{2}{3}\varepsilon_2\rho^2 P_2(\cos\theta_t) + 2\varepsilon_4\rho^2 P_4(\cos\theta_t)] - 2\kappa\hbar\,\mathring{\omega}_\circ\,(l_t.s - \mu(\rho^4 - <\rho^4>_N)) \end{aligned}$$

where the constants κ and μ are related to C and D in equation 2.24 and volume conservation is achieved by a scaling of $\omega_\circ$:

$$\frac{\omega_\circ}{\mathring{\omega}_\circ} = \frac{1}{(1+\frac{1}{3}\varepsilon_2)(1-\frac{2}{3}\varepsilon_2)^{\frac{1}{2}}}\int_{-1}^{+1}\frac{\frac{1}{2}d(\cos\theta)}{1-\frac{2}{3}\varepsilon_2 P_2(\cos\theta)+2\varepsilon_4 P_4(\cos\theta))^{\frac{3}{2}}} \qquad (2.26)$$

The $\rho^4 - <\rho^4>_N$ term is a correction term analogous to the l^2 term in 2.23 (the matrix elements of ρ^4 being the same as those of $-\frac{1}{2}l^2$ apart from additive constants) with $<\rho^4>_N$ being subtracted to lessen the overall shift in energy of the shell N. The parameters κ and μ are optimized to reproduce the experimental level schemes in the region of interest subject to the proviso that at $\varepsilon = 0$ (the spherical case) the level order of the SSM is retained. With increasing amounts of data at different deformations these parameters are constantly being improved. The CSM calculations presented in this work are performed within the Nilsson framework with parameters from [BR85] and an improved set of parameters for the $A \sim 120 - 140$ region has been reported [ZX88]. The κ, μ values used are N dependent which corresponds to the use of a different potential for each oscillator

---

expressions:

$$\begin{aligned} \mathring{\omega}_n &= \mathring{\omega}_\circ\,(1 + \frac{1}{3}\frac{N-Z}{A}) \\ \mathring{\omega}_p &= \mathring{\omega}_\circ\,(1 - \frac{1}{3}\frac{N-Z}{A}) \end{aligned}$$

The use of different oscillator frequencies for proton and neutron levels may also take into account the Coulomb term for the proton levels

[5] or more correctly N_t in the stretched coordinate frame

shell; this does not lead to orthogonality problems provided the complete problem is diagonalised simultaneously.

Finally a note must be made regarding the labelling of the levels in such diagrams. In the limit of small deformations ϵ may be treated as a small perturbation to the SSM eigenfunctions $|Nlj\Omega>$ and these quantum numbers may be used to characterise the levels. At large deformations the spin–orbit and $\mathbf{l}^2$ terms in equation 2.24 become negligible and the levels can be characterised (for an axially symmetric potential) by the quantum numbers of the anisotropic oscillator eigenfunctions $|Nn_z\Lambda\Omega>$. N is the total number of oscillator quanta, n_z the projection of the number operator onto the z-axis and $\Omega = \Lambda + \Sigma$ where Λ is the orbital and Σ the spin angular momentum. The parity of the orbitals is given by $\pi = (-1)^l = (-1)^N$ and each orbital is 2-fold degenerate with respect to $\pm\Omega$.

2.3.4 The Woods-Saxon Potential

A generalised version of the Woods-Saxon (WS) potential is being used with increasing frequency in many varieties of calculations for deformed nuclei. It has the advantage of a more 'realistic' character than the MHO potential in that it incorporates a surface diffuseness, has a 'squarer' bottom and the correct asymptotic behaviour [6]. This removes the need for arbitrary correction terms like the l^2 term in the MHO. The potential does however pose additional computational problems hence its restricted use until recently. The deformed WS potential is of the form:

$$V_{WS}(\mathbf{r},\beta) = \frac{V_0}{1+\exp\{\frac{dist_\Sigma(\mathbf{r},\beta)}{a}\}} \tag{2.27}$$

where $V_0(<0)$ and a are constants representing the potential depth and surface diffuseness respectively and $dist_\Sigma$ represents the distance between the point $\mathbf{r}$ and the nuclear surface Σ, with the negative direction taken to be inside the surface [ND85]. The nuclear surface Σ is defined by

$$\Sigma : R(\theta) = C(\beta_2,\beta_4\ldots)R_0[1+\beta_2 Y_{20}(\cos\theta)+\beta_4 Y_{40}(\cos\theta)+\ldots] \tag{2.28}$$

where $C(\beta_2\beta_4\ldots)$ is found by applying the constant volume constraint and R_0 is the rms radius. The spin-orbit term is still found to be important in reproducing correct level ordering and a classical Coulomb term is generally included. The deformation parameters are as described in section 2.2.2 and may be related to the Nilsson deformation parameters by an expansion of the elliptical Nilsson field in terms of spherical harmonics. Approximate conversion formulae between the parameters may be found in [LVH70].

[6] the MHO potential is infinite and therefore does not possess unbound states whilst the WS potential falls to zero rapidly beyond the nuclear surface as one would expect

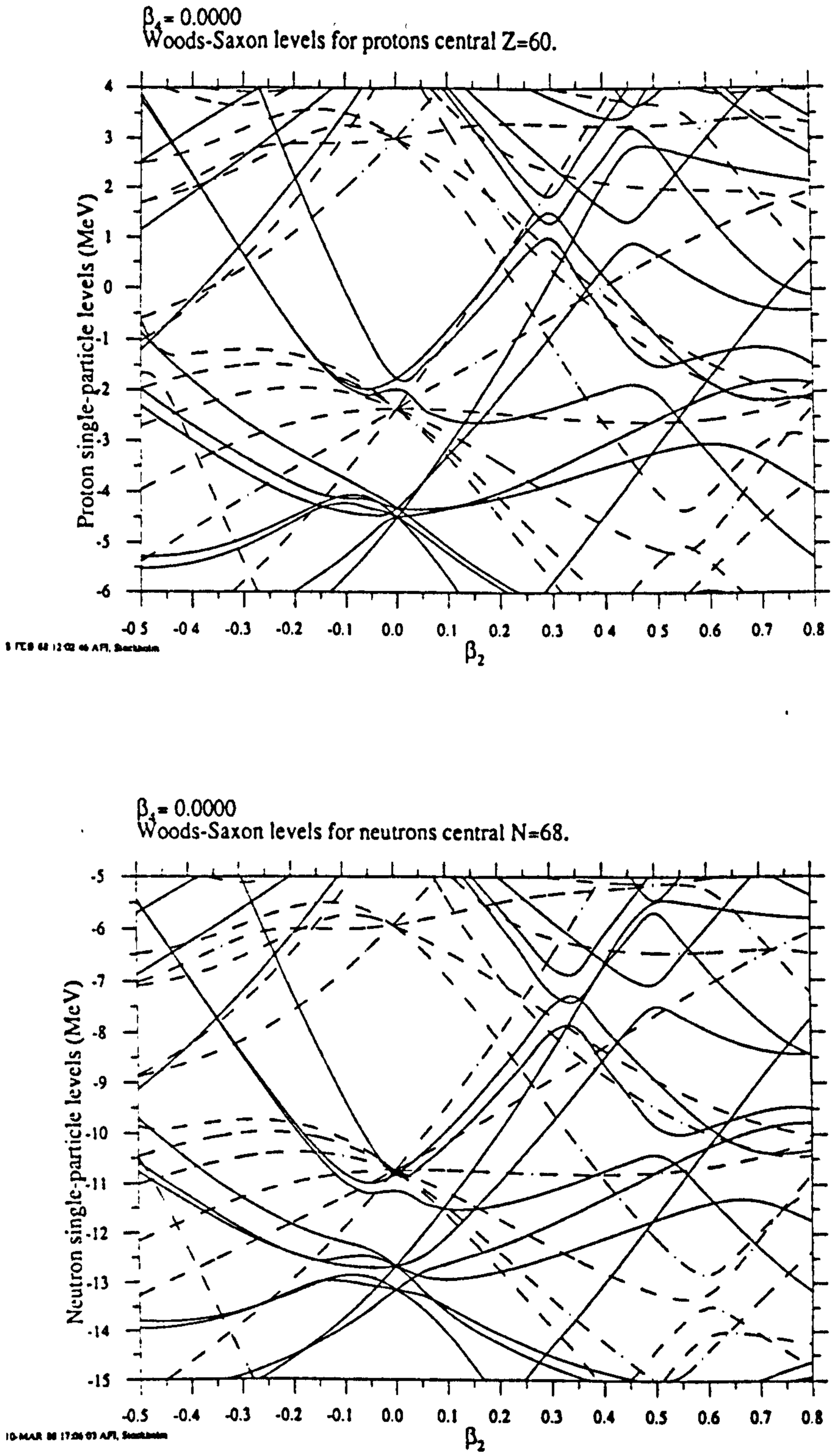

Figure 2.3: Single particle proton *top* and neutron *bottom* levels appropriate to the A=130 region calculated within a Woods-Saxon potential

2.3.5 The Cranking Concept

The idea of cranking [In54] was originally introduced to account for the nuclear moment of inertia which can be derived by rotating an intrinsic wavefunction and evaluating the energy increase. The moments thus calculated were in agreement with the rigid body moment but a realistic reduction to the order of experimental moments requires the inclusion of pairing (see section 2.3.6 and [Be59]). Despite the fact that the derivation of the model is not clear cut [7] nearly all microscopic theories of the nucleus at high spin rely on the cranking formalism. The Cranking model has the advantage of treating collective modes as summed single particle modes and the model thus lends itself to a description of both collective and single particle behaviour on an equal footing. The cranking wavefunctions are solutions to the Hamiltonian

$$H' = H - \omega j_x \tag{2.29}$$

and must be thought of as intrinsic functions. The major drawback with the cranking model is that it violates the rotational invariance of the true Hamiltonian owing to the adoption of an externally imposed fixed rotation axis and thus the resultant eigenfunctions of H' are not eigenstates of angular momentum. Rotational invariance can be restored by the use of projection methods permitting transition rates and magnetic moments (which are very sensitive to admixtures of other states) to be calculated. Such calculations are very difficult computationally. Despite destroying rotational invariance, the cranking term does leave the operation of rotation through π around the cranking axis as a symmetry of the Hamiltonian provided only even shape multipoles are included in the deformed field[8]. Such a rotation is acheived by the operator

$$\hat{R}_x(\pi) = e^{-iJ_x\pi} \quad : \hat{R}_x(\pi)^4 = 1 \tag{2.30}$$

and the eigenvalue of $\hat{R}_x$ is denoted $r = e^{-i\pi\alpha}$. Both α and r are commonly referred to as signature in literature[9], $\alpha = 1/2$ corresponding to $r = -i$ and $\alpha = -1/2$ to $r = i$ etc.

Cranking is most frequently encountered in 2 flavours, the self-consistent Cranked Hartree-Fock Bogoluibov(CHFB) formalism (section 2.3.8) and the simpler Cranked Shell Model (section 2.3.9).

---

[7] the cranking model can be derived classically from a consideration of a body rotating with respect to a stationary(laboratory) system and then making the usual quantum mechanical correspondance between observables and operators [BG85] ; semi-classically by a consideration of the variational principle under the subsidiary condition $< J_x >= I$ [dV83]; quantum mechanically in the limit of large deformation and weak K admixtures ($K << 1$) [RS80]

[8] for odd multipoles this symmetry is destroyed but the Hamiltonian is still invariant to the operation of reflection followed by rotation through π ie $s = r\pi$ is a conserved quantum number where s is termed the simplex and π is the parity

[9] it is more correct to refer to α as the signature exponent

2.3.6 Pairing Correlations

Many experimental facts point to the existence of nuclear pairing (short range particle-particle) correlations; for example, the energy gap seen in the spectra of spherical even-even nuclei and the odd-even ground state mass difference (see figure 2.1). Such correlations are strongest when coupling nucleonic pairs to I=0, M=0 states. This may be understood within the SSM by considering that the spatial overlap between time reversed spherical states is maximal [10] and hence an attractive 2-nucleon force will tend to favour such states [Ma50]. For near spherical nuclei where the states in a j-shell are almost degenerate the Seniority Scheme [RT52] can be used to describe spectra in terms of number of particles within the shell and seniority (the number of particles that are unpaired). This model breaks down for deformed regions, where the levels are no longer degenerate, and a different description of pairing is required.

The pairing term in an IPM Hamiltonian can be represented as

$$-\frac{1}{4}\sum_{k_1k_2k_3k_4}\overline{\nu}_{k_1k_2k_3k_4}a^\dagger_{k_1}a^\dagger_{k_2}a_{k_4}a_{k_3} \tag{2.31}$$

where $\overline{\nu}_{k_1k_2k_3k_4} = \nu_{k_1k_2k_3k_4} - \nu_{k_1k_2k_4k_3}$ represents the anti-symmetrised matrix elements of the interaction ν(i, j). This is often approximated by the pure pairing force $\overline{\nu}_{k_1k_2k_3k_4} = G \;\; \forall\{k\}, k_2 = \overline{k_1}, k_4 = \overline{k_3}$ acting on a restricted space of states in the proximity of the Fermi surface. A description of such a pair force is provided within the BCS framework [BCS57] introduced into nuclear physics by [BMP58]. The ansatz

$$\begin{aligned} |BCS> &= \textstyle\prod_{k>0}(U_k + V_k a^\dagger_k a^\dagger_{\overline{k}})\,|->\\ &\propto |-> + \textstyle\sum_{k>0}\frac{V_k}{U_k}a^\dagger_k a^\dagger_{\overline{k}}\,|-> + \tfrac{1}{2}\textstyle\sum_{k,k'>0}\frac{V_kV_{k'}}{U_kU_{k'}}a^\dagger_k a^\dagger_{\overline{k}}a^\dagger_{k'}a^\dagger_{\overline{k'}})\,|-> + \ldots \end{aligned} \tag{2.32}$$

is made for the ground state even-even wave function with U_k, V_k representing variational parameters to be determined, $|->$ the particle vacuum, and the index k running over half the configuration space .[11]

Such a wavefunction has the disadvantage of being composed of pairwise interacting particles. The simplicity of an IPM may be restored by applying the linear Bogoluibov-Valatin transformation:

$$\begin{aligned} \beta^\dagger_k &= U_k c^\dagger_k - V_k c_{\overline{k}}\\ \beta^\dagger_{\overline{k}} &= U_k c^\dagger_{\overline{k}} + V_k c_k\\ \beta_k &= U_k c_k - V_k c^\dagger_{\overline{k}}\\ \beta_{\overline{k}} &= U_k c_{\overline{k}} + V_k c^\dagger_k \end{aligned}$$

which enables us to rewrite the BCS ground state 2.32 as

$$|BCS>=\prod_{\forall k}\beta_k\,|-> \tag{2.33}$$

---

[10] obviously the overlap of like states is Pauli forbidden

[11] the full space is generated by the states $\{k, \overline{k}\}$, $\overline{k}$ being the time reversed state

Thus we have regained a ground state in terms of a gas of non-interacting fermions known as quasiparticles[RS80]. The pairing term 2.31 is likewise transformed into the quasiparticle basis and the resulting interaction is contracted into a series of normal ordered terms (with respect to the quasiparticle vacuum). The interaction is now truncated to include only terms of order $\beta^\dagger_{\bar{k}}\beta^\dagger_k, \beta_{\bar{k}}\beta_k$ or less. The terms ignored constitute the residual interaction which is assumed to be small. This destroys particle number conservation within the pairing Hamiltonian. However, the trial wavefunction does not have good particle number in the first place so it would not be plausible to expect any approximate interaction to retain this conserved quantity. The ultimate justification of the approximation lies within its success.

The violation of particle number conservation is not a great problem in a statistical system such as a superconductor ($N_{particles} \sim 10^{23}$) but even the heaviest nuclei ($N_{particles} \sim 200$) cannot be considered as statistical in this manner. The addition of a Lagrangian multiplier λ (known as the chemical potential or Fermi energy) into the Hamiltonian:

$$H' = H - \lambda\hat{N} \quad ; \quad \lambda = \frac{\partial E}{\partial N} \tag{2.34}$$

fixes the average particle number to that appropriate to the problem under consideration. If the spectra of nuclei with A in the region of N can be considered similar then it is hoped that the fluctuations in particle number around N are unimportant.

Better results could be obtained by minimisation of the energies of the particle-number projected wavefunction (ie the component of the wavefunction with the correct particle number). This is difficult to do in practice. Lipkin [Li60] proposed an extended form of BCS in which the particle number fluctuation is suppressed by dealing with the Hamiltonian

$$\mathcal{H} = H - f(n) \tag{2.35}$$

where $f(n)$ is chosen such that the different n-particle ground states of H are all degenerate eigenstates of $\mathcal{H}$. Nogami [No64] suggested the Hamiltonian

$$\mathcal{H} = H - \lambda_1 N - \lambda_2 N^2 \tag{2.36}$$

with the subsidiary condition $< \mathcal{H}N^2 >= 0$. The advantage of this treatment of pairing is that it has solutions for all pairing strengths, whereas in the normal BCS treatment the superconducting solution breaks down for pairing strengths less than a critical value[12]. This makes the Lipkin-Nogami method particularly applicable to excited states and odd-A nuclei where the blocking effect (see page 25) reduces the pairing strength.

Note that the form of the pairing Hamiltonian considered is

$$H_{pair} = H_{pp} + H_{nn} \tag{2.37}$$

[12]i.e. the gap equation has no real solution

where the contributions from proton-proton and neutron-neutron pairing are considered seperately and H_{pn} (which would, as one would like, make the pairing term isospin invariant) is neglected. It is possible to generalise pairing theory to include proton-neutron pairing but unfortunately any trial wavefunction of the BCS type then consists of a mixture of even-even and odd-odd nuclei which seems unphysical due to the great differences in observed spectra. One may argue that p-n pairing in medium/heavy nuclei is generally small since the neutrons and protons occupy different shells. Such a line of thought seems implausible in the light of work by Casten (eg.[CBH87]) in which he argues that deformation is dependent on the total number of valence nucleons (irrespective of isospin) which maximise their interaction at the expense of the sphericity of the nucleus. In the neutron deficient light rare earth region in particular, the proton and neutrons occupy the same shells so such effects should be maximal.

2.3.7 Quasiparticles

The general form of the Bogoluibov–Valatin transformation

$$\begin{aligned} \beta_k^\dagger &= \sum_l U_{lk} c_l^\dagger + V_{lk} c_l \\ \beta_k &= \sum_l V_{lk}^* c_l^\dagger + U_{lk}^* c_l \end{aligned} \tag{2.38}$$

defines a set of generalised quasiparticle operators obeying the same fermion commutation relations as the particle operators [BV58]. The transformation to quasiparticle operators may be thought of in terms of 3 successive unitary transformations:

- a transformation amongst the particle operators $a_l^\dagger$ into the canonical basis $c_k^\dagger = \sum_l D_{lk} a_l^\dagger$
- a Bogoluibov transformation distinguishing between 'paired' levels $(u_p > 0, v_p > 0)$ with

$$\begin{aligned} \alpha_p^\dagger &= u_p c_p^\dagger - v_p c_{\bar{p}} \\ \alpha_{\bar{p}}^\dagger &= u_p c_{\bar{p}}^\dagger + v_p c_p \end{aligned}$$

  and 'blocked' levels which are either occupied $(v_i = 1, u_i = 0)$ or empty $(v_m = 0, u_m = 1)$
- a transformation amongst the $\alpha_k^\dagger$

$$\beta_k^\dagger = \sum_{k'} c_{k,k'} \alpha_k^\dagger$$

In order for the $\beta_k^\dagger, \beta_k$ to follow the same algebra as the $a_l^\dagger, a_l$ the transformation matrices U, V must satisfy the orthonormality and closure relations

$$\begin{aligned} U^\dagger U + V^\dagger V &= 1 \qquad UU^\dagger + V^* V^T = 1 \\ U^T V + V^T U &= 0 \qquad UV^\dagger + V^* U^T = 0 \end{aligned} \tag{2.39}$$

which leads us to interpret the $u_{kl}(v_{kl})$ coefficients as the amplitude of a particle(hole) state k in the quasiparticle state l. Obviously if $u_{kl} = 1, v_{kl} = 0$ then the quasiparticle is wholly particle-like and *vice versa*. Note that, due to the lack of distinction between particles and holes, the dimensionality of the problem has been doubled and additive quantities are doubly counted.

The quasiparticle vacuum of a many(M)-body system $|\Phi>$ is such that

$$\beta_k \,|\Phi>= 0 \quad ;\forall k\{1,\ldots M\}$$

$|\Phi>$ may be explicitly constructed from the bare vacuum $|->$ as

$$|\Phi> \propto \prod_k \alpha_k \,|->= \prod_i a_i^\dagger \prod_p (u_p + v_p a_p^\dagger a_{\bar{p}}^\dagger) \,|-> \tag{2.40}$$

where it is understood that $\prod$ is the product of the maximal number of k values such that the operation of any further operator β_q would annihilate $|\Phi>$ subject to the condition that β_q does not make $|->$ vanish identically. $|\Phi>$ is completely determined by the single particle operators a_k in the canonical basis, the occupation probabilities v_k^2 and the condition (2.39). Depending on whether the number of occupied levels i is even or odd (2.40) corresponds to a superposition of states with even or odd 'number parity'. The levels i are referred to as 'blocked' since they may no longer participate in the pairing interaction[13].The levels i must not be included in the gap equation (2.52,2.46). The blocking corrections to the pair field can be particularly large in deformed nuclei where only a few levels may contribute significantly to the gap parameter. The number parity is determined by the coefficients U, V in the transformation (2.38) and these must be restricted to reproduce the correct number parity. The correct mean particle number can be obtained within a variational model by imposing on the particle number expectation the subsidiary condition

$$<\Phi \,|\hat{N}\,|\Phi>= N \tag{2.41}$$

If we consider the fully paired vacuum $|\,\Phi_0>= \beta_1\beta_2\ldots\beta_M\,|->$ then the quasiparticle state

$$|\Phi_1>= \beta_1^\dagger \,|\Phi_0>$$

is vacuum to the operators $\{\tilde{\beta}_1\tilde{\beta}_2\ldots\tilde{\beta_M}\} = \{\beta_1^\dagger\beta_2\ldots\beta_M\}$ which corresponds to exchanging columns 1 in U, V and V^*, U^* from equation (2.38)

$$(u_{l1}, v_{l1}) = (v_{l1}^*, u_{l1}^*)$$

[13]due to the Pauli principle preventing the scattering of nucleons into a level which is already occupied

We may proceed in this manner and define quasiparticle vacua with respect to a new set of operators for each of the many quasiparticle configurations. Implicit in any quasiparticle model is the assumption that the excited states of the system correspond to the quasi-particle excitations of the vacuum, i.e. $\beta^\dagger \mid \Phi_0 >$ and the spectrum of states is given by the energies of these excitations relative to the vacuum.

2.3.8 CHFB Theory

The quasiparticle formalism is not limited to BCS pairing in its application. CHFB (Cranked Hartree Fock Bogoluibov) theory is a variational method searching for the most general independent quasiparticle product wave functions that minimise the Hamiltonian:

$$H = \sum_{k,k'}(\epsilon_{k,k'} - \omega j_{k,k'}(x) - \lambda\delta_{k,k'})a_k^\dagger a_{k'} + \frac{1}{4}\sum_{lkl'k'} V_{lkl'k'}a_l^\dagger a_k^\dagger a_{k'}a_{l'} \qquad (2.42)$$

If the Bogoluibov-Valatin transformation (2.38) is applied to this Hamiltonian and the resulting quasiparticle operator terms are collected into terms of like order then this becomes:

$$H = H_{00} + H_{11} + H_{20} + H_{int} \quad ; H_{int} = H_{22} + H_{31} + H_{40} \qquad (2.43)$$

where constants $\in H_{00}; \alpha^\dagger\alpha, \alpha\alpha^\dagger \in H_{11}; \alpha^\dagger\alpha^\dagger, \alpha\alpha \in H_{20}$ ...etc. By a suitable choice of coefficients U, V from (2.38), H_{20} can be made identically zero and H_{11} can be simultaneously diagonalised. Thus to first order we obtain a system of independent quasiparticles. This leads to a set of non-linear equations:

$$\begin{aligned}
\sum_k[(v^\omega_{k'k} - \lambda\delta_{k'k})U_{ik} + \Delta_{k'k}V_{ik}] &= E_i^\omega U_{ik'} \\
\sum_k[(v^\omega_{k'k}{}^* - \lambda\delta_{k'k})V_{ik} + \Delta^*_{k'k}U_{ik}] &= -E_i^\omega V_{ik'}
\end{aligned} \qquad (2.44)$$

where the eigenvalues E_i^ω are called single-quasiparticle Routhians and the eigenvectors are defined by $U_{ik'}, V_{ik'}$. The equations are non-linear due to the implicit dependance of $v^\omega_{k'k}$ and $\Delta_{k'k}$ on the transformation coefficients U_{ik}, V_{ik}:

$$v^\omega_{k'k} = \epsilon_{k'k} + 4\sum_{l'l} v_{k'l'kl}\rho_{l'l} - \hbar\omega(j_x)_{k'k} \qquad (2.45)$$

$$\Delta_{k'k} = 2\sum_{l'l} \nu_{k'l'kl}\chi_{l'l} \qquad (2.46)$$

The matrices have the following significance:

- $\rho_{l'l}$ is the single particle density defined as

$$\rho_{l'l} = \sum_i V^*_{il'}V_{il} \qquad (2.47)$$

- $\chi_{l'l}$ is the pair density

$$\chi_{l'l} = \sum_i V^*_{il'} U_{il} \tag{2.48}$$

- $v^\omega_{k'k}$ is the self-consistent single particle Routhian
- $\Delta_{k'k}$ is the self-consistent pairing potential

Since (2.44) is non-linear it must be solved iteratively by guessing the matrices v^ω and Δ, solving (2.44) for E^ω, U, V and then using (2.45, 2.46, 2.47, 2.48) to recalculate v^ω and Δ until self-consistency is obtained subject to the constraint imposed by the Lagrange multiplier λ (see section 2.3.6)

$$< N > \equiv \sum_\alpha \rho_{\alpha\alpha} = N \tag{2.49}$$

The calculations are performed at different values of ω and the angular momentum aligned along the rotational axis can then be calculated in terms of ω as

$$I_x = \sqrt{I(I+1) - K^2} = \sum_{k'k} (j_x)_{k'k} \rho_{k'k} \tag{2.50}$$

where the dependance on angular frequency is implicit in $(j_x)_{k'k}$ and $\rho_{k'k}$. Equations (2.44) imply that if E^ω_i is an eigenfunction of the eigenvector $\begin{pmatrix} U_i \\ V_i \end{pmatrix}$ then the conjugate eigenvector $\begin{pmatrix} V^*_i \\ U^*_i \end{pmatrix}$ has an eigenvalue $-E^\omega_i$. Also, since E^ω_i is an approximate solution to the Hamiltonian (2.44), its derivative with respect to ω gives the expectation of the aligned angular momentum:

$$\frac{dE^\omega_i}{d\omega} = < i \mid \frac{\partial H^\omega}{\partial \omega} \mid i > = -\hbar < i \mid j_x \mid i > \tag{2.51}$$

The Hamiltonian does possess simplifying symmetries in that parity and signature are conserved (see page 21) so that the equations of motion (2.44) may be split into 4 independent subsets according to the quantum numbers π and α connected together only by the self-consistency requirements (2.45, 2.46) and the conditions (2.49, 2.50) which must be summed over all contributions. In practicality the problem is still very large since particle number projection is essential for the method to work.

2.3.9 The Cranked Shell Model

Whilst the CHFB model provides a useful tool for following the evolution of nuclear structure with increasing angular momentum, the Cranked Shell Model (CSM) provides an expedient method of interpreting and classifying the vast amount of high spin data now becoming available. The CSM is formally very similar to the CHFB method. Instead of deriving the single particle energies v from the 2-body force ν self consistently the single particle energies are calculated

within a phenomenological potential (eg the MHO or Woods-Saxon potentials) and introduced *ad hoc* into equation (2.45). In the following it will be assumed that CSM implies the use of a Nilsson potential unless otherwise stated. The deformation of the potential is assumed to include the long range and n-p terms in the nuclear field and the second term in (2.45) is ignored. Under these conditions only the short range part of the pairing field need be considered. Generally a pure monopole pairing force (see page 22) of the form (2.37) is introduced which reduces the self-consistency condition for the pair field to a gap equation separable in the proton-neutron degree of freedom involving only one parameter, Δ:

$$\Delta = G \sum_{l>0} \chi_{l\bar{l}} \tag{2.52}$$

The chemical potential λ is chosen to give the correct particle number at $\omega = 0$ and the single quasiparticle levels (or 'Routhians') are calculated at stepped values of ω. It is customary to present CSM diagrams directly in terms of angular frequency rather than adjusting it until the self-consistent constraint $< j_x >= I_x$ is satisfied as is usual within CHFB.

The quasiparticle levels calculated may be tagged by the asymptotic Nilsson quantum numbers but it must be realised that these are only of any relevance at $\omega = 0$ and even then strong interactions may obscure the origin of the level. [14] The only conserved quantum numbers left within CSM at $\omega > 0$ are the parity and signature of the levels and excitations may be characterised by $(\alpha, \pi)_\nu$ where ν is the number of quasiparticle levels of signature,parity (α, π) occupied above the vacuum (or 'reference') configuration. Excitations are often assigned letters as labels; the convention used in this work is that AB,CD (ab,cd) refer to the two signatures of the lowest two positive parity quasi-proton(-neutron) levels and EF,GH (ef,gh) to the analogous negative parity levels. In the light rare earth region the ef,gh levels are unique parity intruder levels being brought down from the $h\frac{11}{2}$ subshell. This convention is at variance with the notation proposed in [BFM86] where A–D are reserved for the lowest lying intruder orbitals which may be of different parities according to the nucleus under discussion.

CSM quasiparticle diagrams predict both the interaction strengths between, and the crossing frequencies, at which different bands interact. Strictly the CSM approach is invalid in the crossing region since the interacting bands at the crossing may have different moments of inertia and thus in the crossing region states of different angular momentum are mixed. The excitation energy and gain in aligned angular momentum of multi-quasiparticle states relative to the reference configuration as well as the additive quantities of total parity and signature may be obtained by summing the contributions from the occupied states above the vacuum. The CSM vacuum has even number parity and is a zero signature even parity state. The validity of such additivity rests upon the validity of the independent quasiparticle approximation; deviations from additivity may be attributed to the residual interaction ignored in 2.43 or to shape changes.

[14] in such cases an examination of the same levels in nearby nuclei where the interacting levels are better separated can be used to achieve an identification

2.4 Macroscopic–Microscopic Methods

2.4.1 The Shell Correction Method

The assumption behind the Macroscopic-Microscopic approach is that the total energy of the nucleus can be separated into two terms

$$E = \tilde{E} + \delta E_{shell} \tag{2.53}$$

where the macroscopic energy $\tilde{E}$ depends smoothly on the number of nucleons and the microscopic or shell correction energy δE_{shell} accounts for local fluctuations due to the non–uniform single–particle density. This is the Strutinsky energy theorem and can be derived from the HFB formalism in which the Hamiltonian is treated self-consistently [BQ81]. In practicality the self-consistency is dropped and a phenomenological model is used to calculate the single particle densities within the model. This is justified solely by the agreement with experiment. The method then consists of minimising this quantity with respect to the shape degrees of freedom to obtain the ground state energy and properties. The great advantage of such an approach over a more microscopic HFB method is that it is computationally much simpler, enabling global predictions to be made for properties such as ground state masses and quadrupole moments.

δE_{shell} is calculated from a single–particle model Hamiltonian as

$$\begin{aligned} \delta E_{shell} &= E_{shell} - \widetilde{E_{shell}} \\ &= \sum_{k=1}^{A} \epsilon_k - \int_{-\infty}^{\tilde{\lambda}} \epsilon \tilde{g}(\epsilon) d\epsilon \end{aligned} \tag{2.54}$$

The ϵ_k are the eigenvalues of the single particle Hamiltonian and $\widetilde{E_{shell}}$ is a smoothed energy calculated by folding the shell model level density

$$g(\epsilon) = \sum_{\alpha} \delta(\epsilon - \epsilon_\alpha); \quad E_{shell} = \int_{-\infty}^{\lambda} \epsilon g(\epsilon) d\epsilon$$

with a smoothing function $\xi(\frac{\epsilon' - \epsilon}{\gamma})$ over a large energy interval γ of the order of the shell spacing $\hbar\omega_0$:

$$\tilde{g}(\epsilon) = \int_{-\infty}^{+\infty} \xi(\frac{\epsilon' - \epsilon}{\gamma}) g(\epsilon') d\epsilon'$$

There is no *a priori* correct smoothing procedure. [15] It is merely required that $\tilde{g}(\epsilon)$ does not exhibit shell fluctuations and that the averaging procedure does

[15] Strutinsky used the function

$$\xi(\epsilon) = \frac{1}{\sqrt{\pi}\gamma} \sum_k \exp(\frac{\epsilon - \epsilon_k}{\gamma})^2$$

not depend critically upon the interval γ[16]. The smoothed energy is then given as:

$$\widetilde{E_{shell}} = \int_{-\infty}^{\tilde{\lambda}} \epsilon \tilde{g}(\epsilon) d\epsilon$$

where $\tilde{\lambda}$ is the Fermi energy of the smoothed level distribution determined from the particle number condition

$$N = \int_{-\infty}^{\tilde{\lambda}} \tilde{g}(\epsilon) d\epsilon$$

Within δE_{shell} one must also include a pairing correction given as

$$\delta E_{pair} = E_{pair} - < \widetilde{E_{pair}} >$$

where E_{pair} is the difference in expectation value of the model Hamiltonian with and without pairing. Other residual interactions are assumed to vary slowly with single particle density and are hence included within $\tilde{E}$. In general δE_{pair} tends to oppose the single particle shell correction since the pairing interaction is strong and negative for high level densities where the shell correction is large and positive and weak in the case of low level densities and weak single particle shell corrections. Thus the pairing interaction tends to smooth out the shell correction as a function of shape and nucleon number. The macroscopic energy $\tilde{E}$ may be treated either using a liquid drop model (in which case we have a Strutinsky formalism [St66]) or from a more 'fundamental' model such as the Yukawa plus exponential model used in [MN81].

2.4.2 Energy Surfaces

The early ground state deformation calculations (eg [MPS63]) summed Nilsson levels at a series of ε_2 values and predicted the deformation as the interpolated energy minimum between these points. The macroscopic-microscopic methods were then introduced and entail the minimisation of both the macroscopic and microscopic terms at the same deformation. Rather than simply minimise the total energy with repect to the deformation parameters, it is instructive to calculate the energy on a grid of deformation parameters and present the results as a contoured potential energy surface (PES). Such surfaces give some idea of the rigidity of the nuclear shape with respect to the different deformational degrees of freedom. Care must be taken in interpreting a broad minimum in terms of softness [Na86] however, since a PES is usually an average envelope of the behaviour of the set of lowest single particle states at each grid point. This set of states will change with deformation. This problem can be avoided by constraining the PES to a specific configuration and following its behaviour as a function of shape. The minima shown by such constrained surfaces are, as a general rule, less soft with respect to the various deformations than those obtained in unconstrained calculations.

[16]This is known as the 'Plateau condition' expressed as $\frac{\partial(\delta E_{shell})}{\partial \gamma} = 0$

2.4.3 Cranked Macroscopic-Microscopic calculations

In principle the extension of the method described in the preceding section to non-zero angular momentum is simple, except that now the smearing procedure must also account for angular momentum density. Such calculations have been performed without taking pairing into account (see [ALL76]). A more recent approach is a calculation of the total Routhian [WNJ87] defined as

$$\begin{aligned} E^{\omega}(\beta,N,Z,\nu) &= E^{\omega=0}_{strutinsky}(\beta,N,Z,\nu) + \\ &\quad (< \Psi^{\omega} \mid H^{\omega} \mid \Psi^{\omega} >_{\beta,N,Z,\nu} - < \Psi^{\omega} \mid H^{\omega} \mid \Psi^{\omega} >^{\omega=0}_{\beta,N,Z,\nu}) \end{aligned}$$

where the first term on the right hand side represents the Strutinsky energy as outlined in section (2.4.1) and the second term represents the energy gain due to collective rotation and single particle alignment calculated within a CSM framework. The variable β represents a set of deformation parameters and ν a configuration defined in terms of the number of excited quasiparticles of specific signature and parity. The calculations presented in this work were performed using a Woods-Saxon code and are therefore presented in terms of β_2, β_4, γ with β_4 set to the value favoured by the liquid drop model. Pairing is included in the calculation, the pair gap (Δ_0) at zero frequency being calculated self-consistently within the BCS model. At higher frequencies the pair gap was allowed to decrease gradually according to the formula:

$$\Delta(\omega) = \begin{cases} \Delta_0(1 - \frac{1}{2}(\frac{\omega}{\omega_c})^2) & \text{, if } \omega \leq \omega_c \\ \Delta_0 \frac{1}{2}(\frac{\omega_c}{\omega})^2 & \text{, if } \omega > \omega_c \end{cases}$$

where $\hbar\omega_c = 0.7$MeV has been obtained from particle number projected self-consistent pairing calculations for a few specific nuclei at selected deformations. The results are presented as a Total Routhian Surface(TRS) in which the total Routhian is plotted as a function of β_2, γ for a given configuration at a given angular frequency. Such a calculation allows the evolution of nuclear shape for specific configurations and the relative excitations of such configurations to be followed as a function of angular momentum.

Figure 2.4: *Overleaf* TRS calculations for the nuclei discussed in this work provided by the Warsaw/Lund collaboration. Calculations are included for ^{129}Pr, ^{129}Nd and ^{131}Nd for the lowest positive (A,B) and negative (E,F) parity configurations at low frequency. The minima are all axial prolate and remain largely unchanged over the range of experimentally observed frequencies. Note that the positive parity surface for ^{129}Pr shows two competing minima and the negative parity minima in the Nd nuclei appear to be hardening with respect to triaxiality as the neutron number is lowered.

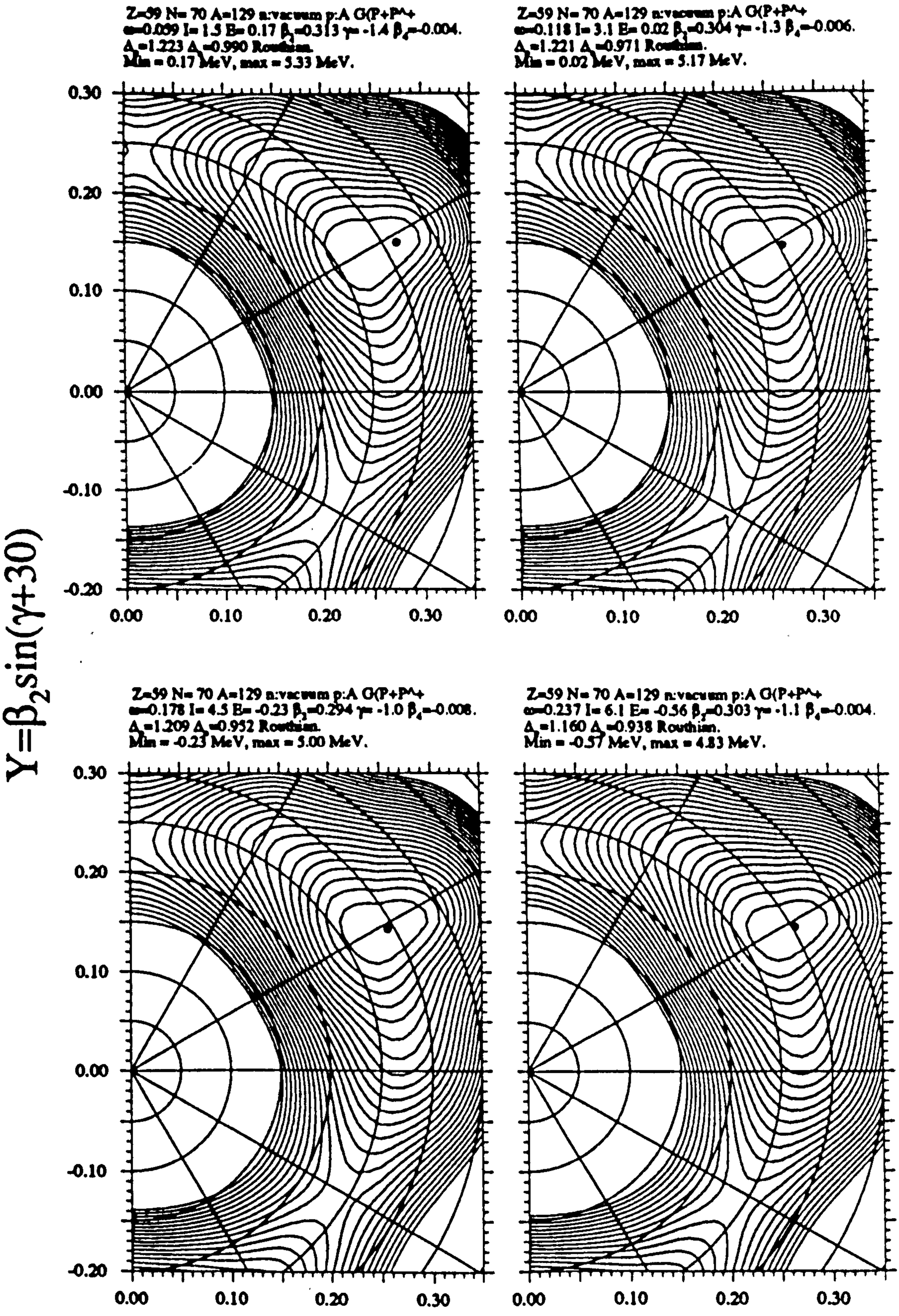

31-MAR-88 13:28:55 API, Stockholm

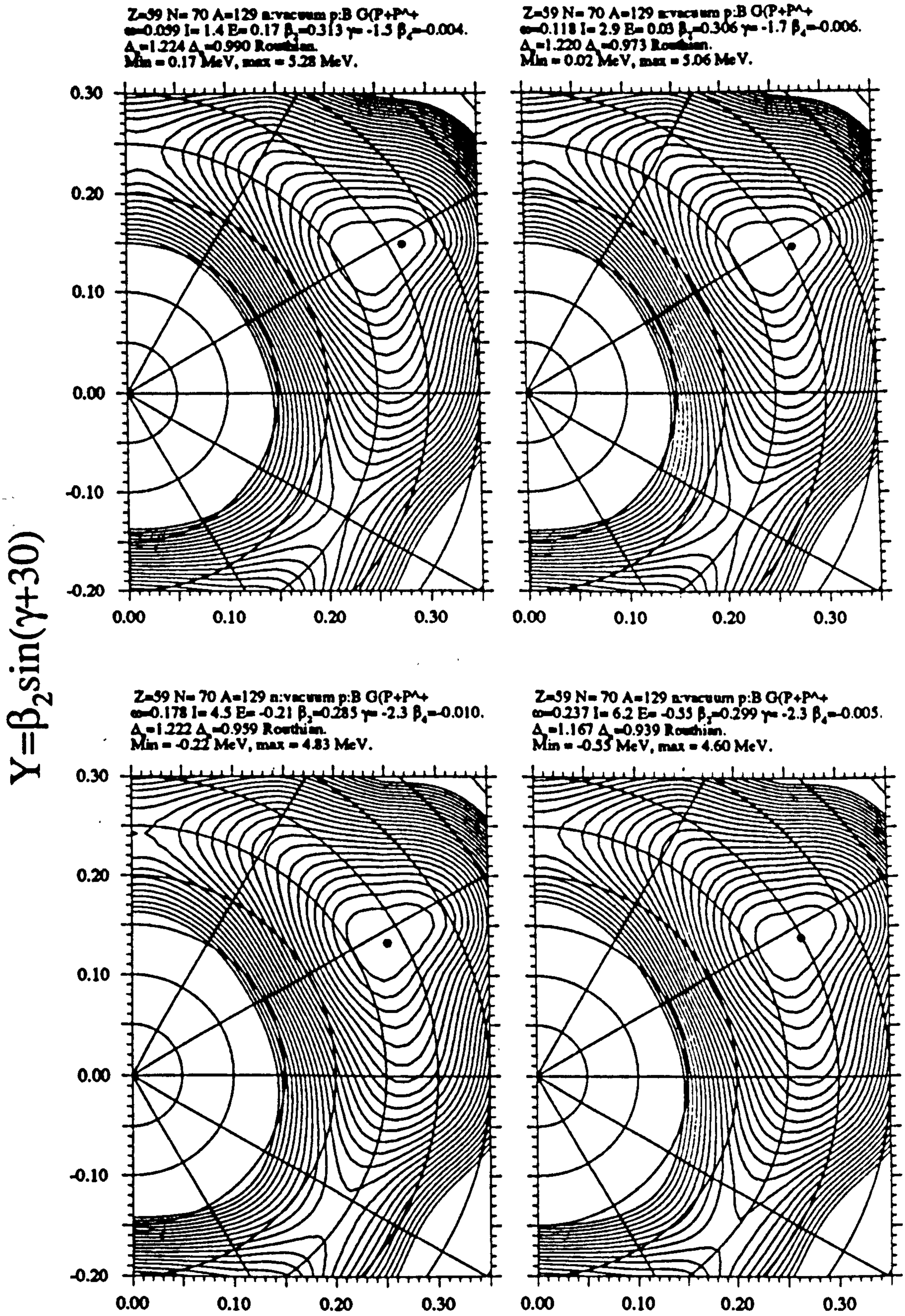

31-MAR-88 13:51:37 AFI, Stockholm

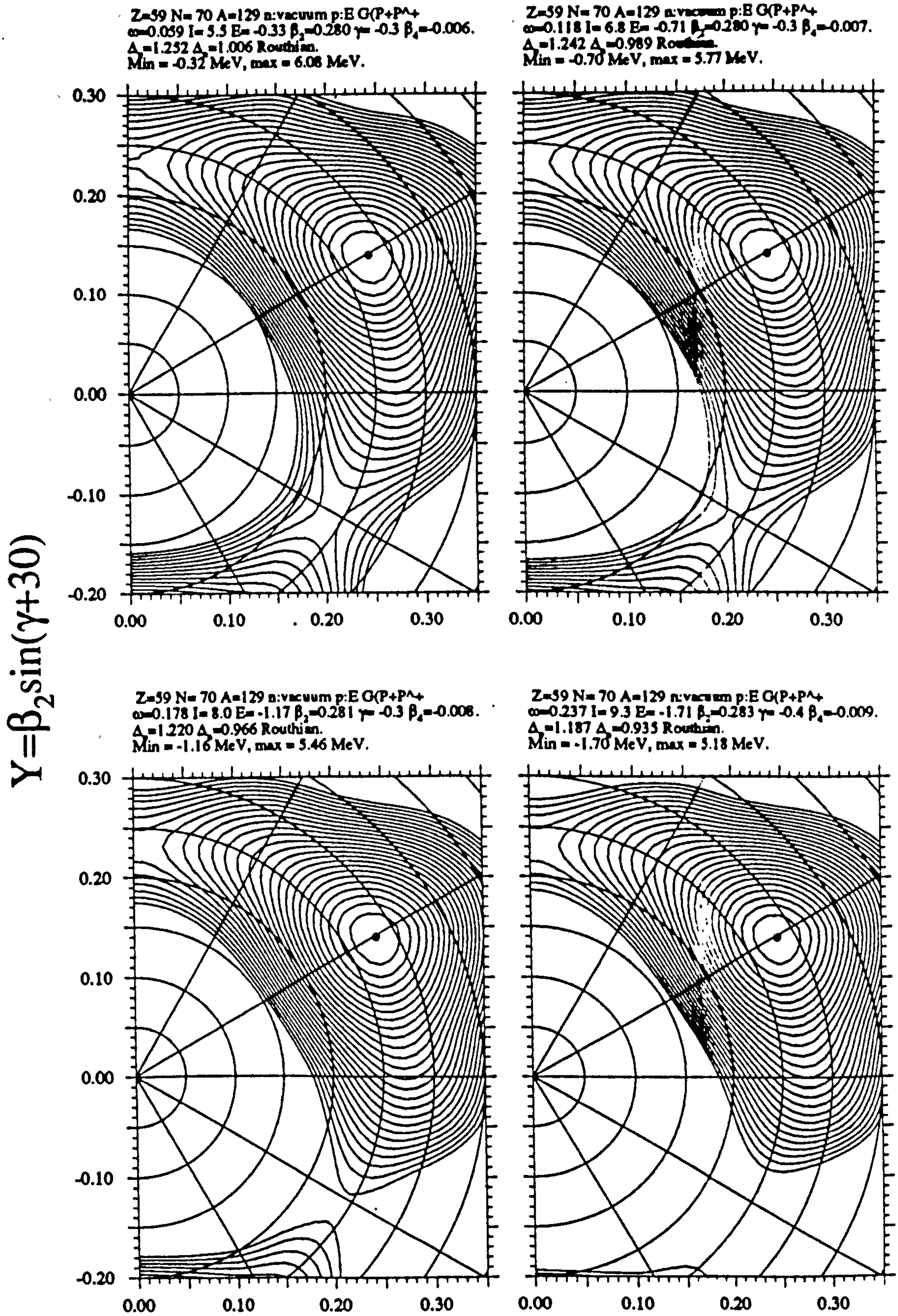

31-MAR-88 06:11:52 AFI, Stockholm

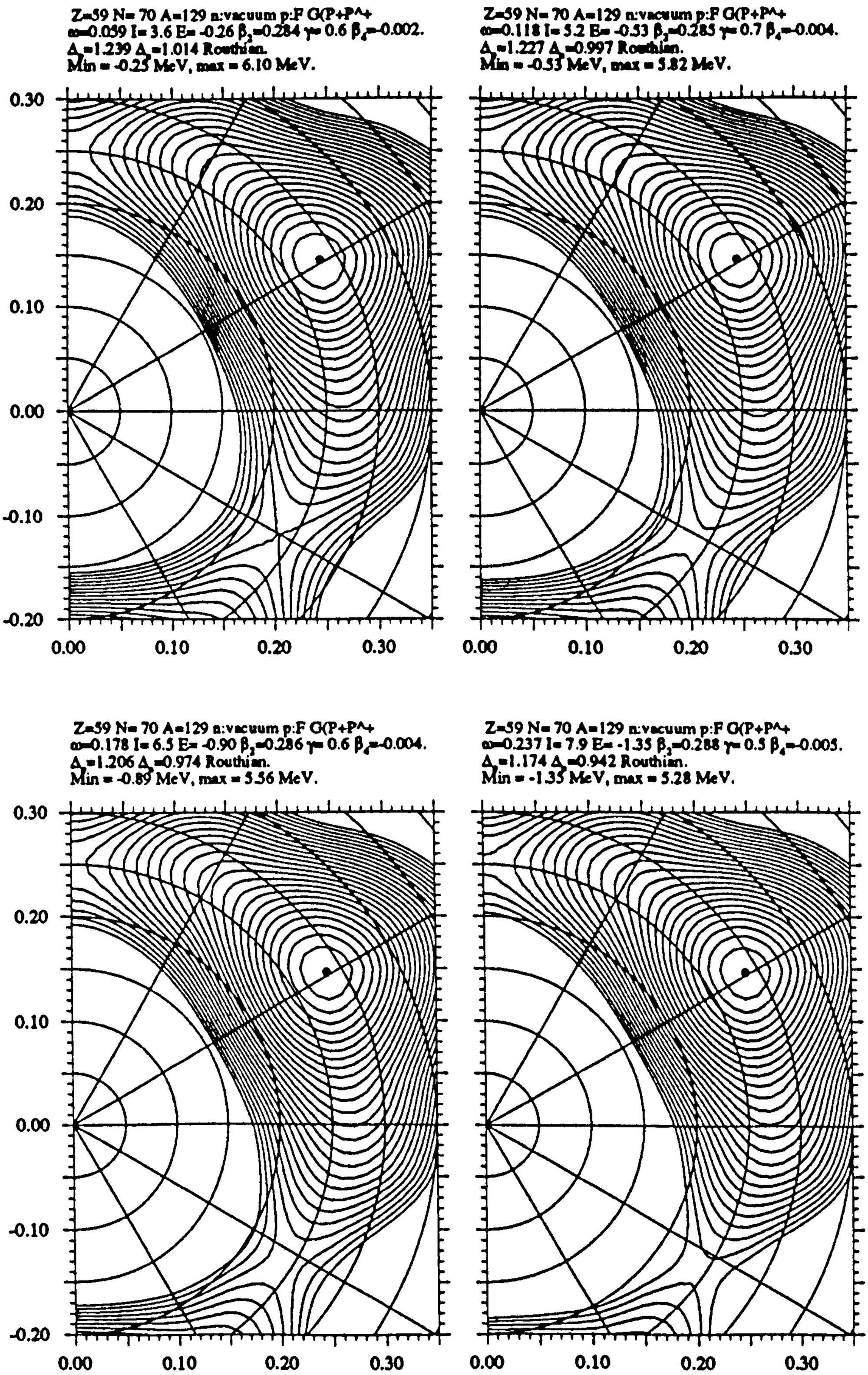

31-MAR-88 07:17:23 AFI, Stockholm

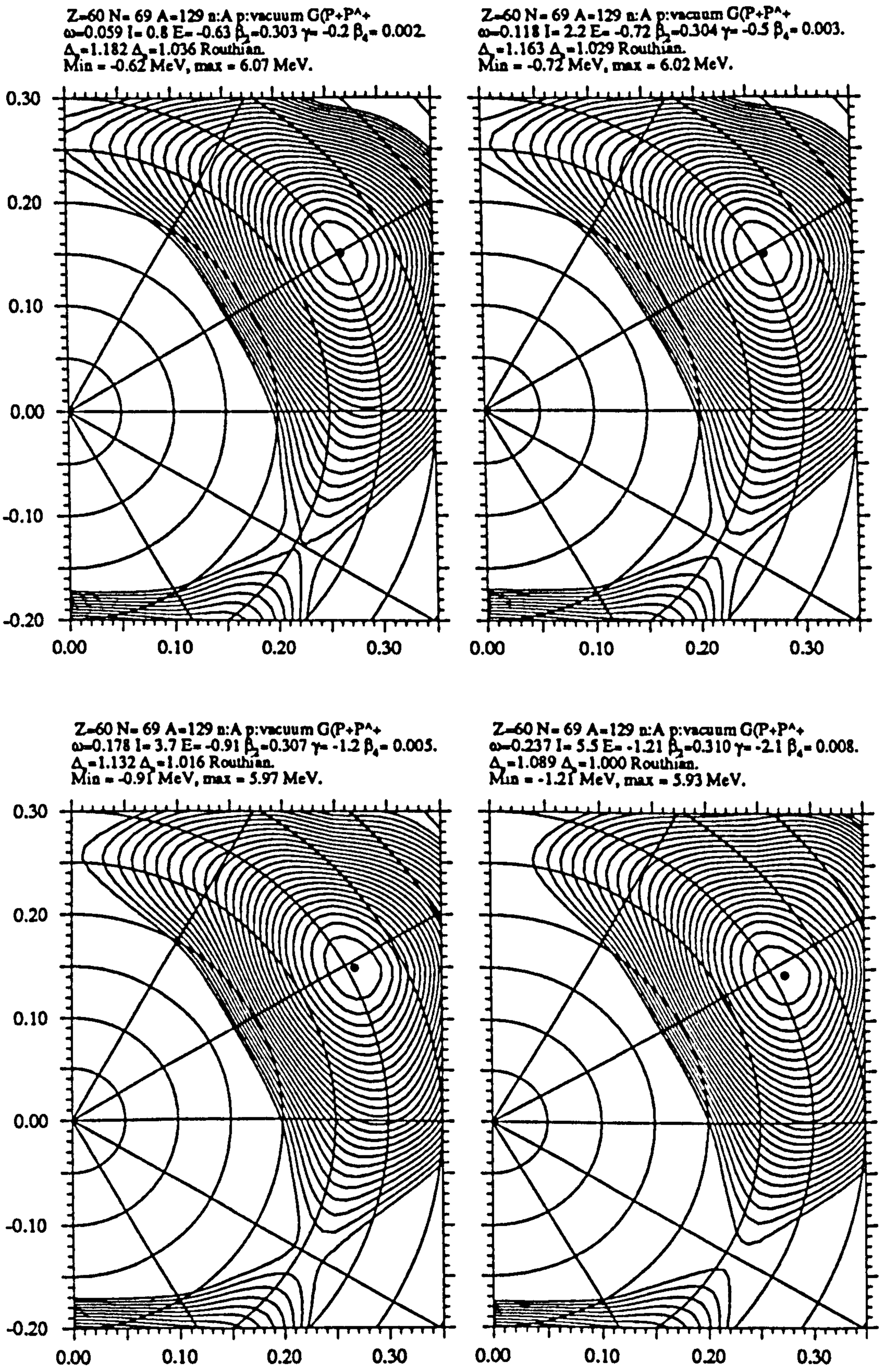

13-MAR-88 00:35:46 AFT Stockholm

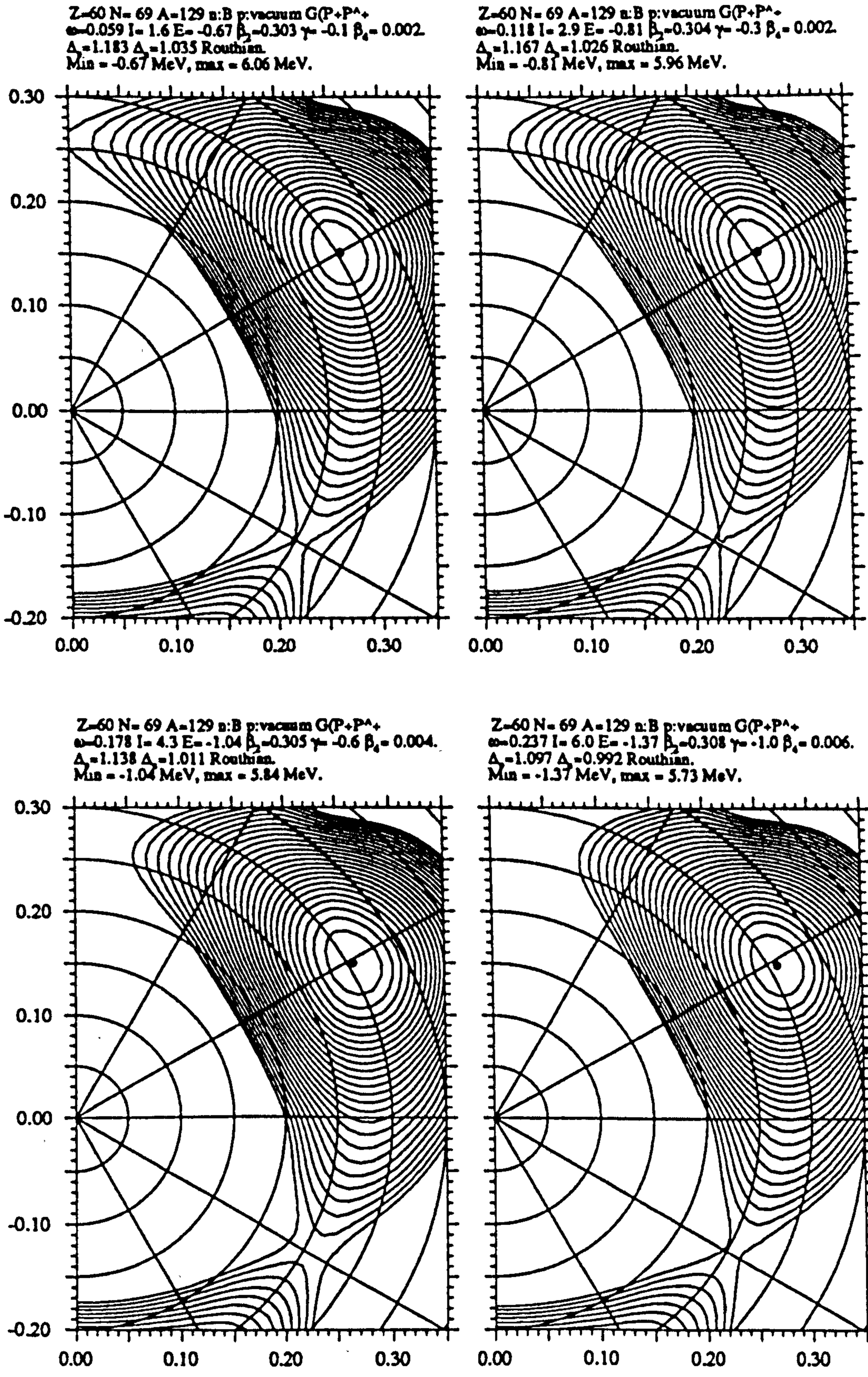

23-MAR-88 01:26:04 AFI, Stockholm

Z=60 N= 69 A=129 n:E p:vacuum G(P+P^+
ω=0.059 I= 2.1 E= -0.75 β_2=0.299 γ= 0.0 β_4=-0.002.
Δ_n=1.201 Δ_p=1.026 Routhian.
Min = -0.74 MeV, max = 5.84 MeV.

Z=60 N= 69 A=129 n:E p:vacuum G(P+P^+
ω=0.118 I= 4.0 E= -0.94 β_2=0.299 γ= -0.1 β_4=-0.001.
Δ_n=1.187 Δ_p=1.016 Routhian.
Min = -0.94 MeV, max = 5.52 MeV.

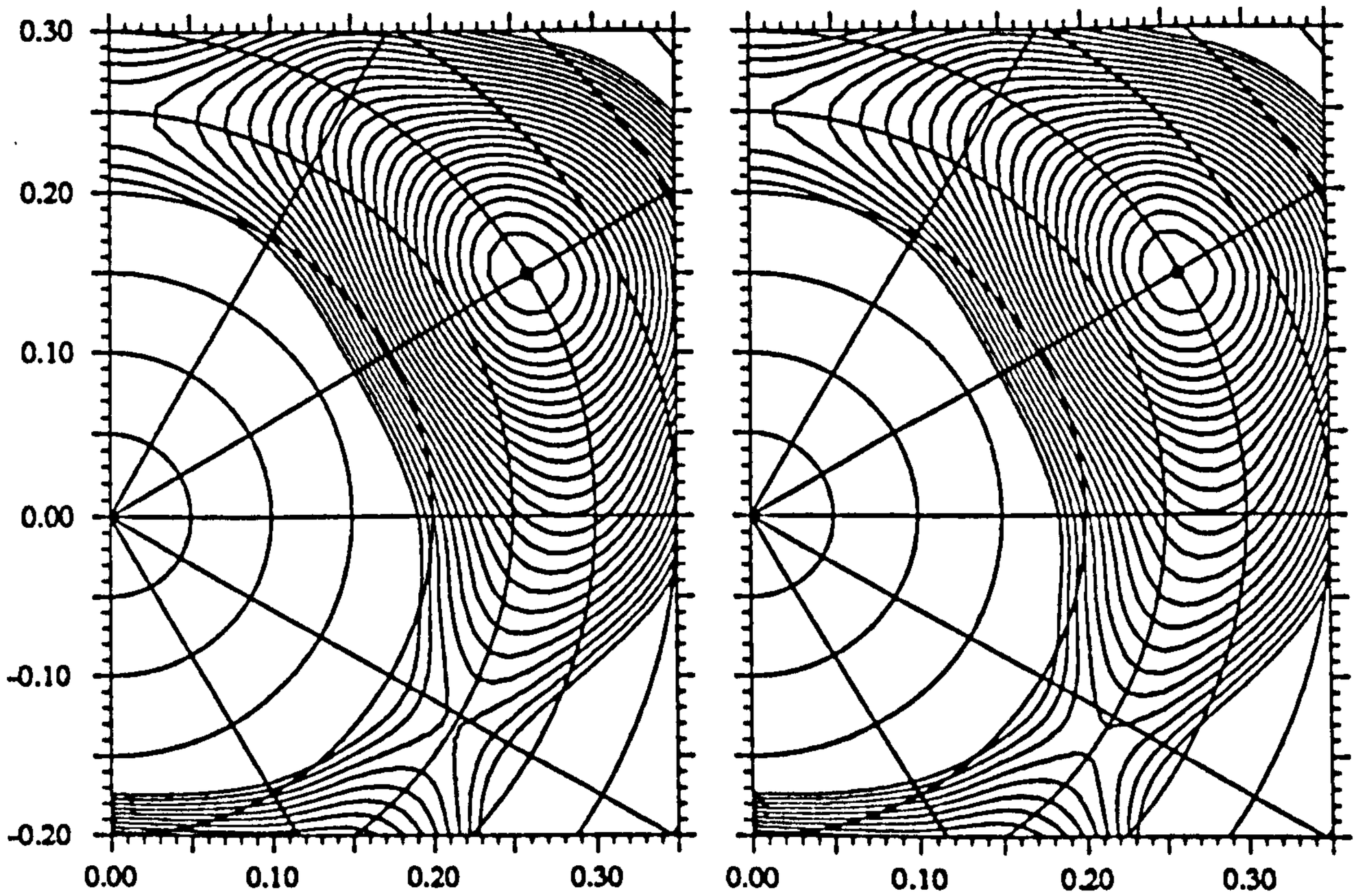

$Y=\beta_2\sin(\gamma+30)$

Z=60 N= 69 A=129 n:E p:vacuum G(P+P^+
ω=0.178 I= 5.8 E= -1.25 β_2=0.299 γ= -0.3 β_4= 0.000.
Δ_n=1.161 Δ_p=1.001 Routhian.
Min = -1.24 MeV, max = 5.18 MeV.

Z=60 N= 69 A=129 n:E p:vacuum G(P+P^+
ω=0.237 I= 7.6 E= -1.67 β_2=0.300 γ= -0.5 β_4= 0.002.
Δ_n=1.122 Δ_p=0.980 Routhian.
Min = -1.66 MeV, max = 4.84 MeV.

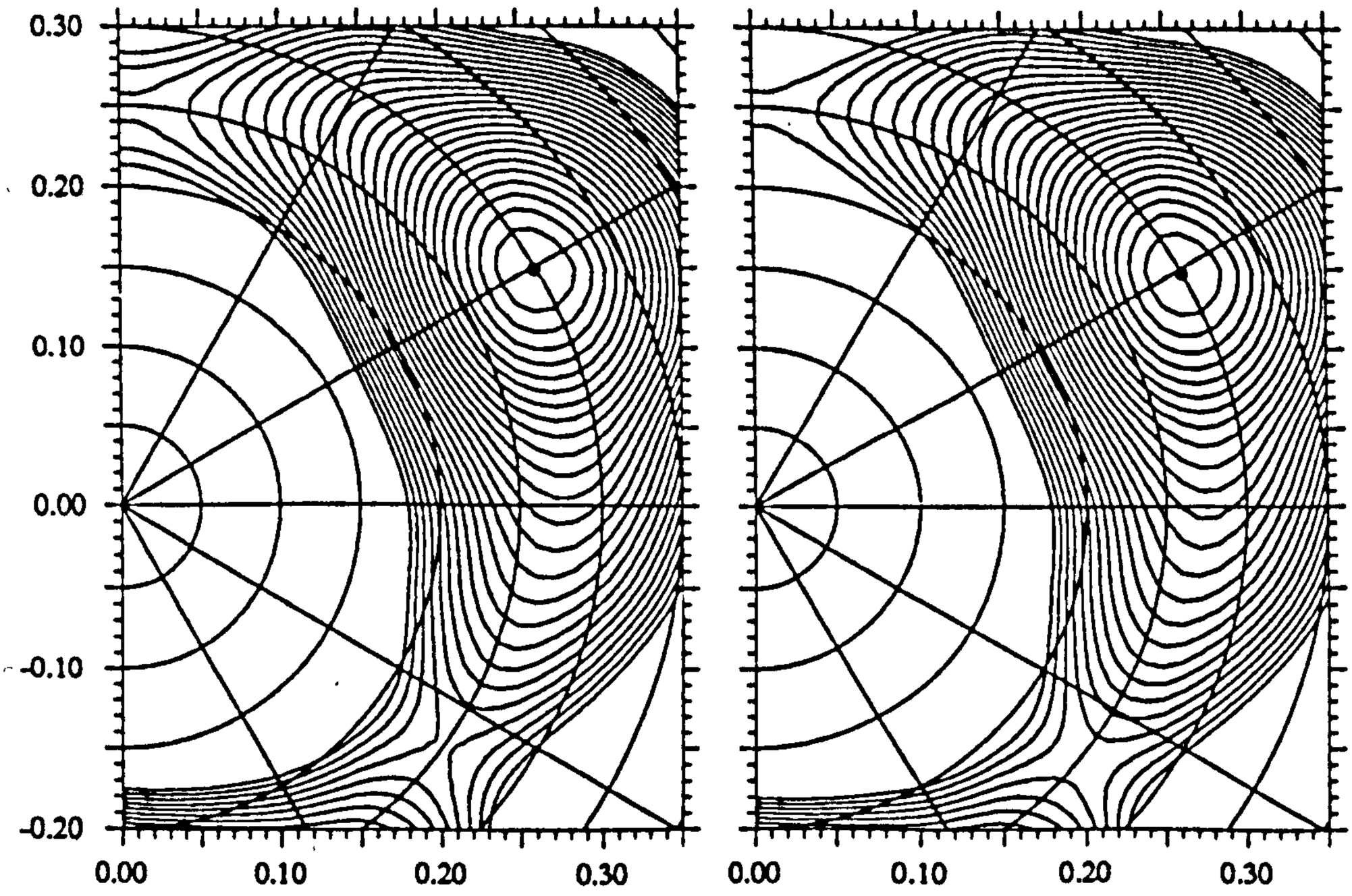

$X=\beta_2\cos(\gamma+30)$

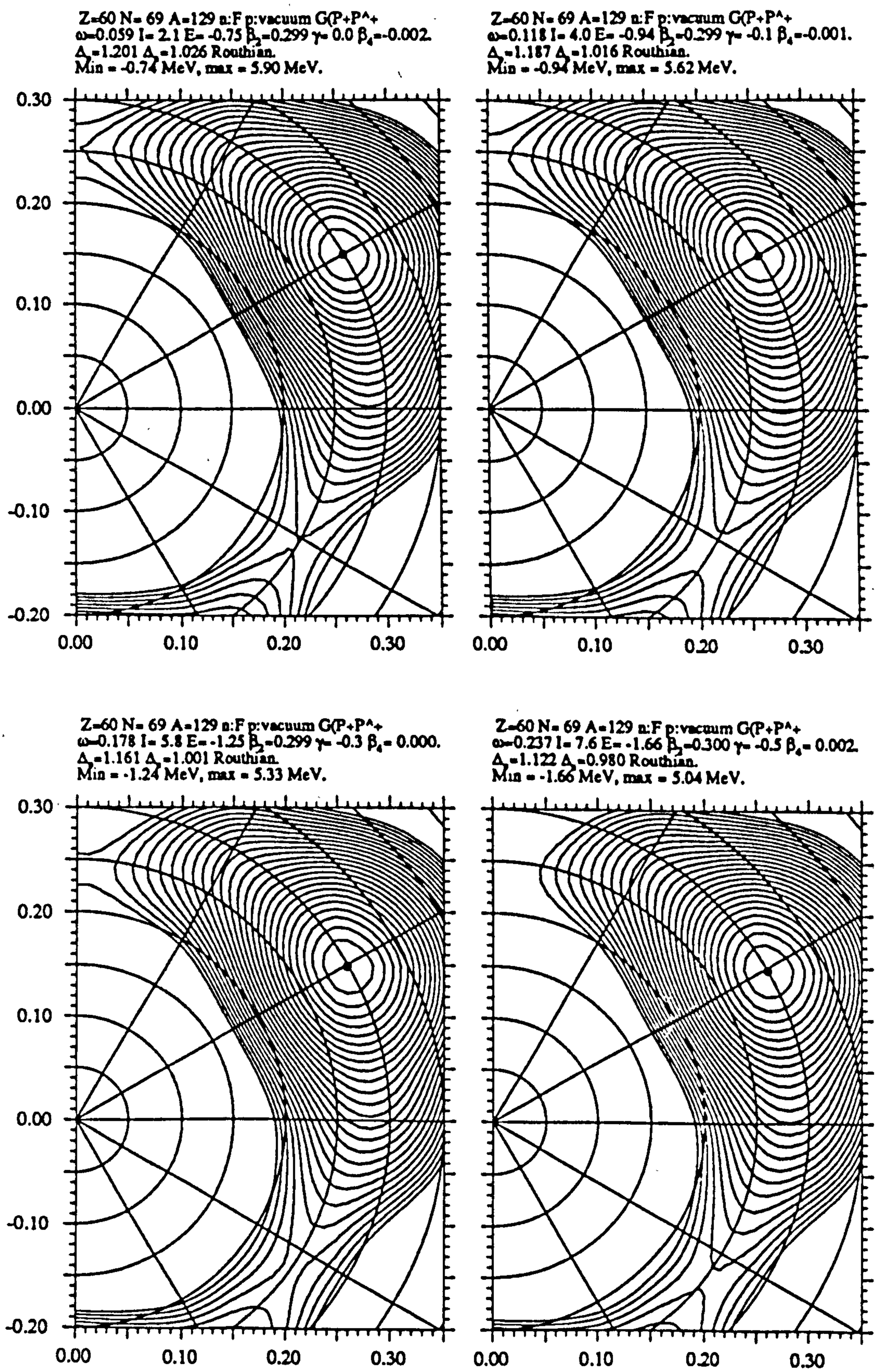

22-MAR-88 23:45:50 AFI. Stockholm

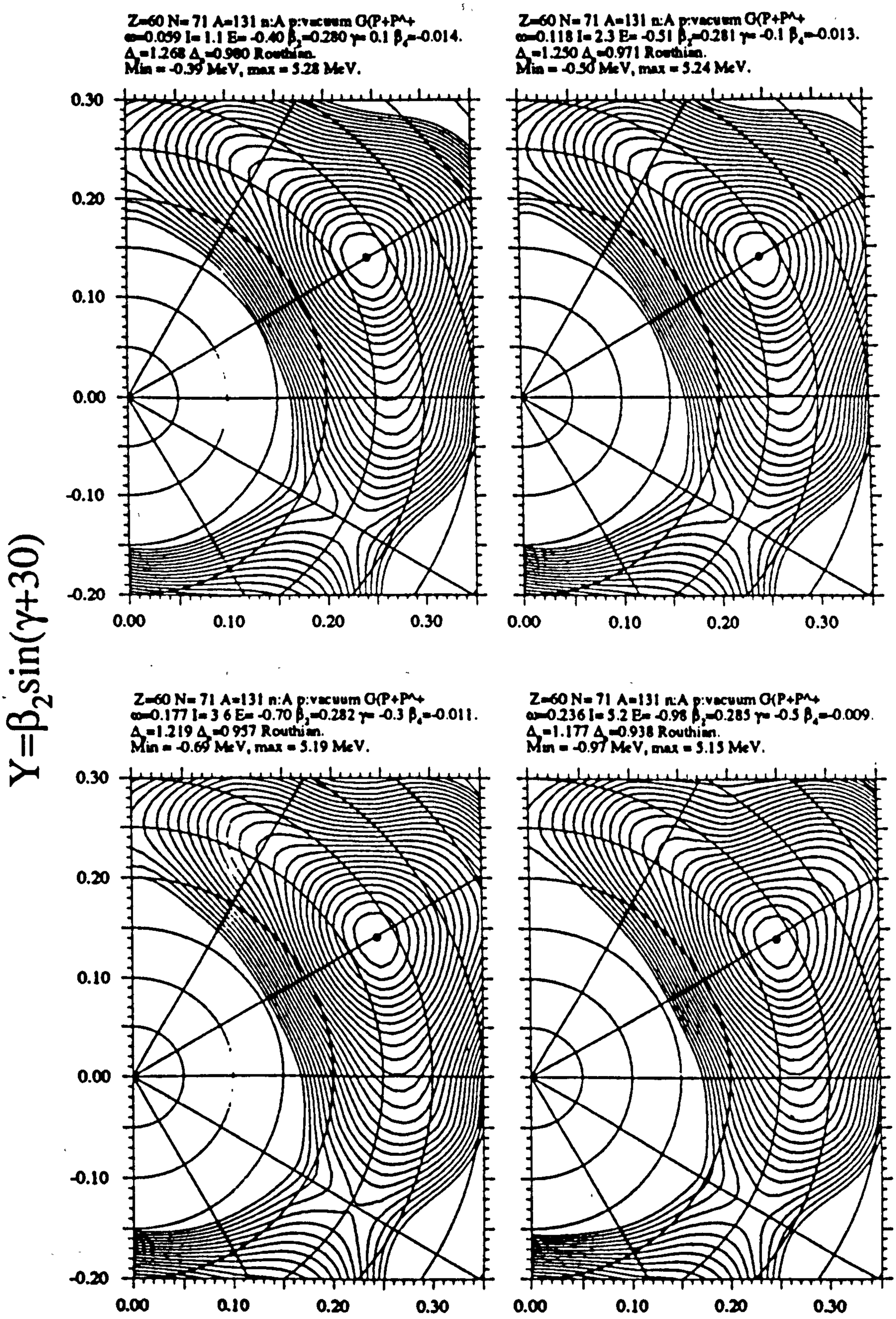

14-APR-88 02:33:17 API, Stockholm

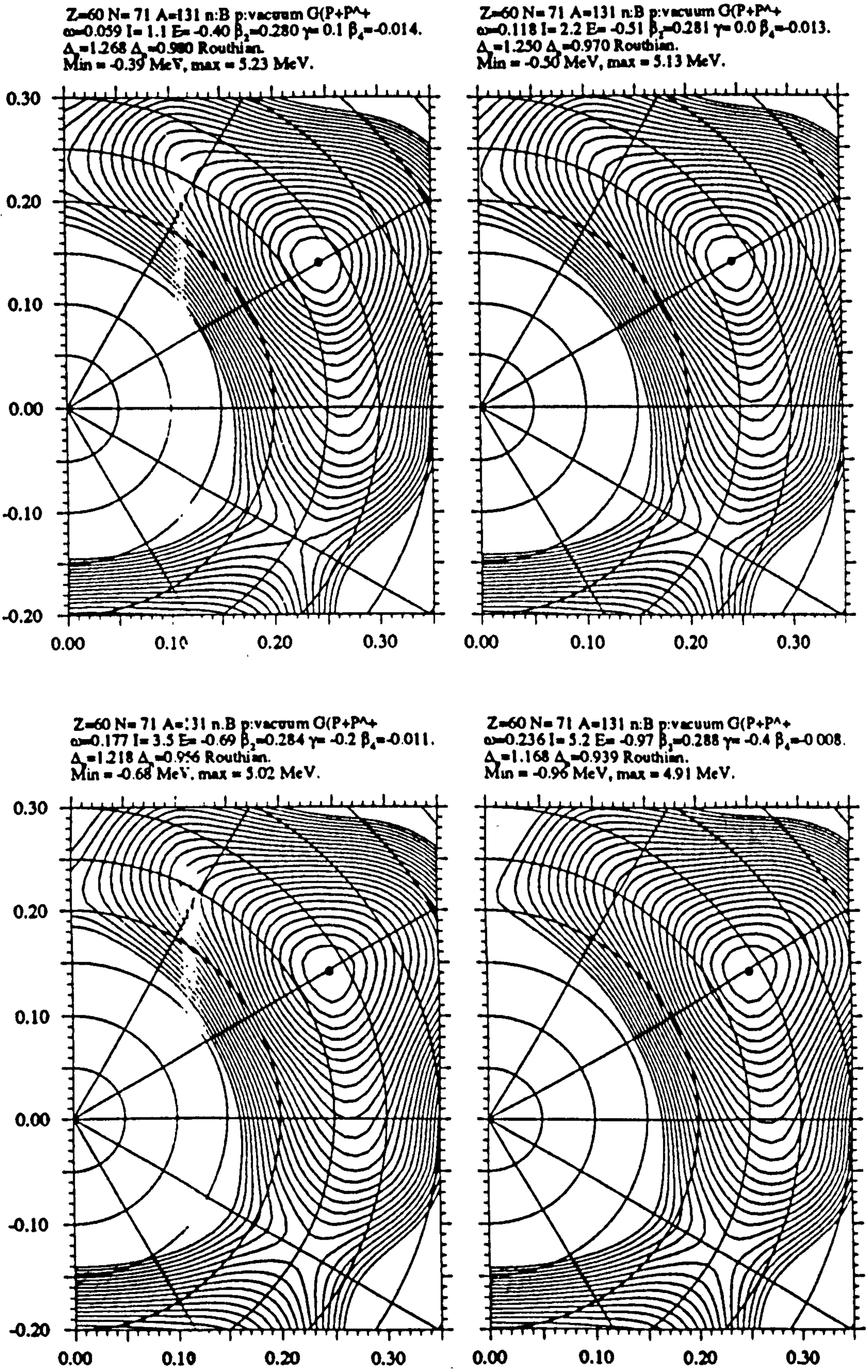

14-APR-88 03:03:48 AFI, Stockholm

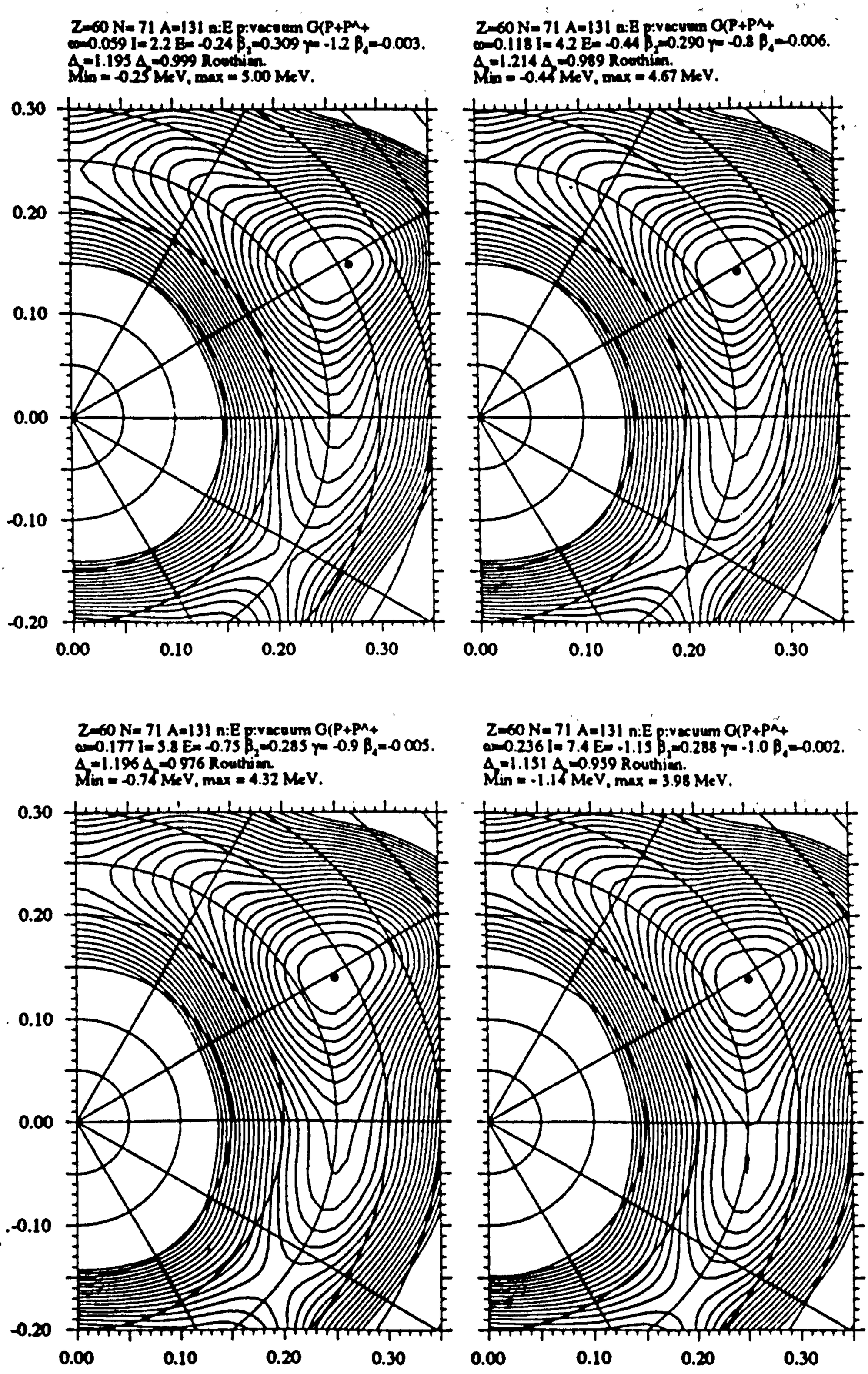

14-APR-88 01:24:45 AFI, Stockholm

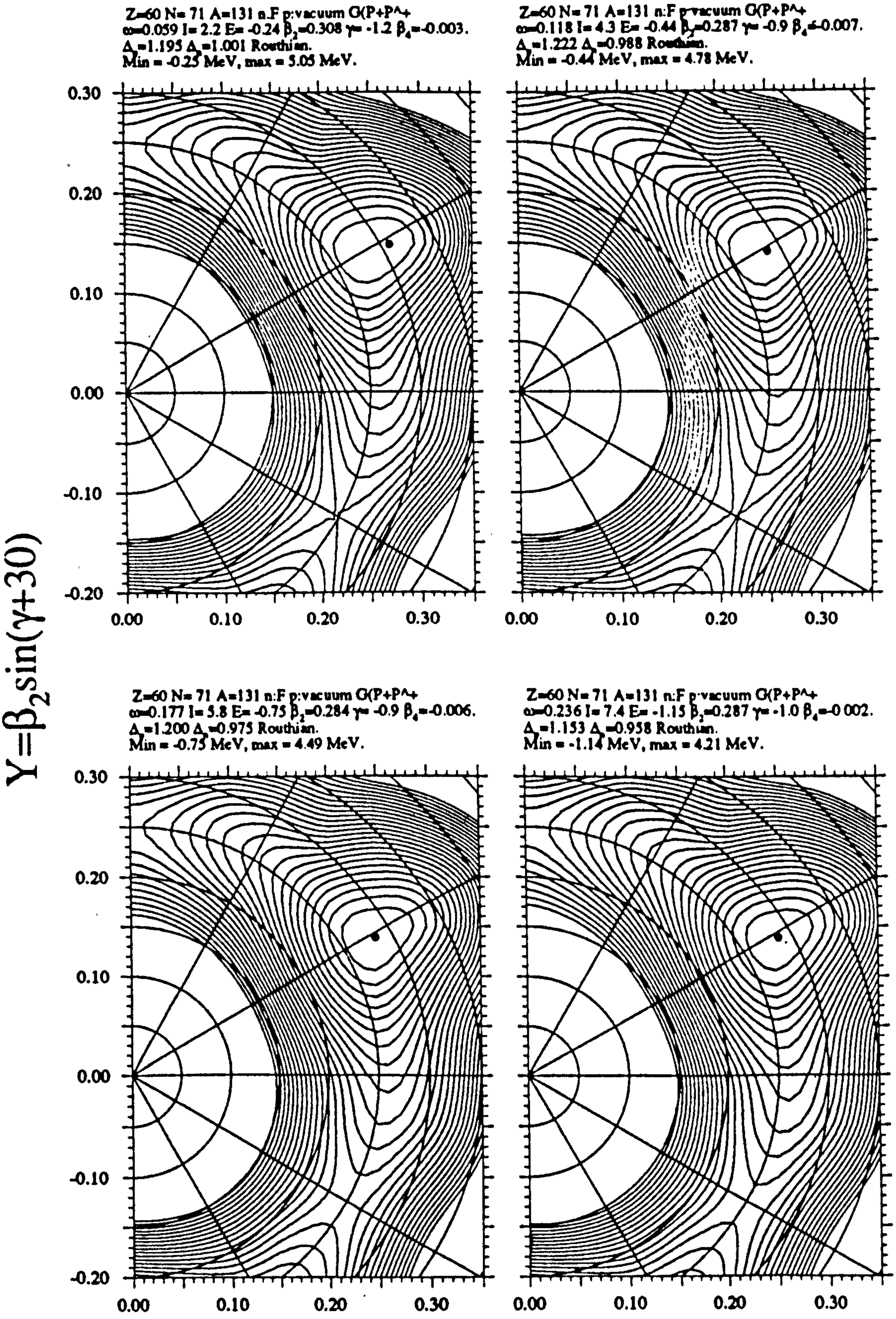

14-APR-88 02:00:43 AFI. Stockholm

Chapter 3

Apparatus and Techniques

3.1 Introduction

In any gamma ray experiment the critical factors for success are good resolution and high efficiency. In a compound nuclear reaction many products may be formed, so the resolution factor encompasses both resolution in energy of the gamma rays emitted and resolution between the various final products. These aims are often contradictory.

Results from four experiments will be presented in the following chapter; two exploratory experiments performed on the Recoil Separator (RS) [JMY88] using the Polytessa Array [NGT85] and designed with the aim of identifying γ-rays with specific reaction channels, and two high statistics γ-γ coincidence experiments using the ESSA-30 array [SS88] to further investigate some of the properties of the products identified in the first two experiments. This chapter describes the experimental techniques and apparatus used to obtain the data and general details of the subsequent analysis.

3.2 Techniques

3.2.1 Coincident Spectroscopy

The technique central to this work is that of coincident γ-ray spectroscopy whereby data is only recorded if one valid event is followed by a second within a preset time period. If this condition is satisfied then *all* events within a time window after the first event are recorded thus allowing events to be correlated in time. If correlations are observed between γ-rays it is implied that they belong to the same decay path. Similarly, if a γ-ray is correlated to a recoil, then it is statistically likely that the γ-ray was emitted from that nucleus. If the properties of the recoil are measured then the nucleus can be identified and the γ-ray can be directly identified with the decay of a particular nuclear species. γ-γ correlations can then be used to determine the structure of the decay sequences. Each pair of correlated events has a characteristic time interval associated with it. This

interval can be measured using the arrival of the first and second valid event signals to stop and start a TAC (Time-to-Amplitude Convertor) respectively. This information can then be used in the subsequent analysis to veto events in which the correlation time is un-characteristic (i.e. those events which are likely to be due to spurious coincidences) and also possibly to obtain lifetimes for long lived states ($\tau \geq 10$ ns, i.e. of the order of the timing resolution of a Ge detector).

3.2.2 The Doppler Shift Attenuation Method

The compound nuclear reaction is particularly well suited to the investigation of lifetimes using recoil methods by virtue of the well defined velocity of the recoiling nucleus. Since the results presented in Section 4.2 are of a qualitative nature only, this discussion of the Doppler Shift Attenuation Method (DSAM) [NS-S79] is limited to a brief synopsis. The range of lifetimes accessible via this technique is dependent upon the characteristic stopping time for the recoiling nucleus in the target/stopper combination, typically of the order of $10^{-14} - 10^{-11}$s. DSAM relies on the fact that a nucleus decaying in flight will emit γ-rays Doppler shifted according to

$$E = E_{\circ}\left(1 + \frac{v(t)}{c}\cos\theta\right) \tag{3.55}$$

where θ is the angle at which the γ-ray is detected with respect to the recoil velocity $v(t)$. The time t referred to is the time after the formation of the compound nuclear system and the velocity is time dependent due to the progressive slowing of the recoil in the target/stopper composite. DSAM does not measure the lifetime of a state directly; it does measure the apparent lifetime of a state i.e. the average cumulative time from formation of the compound system up to decay of the particular state of interest. A series of apparent lifetime measurements can then be fitted to certain assumptions about the intrinsic lifetimes (and hence the quadrupole deformation in a rotational band) to give a measure of the intrinsic lifetimes within the band. DSAM lifetimes can be strongly dependant on the feeding mechanism assumed for the band of interest and are always sensitive to the description of the stopping processes occurring in the target/stopper. Two effects are observed in spectra obtained at a specific angle with respect to the beam direction [1]:

- If the effective lifetime of a state is comparable to the characteristic stopping time of the target and backing then a fraction of the nuclei observed will decay in flight and exhibit a shift in observed γ-ray energy whilst the rest will decay at rest. In principle the effective lifetime of the state can then be fitted to the observed lineshape. Such an analysis requires high statistics and clean spectra (any contaminant in a spectrum will distort the lineshape

[1] This is assumed to be the recoil direction also. The stopping process itself scatters recoils away from this direction producing a spread in recoil angle and thus velocity. This effect is particularly important in the recoil energy regime where nuclear stopping becomes dominant since these low energy collisions are capable of producing large angular deflections.

and invalidate the measurement). At the low recoil velocities where such effects are observed nuclear stopping has a major effect on the stopping mechanism[1].

- States with effective lifetimes significantly shorter than the characteristic stopping time decay completely within flight and exhibit a shift in energy directly proportional to the mean velocity of the nucleus emitting the γ-ray. Thus the effective lifetime may be determined from a simple centroid shift measurement.

3.2.3 Angular Correlation and Distribution

The kinematics of the compound nuclear reaction restrict the initial angular momentum of the compound system formed to be aligned perpendicularly to the beam axis. The alignment is somewhat smeared out by collision processes in the target but the overall cylindrical symmetry of the system is preserved. By virtue of this alignment the distribution of γ-ray intensity is dependent upon the angle θ between the beam axis and the detector. The distribution can be expressed as:

$$W(\theta) = \sum_{k=0,2\cdots} a_k P_k(\cos\theta) \quad ; \quad k \leq 2J_i, k \leq 2\overline{L} \tag{3.56}$$

The restrictions on k are due to the consevation of angular momentum with J_i being the angular momentum of the system and $(\overline{L})$ the maximum multipolarity contributing to the transtion $J_i \rightarrow J_f$. A full discussion of angular distribution from a theoretical point of view can be found in [RB67]. For the purposes of this work it is sufficient to note that the the a_k are dependent upon the structure of the foregoing cascade, the angular momenta of the initial and final states and (assuming, as is experimentally plausible, that $\overline{L}$ is restricted to $L+1$) the mixing ratio (δ) between the amplitudes of the multipoles contributing to the transition. The Polytessa array does not permit a full angular distribution experiment to be performed due to the limited number of angles for detectors. Some distinction between the ditributions of γ-rays of different multipolarity is obtainable from the ratio:

$$R = \frac{W(143)}{W(101)} \tag{3.57}$$

If we substitute into 3.57 the a_k's measured for typical M1 and E2 transitions (the values used are taken from an angular distribution experiment on the nucleus ^{135}Nd described in [PBF87]) as below we find that R should distinguish well between different multipolarities at the angles allowed by the array.

J_i	J_f	a_2	a_4	δ	R
13/2	9/2	+0.247	+0.004	—	1.25 (E2)
13/2	11/2	-0.57	-0.03	-0.89	0.61 (M1/E2)
17/2	13/2	+0.387	-0.089	—	1.50 (E2)
17/2	15/2	-0.383	0	0	0.74 (M1)

It is possible to obtain similar information from a γ-γ correlation and this information could be derived from the ESSA-30 data. In this case the intensity is described by the more complex expression [LF61]

$$W(\theta_1, \theta_2, \phi_{12}) = \sum_{k_1, k_2, \kappa} a^{\kappa}_{k_1 k_2} P^{\kappa}_{k_1}(\cos\theta_1) P^{\kappa}_{k_2}(\cos\theta_2) \cos\kappa\phi_{12} \qquad (3.58)$$

3.3 The Recoil Separator

3.3.1 Why use the Recoil Separator?

There are several approaches to channel selection in a γ-spectroscopy experiment; coincident particle (α,p,n) detection (e.g. [VLM84]), sum energy-multiplicity requirements (e.g. [TNA83]) and detection of the actual residual species. This last method was employed for the exploratory experiments described in this work.

For moderately low energies and light ions solid state detectors can be used to resolve different species but, for heavy ions, damage to the detector becomes significant. Identification of heavy ions is best achieved using some form of dispersive magnetic transport system in conjunction with a focal plane detector. Such a system is inherently superior for work at 0° where it can take advantage of the forward coning of reaction products due to the kinematics of heavy ion reactions and provide rejection of the beam which would otherwise swamp a purely solid state particle identification system.

3.3.2 General Description

As the name implies, the Recoil Separator was designed to separate recoiling nuclei. The separation is at 2 levels; firstly separation of the residual nuclei from the immense background of beam particles which have not interacted with the target, and secondly physical separation of the residual nuclei according to mass/charge (A/q) ratios.

When used in conjunction with an ionization chamber, it is possible to identify the atomic number of the recoils providing unequivocal identification of the nuclear species produced in a reaction. The main features of the RS are shown in (Figure 3.1). The initial components up to the velocity slits serve to form a velocity dispersed image on the velocity slits and provide beam rejection in the first crossed field device (XFD). The remaining components serve to re-focus the velocity dispersed image and disperse the beam in terms of A/q at the final focus on the position sensitive detector. The recoils then pass into the ionization chamber where the energy loss characteristics are used to provide atomic number identification.

The apparatus is maintained at a vacuum of 10^{-7} Torr or better using a system of turbo-pumps and helium cooled cryo-pumps. The technical specifications of the various components are given in [Yi86]. In the following the various sections of the RS are described in more detail.

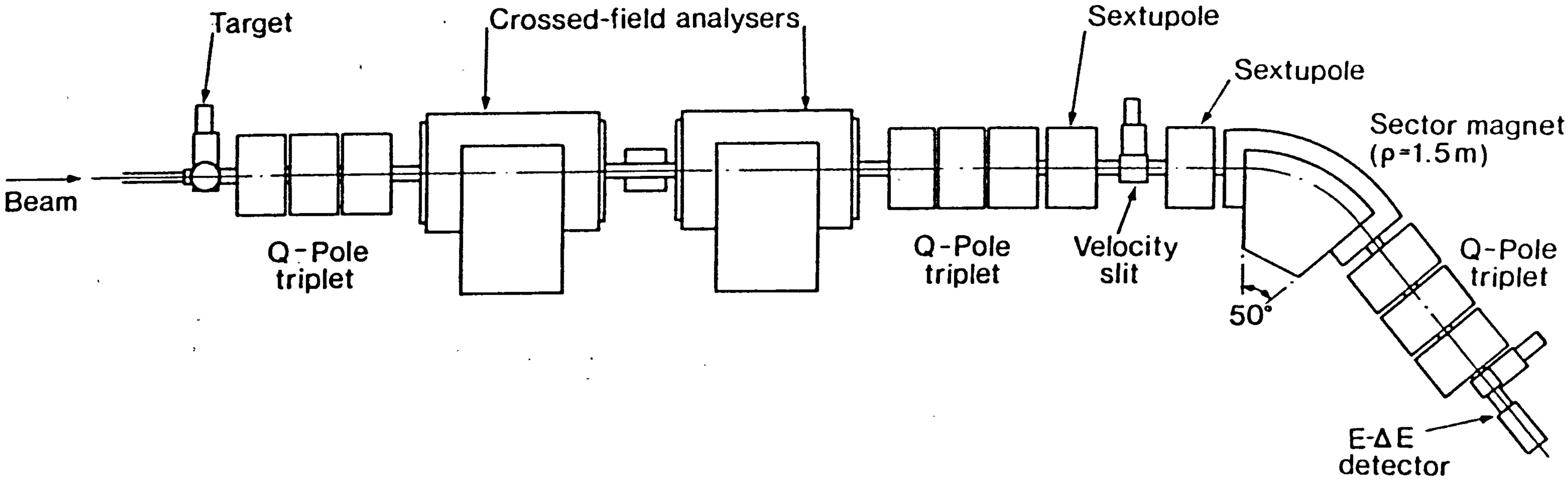

Figure 3.1: Schematic diagram of the Recoil Separator

3.3.3 Target Chamber

The target chamber used accommodates three targets on a screw-adjustable ladder. Situated behind this a second sliding ladder supports a quartz glower, to aid steering of the beam from the accelerator onto the target, and a thin ($20\mu gcm^{-2}$) carbon foil. Once the beam has been located using the quartz glower, it is replaced by the carbon foil.

Several processes occur within the target which affect the performance of the RS. Firstly, the target material will slow down both the primary beam and the recoiling compound nuclei [NS70] producing a velocity spread. Multiple scattering within the target will dissipate the forward coning of reaction products and the emission of light particles in the de-excitation of the compound nucleus will increase both the velocity and angular spread of the products. This last process is termed kinematic spread and is dominant for thin targets, the other effects becoming more important with increasing target thickness. The angular spread of recoils makes it desirable for the RS to have a fairly wide angular acceptance to improve efficiency. To this end, two sets of quadrupole triplets are situated before and after the XFD's to increase angular acceptance.

The nuclei emerge from the target with a spread of charge states [ND68] which may change due to in-flight decay by internal conversion. The carbon foil serves to reset the the charge distribution to normal following such a decay. Obviously, this is only effective for decays close to the target, and nuclei which susequently decay during transit through the RS will be detected with lower efficiency. Charge state changes due to collisions with gas atoms are minimised by the good vacuum within the system.

3.3.4 Crossed Field Devices

The cross field device (XFD) or Wien filter is the component which provides the velocity dispersion. This section is split into two independently set devices, the first of which disposes of the beam–like particles (using the large velocity difference between beam–like and compound particles) and the second controls the velocity dispersion in the intermediate focal plane at the velocity slits.

Each XFD provides a mutually perpendicular electric and magnetic field which influences the recoiling ions according to the Lorentz force

$$\mathbf{F} = q\epsilon(\mathbf{E} + \mathbf{v} \wedge \mathbf{B})$$

This force is zero if

$$V = - \mid E \mid / \mid B \mid$$

and the fields are set such that this condition is satisfied for the velocity of the compound system of interest. The magnitudes of the fields are governed by three factors. First, the dispersion of the XFD's must be sufficient to obtain the required mass resolution (the RS was designed to give 1/300 mass resolution) which is directly proportional to the velocity resolution. Secondly the dispersion must enable clear separation of the primary beam and finally the dispersion must

match that of the dipole sector magnet which cancels the velocity dispersion effects.

There is an intermediate vertical focus between the two sextupole elements and the spread in velocity of recoils progressing beyond this focus is determined by a pair of adjustable slits. The dispersion at this point is ~1cm per % velocity deviation from the velocity the system is set to transmit.

3.3.5 Sextupoles

Two sextupole magnets are included in the system which serve to correct for second order aberrations in the intermediate velocity image. The actual aberrations corrected for are designated $(x/\theta \quad \delta v)$ and $(x/\delta v \quad \delta v)$ in TRANSPORT notation [Br67] and correspond to second order achromatic focussing and dispersion. The beam optics are found to be rather insensitive to other second order aberrations [Yi86]. It is important to correct for these aberrations since the final mass resolution is determined by the velocity resolution.

3.3.6 Dipole Sector Magnet

The field in the dipole magnet is set such that the magnetic rigidity of the desired recoil with the mean velocity transmitted by the system matches the rigidity of the magnet.

$$B\rho = \frac{mv}{q}$$

where ρ is the radius curvature of the central trajectory through the magnet. The magnet itself is a 50° sector magnet with a uniform field and a rigidity dispersion which matches that of the XFD's so that the final image is not dispersed in velocity but is dispersed in A/q. The actual dispersion at the final focal plane is ~6mm per %rigidity which is sufficient to easily resolve A/q peaks in the mass 130 region. The final quadrupole triplet provides focussing for ions which entered the system at non-zero angles which would otherwise be focussed differently by the system, resulting in poorer mass resolution.

As mentioned in section 3.3.3 the ions entering the system are not in a single charge state but possess a distribution about a mean charge state (typically the 3-4 most intense charge states account for < 20% of the recoils[Ja87]). This leads to the possibility of A/q ambiguities whereby an ion having the same mass/charge ratio $(A'/q' = A/q)$ but a different mass and charge is brought to a focus in a similar region for a particular velocity. In the mass 130 region this can occur for products produced by alpha channels and discrimination against these is important since these channels may be produced with comparable intensity to those of interest. Such discrimination is provided within the ion chamber.

3.3.7 Detection System

The detection system comprises two distinct parts: a position sensitive detector (PSD) at the final focal plane of the RS followed by a removable ion chamber. This can be replaced by other detectors; for example solid state detectors for implantation experiments [WBF87] or magnetic tape transport systems [MCC87].

The position-sensitive detector [CP82] consists of a thin carbon foil through which the recoils pass (see figure 3.2). In doing so secondary electrons are liberated which are accelerated through a grid onto a pair of cascaded microchannel plates followed by a resistive anode. Outputs are taken from either end of the anode and doubly differentiated, the crossing time being a measure of the pulse rise time. The zero crossings are detected by cross-over pick-off (COPO) discriminators which are used to start and stop a TAC (Time Amplitude Convertor). The signal from this is used to determine the x-coordinate of the recoil on the PSD and hence the A/q of the ion. A typical signal is shown in Figure 3.3. The advantage of such a detector is that it causes minimum energy loss to the passing ion and provides a fast timing signal which may be used in conjunction with a signal from the beam buncher or chopper to provide a time-of-flight measurement and hence a mass measurement.

The following ion chamber [JMY88] records the energy loss characteristics of the evaporation residues in isobutane by charge collected from two anodes. It is separated from the high vacuum in the RS by a $50\mu gcm^{-2}$ polypropylene window.

The rate of energy loss of an ion in a material is a function of the atomic number and velocity (i.e. energy and mass) of the ion. Since the recoils are velocity selected, a measurement of the total charge deposited on both anodes will be proportional to the kinetic energy(E), and hence mass, of the ion and can be used to resolve the A/q ambiguities mentioned in the previous section. As the rate of energy loss is dependent on Z the energy deposited in the first anode (ΔE) will be a measure of Z. The resolution in Z is determined by both $\delta(\Delta E)$ (the FWHM of the ΔE peak) and $\Delta(\Delta E)$ (the separation between the ΔE peaks). From Figure 3.5 it is clear that for $\Delta(\Delta E)$ to be appreciable the recoils need an energy >1 MeV/nucleon (corresponding to a recoil velocity of $v/c = 4.6\%$). Below $v/c \sim 2\%$ the stopping power ($S = -dE/dx$) loses its Z sensitivity. The FWHM $\delta(\delta E)$ roughly follows the law [SH78]

$$\delta(\Delta E) = K\Delta E^{0.53}\frac{S(E-\Delta E)}{S(E)}\left\{\frac{Z_{ion}}{Z_{ion}^{1/3}+Z_{material}^{1/3}}\right\}^{1/2} \tag{3.59}$$

where K=0.067 is appropriate for isobutane. A detailed discussion of the energy loss processes within an ion chamber similar to the one used in these experiments can be found in [JBM83] including stopping power oscillations due to atomic structure and energy losses measured within the polypropylene ion chamber entrance window. Figure 3.5 implies that the maximal Z resolution is obtained if the first anode extends to the point at which the energy loss curves for the different Z's cross and that $\Delta(\Delta E)$ increases with increasing energy. Equation

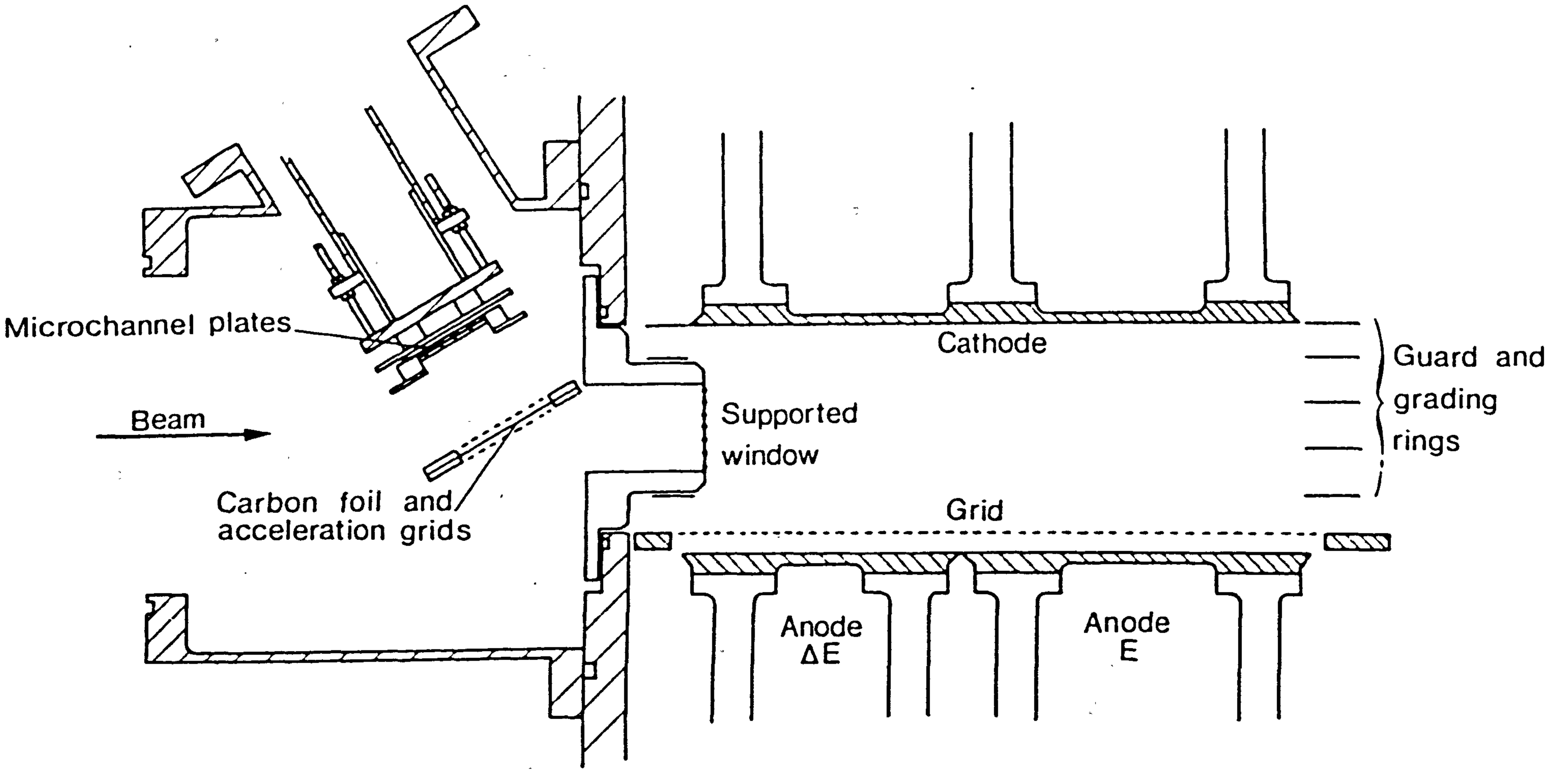

Figure 3.2: Schematic diagram of the Ion Chamber

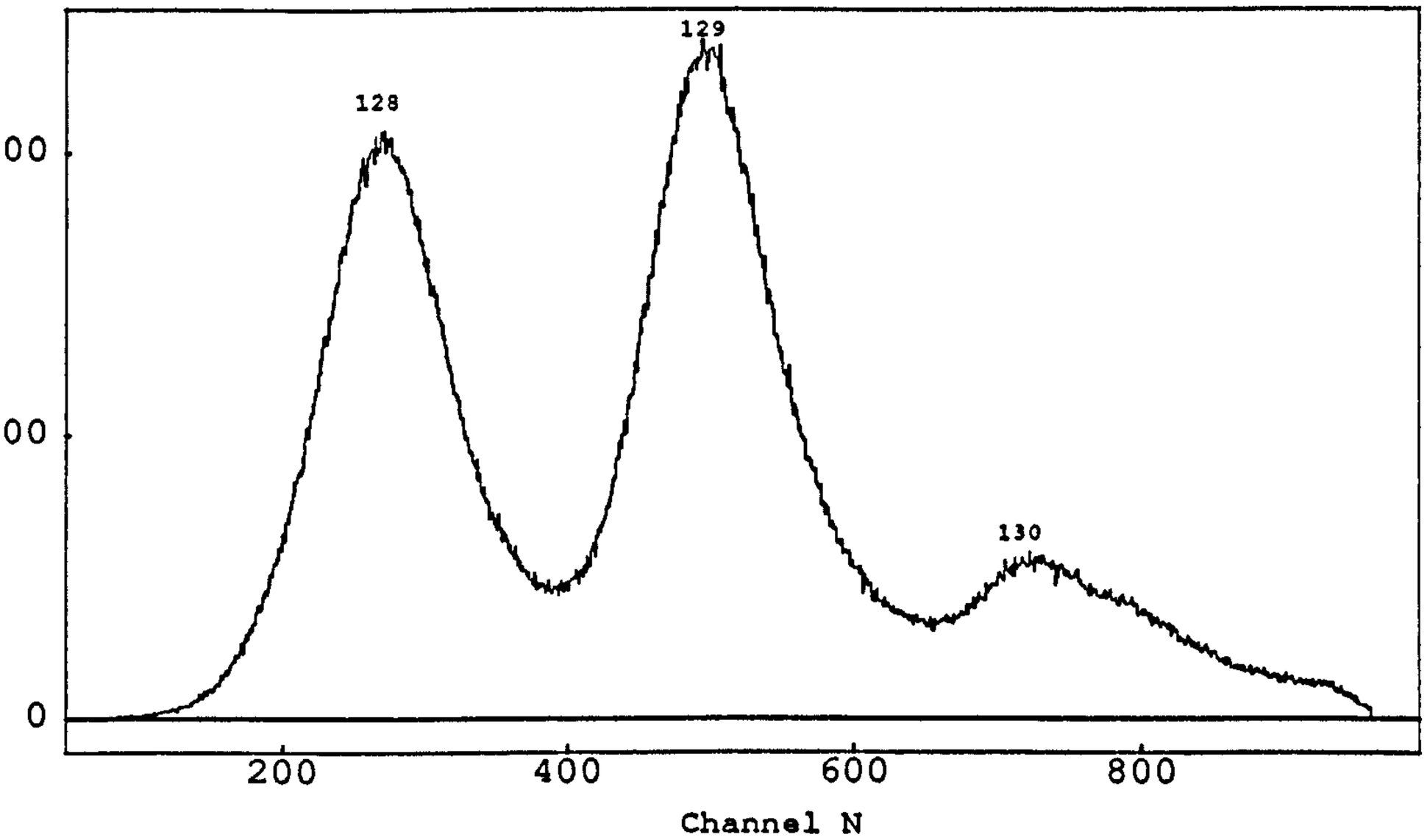

Figure 3.3: Typical TAC signal between the signals from the resistive anode of the position sensitive detector showing the unequivocal mass separation acheived by the RS. The particular spectrum shown here shows A/q peaks corresponding to the masses labelled on the diagram. Note the rather distorted appearance of the A=130 peak which can be accounted for by an A/q ambiguity (see section 3.7.3).

3.59 shows that as E (and hence ΔE) increases, $\delta(\Delta E)$ increases and that $\delta(\Delta E)$ is minimised for large ΔE due to the stopping power fraction term. However, if ΔE is increased beyond the crossing point of the energy loss curve, $\Delta(\Delta E)$ is reduced. A balancing of all these factors together with the fact that the ion chamber must completely stop the ions entering it produces the rule of thumb that Z resolution in the ΔE signal is maximised for ions entering the ion chamber at an energy near to that of the Bragg peak and that $\sim 70\%$ of the energy is lost in the first anode [Ja87]. The energy loss within the isobutane can be controlled by its pressure (subject to an upper limit of 30 Torr imposed by the polypropylene window), whilst the energy of entrance into the ion chamber is controlled by the reaction employed and the beam energy.

3.3.8 Control System

The RS is operated using a computer system [Mo86] which continually monitors and controls all the components. Proportional voltages are taken from the power supplies and the magnets are monitored using Hall probes, the output voltages being corrected for supply current and temperature variations. The processor

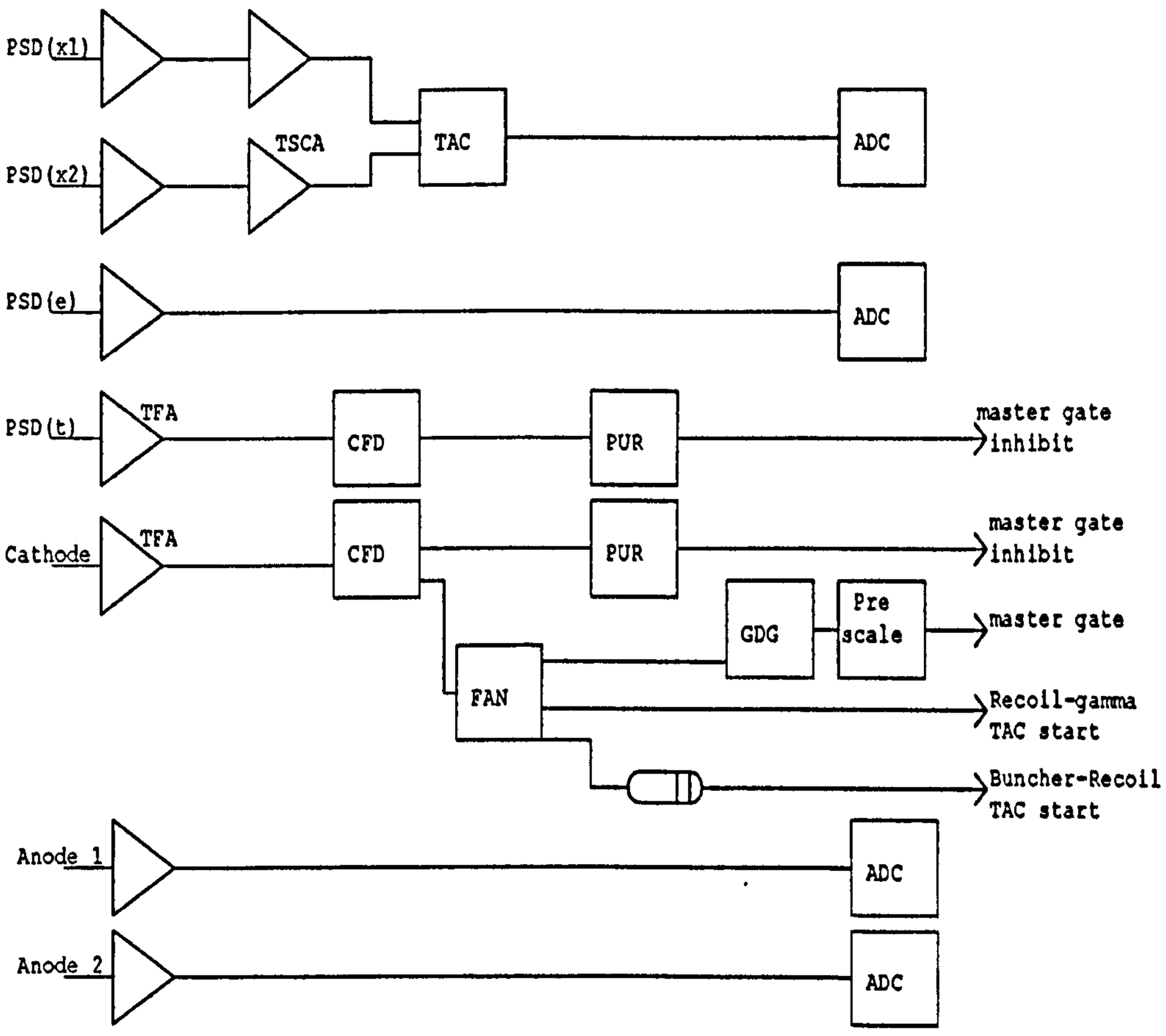

Figure 3.4: Schematic electronics associated with the collection of signals from the PSD and the ion chamber.

can be linked to external computer systems allowing remote control of the whole apparatus. A set of standard field settings is stored on disc and these can be scaled for a particular reaction and product (recoil velocity and mass/charge ratio) according to the magnetic and electric rigidities below.

$$B' = B\left(\frac{P'}{Q'}\right)\left(\frac{P}{Q}\right)^{-1} \quad E' = E\left(\frac{P'^2}{A'Q'}\right)\left(\frac{P^2}{AQ}\right)^{-1}$$

where A, P and Q are the mass number, momentum and charge state respectively of the standard fields stored within the system and primed quantities refer to scaled settings. The system continually logs the status of the RS and gives easy fine tuning of the beam optics. This permits the velocity and charge/mass ratio to be scanned on line to optimise field settings for the actual rather than calculated recoil velocities and charge states.

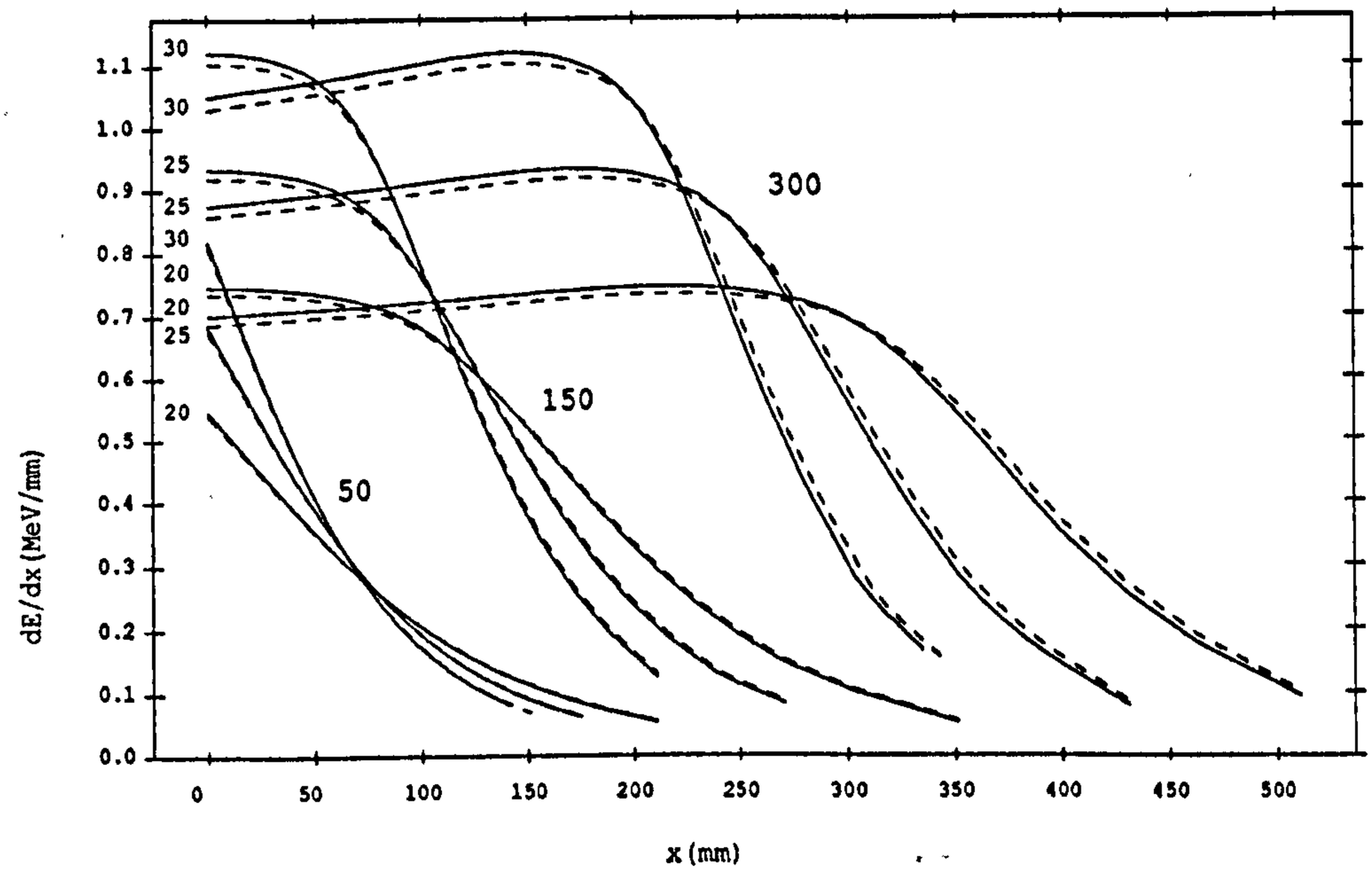

Figure 3.5: Rate of energy loss as a function of distance (x) travelled in iso-butane for ^{129}Nd and ^{129}Pr ions for a series of energies and pressures. In all cases the solid line refers to Nd and the dotted line to Pr, the pressures (Torr) are indicated on the left portion of the diagram by each curve and the initial ion energy for each set of curves by the remaining labels. The energies 50, 150 and 300 MeV correspond to recoil velocities of the order of 3,5 and 7 %v/c. The length of the first anode in the RS ion chamber is 100mm and the total length is 300mm. It is apparent that the maximal differentiation between species is obtained by a measurement of the energy deposited before the curves cross. The curves were obtained by numerical integration of the stopping power data given in [NS70].

3.4 Gamma-ray detection

3.4.1 Basic Principles

The detection of γ-rays relies upon the interaction of the γ-rays with matter, generally a semi-conductor for γ-ray calorimetry. This interaction occurs via three processes

- The Photo-Electric Effect: the γ-ray excites electron-hole pairs. Within a semi-conductor the excitation is into the conduction band and the application of an electric field permits the pairs to be swept out of the crystal.The integrated charge collected is used as a measure of the energy deposited.This is the process crucial to γ-ray spectroscopy.

- The Compton Effect: the γ-ray scatters quasi-elastically from an electron and loses only a small amount of energy. This, unfortunately, is the dominant process within the energy regime of interest in discrete line γ-ray spectroscopy $50 \leq E_\gamma \leq 2500$ keV and only serves to scatter photons out of the detector which therefore registers a lower energy than the true energy.This means that a simple detector will always have a continuous low energy background below a peak due to scattered events

- Pair Production: if the γ-ray has an energy in excess of the rest mass of two electrons (1.022MeV) then an e^+e^- pair may be formed. The positron will subsequently annihilate with an electron to produce two 'back-to-back' 511keV γ-rays. If one or both of these then escapes from the detector, secondary escape peaks will be observed at energies 511 and 1022 keV below the true photo-peak. The 511 keV γ-rays themselves are also generally seen strongly.

The probability of photo-absorption per atom is proportional to Z^5/E_γ^3 so the ideal photo-absorber is of high density and high Z. In general Germanium detectors are used since they have

- good energy resolution: the FWHM of a Germanium detector is $\sim$ 2.0–2.5keV at 1.3MeV .This is due to the low energy required to excite electron-hole pairs into the conduction band (2.95 eV at 80K compared with 3.72 eV for Silicon).

- relatively good timing characteristics: charge collection times are generally $\leq 1\mu s$.

- good photo-peak efficiency: this is due to the relatively high Z of Germanium.

In general Germanium detectors have the following disadvantages:

- they must be operated at LN_2 temperatures (77K) in order to avoid thermal excitation of electron-hole pairs into the conduction band which would give rise to a spurious background of thermal noise. To this end detectors are provided with a 'cold finger' from a LN_2 dewar which must be filled at ~8hr intervals.

- they are prone to neutron damage which causes dislocations within the crystals. This leads to poor charge collection and hence poor energy resolution. Neutron damaged detectors can be identified due to tailing on the low energy side of photo-peaks and can sometimes be repaired by annealing.

- the size of the single crystals which can be produced currently is limited. The use of larger crystals would be desirable as this increases photo-peak efficiency. There would, however, be some penalty in using increased volume crystals in terms of slower and position dependent charge collection.

The detectors used in the arrays described in this work were of the Gamma-X type being made of hyper-pure Germanium (HpGe) as opposed to the Lithium drifted Ge(Li) detectors used previously. These have the following advantages over the older detectors

- they are less susceptible to neutron damage (by a factor of $\approx$2).

- they do not require to be stored at LN_2 temperatures.

- the implanted Boron surface contact is much thinner ($0.3\mu m$ as opposed to 500-1000μm).This reduces the dead layer thus improving the photo-peak efficiency from $\approx$18% to $\approx$21% and the Compton suppression factor by reducing the absorption of scattered radiation.

Other materials commonly encountered in γ-ray spectroscopy are the scintillators

- **NaI(Tl)** NaI(Tl) has long been used as a scintillator in the field of nuclear physics and has the advantages of good detection efficiency, a high light yield and availibility in large crystals. The disadvantage of NaI(Tl) is its poor energy resolution

- **BGO** Bismuth Germanate (BGO) has a stopping power $\approx$ 2.5 times that of NaI and hence only 1/16th of the volume of BGO is required to get the same performance as NaI. BGO is also less sensitive than NaI to neutrons below 4MeV and is thus an attractive material for anti-Compton shields. BGO also has good timing characteristics and is thus often used within multiplicity -sum energy balls in arrays.

- **CsF** The main usage of CsF detectors is to provide a start signal by which the timing in an experiment may be measured due to the fast response of the material. As a detector the material has poor energy resolution and a low efficiency.

3.4.2 Compton Suppression

As detailed in the previous section the γ-ray events of interest are those in which all the energy is absorbed within the detector crystal. For a single γ-ray detector the probabilty of such a photo-peak event is about 20% of the total events recorded. When two γ-rays are required to be observed in coincidence the probability of a photo-peak — photo-peak coincidence is 4% of all $\gamma - \gamma$ events and for higher multiplicity events the proportion is similarly dramatically reduced. Clearly, such a large Compton background impairs the resolution of the system. Large improvements can be made by employing Escape Suppressed Spectrometers (ESS) [Dr81].

The principle of the ESS is that any Compton scattered events escaping the detector crystal are themselves detected and used to veto the signal from the calorimeter. The critical criterion for the anti-Compton shield (ACS) is that it should be efficient; energy resolution is unimportant. Hence it can be made from cheaper scintillators such as NaI(Tl) or BGO. The ESS used in the arrays described in section 3.4.3 [NGT85] is illustrated in figure 3.6. The ACS consists of eight optically separate BGO crystals forming a cylindrical body of minimum wall thickness 35mm. Each crystal is viewed using an angled photo-multiplier tube. In order to detect backscattered γ-rays the front of the ACS is made from one piece of NaI which is optically coupled to the BGO. The catcher behind the crystal was not present in these experiments. The great advantage in using BGO in the shield is its high density enabling more compact shields to be constructed and paving the way for many-detector arrays. NaI is utilised in the nose due to it's superior light output. The adoption of anti-Compton suppression increases the peak-to- total of a single detector to ~50% and for a coincident event to $\sim 25\%$

The complete ACS is collimated with lead or tungsten in order to shield it from direct γ-rays which would otherwise veto valid events. The entrance port to the detector is sometimes collimated further to reduce the angle of acceptance and hence Doppler broadening in detectors near perpendicular to the beam direction.

3.4.3 Detector Arrays

The idea behind arrays of detectors is a simple one — the more detectors the greater the efficiency. The efficiency of detection of $\gamma - \gamma$ coincidences is proportional to $N(N-1)$ where N is the number of detectors so as the number of detectors is increased the efficiency increases roughly as N^2. Similarly for triple $\gamma - \gamma - \gamma$ events the probability of detection increases roughly as N^3. As detector technology improves, the size of the individual detector decreases, enabling more of them to be packed around the target. It was the use of BGO in the ACS which facilitated the construction of the array described below. The aim of the geometry adopted was to pack as many detectors as close as possible to the target.

Both the Polytessa (Figure 3.7) and ESSA-30 arrays possess the same geom-

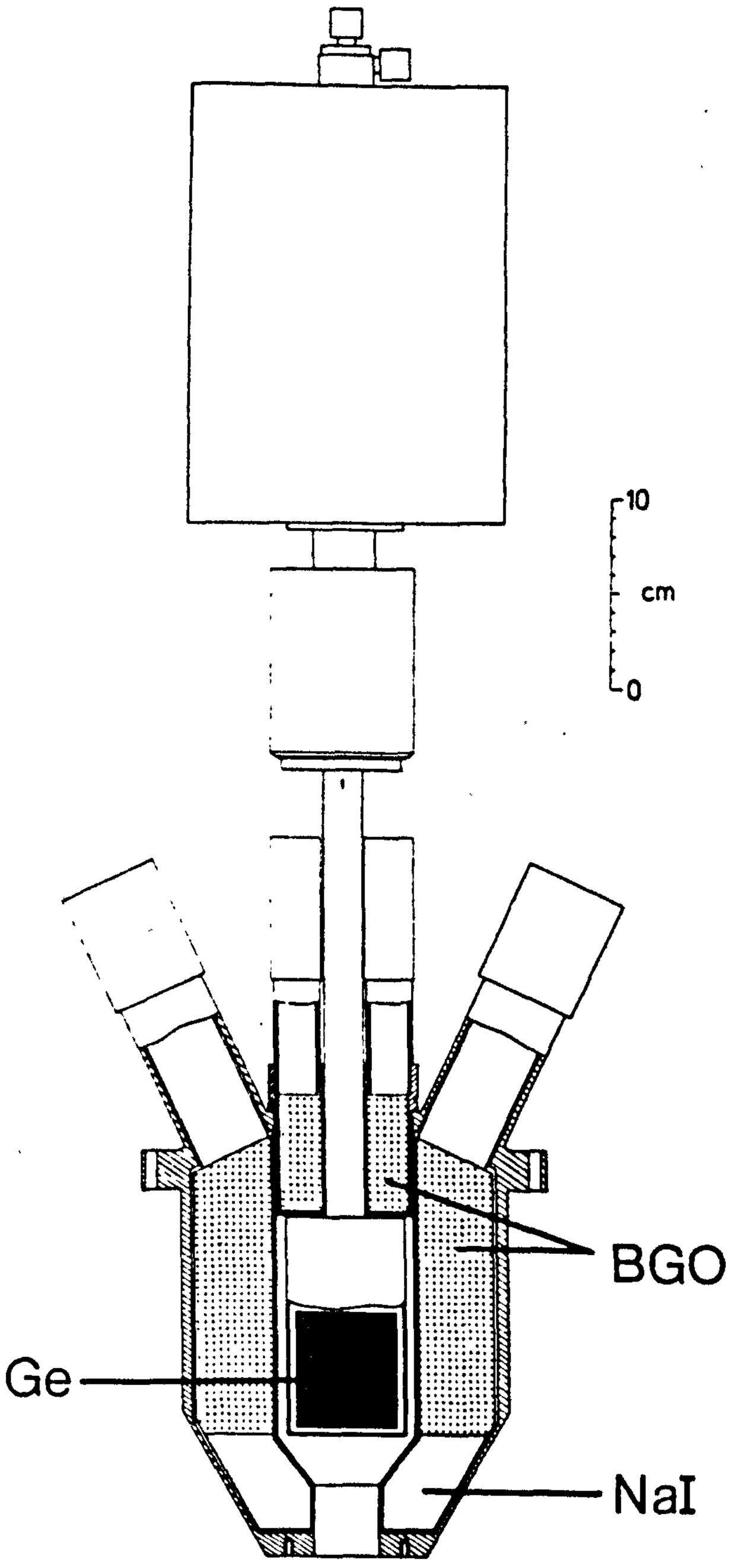

Figure 3.6: Section through a Compton suppressed Germanium detector of the type used for the experiments described.

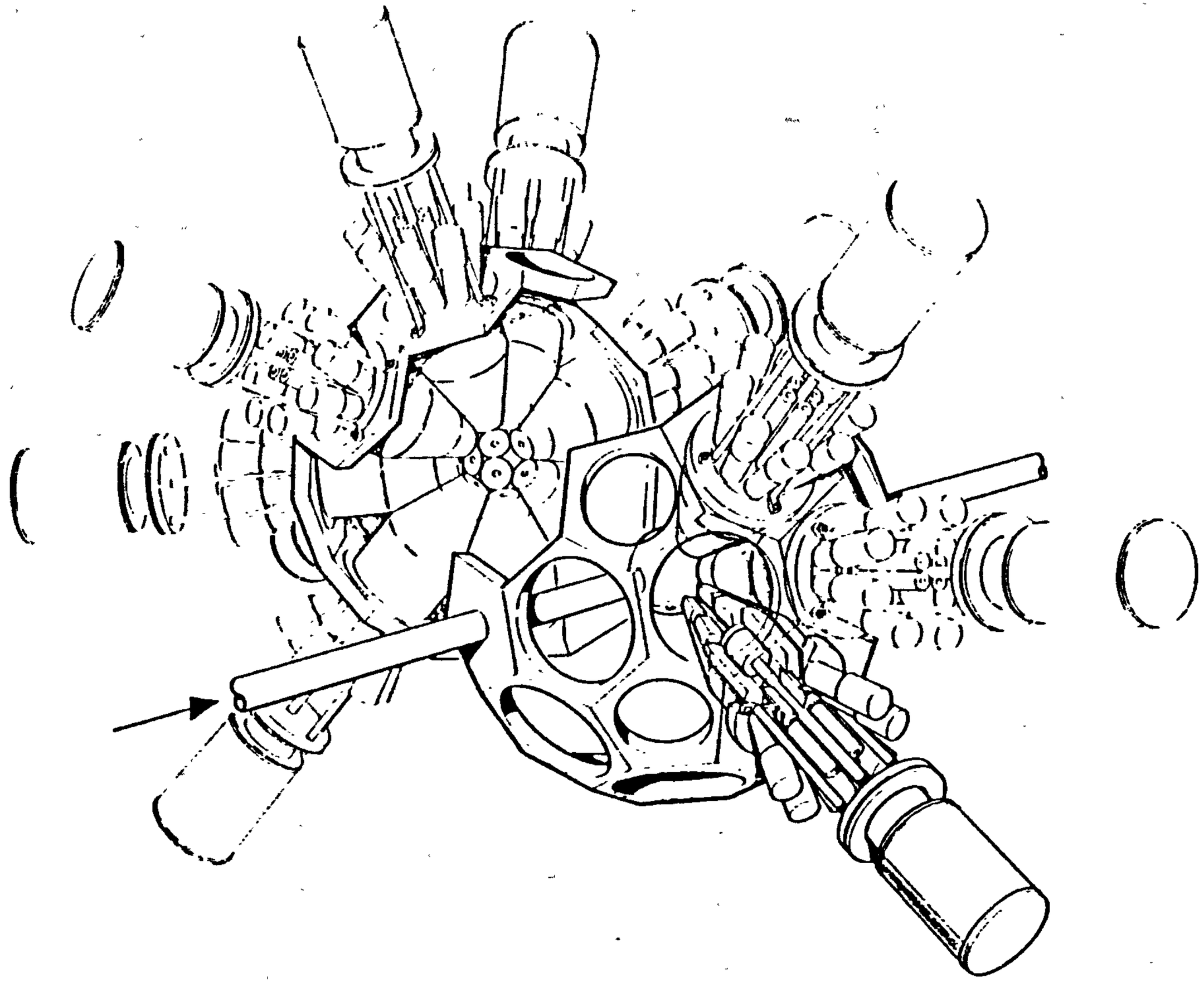

Figure 3.7: The Polytessa array

etry, that of a truncated icosahedron. Roughly translated this means that the detectors sit in six rings at 37°, 63°, 79°, 101°, 117° and 143° to the beam axis supported by hexagonal and pentagonal frames. The centre of the detector is 24cm in the 63° and 117° rings and 20.5cm away from the target in the other rings. In the Polytessa array the first two rings of detectors are missing in order to place the array at the front end of the RS with the result that it accomodates twenty detectors as opposed to thirty in ESSA-30. The 101° and 117° detectors were collimated in the RS experiment to reduce Doppler broadening which was significant due to the high recoil velocity. With the Polytessa array on the RS the primary motive was the collection of Recoil-γ coincidences and channel selection was provided by the RS. There was no method of channel selection employed for $\gamma - \gamma$ data for either the RS or ESSA-30 experiments.

3.5 Data Collection

3.5.1 Data Acquisition

The data acquisition system comprises an accumulation machine (GEC 4085 processor), a control machine (GEC 4190), a resources machine (GEC 4190) and an Event Manager. The Event Manager is an intelligent interface between the flexible experimental electronics and the computer system. The device clears down the ADC's at the end of an event, verifies and buffers user defined multiparameter events and kicksorts ADC data. Multiparameter events are controlled by a 'Trigger Manager' which accepts logic signals defining a subset of ADC's to be included in an event. The trigger used for the experiments described here was the 'External Indirect Trigger' whereby all ADC's in preconversion at the arrival of the trigger are included in each event. The signal used as the external indirect trigger is referred to as the 'master gate'. The Event Manager is set up and controlled by the accumulation processor which also reads and sorts blocks of multiparameter data (sent from the Event Manager via a Camac serial branch) and dispatches multiparameter blocks to the resources machine for writing to magnetic tape. Interactive control of an experiment is provided by the control machine which has access to the accumulation processor.

3.5.2 Array Electronics

The basic Ge detector electronics are shown in Figure 3.8. Two analogue energy signals from the detector pre-amplifier and a signal from the ACS are taken for each detector. One energy signal is used to verify that the event recorded was 'good' by requiring two levels of coincident conditions to be satisfied.

- the first coincidence requirement is that a fast Ge signal from the TFA must be present while the busy signal from the amplifier is low. This prevents pile-up of events. Output from this stage is vetoed by the detection of a pulse in the ACS providing Compton suppression. The output from this

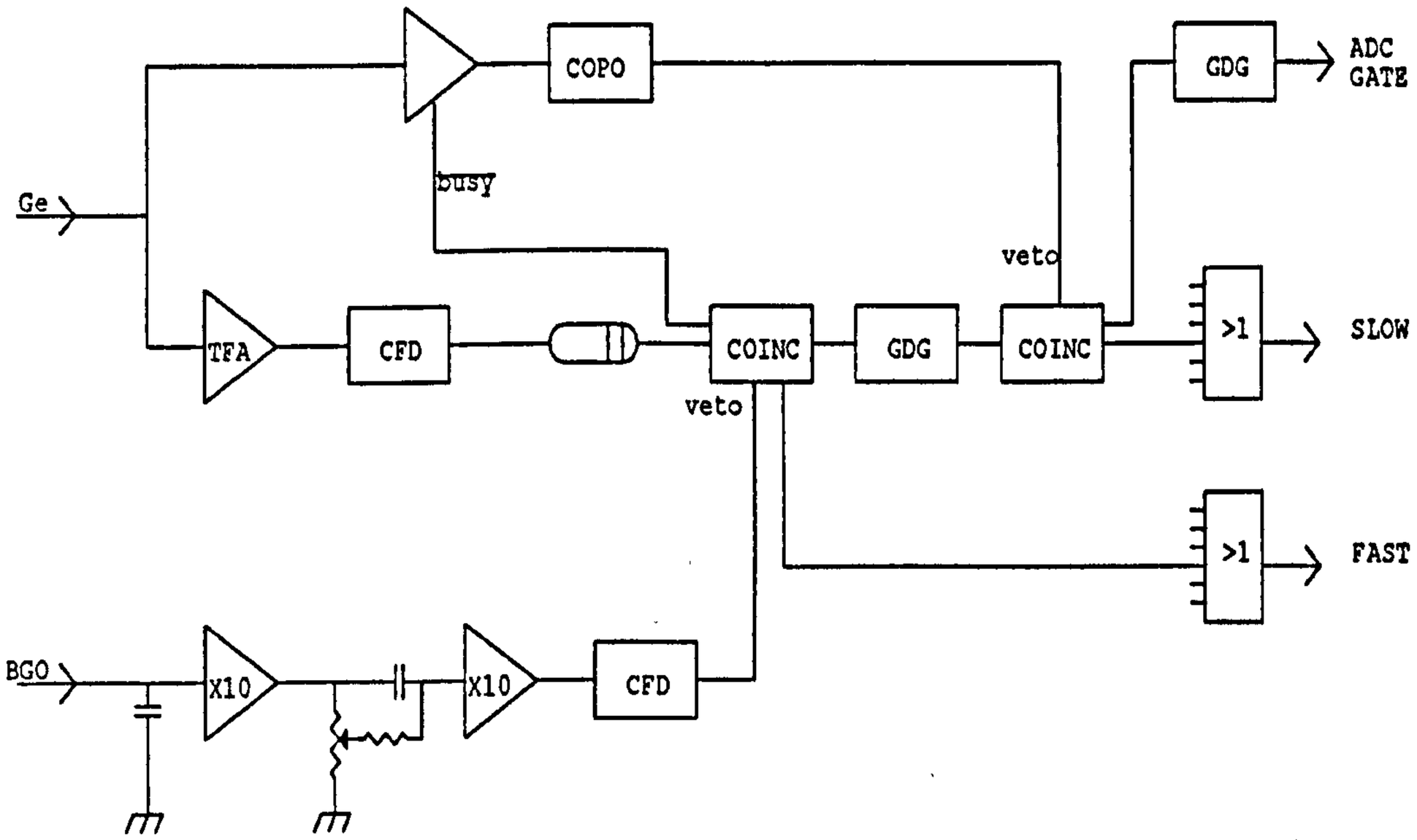

Figure 3.8: Schematic electronics associated with the derivation of valid Compton suppressed signals from a Germanium detector.

stage is fast, the slowest element being the BGO signal, and hence it is used subsequently as an input in the experimental logic.

- the second coincidence requirement is that the first be satisfied and that the amplifier should collect the charge within a specified time window. Events that fall outside this window correspond to badly shaped Germanium pulses due to pile-up or poor charge collection and would otherwise contribute to the background. The output from this stage is delayed since the amplifier must collect the charge before the arbitration is made. This signal is used to gate the ADC conversion of the second Ge signal once it has been amplified.

The valid Ge signals at the first level are fed into a multiplicity unit which outputs a logic pulse and an $N \times 50mV$ pulse if more than N events are detected coincidently (N being set by the user). A discriminator can be set on the $N \times 50mV$ signal to distinguish γ,$\gamma - \gamma$ and γ-γ-γ events and used to stop TAC's between a γ and a γ-γ or γ-γ-γ event (see Figure 3.9). In the ESSA-30 experiment both γ-γ and γ-γ-γ TAC's were recorded whilst only γ and γ-γ signals were derived for the RS experiments.

3.5.3 RS Electronics

The main problem that the RS poses is that the signals from the recoil detectors do not begin to be processed until $\sim 1\mu s$ after the γ-ray signals. This

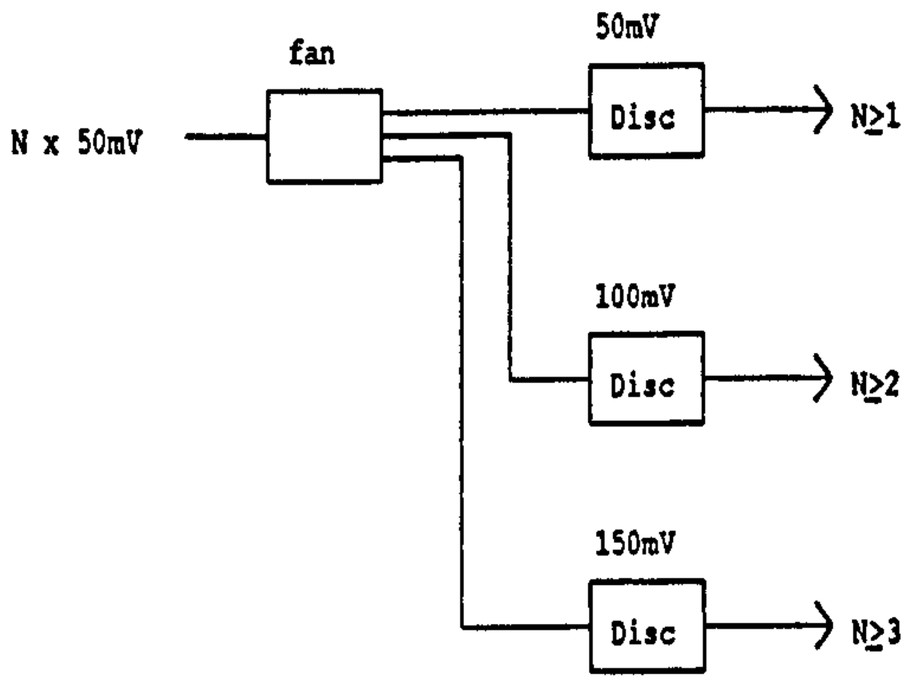

Figure 3.9: Schematic electronics for the derivation of signals corresponding to the detection of different numbers of coincident γ-rays.

timing difference must be compensated for by the inclusion of appropriate delays and the synchronisation of recoil and Germanium events must be done 'in-beam'. The RS was used in conjuntion with a bunched beam which required a signal to stabilise the buncher. This was acheived using a CsF detector placed close to the target chamber to signal the arrival of a beam bunch and gating the TAC between this and the trigger by a processed energy signal from the CsF detector to cut out noise. The bunching enabled correlation between the presence of the beam and the arrival of recoils so that events recorded out of beam (i.e. background events) could be filtered out using the buncher-recoil TAC signal (Figure 3.11). The Recoil-γ TAC provided a velocity selection against beam scattered through the system. To further reduce background the event manager was disabled and beam cut off when the RS was being controlled.

The RS data requires that single γ-ray events be recorded in coincidence with valid recoil events as well as γ-γ events so the master gate for the Event Manager is a composite signal generated as in (Figure 3.12). The master gate is vetoed by any pile-up of events in the ion chamber.

3.6 Choice of Beam and Target

The reactions available to populate very neutron deficient species are limited by available beam/target combinations. It is well known that nuclei have a neutron abundance which increases with increasing Z due to the influence of Coulomb forces; hence when two nuclei fuse to form a compound nucleus, the compound nucleus is inherently neutron deficient. In order to make the most neutron deficient nuclei, combinations of particularly neutron deficient beam and target are required. The beam and target are required to be stable under normal circumstances and this limits the combination to be used. It is also desirable that the target be mechanically robust (though sometimes a fragile material can be supported on another relatively inert one) and reasonably chemically stable

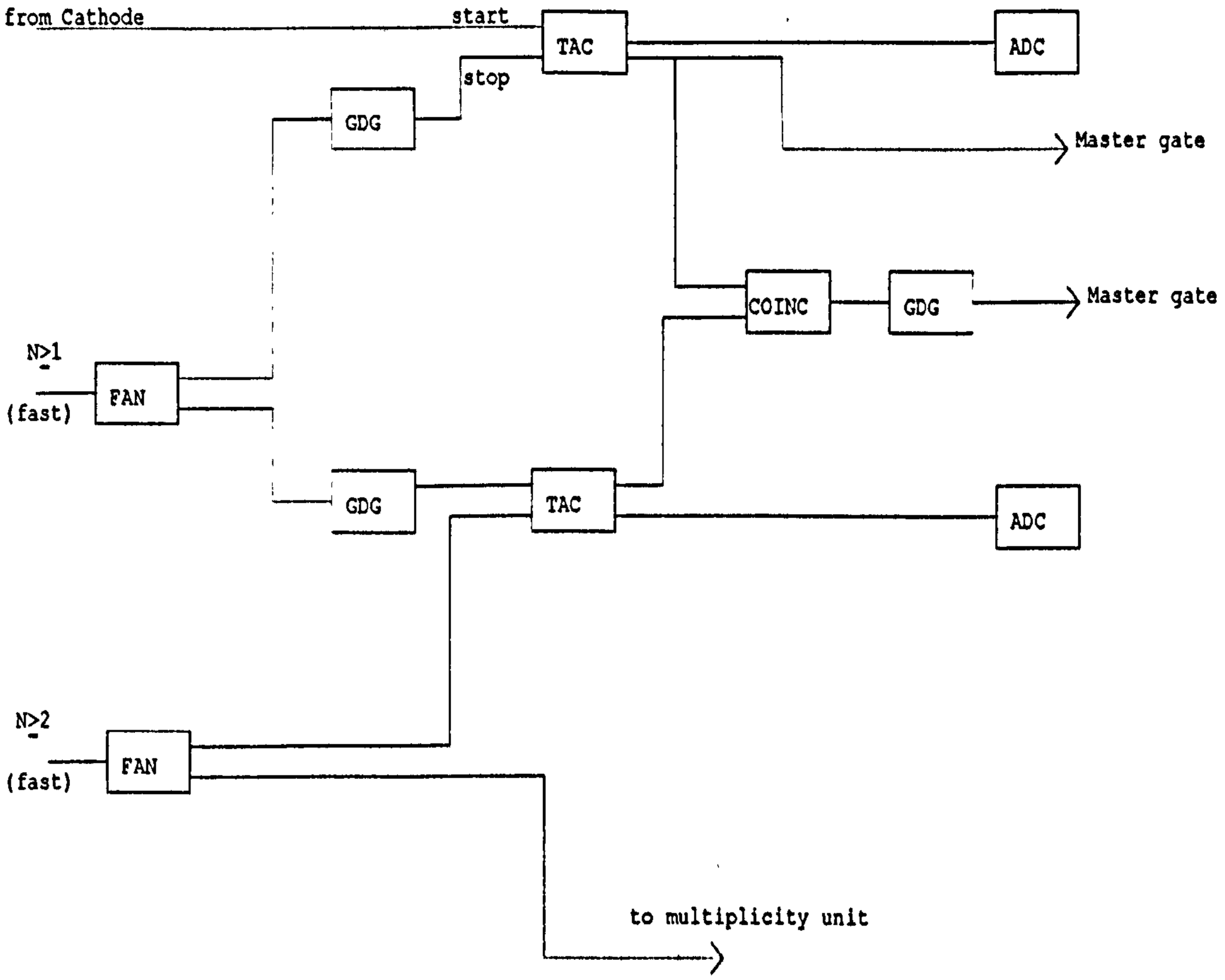

Figure 3.10: Schematic electronics showing the derivation of TAC signals for both Recoil-γ and γ-γ events.

to processes such as oxidation.

The target thickness chosen depends on the purpose of the experiment. For RS experiments a thin target is necessary to allow the recoils to be detected. The thickness is chosen as a compromise between minimising energy (and hence velocity) straggling from within the target and keeping a reasonable reaction rate. To this end 500μgcm^{-2} targets were used so that kinematic spread was the dominant process occurring within the target.

For the RS experiments the beam/target combination must be chosen to maximise the resolution in the ion chamber between different isotopes with the same mass. With the maximum pressure, and hence the stopping power of the iso-butane in the ion chamber, limited to 30 Torr by the thickness of the polypropylene window, the only way to approach the Bragg peak and achieve good Z resolution for the A $\sim$ 130 nuclei is to use the most inverse reactions available.

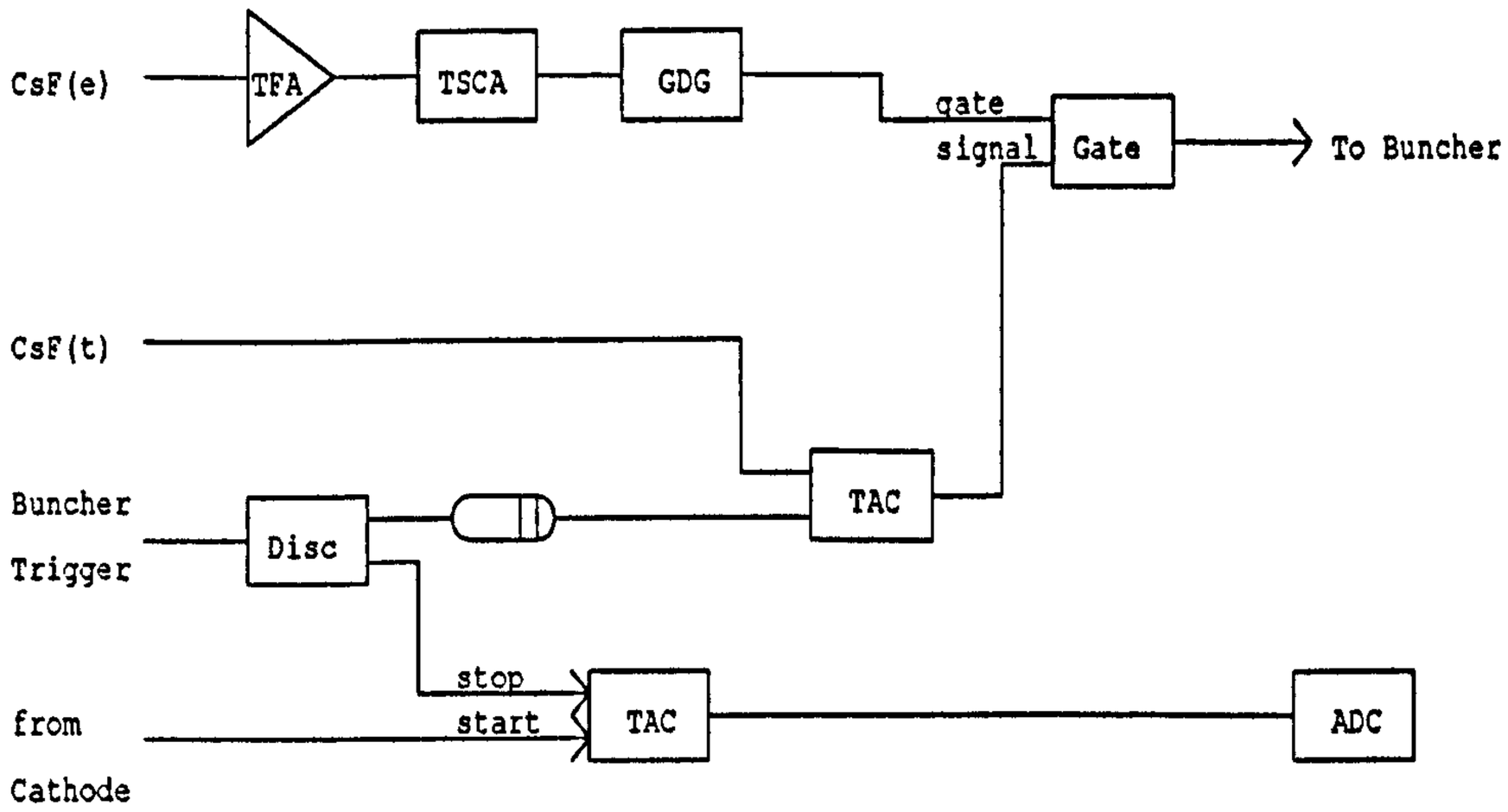

Figure 3.11: Schematic electronics for the buncher stabilisation and derivation of the buncher-recoil TAC.

Even when the recoils are not to be transported, a thin target is desirable since the velocity spread of the recoils contributes towards the energy resolution of the gamma-ray detectors via Doppler effects. Thus a 500μgcm^{-2} target thickness was also employed for the ESSA-30 experiments. One of these was gold backed in order to stop the recoils and look for fast lifetimes using the Doppler Shift Attenuation Method. The use of a thin target has the drawback of reducing the reaction rate. Gold was used as a backing since its high Z means that the Coulomb barrier is not exceeded and a secondary reaction is not introduced. However the quality of the spectra was still impaired both by Coulomb excitation of the gold backing and by the build up of beta decay products in the target.

3.7 Data Analysis

3.7.1 Terminology

Multi-parameter event processing has given rise to several jargon terms which are freely, if sometimes confusingly, referred to. In order to avoid any confusion, defined below are some of the offending terms as used in this work:

- *EVENT*-the set of values read by the ADCs and subsequently recorded onto tape when a signal from the master gate was present at the event manager.

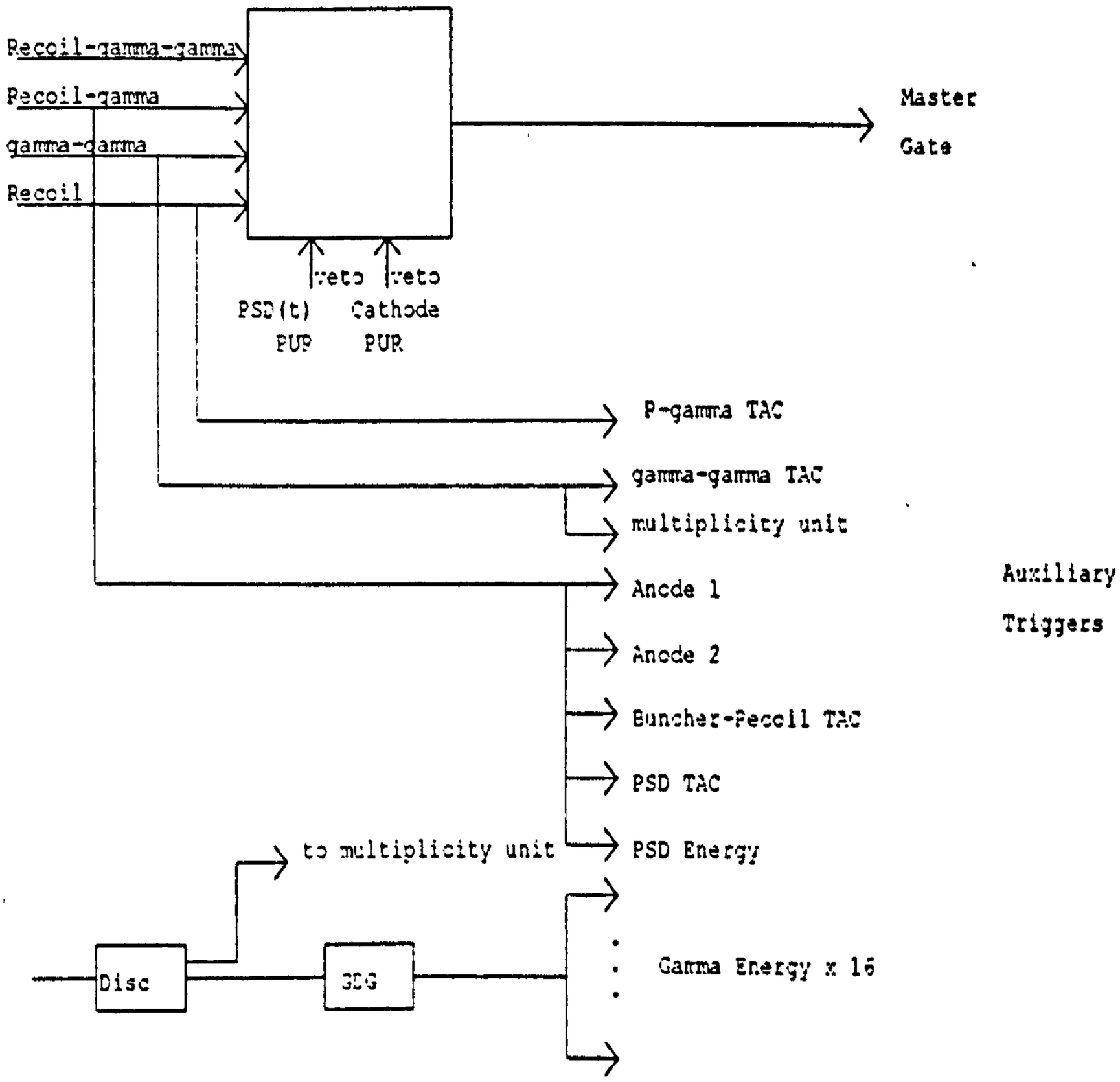

Figure 3.12: Schematic electronics for the derivation of the gating signals for the event manager on the Recoil Separator. Note that a master gate will be present for Recoil-γ and γ-γ events, the former being vetoed by any pile-up detected in the ion chamber signals.

- *SORT*-a program designed to read events back from tape and process the data by testing the values of sortwords and incrementing spectra or matrices if these tests are satisfied.

- *SORTWORD*-a combination of ADC values and/or constants in a particular event.

- *SPECTRUM*-a binned frequency histogram for a sortword. The bins represent ranges of ADC values and are individually referred to as *channels*.

- *MATRIX*-a 2-dimensional binned frequency array in which the value held in an element corresponds to the frequency with which bi-sortword events occur. Matrices may be further analysed by placing windows on one parameter and projecting out the spectrum of the second sortword in coincidence with values of the first sortword lying within the window. Such manipulation is carried out using separate software.

- *WINDOW*-a pair of values defining a condition on a sortword which is required to be satisfied in order for a spectrum to be updated by the sort program. *POLYGONAL* windows may be defined on 2 parameters simultaneously as a set of numbers corresponding to the vertices of a closed polygon defined on a matrix formed by the two sortwords.

- *GATE*-a spectrum incremented when values of a particular sortword fall within a specified window. Confusingly the spectrum is termed 'gated' on the window.

- *TOTAL PROJECTION*-the summed spectrum over all values of one sortword within a matrix. The projection may be onto either the 'X-axis' or 'Y-axis' according to whether the summation is over the first or second sortword.

3.7.2 $\gamma - \gamma$ Data analysis

Matrices of $E_{\gamma 1}$ v $E_{\gamma 2}$ were used to examine the coincidences between two gamma-rays. Windows were set on $E_{\gamma 1}$ so that the spectrum of $E_{\gamma 2}$ showed the coincident γ-rays. Background events corresponding to random coincidences and events with incomplete deposition of energy in the detectors were removed either by subtracting counts in coincidence with an equivalent energy range adjacent to the $E_{\gamma 1}$ range 'gated' on or by subtracting an appropriate fraction of the total projection of the matrix. The decision as to whether the background subtracted is 'meaningful' is somewhat arbitrary so the subtraction process introduces errors in the peak intensities observed. Such errors obviously increase as the intensity of the peaks decrease relative to the background. The problem of background can be greatly reduced by considering only triply coincident events. Coincident $\gamma - \gamma - \gamma$ triples were recorded in the ESSA-30 experiments and these proved to be of great utility, especially in the backed target experiment where γ transitions

associated with β-decays dominate many of the γ-rays of interest. The low multiplicity of events following β-decay and of gold Coulex means that triple events are much more likely to be events of real interest. Thus in these experiments triple coincidences were used simply to select channels of interest by sorting into $\gamma - \gamma$ matrices already gated upon transitions established in particular bands. Generally several alternative windows were used to increase statistics; events satisfying more than one window were included multiply and all γ-rays in events of multiplicity greater than 3 were considered.

3.7.3 Recoil Separator Data analysis

The data recorded within the ion chamber and position sensitive detector (PSD) provide two levels of recoil identification: mass recognition and atomic number selectivity. Whilst almost all of the recoils detected within the PSD are subsequently detected in the ion chamber, the manipulations required to achieve Z selection drastically reduce the intensity of Z selected γ-ray spectra as compared to mass selected spectra.

The positional signal from the PSD TAC provides a direct observation of the mass of the recoil (see Figure 3.3). Windows set between suitable limits were used to generate mass gated Recoil $-\ \gamma$ spectra and Recoil $-\ \gamma - \gamma$ matrices. It was hoped that the RS experiments would produce sufficient statistics to enable Recoil-γ-γ events to be utilised in the analysis. Unfortunately the number of events recorded proved too few for such data to have any advantage over the conventional γ-γ data. For completeness a comparison of spectra gated from the same γ-ray window from a mass gated Recoil-γ-γ matrix and an ordinary γ-γ matrix is shown in (Figure 3.14). Mass selected Recoil-γ spectra were obtained for each detector angle with respect to the beam and the I(143)/I(101) ratios obtained from them used to differentiate between different transition multipolarities. Such assignments would have been less ambiguous had the statistics permitted the use of Z-selected spectra at the various angles since there would have been fewer interfering γ-rays. In most cases a simple condition on the PSD

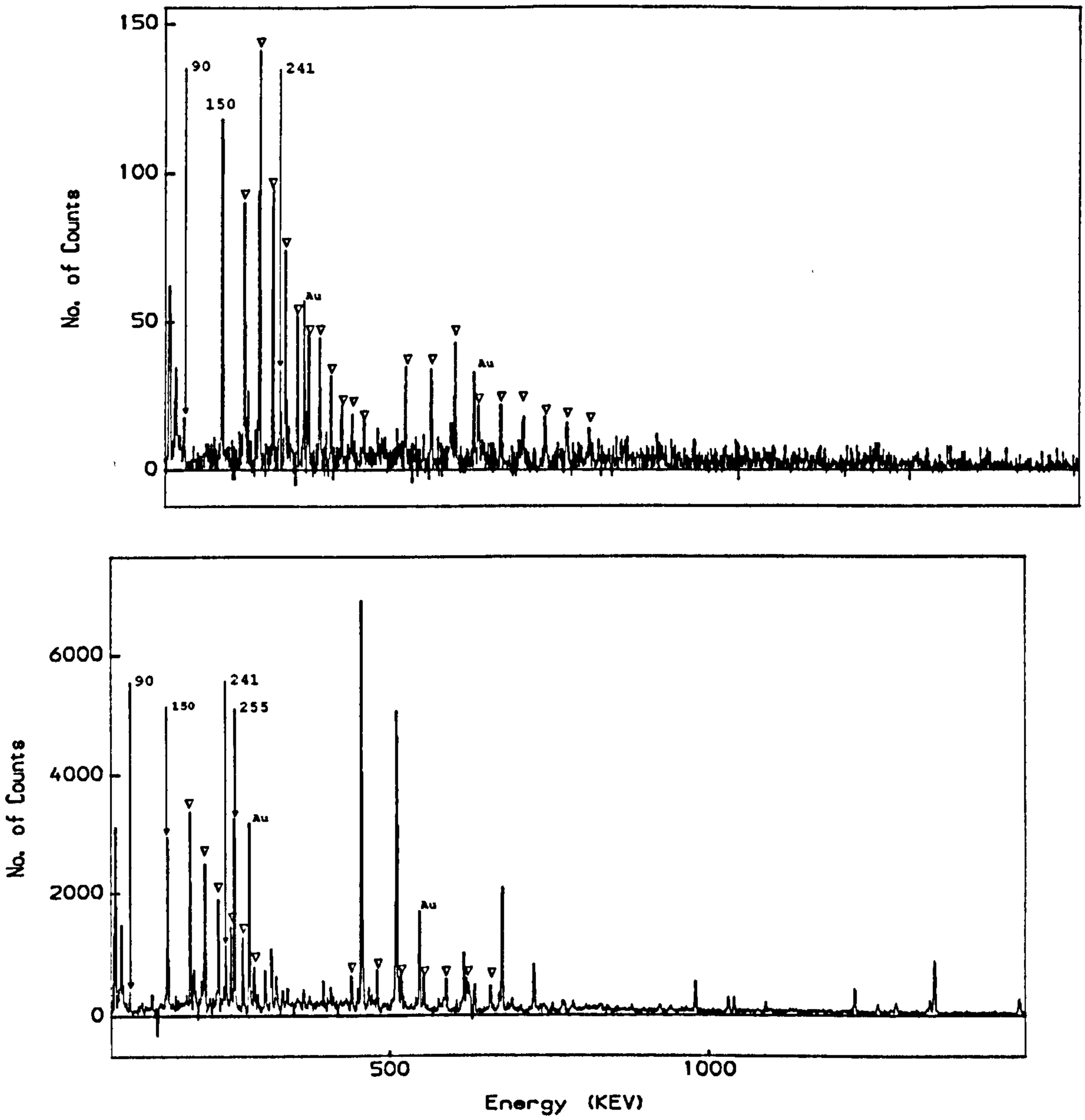

Figure 3.13: Spectra observed in coincidence with the 255 keV transition feeding out of Band 4 in ^{129}Pr (see Section 4.2) using the same window and background regions. The bottom spectrum is derived from an ordinary $\gamma-\gamma$ matrix and the top spectrum from a $\gamma-\gamma$ matrix of triple γ-ray events, one of which was required to be within windows set on the 'clean' transitions in Bands 4/5 (the windows actually set were on the 185,250,286,303 and 623 keV transitions). Note that in the lower spectrum the 255 keV transition is strongly in coincidence with itself and with other transitions much stronger than those of interest. In the upper spectrum such obscuring peaks are entirely absent though at the expense of much reduced statistics. The only 'alien' peaks in the upper spectrum are those due to Coulomb excitation of the Au stopper.

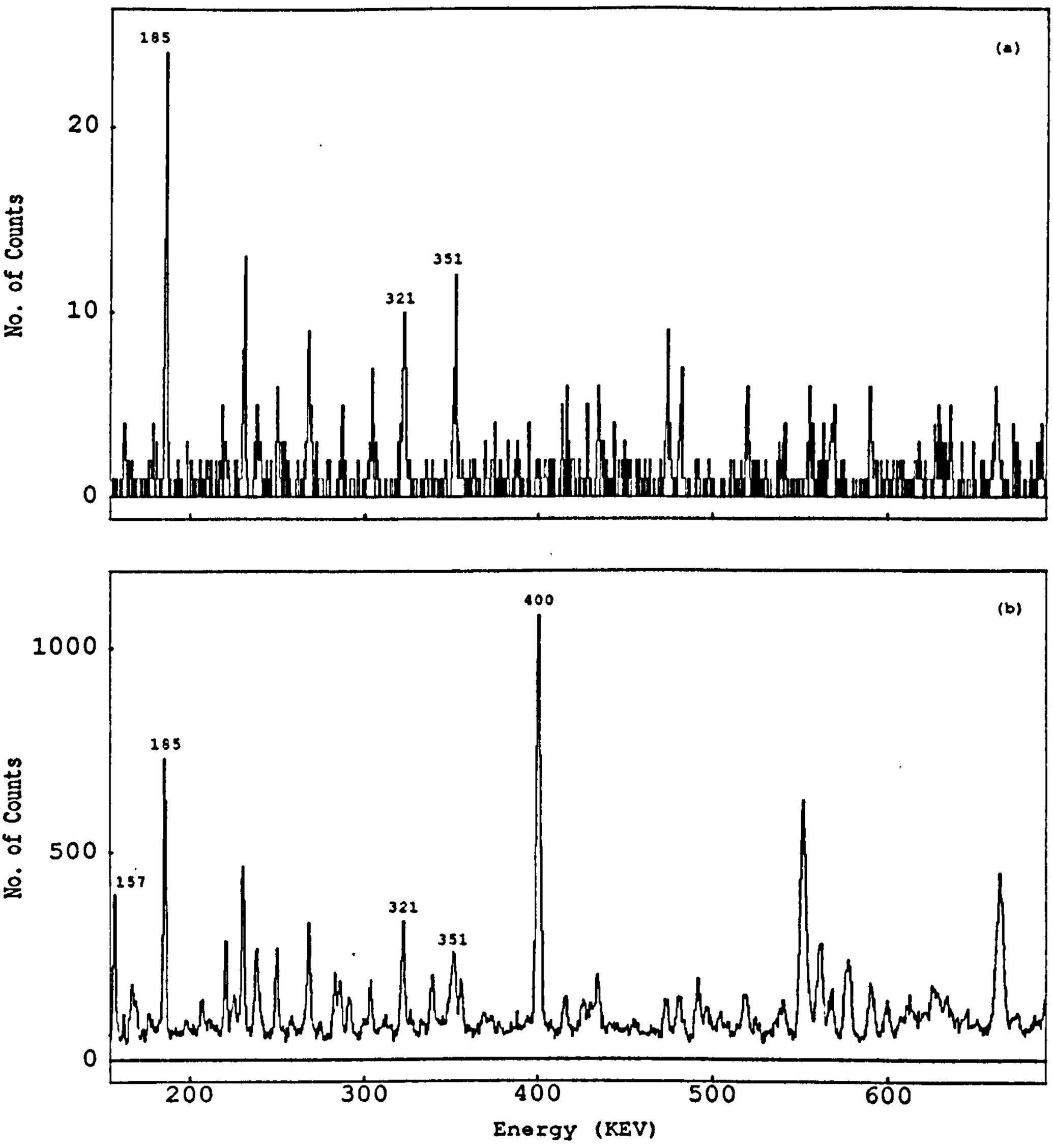

Figure 3.14: A portion of two spectra obtained from a mass gated (A=129) Recoil-γ-γ matrix (a) and a standard $\gamma - \gamma$ matrix (b) in coincidence with a window on the 208keV transition. No background has been subtracted from either spectrum and the same data was sorted in both cases. Spectrum (a) clearly shows transitions in coincidence with the 208/209 keV transitions observed in Band 4,5 in ^{129}Pr and in Bands 3 and 4 in ^{129}Nd, the strongest of which are labelled. The 400keV and 157keV transitions from the yrast bands of ^{128}Ce and ^{128}Pr show strongly in (b) but are totally absent in (a) which is also practically free of any background. Note, however, the great difference in numbers of counts between the 2 spectra and that the transition chosen is one of the strongest in each of the decay sequences in the A=129 nuclei. One must conclude that before Recoil-γ-γ spectroscopy could become a viable tool for the elucidation of decay schemes the Recoil-γ-γ efficiency would have to be improved by a factor of at least 10.

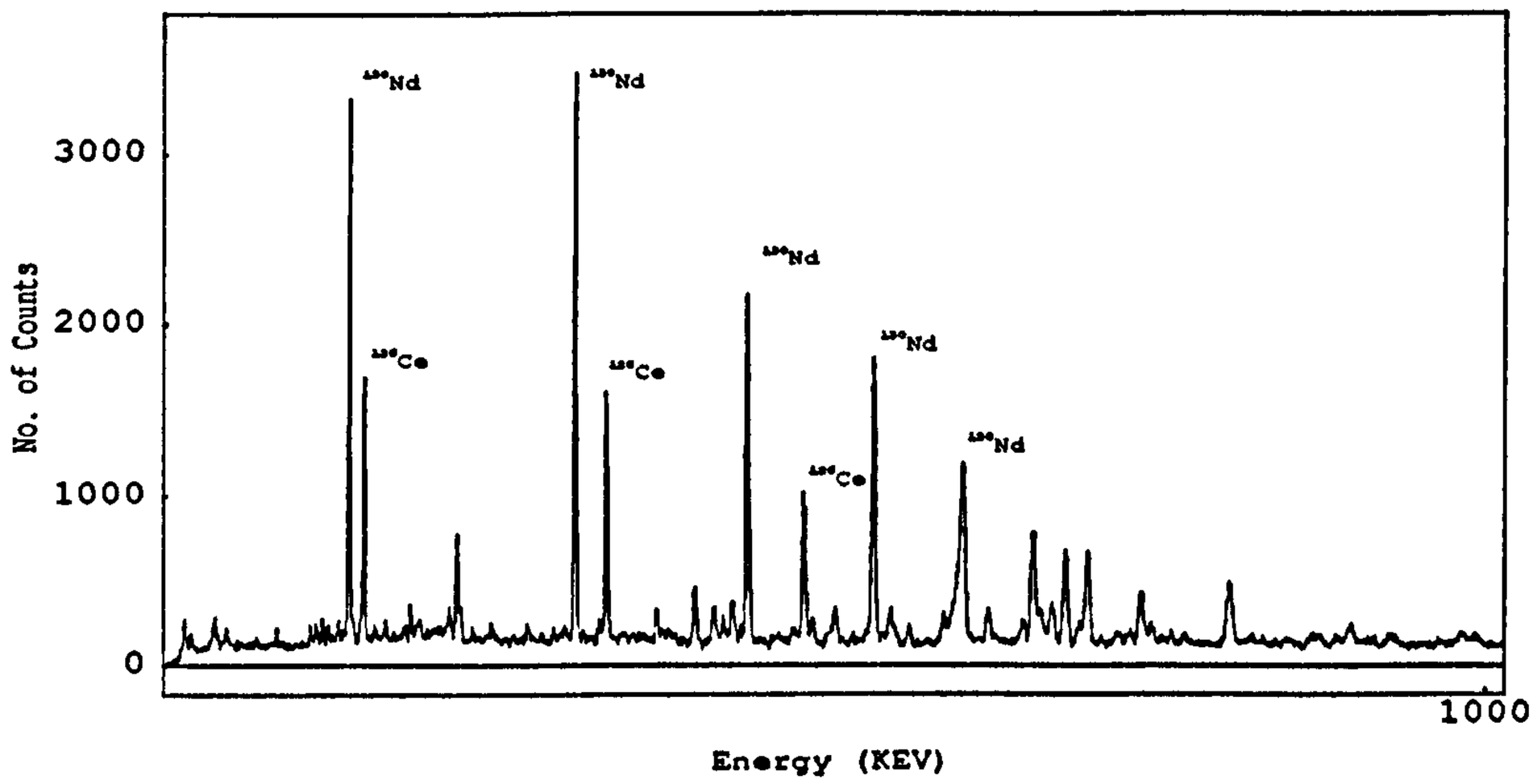

Figure 3.15: Spectrum selected on the PSD TAC only showing the contamination from ^{126}Ce in a ^{130}Nd spectrum due to an A/q ambiguity.

TAC is sufficient to resolve masses. However, as noted in Figure 3.3 the possibility of A/q ambiguity can arise since each mass accepted into the RS actually has a distribution of possible charge states. A spectrum gated solely on the PSD TAC corresponding to the mass 130 peak in Figure 3.3 is shown in Figure 3.15 and quite clearly contains another mass (the only mass 130 species that could be formed in the reaction was ^{130}Nd). This turns out to be ^{126}Ce. This is explicable if we assume a charge distribution peaking at around 30 (as calculated). The A/q ratios for ^{130}Nd and ^{126}Ce in states q and q-1 with q=30 are then 4.33 and 4.34 respectively. This ambiguity can easily be resolved by placing an additional condition on the total energy loss in the ion chamber which is a direct mass measurement since the XFD's select a specific velocity window. An alternative measurement which can be used to provide equivalent information if the ion chamber is replaced with another detection system is the energy signal from the PSD itself. An appropriate polygonal window to acheive unambiguous mass selection is shown in Figure 3.16.

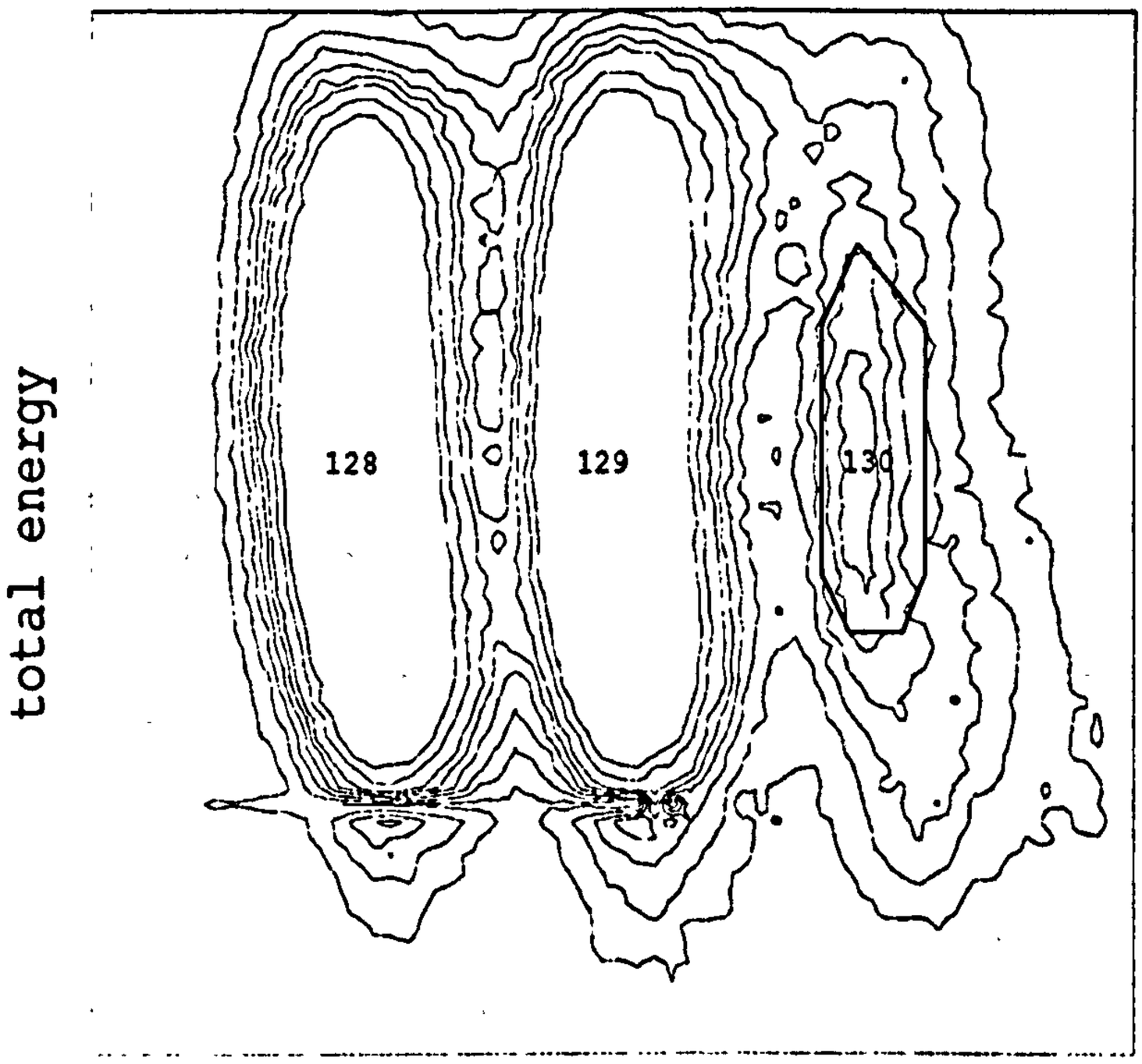

Figure 3.16: In order to select recoils according to Z the mass must be identified unambiguously. This is acheived by placing requirements on both the total energy (mass) of the recoil and the A/q of the recoil as recorded by the PSD TAC. Such a suitable window to exclude the A=126 component present in Figure 3.15 is shown around the A=130 'blob'. The A=126 recoils can be seen as a bulge on the lower right hand side of the spectrum.

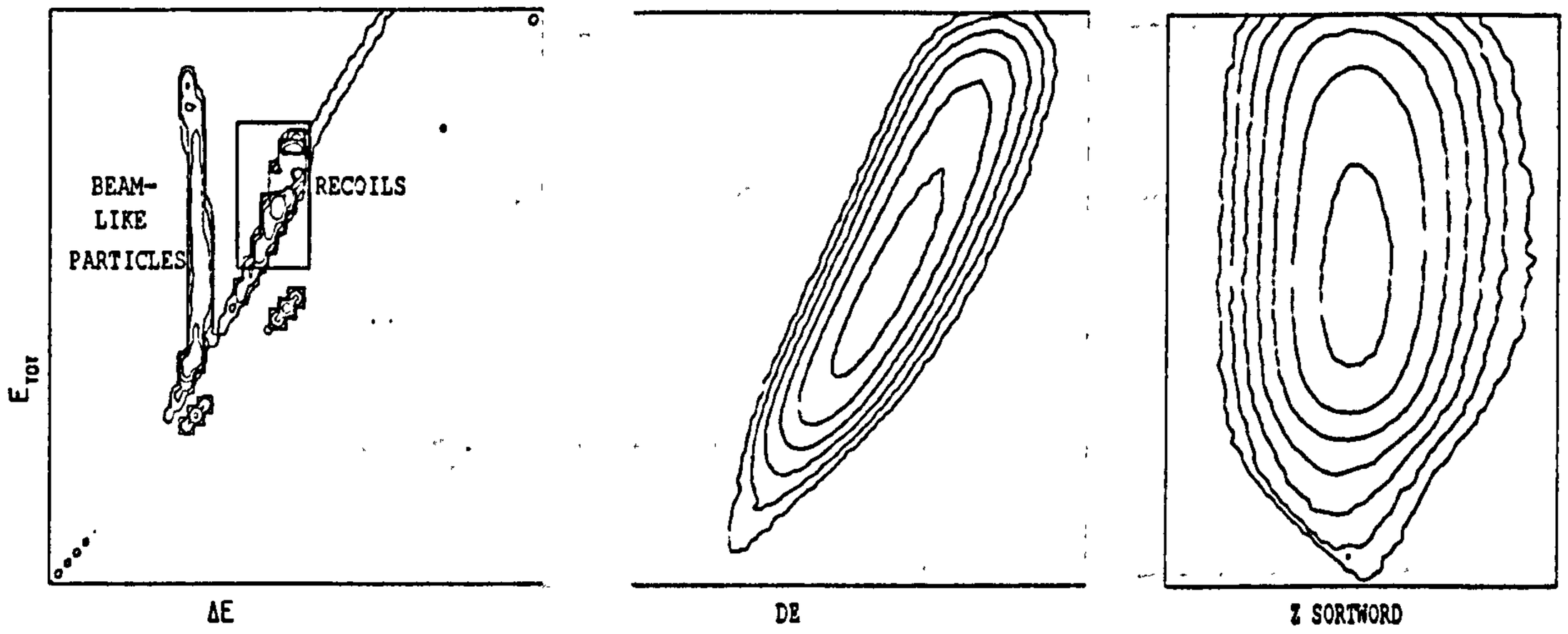

Figure 3.17: The steps towards Z-resolution:
left: 2-dimensional plot of the energy loss in the first anode as a function of the total energy loss in the ion chamber. A window is placed on the E and ΔE signals in order to reject the events which have invalid energy loss characteristics.
centre: A mass gated (A=128) spectrum derived by focussing in on the region outlined above. The ΔE centroid as a function of E is measured and fitted to with quadratic expression:

$$\Delta E(E) = \Delta E_o + AE + BE^2$$

right: The 'Z' sortword is finally derived as

$$Z = \text{const} + \Delta E - \Delta E(E)$$

and is a function with Z dependence but without energy dependence as can be seen from the right hand spectrum.

Figure 3.18: *(see overleaf)* Diagrammatic representation of the steps toward acheiving a spectrum for a single nuclide. The data is sorted into a matrix of 'Z' (as derived above) v E_γ (A) with all the requirements previously mentioned placed upon the data. The 'Z' centroids of the γ rays are then measured and are seen (in this case) to fall into two distinct groups. Pure spectra are then generated by projecting spectra from the matrix either side of the division in 'Z' centroid and then forming combinations of these spectra to eliminate one channel from each. The method clearly generalises to more than 2 isotopes present with the same mass. The spectra thus obtained for ^{129}Nd (B) and ^{129}Pr (C) are shown along with the 'Z'-separation between the two channels indicated by the projection in coincidence with the strongest γ transition in each nucleus (D).

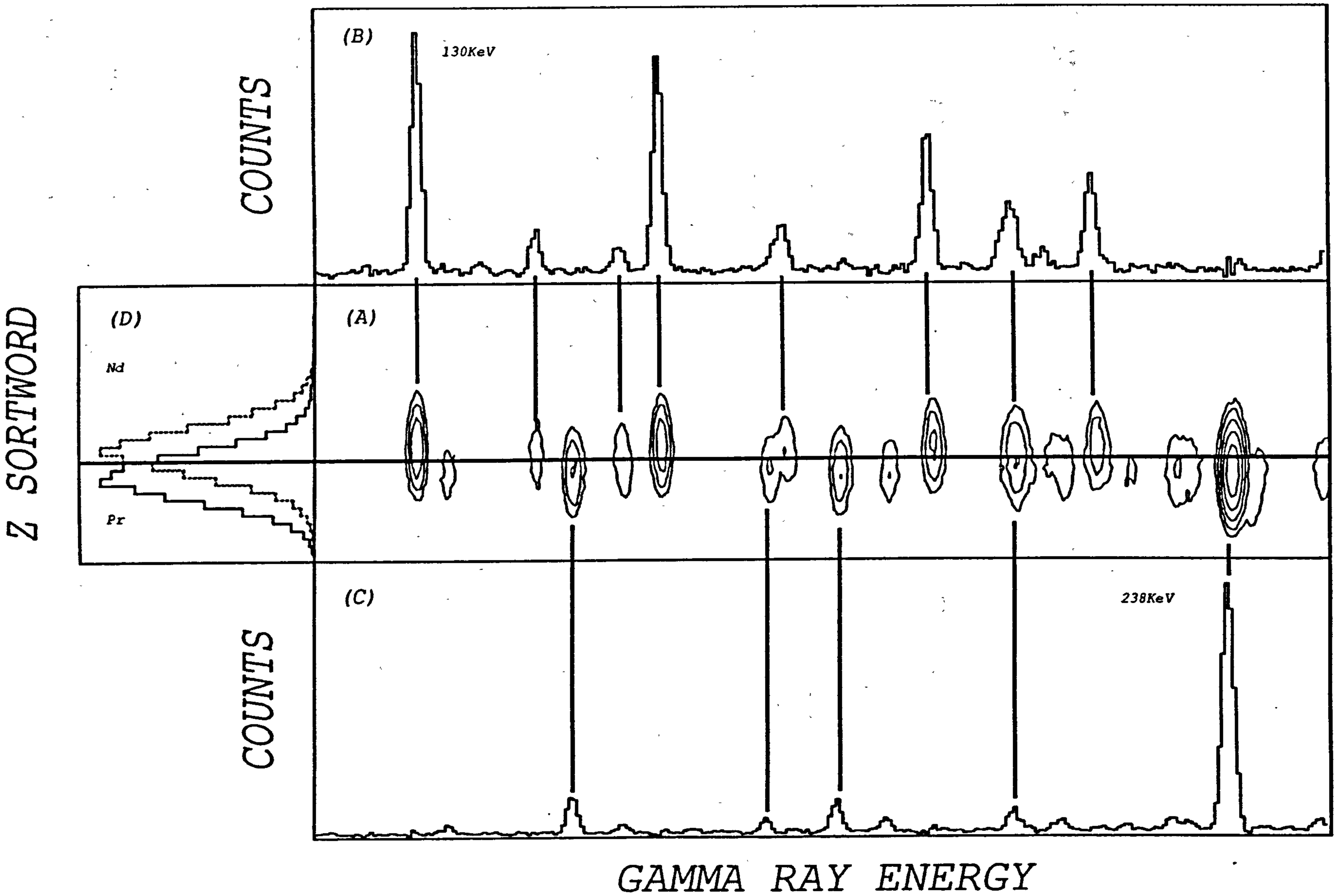
(B)
130KeV
COUNTS
(D)
Nd
Pr
(A)
Z SORTWORD
(C)
238KeV
COUNTS
GAMMA RAY ENERGY

Chapter 4

Experimental Results

4.1 General Comments on the Data

The total projections from γ-γ matrices for the various experiments are shown in Figures 4.1 and 4.2. From these spectra it is apparent that the inverse reactions performed on the RS were in fact 'better' in that they produced higher cross-sections for the nuclei of interest (Pr and Nd) relative to the contaminants (Ce and La). In the case of the backed target experiment the huge Au peaks can be seen to dominate the total projection due to the fact that the stopper used was too thick (50mg cm^{-2}). The backed target data was also contaminated by γ transitions associated with β-decay which obscured many of the weaker transitions and added to the general background. The RS data was contaminated by broad coincident spikes at energies ~200, 430, 640, 720 keV which appears consistent with the Coulomb excitation of the beam. This caused particular problems in the 640 keV region where the bands tend to cross and Doppler broadening is starting to affect the peaks seriously. No claim is made that the spectra shown are typical — they are creamed from the best. A typical spectrum would generally contain several contaminants and would require several pages of explanatory notes!!

The spectra were calibrated and efficiency corrected using a ^{152}Eu source. The peaks in the stopped experiment were observed to be much narrower due to a lack of Doppler broadening and the errors involved in calibration were also reduced since calibration could be done directly from the source without requiring an accurate value for the recoil velocity. Hence the energies obtained for transitions from this experiment were preferred to those of the inverse reaction. At energies in excess of ~1 MeV the discrepancy in calibration between the RS (using a calculated recoil velocity) and stopped ESSA-30 experiment was quite significant (of the order of 2 keV) for the A~129 experiments. In the case of the A~131 experiments the recoil velocity was measured experimentally from the Doppler shift of γ rays in detectors at different angles and the calibration from the source corrected accordingly. The energies quoted in the tables from Z selected spectra are approximate as the peaks are often multiplets or have poor statistics. The transition energies to rely upon are those in the tables accompanying the

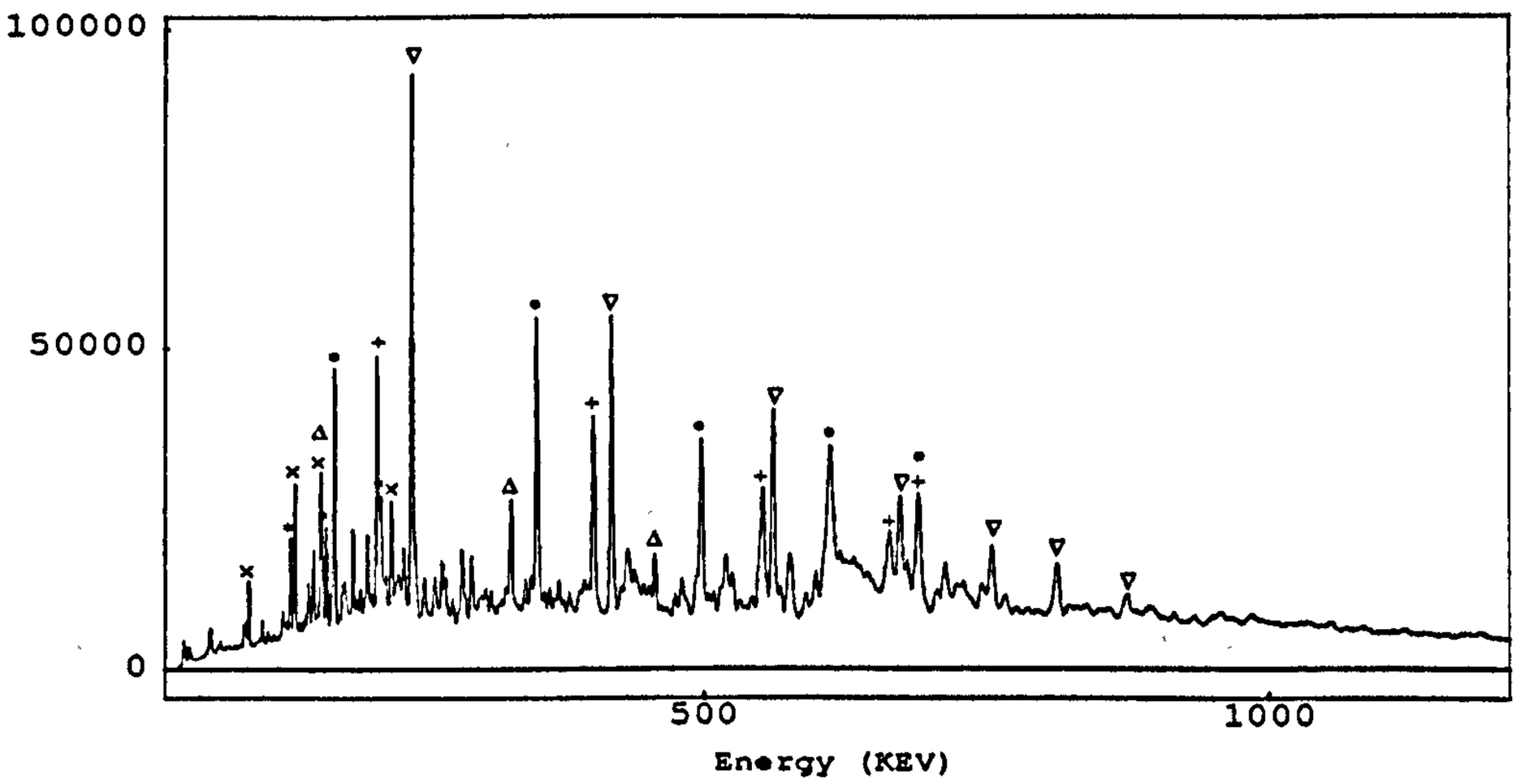

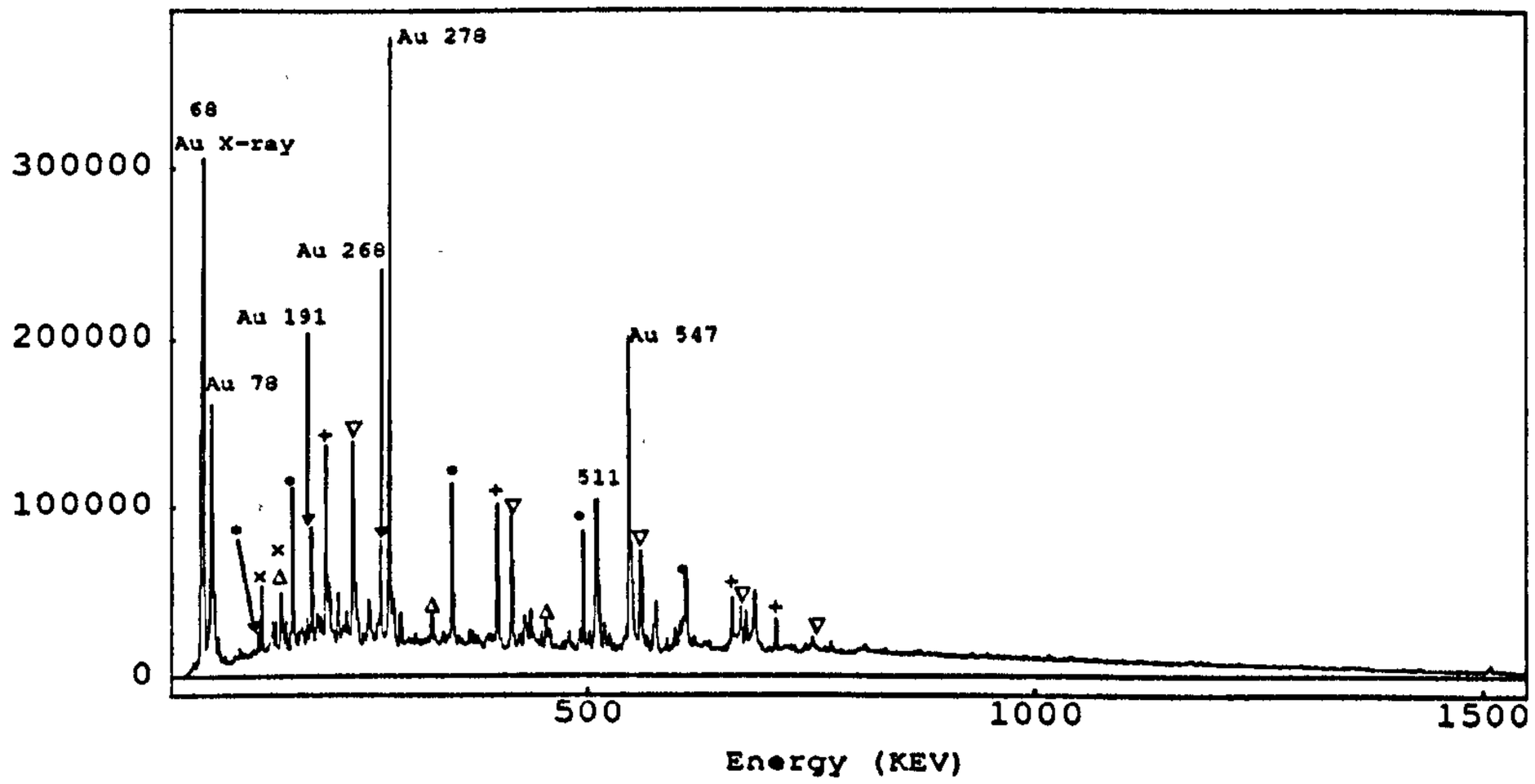

Figure 4.1: Total projections through γ-γ matrices from reactions populating the compound nucleus ^{132}Sm as below:

top	^{74}Se(^{58}Ni	300 MeV	RS + Polytessa
bottom	^{40}Ca(^{92}Mo	180 MeV	ESSA-30

Note the predominance of the Au Coulex over the reaction channels and the relatively sharp high energy transitions in the projection from the ESSA-30 experiment.

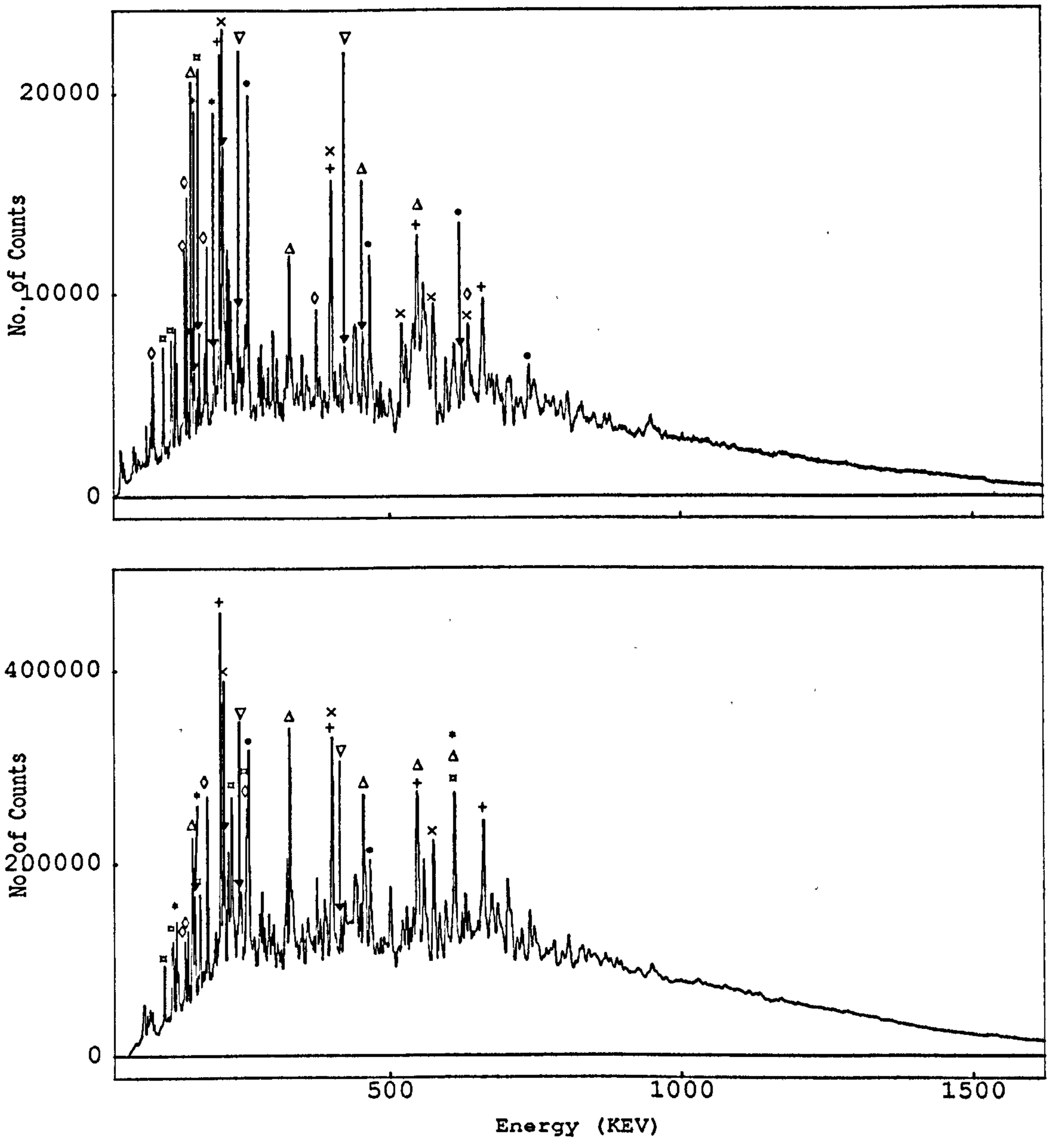

Figure 4.2: Total projections through γ-γ matrices from reactions populating the compound nucleus ^{134}Sm as below:

top	^{76}Se(^{58}Ni	300 MeV	RS + Polytessa
bottom	^{40}Ca(^{94}Mo	180 MeV	ESSA-30

Residue	RS	ESSA-30
^{124}La	$< 5\%$	$< 1\%$
^{125}La	$< 10\%$	$< 5\%$
^{125}Ce	$< 5\%$	$< 1\%$
^{126}Ce ($\bullet$)	76%	83%
^{128}Ce ($+$)	49%	100%
^{128}Pr ($\times$)	21%	10%
^{129}Pr (∇)	100%	100%
^{128}Nd	$< 13\%$	$< 3\%$
^{129}Nd ($*$)	11%	3%
^{130}Nd (Δ)	22%	5%

Table 4.1: As a rough estimate of the relative cross sections for the various channels the intensity of the strongest γ ray in each channel was measured. This may be compared to the CASCADE predictions but one must bear in mind that this is a VERY crude estimate and that the code was run using default parameters due to lack of knowledge of the true input parameters. In particular the odd-A nuclide strengths will be underestimates by a factor of perhaps 3. The symbols marking the channels in (Figure 4.1)

description of each band.

The efficiency of collection of low energy (<120 keV say) γ rays was severely impaired in the ESSA-30 experiments by lead shielding around the target chamber designed to suppress the detection of X-rays. In general the efficiency calibrations would appear to be poor at low energies since many of the bands observed have low energy transitions at the bottom which are of lower intensity than the transitions feeding them. This may be because the calibration spectra were collected without any coincidence requirement in contrast to the experimental data. In the following tables, a second intensity is quoted for many transitions. This is the intensity corrected for internal conversion according to the tables of [HS68]. This process becomes important, and even dominant at low energies. The corrections were applied assuming pure E2 or M1 character for the transition as appropriate in the relevant decay scheme.

A further problem encountered with the ESSA-30 data was that of detector reliability in terms of both gain shifts and failure of some of the detectors during the experiments. Corrections for the gain shifts were made in the analysis on a tape by tape basis for each detector (a mind-bogglingly tedious task!!). The periods of absence of some of the detectors made it impossible to extract any angular information from this data.

An attempt was made to look at Recoil $-\gamma$ angular distributions in order to access the mixing ratios of some of the inter-band transitions. It was found

Residue	RS	ESSA-30
^{127}Ce	$< 10\%$	$< 15\%$
^{128}Ce (+)	94%	100%
^{130}Ce	$< 15\%$	$< 40\%$
^{129}Pr (∇)	22%	28%
^{130}Pr ($\otimes$)	49%	20%
^{131}Pr ($\bullet$)	80%	100%
^{129}Nd ($*$)	15%	19%
^{130}Nd (Δ)	66%	88%
^{131}Nd ($\diamond$)	46%	16%
^{132}Nd ($\times$)	95%	52%

Table 4.2: Estimates of the relative intensities of the channels in the mass 131 experiments and key to the labelling of the transitions in Figure 4.2 It is rather surprising that transitions belonging to ^{129}Pr are seen so strongly. This could be due to the targets being impure and would explain the fact that the data in the mass 131 experiments was of poorer quality. The natural abundances of the target materials certainly favour the more neutron deficient isotope. That this was the case is supported by the fact that transitions belonging to ^{126}Ce can also be seen in both data sets.

that the distribution was unphysical and highly asymmetric between forward and backward angles which would be expected to show the same intensity. The I(143)/I(101) ratios do indeed seem to differentiate between transitions of different multipolarity but the angular effects from the distribution are superimposed on some much larger effect. This implies that the detectors were not focussed on the target. The total intensities (after efficiency correction of each detector) for the different detector angles is given below as a percentage of the intensity observed at the backward angle.

143°	117°	101°	79°
100%	22%	81%	10%

Branching ratios and hence B(M1)/B(E2) ratios were measured in several ways. The method of measurement for the values quoted in the following tables is indicated as below. No attempt was made to correct for angular distribution effects and the mixing ratio was assumed to be negligible. The RS methods are generally reasonably self consistent. Differences between the absolute values for the ESSA-30 and RS estimates may be attributable to the differing angular effects in the different arrays. A comparison is not sensible due to the unexplained distribution noted above.

[1] Z-selected Recoil $-\gamma$ spectrum

[2] Mass(A=129)-selected Recoil $-\gamma$ spectrum

[3] Sum of γ-γ spectra gated on the transitions feeding into the level of interest from the RS data

[4] As [3] but from the ESSA-30 data

Table 4.3: Key to the techniques used in the elucidation of branching ratios as indicated by superscripts in the subsequent tables.

4.2 ^{129}Pr

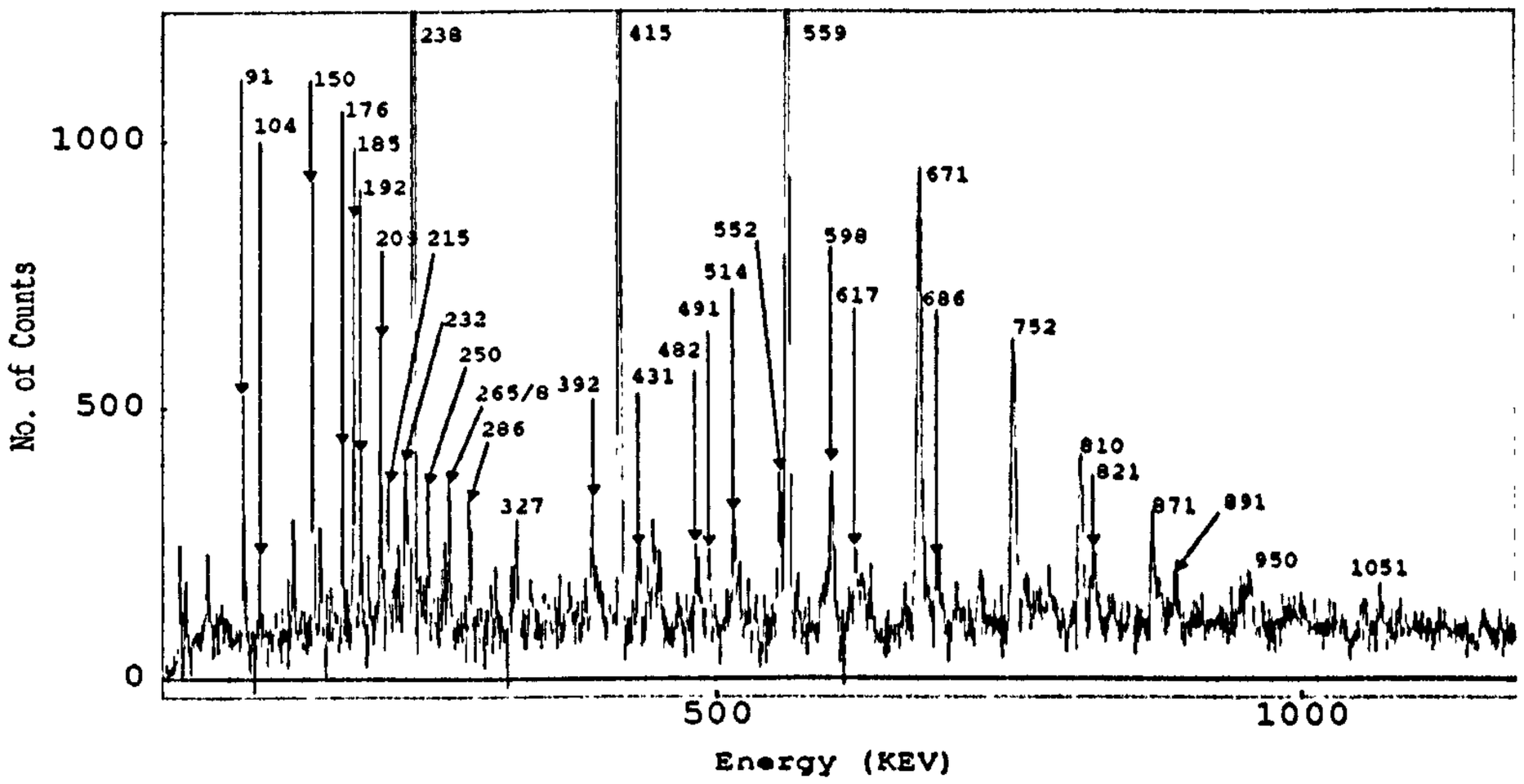

Figure 4.3: Z-selected spectrum for ^{129}Pr. Note the Y axis has been greatly expanded to make the low intensity structures visible. In order to appreciate the weakness of other structures compared to Band 1, the 238 keV transition in this band has a peak count of ~6000. Relative intensities for the transitions can be found in the following table 4.4.

A careful application of the Z-selection procedure described in Section 3.7.3 produced the above spectrum for ^{129}Pr. There is no evidence of breakthrough from other channels. The transitions identified in this spectrum are tabulated below. The intensities quoted have not been efficiency corrected in order to give some handle on the certainty of the assignment/existence of each transition in the nucleus.

Five distinct decay sequences are observed in this nucleus. Bands 2/3 have been positively shown to decay into the yrast Band 1 and possibly also into the coupled bands 6/7. Bands 4,5 feed via an isomeric level into Band 6 and Band 8 would appear to populate Bands 6/7 via an undetermined path. Approximate relative intensities for these structures as estimated from the strongest distinct transitions in the efficiency corrected Z-selected spectrum are:

1	100%	2	15%	3	8%	4/5	10%	6/7	4%	8	5%

It can be seen that the majority of transitions identified have been fitted into the decay sheme.

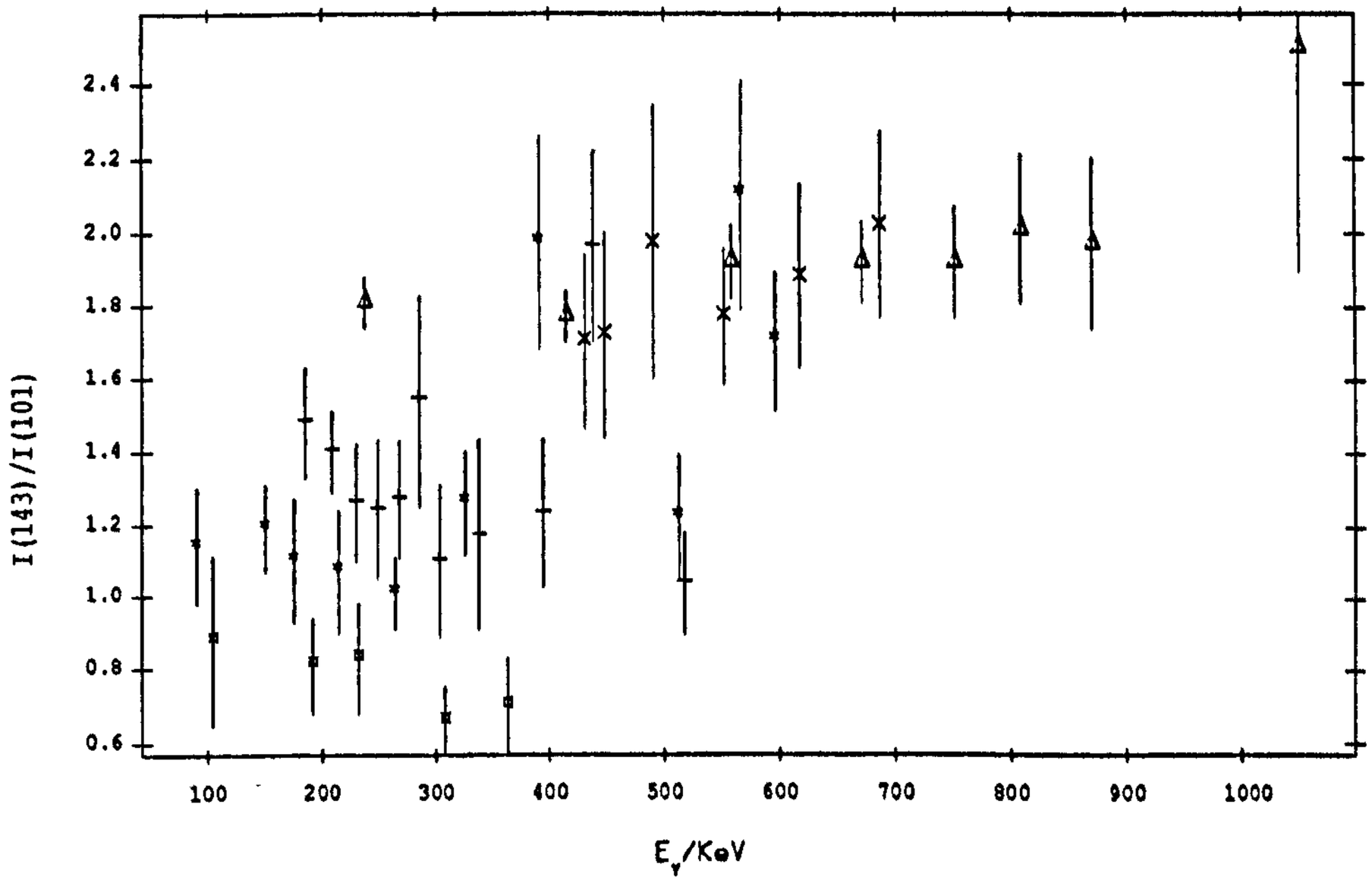

Figure 4.4: I(143)/I(101) ratios for the γ rays from the various structures observed in ^{129}Pr. The symbols refer to transitions from bands as labelled in Figure 4.5 as follows:
Band 1 (Δ), Bands 2/3 ($\times$), Bands 4/5 ($+$), Bands 6/7 ($*$), and Band 8 ( ). The $\Delta J = 1$ transitions, i.e. those with ratios below $\sim$1.5, fall into bands of different character as would be expected for transitions of different mixing ratio. It is noted that the ratios for some of the transitions assumed to be $\Delta J = 2$ in Bands 4/5 and 6/7 are too low but this may be due to contaminants as the spectra were gated on mass only as noted in Section 3.7.3 or to dealignment.

E_γ(keV)	I_γ (%)	I(143)/I(101)	Assignment
91.0	7(1)	1.14(0.16)	7→6
104.7	2(1)	0.88(0.23)	8
134.0	3(1)	1.04(0.17)	
150.7	13(1)	1.19(0.12)	6→7,8
157.3	3(1)	—	
166.4	1(1)	0.89(0.26)	
176.3	4(1)	1.10(0.17)	7→6
185.7	11(1)	1.48(0.15)	5→4
192.1	5(1)	0.81(0.13)	8
209.1	9(1)	1.40(0.11)	4→5
215.2	5(1)	1.07(0.17)	6→7
223.9	2(1)	0.79(0.20)	
230.1	6(1)	1.26(0.16)	5→4
232.3	4(1)	0.83(0.15)	8
237.7	100(1)	1.81(0.07)	1
249.6	4(1)	1.24(0.19)	4→5
264.3	2(1)	1.01(0.10)	8
268.0	5(1)	1.27(0.16)	7→6,5→4
285.8	4(1)	1.54(0.29)	4→5
303.5	1(1)	1.10(0.21)	5→4
308.4	1(1)	0.66(0.09)	8
325.8	5(1)	1.26(0.14)	7
338.3	1(1)	1.17(0.26)	5→4
363.3	1(1)	0.70(0.13)	8
371.5	2(1)	—	5→4
385.4	2(1)	—	
391.7	6(1)	1.97(0.29)	6
394.9	3(1)	1.23(0.20)	4
397.6	2(1)	1.67(0.34)	
414.9	66(1)	1.77(0.07)	1
427	1(1)	—	
431.5	5(1)	1.70(0.24)	2
439.2	3(1)	1.96(0.26)	5
444.0	5(1)	1.80(0.29)	
448.5	4(1)	1.72(0.28)	3
465.3	2(1)	—	
481.6	5(1)	1.46(0.27)	7,4
490.8	4(1)	1.97(0.37)	2
512.7	7(1)	1.22(0.17)	6
517.2	4(1)	1.04(0.14)	5

E_γ(keV)	I_γ (%)	I(143)/I(101)	Assignment
552.2	9(1)	1.77(0.19)	3,4
559.0	48(2)	1.92(0.10)	1
567	1(1)	2.10(0.31)	3→6
596.5	11(1)	1.70(0.19)	6
617.7	5(1)	1.88(0.25)	2
623.5	5(1)	—	4
671.3	33(1)	1.92(0.11)	1
687.0	6(1)	2.02(0.25)	3
723	4(1)	2.00(0.27)	
751.6	22(1)	1.92(0.15)	1
783	3(1)	2.01(0.30)	
808.8	13(1)	2.01(0.20)	1
820	7(1)	2.00(0.26)	
870.3	9(1)	1.97(0.23)	1
890	4(1)	2.5(0.5)	
948	3(1)		
950	5(1)	1.90(0.3)	1
1051	4(1)	2.5(0.6)	1
1065	3(1)	1.5(0.4)	3→1
1184	3(1)	1.9(0.5)	3→1

Table 4.4: Energies, Intensities and Angular Distribution ratios for transitions assigned to ^{129}Pr. The final column in this and subsequent tables corresponds to the placement of observed transitions in the corresponding decay scheme (Figure 4.5 in this case). The intensities given are not corrected for efficiency.

Figure 4.5: Decay Scheme for ^{129}Pr

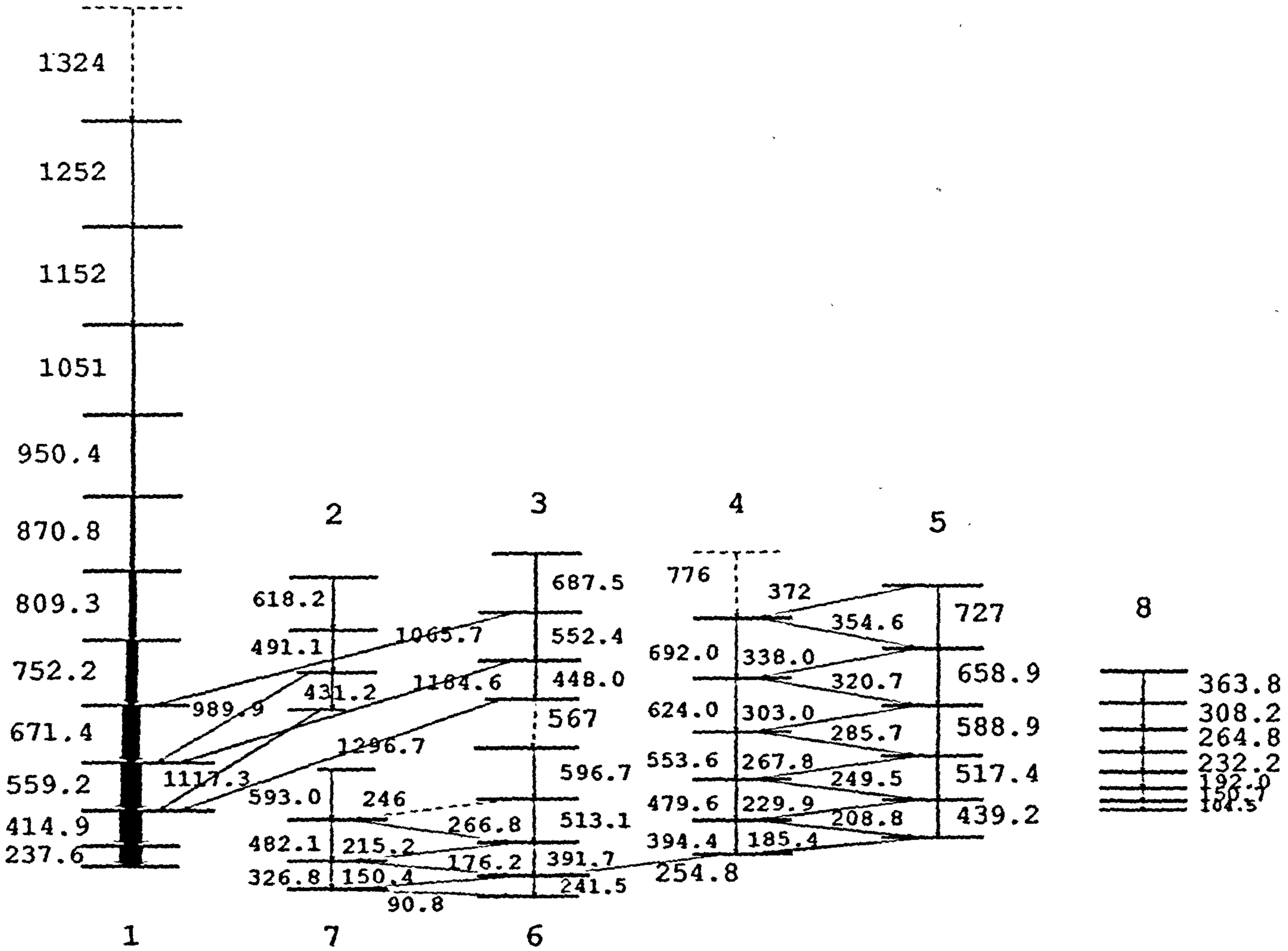

4.2.1 Bands 1,2 and 3

Band 1 is yrast in ^{129}Pr and consists of stretched E2 transitions as evidenced by the I(143)/I(101) in Table 4.4. The top transitions in the band as shown in Figure 4.5 are visible only in summed spectra and are therefore tentative. Bands 2 and 3 feed into Band 1 as shown in Figure 4.7 and would appear to be

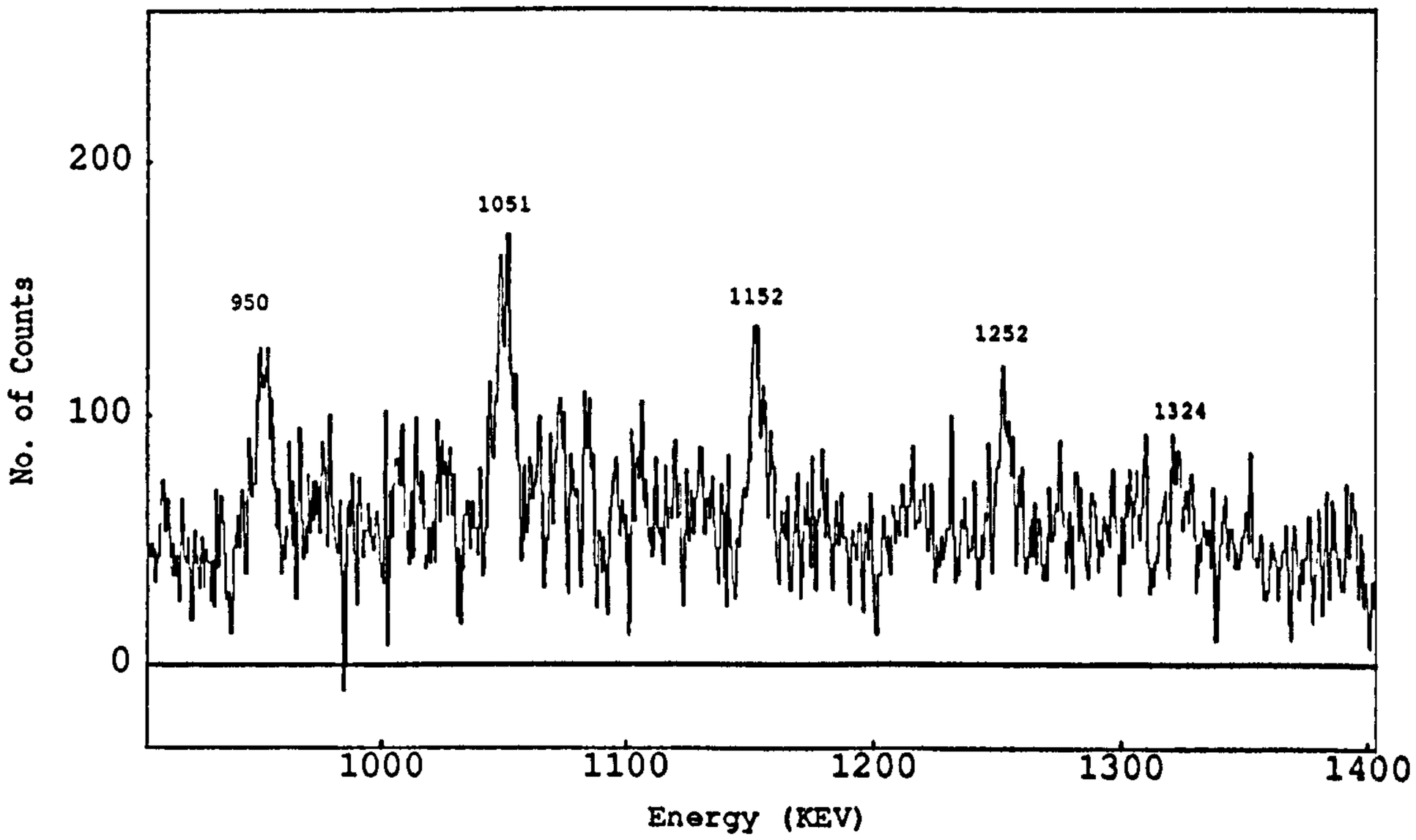

Figure 4.6: Sum of spectra in coincidence with the 950,1051 and 1152 keV transitions showing possible extensions to Band 1.

2 different signatures of the same band. There is, however, no evidence of any linking transitions between the bands though this may be attributable to lack of statistics.

The branching ratios for the 2261 and 2397 keV levels of table 4.5 have been measured from efficiency corrected gates on the 491 and 552 keV transitions:

E_{ex}/keV	T(out of band)/T(in band)
2261	0.39(4)
2397	1.35(4)

Several other transitions (notably 821,891,948 and 1024 keV) can be identified in coincidence with Band 1 and as transitions in ^{129}Pr but it has not been possible to place these from the data. It is possible that they belong to the sequence of opposite signature to Band 1 or that they are part of (or feed out from) Bands 2 and 3. The hypothesis that they are part of bands 2,3 looks unlikely from the spectra shown in Figure 4.7 which would be expected to show some hint of these transitions if they were indeed continuations of these bands. The majority of the

E_{ex} (keV)	E_{γ} (keV)	I_{γ} %
237.6	237.6(0.1)	100 ; 108
652.5	414.9(0.1)	100(1) ;102
1211.7	559.2(0.1)	91(1)
1883.1	671.4(0.2)	73(1)
2635.3	752.2(0.2)	50(1)
3444.6	809.3(0.3)	31(1)
4315.5	870.8(0.6)	18(1)
5266	950.4(0.6)	14(3)
6317	1051(1)	6(1)
7469	1152(1)	4(1)
8721	1252(1)	<1
10045	1324(1)	<1
—	821(1)	17(1)
—	888(1)	11(1)
2260.6	431.2(0.3)	4(1)
2752	491.1(0.2)	5(1)
3370	618.2(0.5)	3(1)
2397.2	448.0(0.2)	3(1)
2950	552.4(0.2)	9(1)
3636	687.5(1)	8(1)
2260.6	989.9(0.3)	1(1)
1769.8	1117.3(0.2)	4(1)
2950	1065.7(0.5)	4(1)
2397.2	1184.6(0.5)	6(1)
1949.2	1296.7(0.5)	3(1)

Table 4.5: Excitation energies, transition energies and relative intensites for transitions and levels associated with bands 1,2 and 3 as shown in Figure 4.5. The energies were measured in the cleanest available spectra and the relative intensities of the 871 keV transition and below in band 1 were measured from an efficiency corrected Z-selected spectrum. The relative intensities of the remaining transitions in band 1 are taken from a sum of gates on the lowest 2 transitions in band 1 from the RS data and are normalised to the 559 keV transition except for that of the 950 keV which is taken from the 671 keV transition and normalised to the 809 keV transition due to a coincident contaminant of energy $\sim$ 948 keV which appears to feed into the band below the 671 keV transition. The intensities for bands 2 and 3 are taken from an efficiency corrected gate on the 238 keV transition in the ESSA-30 data and are normalised to the 415 keV transition in band 1. The 821 and 888 keV transitions are included in this table since they are clearly in coincidence with Band 1 although it proved impossible to place them from the data.

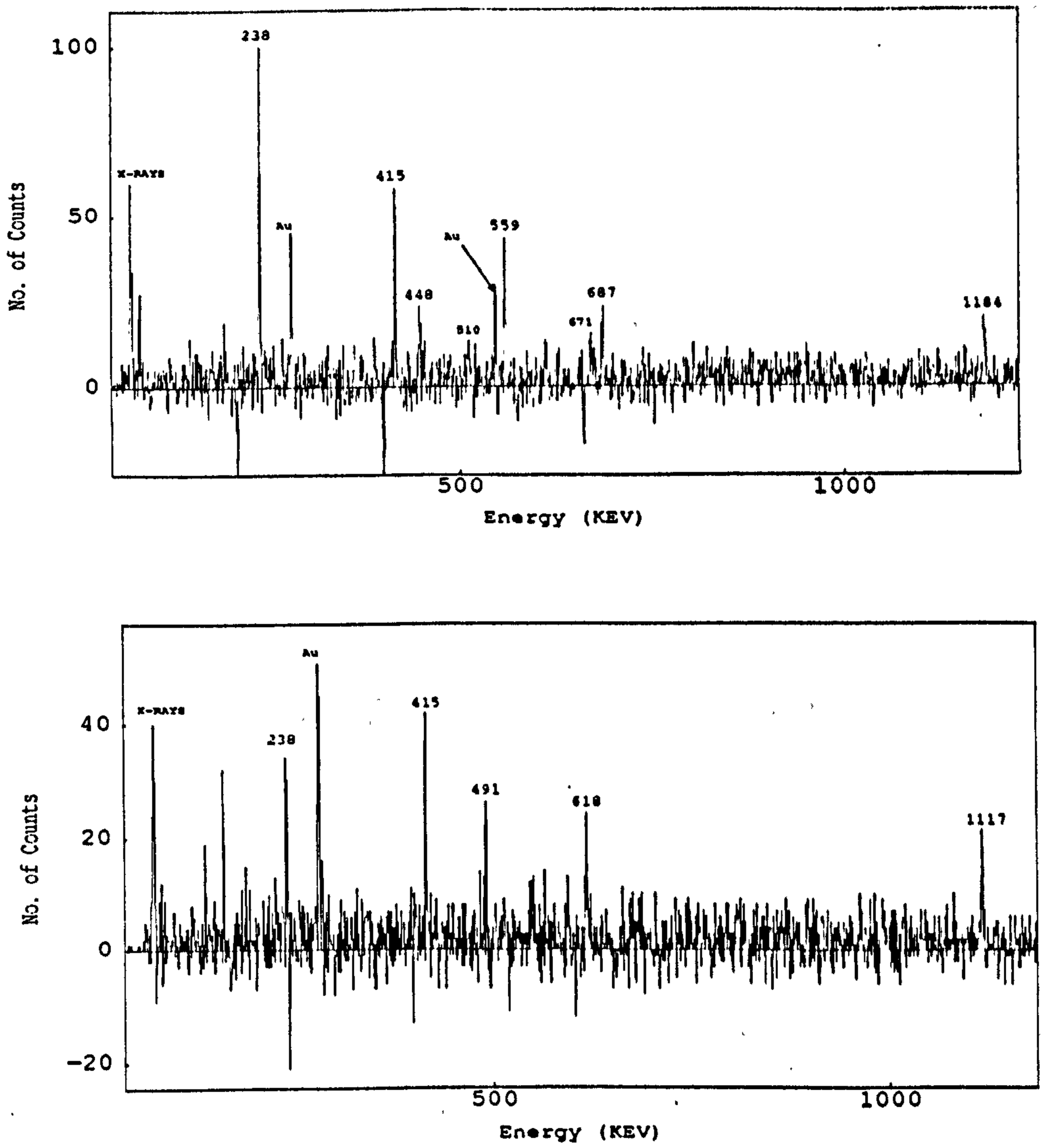

Figure 4.7: Spectra in coincidence with the 552 keV (*top*) and the 432 keV (bottom) transitions from γ-γ matrices sorted with the requirement of a third transition also in Bands 2/3 respectively. The high energy transitions de-populating the bands are clearly discernable whereas spectra from ordinary γ-γ data are inconclusive.

intensity of these transitions feeds into Band 1 below the 752 keV transition as evidenced by the clean spectrum seen in Figure 4.8d as opposed to the spectra with 'bumps' at the appropriate energies in Figure 4.8a–c.

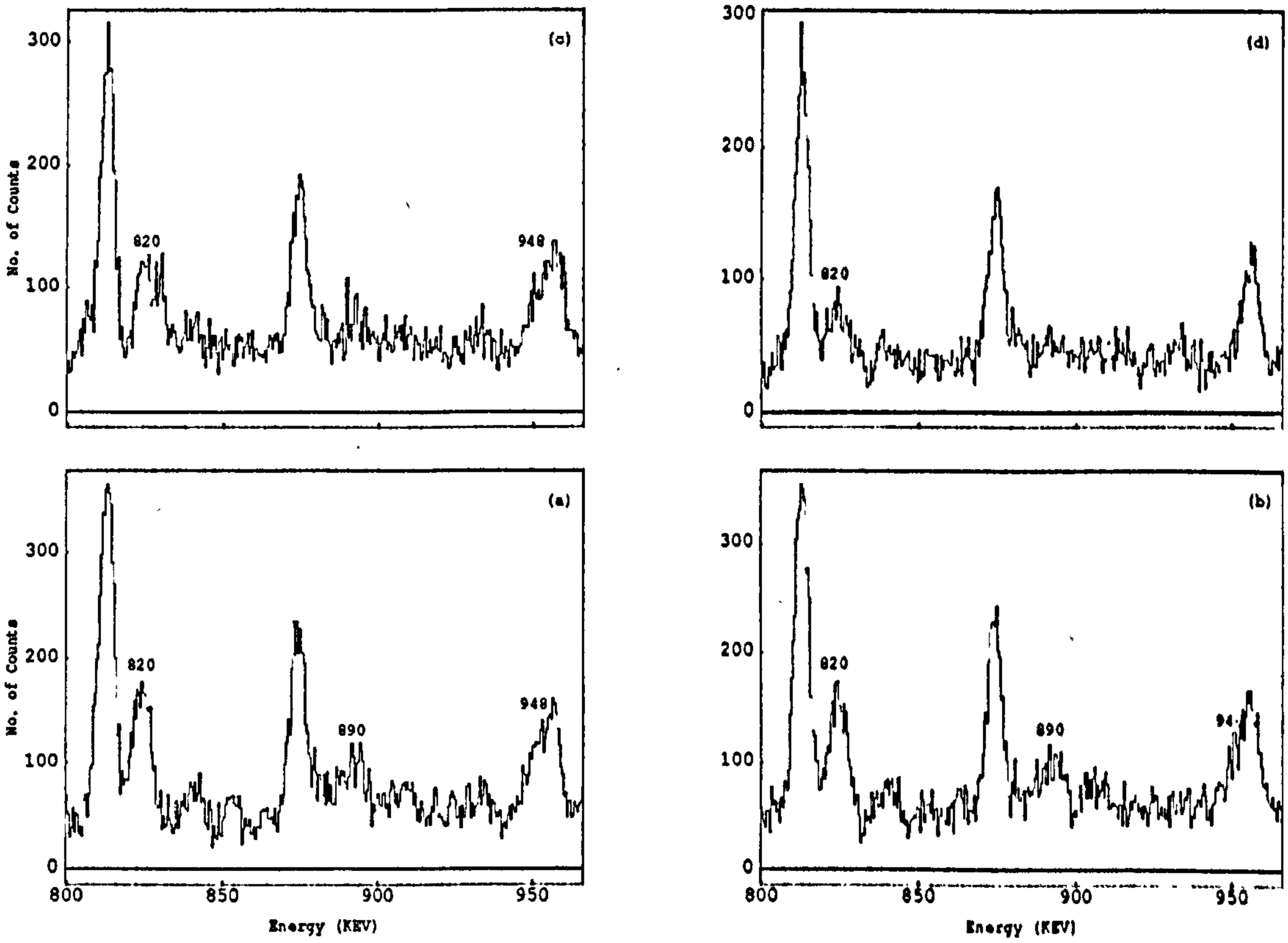

Figure 4.8: Fragments of spectra observed in coincidence with the following transitions: 238 keV (a), 415 keV (b), 559 keV (c) and 671 keV (d). Note the gradual disappearance of the low energy shoulder on the 950 keV peak and the diminishing relative intensities of the 820 and 890 keV peaks. A window on the 752 keV transition is completely clean of all peaks except those belonging to Band 1.

When the backed target data was sorted according to detector angle the transitions above the 415 keV transition are observed to exhibit progressive line shapes before becoming shifted (Figure 4.9). This indicates that these states must have effective lifetimes of the order of or less than the characteristic stopping time of the target/backing combination. The shift in energy of the centroids of the peaks is detailed below as a fraction of the full shift one would expect to observe for a transition of that energy.

E_γ (keV)	ΔE_γ (keV)	F
671.4	1.2(0.2)	0.08(0.01)
752.2	5.5(1.0)	0.32(0.06)
809.3	7(3)	0.39(0.17)
870.8	9(3)	0.46(0.16)
950.4	15(2)	0.67(0.10)
1051	21(3)	0.87(0.14)

As noted in Section 4.1 the ESSA-30 data was rather dirty. This, coupled with the fact that both resolved and unresolved structures are seen to feed into Band 1 renders any attempt at a reliable extraction of lifetimes from an analysis of the centroid shifts untenable. A lineshape analysis may be possible for the 752 keV peak but would be of dubious merit in view of the problems with detector stability noted in Section 4.1 and visible in the poor shapes of the 809/871 keV peaks in Figure 4.9. In order to get some idea of the order of magnitude of the lifetimes of these levels a plot of F as a function of time for the reaction and target/stopper used is shown in Figure 4.10. A comparison shows the effective lifetimes to be of the order of a few hundred fs. Any further analysis would be difficult since the shifts and shapes seen occur in the region of the up-bend (see Section 5.3) where one would expect the intrinsic structure of the nucleus to be changing. It does appear, however, that the occurence of the up-bend may cause some hinderance. Re-sorting the data for shifted peaks may prove of some worth but would be very time consuming due to the drifting problems already noted.

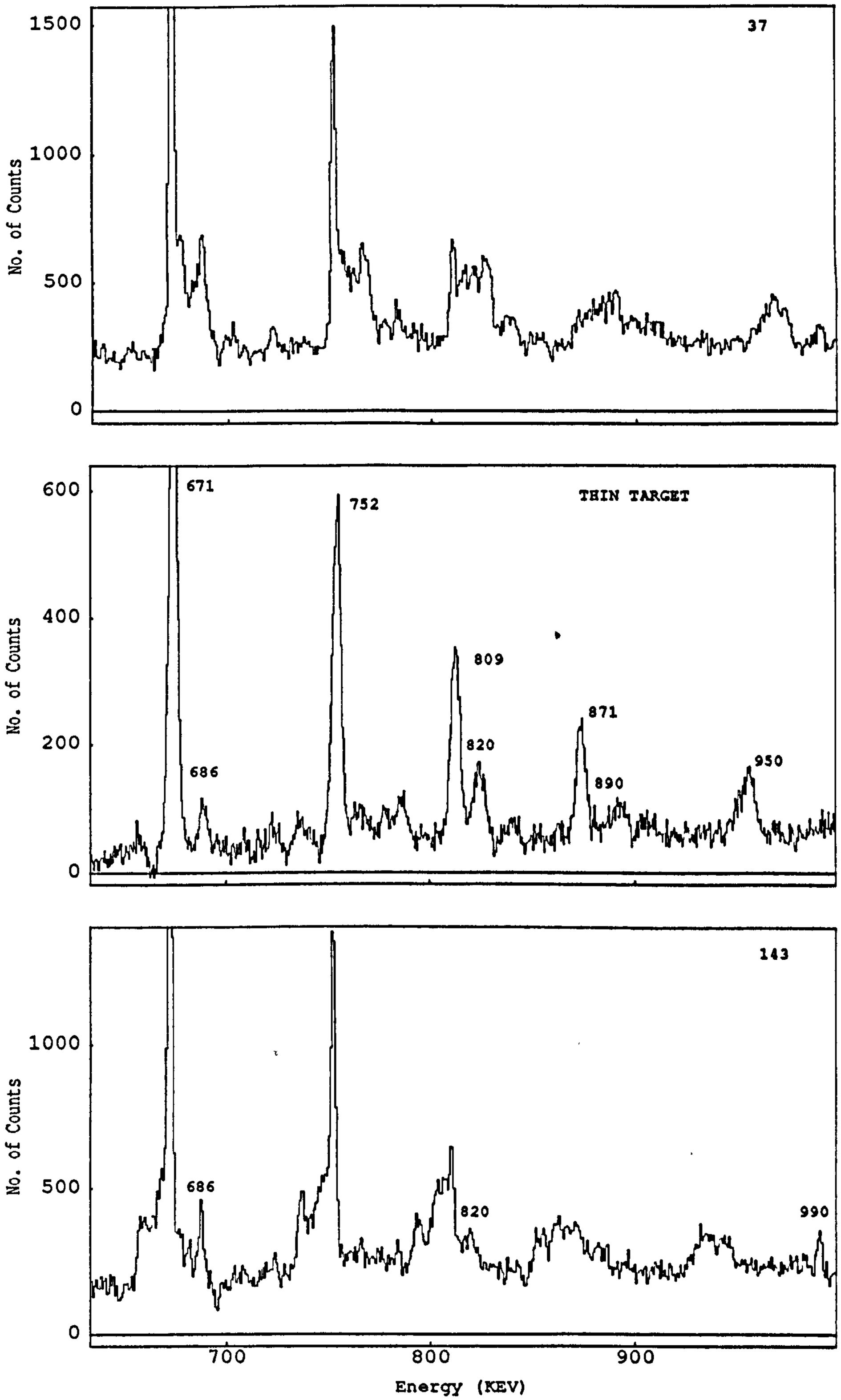

Figure 4.9: Spectra in coincidence with the 415 keV transition of Band 1 as observed in the RS data (*centre*) and in the ESSA-30 data with a backed target at forward (37°) and backward (143°) angles (*top* and *bottom* respectively) showing the Doppler effects referred to in the text.

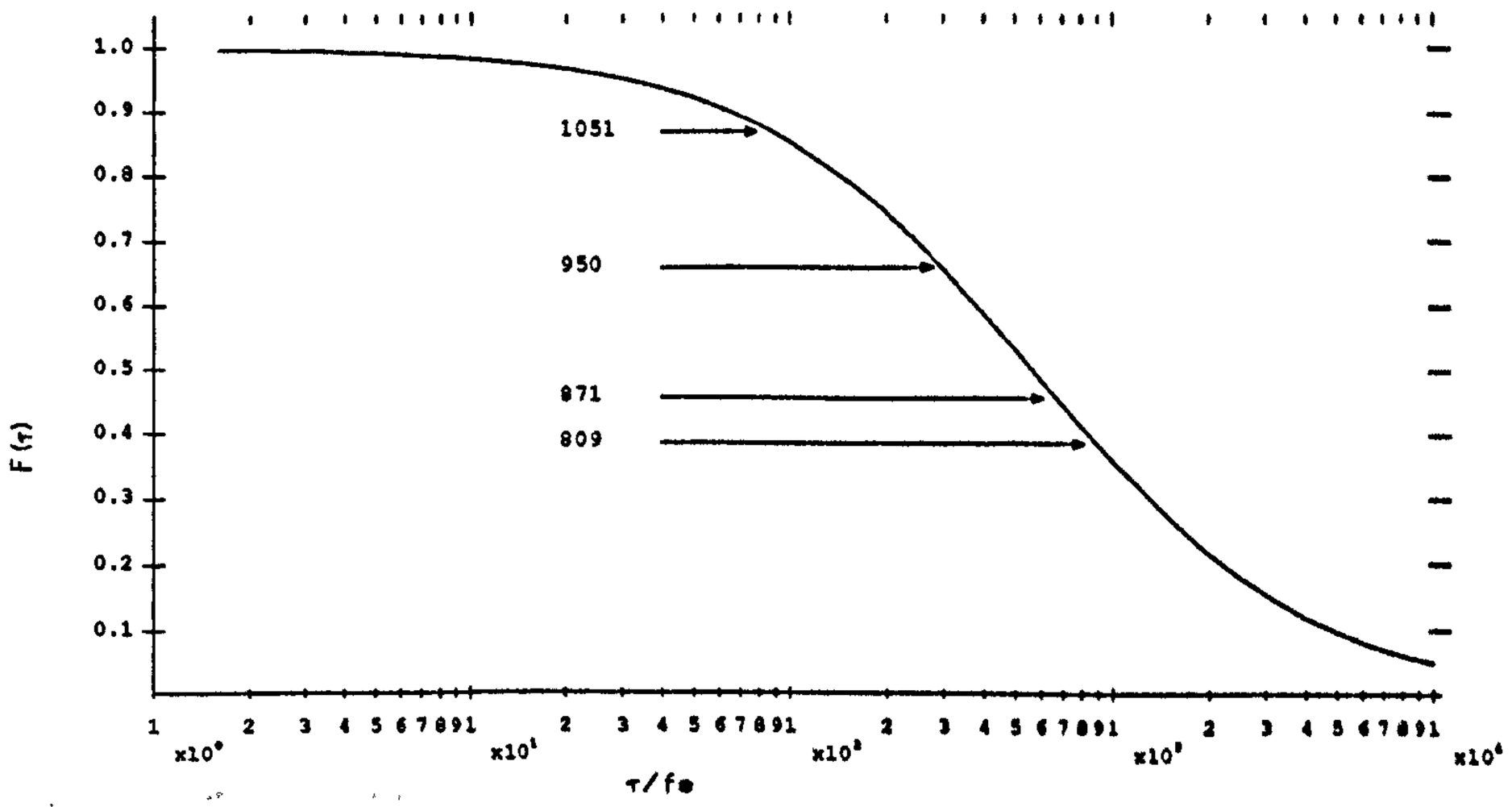

Figure 4.10: F(τ) as a function of τ as calculated using the program FTAU courtesy of Dr D.J.G. Love. The figure is intended only to give an impression of the order of the lifetimes observed.

4.2.2 Bands 4 and 5

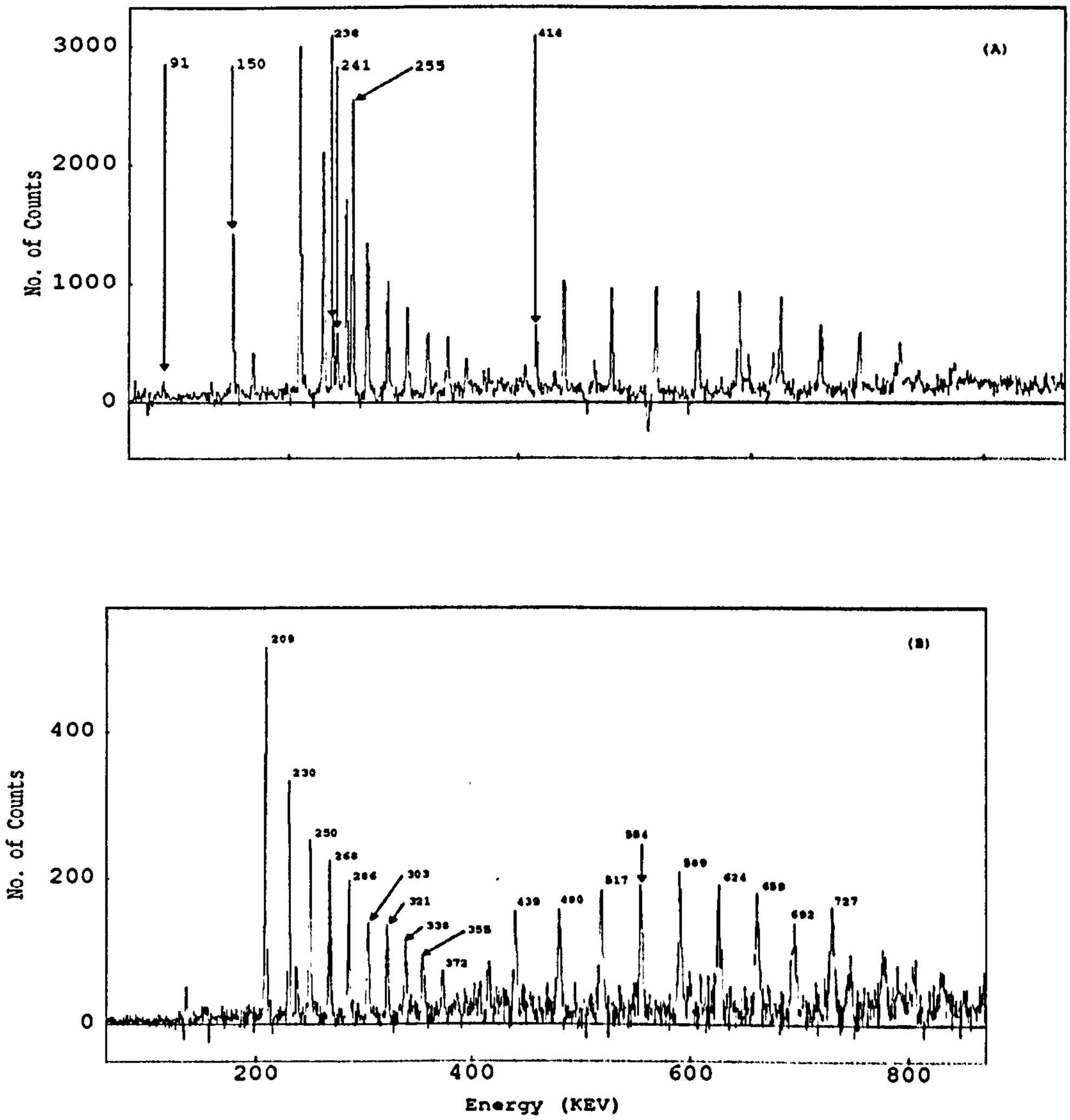

Figure 4.11: Efficiency corrected spectra in coincidence with the 185 keV transition in Band 4 from the ESSA-30 data with Au stopper (a) and the thin target RS data (b). The upper spectrum clearly shows the bottom 3 transitions in Bands 6 and 7 and the 255 keV transition which is interpreted as feeding between these two structures. The corresponding transitions are seen to be entirely absent from the thin target data.

Bands 4 and 5 are strongly linked by inter-band transitions. These are of $\Delta J = 1$ character as evidenced by the I(143)/I(101) ratios in Table 4.4. The thin target data shows the transitions of Bands 4/5 in isolation whereas the backed target data shows a single 255 keV linking transition between Bands 4

and 6. The fact that this transition is absent from the thin target data forces one to the conclusion that the decay from Band 4 is isomeric and occurs after the recoiling nucleus has left the line of sight of the detectors. A simple geometrical model of a recoiling point source progressively masked from the detectors by the collimation of the shielding on the front of the detectors is shown in Figure 4.12 and shows that the γ-γ rate would be expected to drop by a factor of 10 for a lifetime of only 3 *ns*. Such a model is hardly realistic since it ignores effects such as the spread in recoil angle and velocity, variation of the detector efficiency with angle of incidence, the lifetime of the state itself and the finite size of the target. The overall effect of these factors should be to increase the rate at which the efficiency drops off as compared to the model. The model does show that a lifetime of several *ns* could explain the invisibility of the 255 keV transition in spectra from the thin target data. Conversely the strong appearance of the transition in the backed target data implies that the mean lifetime is significantly less than the coincidence resolution time within the electronics (i.e. $\tau_{\frac{1}{2}} < 40$ns). Attempts to extract a lifetime directly from the γ-γ TAC recorded during the ESSA-30 experiment proved fruitless. The 255 keV transition itself is swamped by a self-coincident doublet (presumably associated with a β-decay – see Figure 3.13) but sorting the TAC in coincidence with the 185 keV transition would be expected to clean this up. As the TAC signal was identical to that of any other pair of prompt γ-rays the lifetime must be of the order of or less than the timing resolution of the Ge detectors ,$\sim 10ns$. These two limiting pieces of data probably place the lifetime of the state at the bottom of Band 4 in the range $1 < \tau < 10ns$.

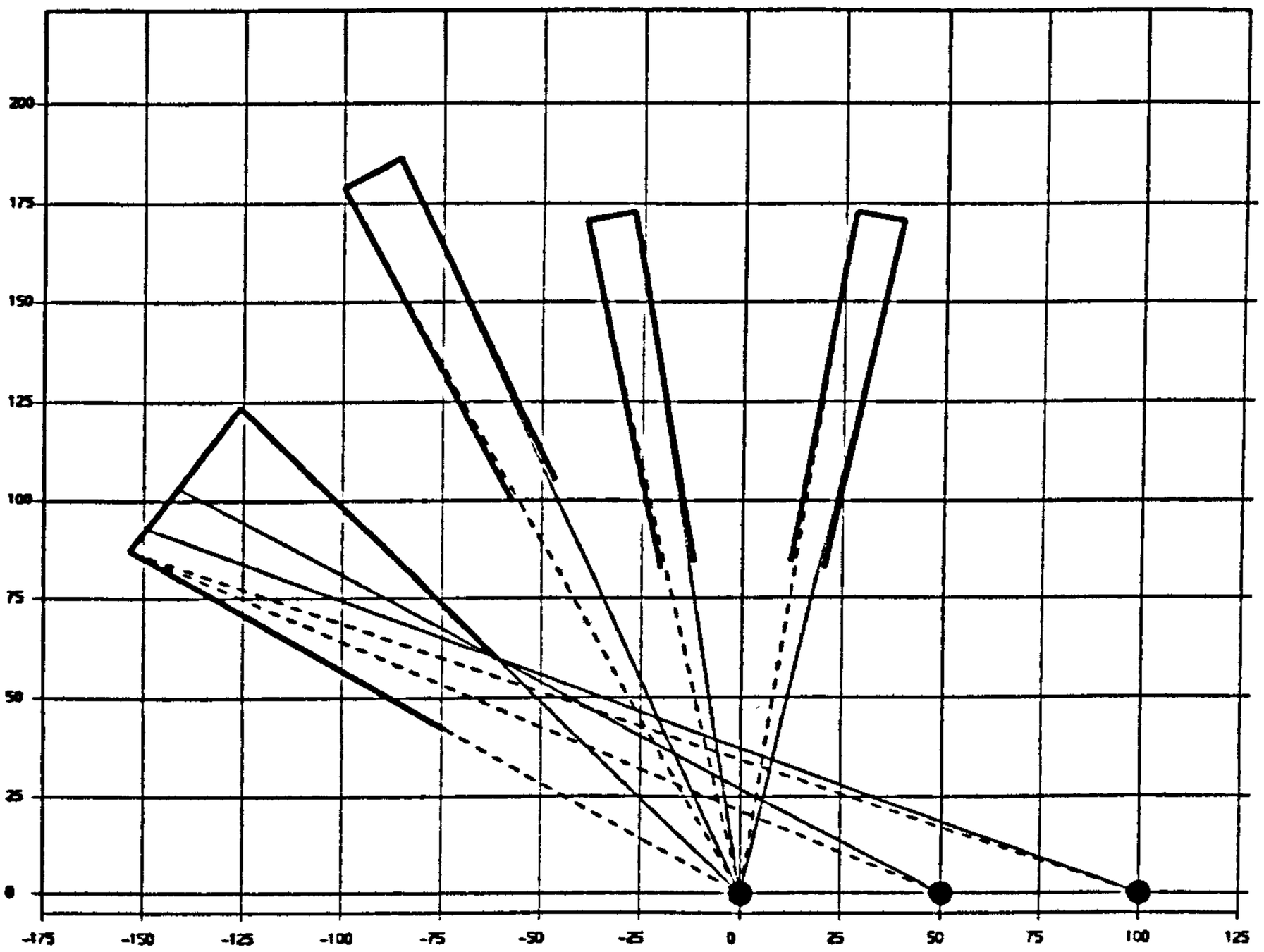

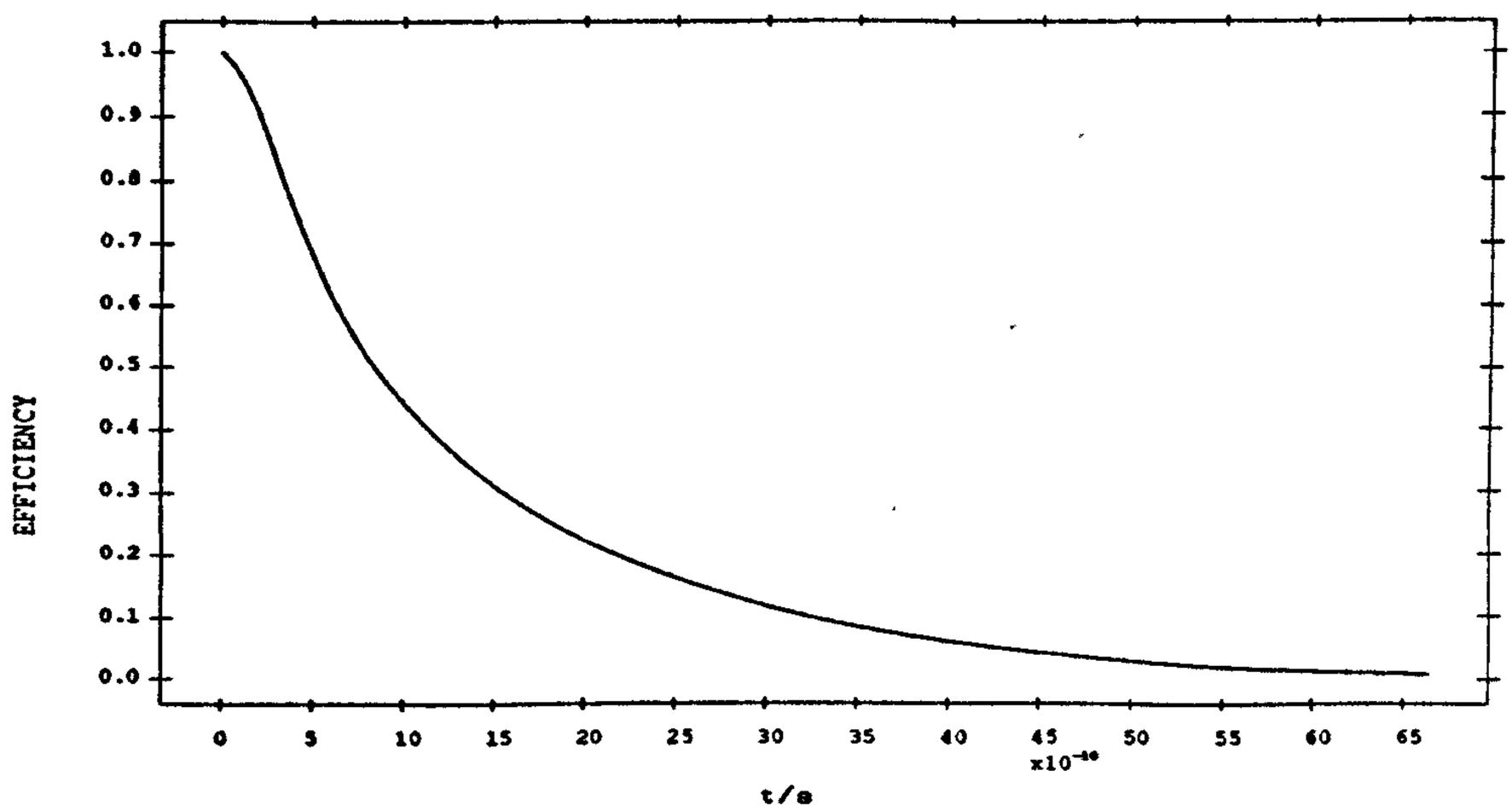

Figure 4.12:
top: Geometrical model of the solid angles subtended at the detector face by a recoiling nucleus as it flies past the collimated detectors of the Polytessa array.
bottom: Predictions from the above model for the efficiency of detection of a delayed transition as determined by the solid angle subtended by the detectors. The efficiency is given as a fraction of that calculated for a prompt decay at the target.

E_{ex} (keV)	$E_\gamma(\Delta J = 1)$ (keV)	I_γ (%)	$E_\gamma(\Delta J = 2)$ (keV)	I_γ (%)	B(M1)/B(E2) $\mu_N^2(eb)^{-2}$
241.4					
496.2	254.8(0.2)	—	—	—	
681.6	185.4(0.2)	94(13) ; 113	—	—	
890.4	208.8(0.2)	86(12) ; 100	394.4(0.4)	10(1)	$1.7(2)^1$, $1.7(1)^3$, $3.0(3)^4$
1120.3	229.9(0.2)	62(9) ; 70	439.2(0.2)	26(4)	$1.1(1)^1$, $0.9(1)^2$, $2.1(1)^4$
1369.8	249.5(0.3)	53(7) ; 58	479.6(0.2)	27(4)	$0.70(7)^1$, $0.87(9)^3$, $2.0(2)^4$
1637.6	267.8(0.2)	42(6) ; 45	517.4(0.3)	42(6)	$1.16(6)^1$, $1.35(14)^3$, $3.0(3)^3$
1923.3	285.7(0.2)	26(4) ; 28	553.6(0.2)	30(4)	$1.4(2)^3$, $2.2(3)^4$
1226.3	303.0(0.2)	24(3) ; 25	588.9(0.3)	30(4)	$0.51(4)^1$, $0.57(7)^3$, $1.02(8)^4$
1547.0	320.7(0.3)	30(4)	624.0(0.3)	—	$0.33(5)^1$, $0.32(9)^3$
1885.0	338.0(0.6)	16(2)	658.9(0.3)	31(4)	$0.40(7)^2$, $0.29(5)^3$
2239.6	354.6(0.7)	12(2)	692.0(0.6)	1(1)	$0.5(1)^2$, $0.29(6)^3$
2612	372(1)	12(2)	743(1)	1(1)	

Table 4.6: Energies and relative intensities for Bands 4 and 5 as shown in Figure 4.5. Excitation energies are given relative to the lowest state in Band 6. Intensities are taken from an efficiency corrected gate on the 255keV transition feeding out of the band as a % of the intensity of the 150keV (100%) transition presumed to be purely that in Band 5. No intensity is given for the 624 keV transition as this appears to be contaminated in this spectrum. In the same spectrum the 241 keV transition in Band 5 is seen at an intensity of 42(6)% relative to the 150 keV transition. The intensity of the 90 keV transition is meaningless due to doubts over the efficiency calibration at this low energy. It would appear likely that there is a further transition of energy 774 keV feeding into the top of this structure although lack of statistics prevent it from being assigned to either band specifically.

4.2.3 Bands 6 and 7

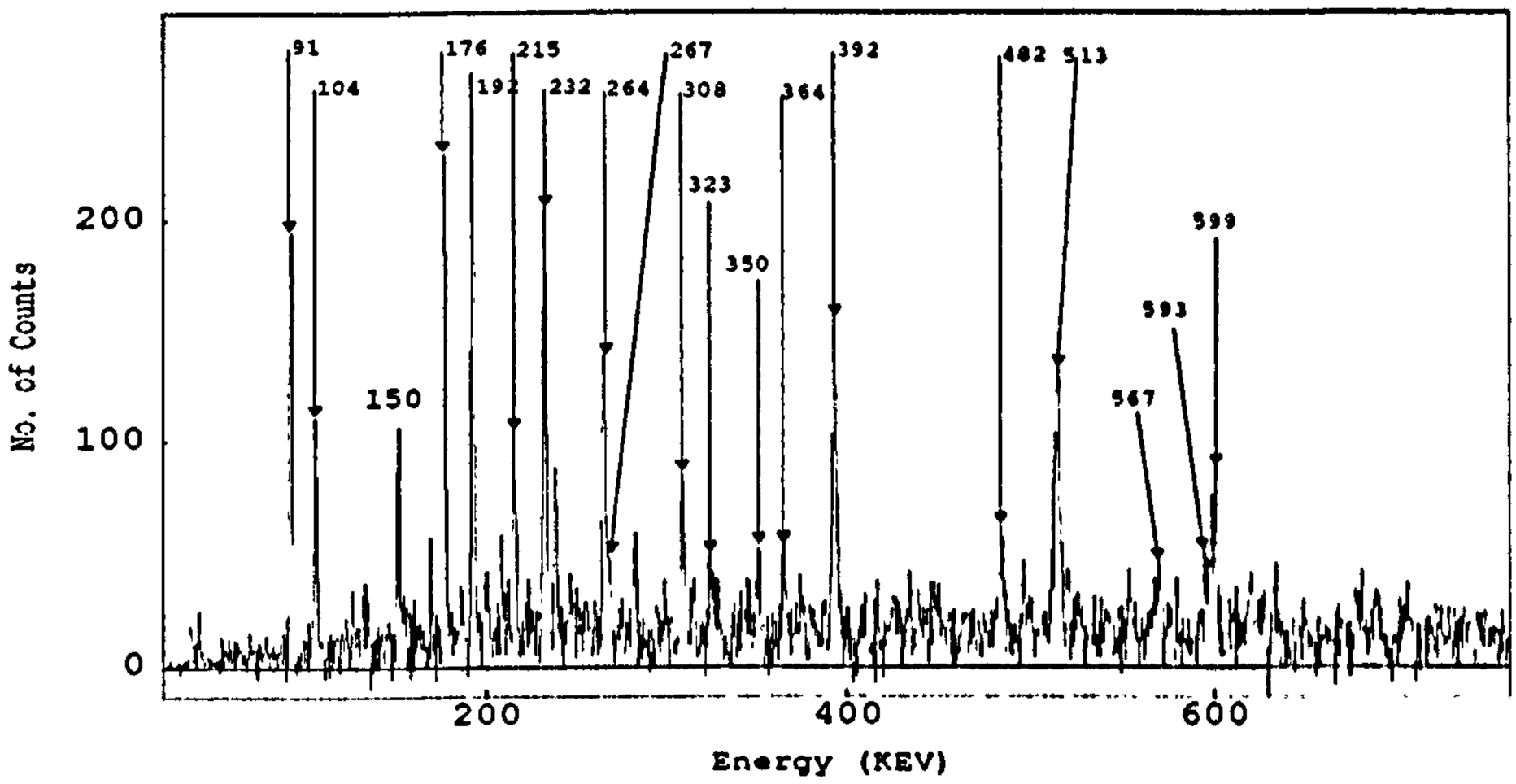

Figure 4.13: Spectrum in coincidence with the 150 keV transition taken from the RS data. Note that the transition is in coincidence with all appropriate transitions in Bands 6/7, including the tentative 567 keV transition and with itself and all transitions in Band 8.

Bands 6/7 are again strongly coupled with transitions of $\Delta J = 1$ character. The sequence is not populated as strongly as that of Bands 4/5 but must be placed lower in excitation by virtue of the linking transition described in Section 4.2.2. Due to this weakness and contamination of the spectra associated with transitions in this band, reliable estimates of the branching ratios were difficult to obtain. Qualitatively it appears that the inter-band transitions dominate at low spin whilst the intra-band transitions dominate higher up the bands. The only estimable branching ratios were those of the 417 and 633 keV levels which are significantly lower than those of the corresponding levels in Bands 4/5:

Method of measurement	E_{ex} (keV)	B(M1)/B(E2) $\mu_N^2(eb)^{-2}$
RS Z-selected spectrum	417	0.29(5)
RS sum of gates feeding level	417	0.45(3)
RS gate on 513 keV transition	633	0.32(3)

There is a probably a link between Bands 3 and 6 via the 567 keV transition as seen in Figures 4.13 and 4.14. The data is, however, not conclusive. Note that there is a (possible) 567 keV transition observed in the Z-selected spectrum. The 567 keV transition itself appears in several nuclei produced in this experiment.

E_{ex} (keV)	E_{γ} (keV)	I_{γ} (%)
90.8	90.8(0.1)	—
241.2	150.4(0.2)	100 ; 146
417.4	176.2(0.1)	28(3) ; 36
632.6	215.2(0.2)	28(3) ; 33
899.4	266.8(0.4)	9(2) ; 10
1146	246(1)	—
241.2	241.5(0.4)	—
632.6	391.7(0.2)	69(5)
1146	513.1(0.2)	75(6)
1743	597.6(0.2)	63(6)
417.4	326.8(0.1)	48(4)
899.4	482.1(0.2)	40(4)
1492	593.0(0.5)	47(6)

Table 4.7: Energies and Intensities for Bands 6 and 7. The intensities quoted are those observed in the 91 keV gate. Also observed in this gate are the 192 and 232 keV transitions from band 8 at 19 and 18 % intensity relative to the 150 keV tansition so the intensity of the 150 keV transition is probably an overestimate by ~20%. These figures are purely to show that they do not contradict intensity arguments for the proposed structure ; an accurate determination of the relative intensities was rendered unfeasible by the weakness of the bands and the number of interfering γ−rays , particularly the 150 keV doublet with Band 8 and the 265/266 doublet which is further compounded by the 268 keV transition in bands 4 and 5. All measurements were taken from the RS data as the ESSA-30 data were too contaminated.

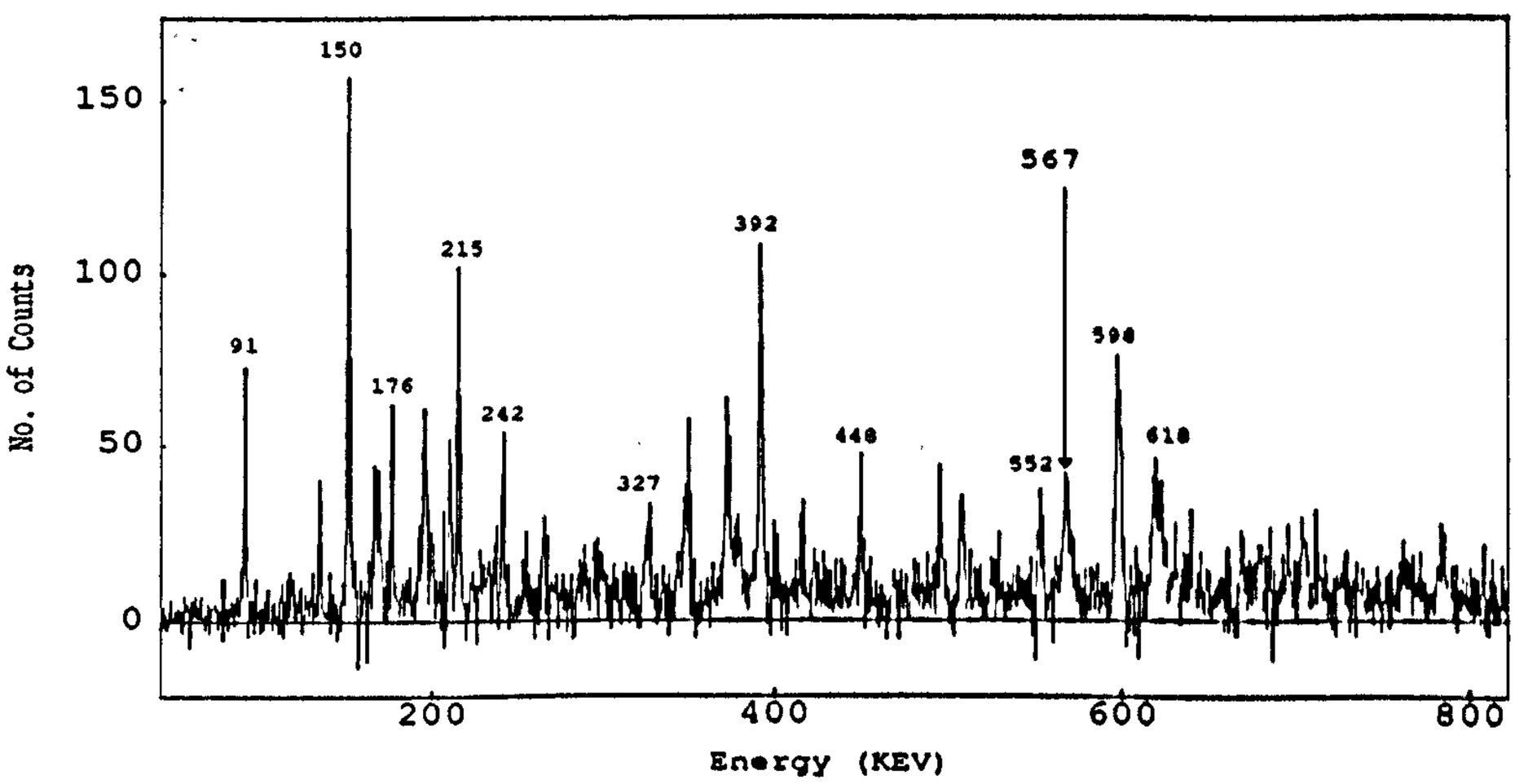

Figure 4.14: Spectrum in coincidence with the 513 keV transition taken from the RS data. The 567 keV transition and transitions in Band 2 are clearly visible.

4.2.4 Band 8

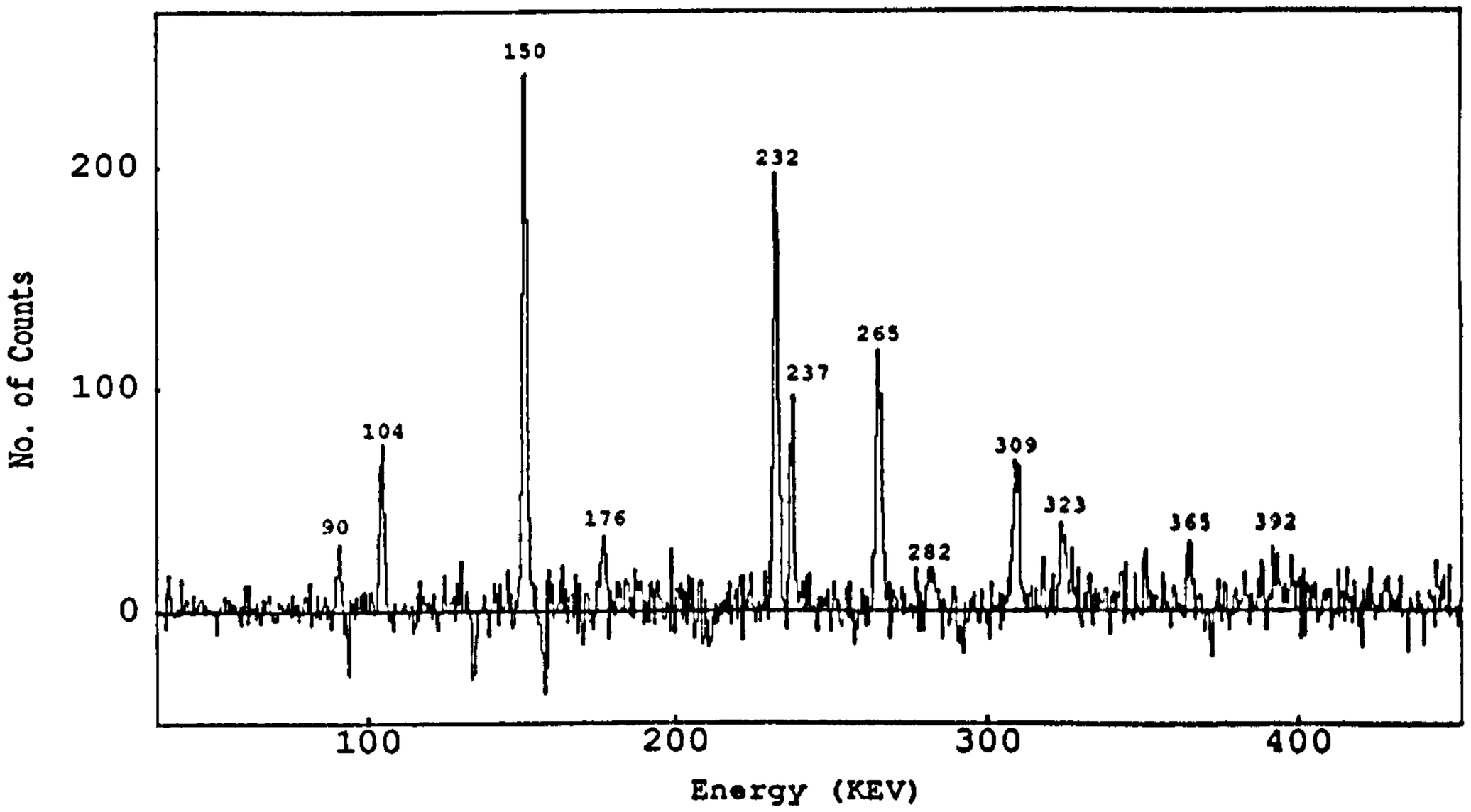

Figure 4.15: Spectrum of γ-rays in coincidence with the 192 keV transition in Band 8. The appearance of the 237 keV transition may be spurious although the 237 keV transition does appear to be in coincidence with a 104 keV transition.

From the I(143)/I(101) ratios of Table 4.4 it would appear that Band 8 transitions are of different character since these ratios are consistently lower than those of observed for Bands 4,5,6, and 7. The band is thus interpreted as a $\Delta J = 1$ band. There is no hint of $\Delta J = 2$ transitions within the band enabling a lower limit of $> 7\ \mu_N^2 (eb)^{-2}$ to be put on the B(M1)/B(E2) ratio for this band under the assumption of a negligible mixing ratio (which seems unlikely due to the obviously lower I(143)/I(101) ratio).

The excitation of this band is unknown. As noted in Section 4.2.3 the 150 keV transition is a self-coincident doublet and the remaining transitions in the band are probably weakly coincident with the lower transitions of Band 6/7 but not higher ones. It would thus appear likely that Band 8 feeds into Bands 6/7 from a higher energy via an undetermined path. The 104 keV transition is placed as the lowest transition in the band by virtue of the smoothly decreasing intensity pattern observed in a gate on this transition.

E_{ex} (keV)	E_γ (keV)	I_γ (%)
104.5	104.5(0.2)	26(2) ; 58
255.2	150.7(0.4)	100 ; 146
447.2	192.0(0.2)	—
679.4	232.2(0.2)	88(4) ; 99
944.2	264.8(0.2)	78(4) ; 84
1252.4	308.2(0.2)	44(3) ; 46
1616.2	363.8(0.4)	14(2) ; 15
—	323(1)	22(3) ; 23
—	350(1)	14(2) ; 15

Table 4.8: Energies and relative intensities for transitions in band 8. The energies were taken from the cleanest gates and the intensities from the 192 keV gate. This gate also shows the 176 and 90 keV transitions in Bands 7 and 8 at 13 and 9 % respectively. The observed intensity of the 150 keV transition is thus probably an overestimate. The low intensity of the 104 keV transition in this spectrum probably indicates that a major fraction of the intensity of the band feeds out at the 255 keV level. The 323 and 350 keV transitions are included here as they appear to be connected with this band, possibly feeding from it although this cannot be ascertained definitely. The excitation energies shown are relative to the bottom of the band.

4.3 ^{128}Pr

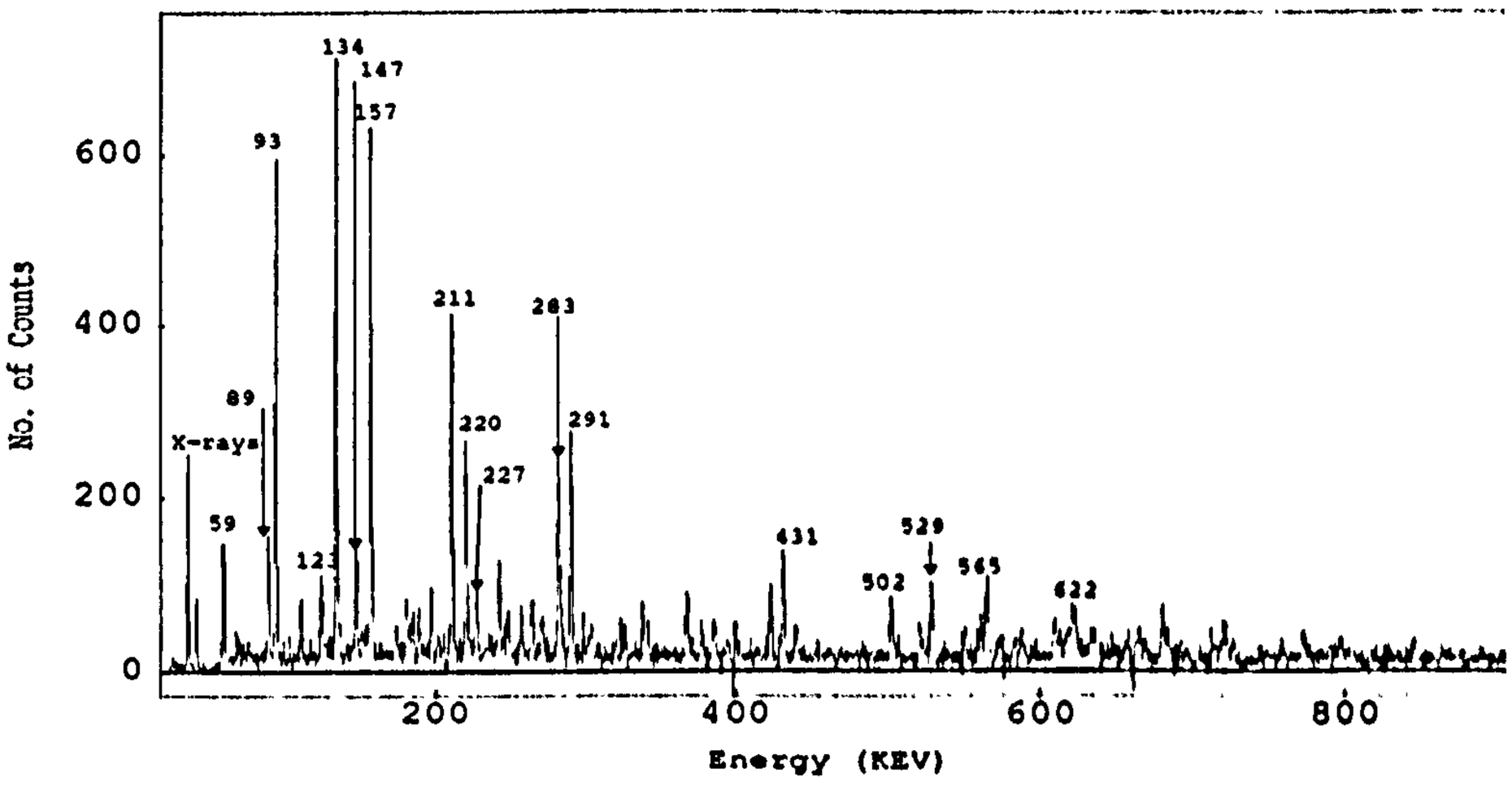

Figure 4.16: Z-selected spectrum for ^{128}Pr. Energies and intensities for the transitions can be found in the following table. A careful examination of the energies shows that some breakthrough of the ^{128}Nd channel seems likely. Transitions of similar energy in the two isobars are noted in Table 4.9

Many of the transitions attributed to ^{128}Pr have been placed in Bands 1/2 which are yrast over the excitation region observed. The remaining transitions are very weak, the strongest being the 123 and 147 keV transitions at ~13% and 17% of the intensity of the 143 keV transition. The contamination of the above spectrum with ^{128}Nd does not affect the assignment of Bands 1/2 to this nucleus as the transitions are quite clearly different from those of the yrast band in ^{128}Nd.

E_γ (keV)	I_γ (%)	I(143)/I(101)	Assignment
59.0	25(2)	1.13(0.02)	1→
88.8	22(2)	0.97(0.02)	
93.4	76(3)	1.06(0.01)	2→1
110.3	10(3)	0.94(0.03)	
123.6	15(2)	1.14(0.03)	
133.9	100(3)	1.03(0.01)	1→2, ^{128}Nd
146.8	18(3)	1.14(0.03)	
156.7	85(3)	0.92(0.01)	2→1
173.2	6(2)	0.96(0.04)	
180.4	14(2)	0.98(0.03)	
184.7	9(2)	1.15(0.04)	
189.1	6(2)	0.94(0.03)	
196.6	7(2)	1.05(0.03)	
210.8	60(3)	0.88(0.01)	1→2
220.2	39(2)	0.86(0.01)	2→1
227.0	13(2)	1.19(0.03)	1
242.4	18(2)	1.57(0.04)	
248.1	13(2)	1.87(0.08)	
257.0	13(2)	0.83(0.03)	
264.3	13(2)	1.19(0.03)	
271.1	11(2)	1.74(0.06)	
282.5	48(3)	0.91(0.01)	1→2,2→1
290.7	42(3)	1.82(0.03)	2, ^{128}Nd
298.9	5(2)	1.38(0.05)	
303.8	12(5)	1.70(0.06)	
326.0	7(2)	0.86(0.03)	
338.5	11(2)	1.13(0.03)	1→2
341.6	5(2)	1.01(0.03)	2→1
367.7	17(2)	2.06(0.05)	1
377.2	7(2)	0.91(0.03)	1→2
385.9	10(2)	2.02(0.08)	
395.0	4(2)	1.13(0.05)	2→1
400.2	5(2)	—	1→2
422.8	16(1)	1.50(0.03)	
431.0	25(1)	1.91(0.03)	2, ^{128}Nd
439.7	9(1)	1.91(0.06)	
453.6	4(2)	—	
502.5	16(1)	2.35(0.07)	1
520.9	10(1)	2.01(0.06)	

E_γ(keV)	I_γ (%)	I(143)/I(101)	Assignment
528.8	19(1)	2.16(0.06)	^{128}Nd
550.2	7(3)	—	
561.0	11(2)	1.96(0.03)	
564.8	21(2)	1.93(0.05)	2
587.6	7(2)	2.28(0.07)	
610.0	18(4)	1.84(0.06)	^{128}Nd
621.3	33(6)	2.22(0.05)	1
634.8	19(6)	2.04(0.06)	
681.4	20(6)	1.89(0.05)	2
666.5	17(5)	—	
719.8	18(5)	2.02(0.04)	1
772.4	9(3)	1.80(0.06)	2
845.8	11(4)	1.49(0.05)	2

Table 4.9: Transitions observed in the Z-selected spectrum of ^{128}Pr. The I(143)/I(101) ratios are taken from spectra recorded at the appropriate angles and selected on mass (128) only and therefore are contaminated in several cases by peaks in ^{128}Ce and to a lesser extent ^{128}Nd. Where the ^{128}Pr peak clearly lies under a strong ^{128}Ce peak the ratio is left unassigned. The intensities listed are relative to the 134 keV peak which has a total area of $\sim$ 2700 counts and are provided to give some idea of the reliability of the existence/assignment of the peak within the decay scheme of ^{128}Pr. These intensities are not efficiency corrected. The assignments refer to bands in ^{128}Pr as labelled in figure 4.17.

The only structures that can be definitely deciphered in this nucleus are the strongly coupled Bands 1/2. The coincident doublet (282/3 keV) in the decay scheme is well established since it is of abnormally large intensity, is self coincident and is consistent with the other transitions observed. The upper members of the bands woud appear to possess lineshapes in the backed target data indicating short apparent lifetimes, in the region of $\sim 1ps$.

The remaining γ transitions in ^{128}Pr are of low intensity and are hence difficult to place reliably. The unlabelled structures shown in Figure 4.17 represent a best attempt to classify the decays into bands. The spectrum in Figure 4.20 shows most of the strongest transitions feed into the level above the 89 keV transition. The 123 and 147 keV transitions are not, however, in coincidence. The dotted transitions in Figure 4.17 are from the backed target data and are tentative as they are not seen in the cleaner RS data. This may be due to isomeric behaviour of some of the levels but the spectra are not clean enough to definitely associate

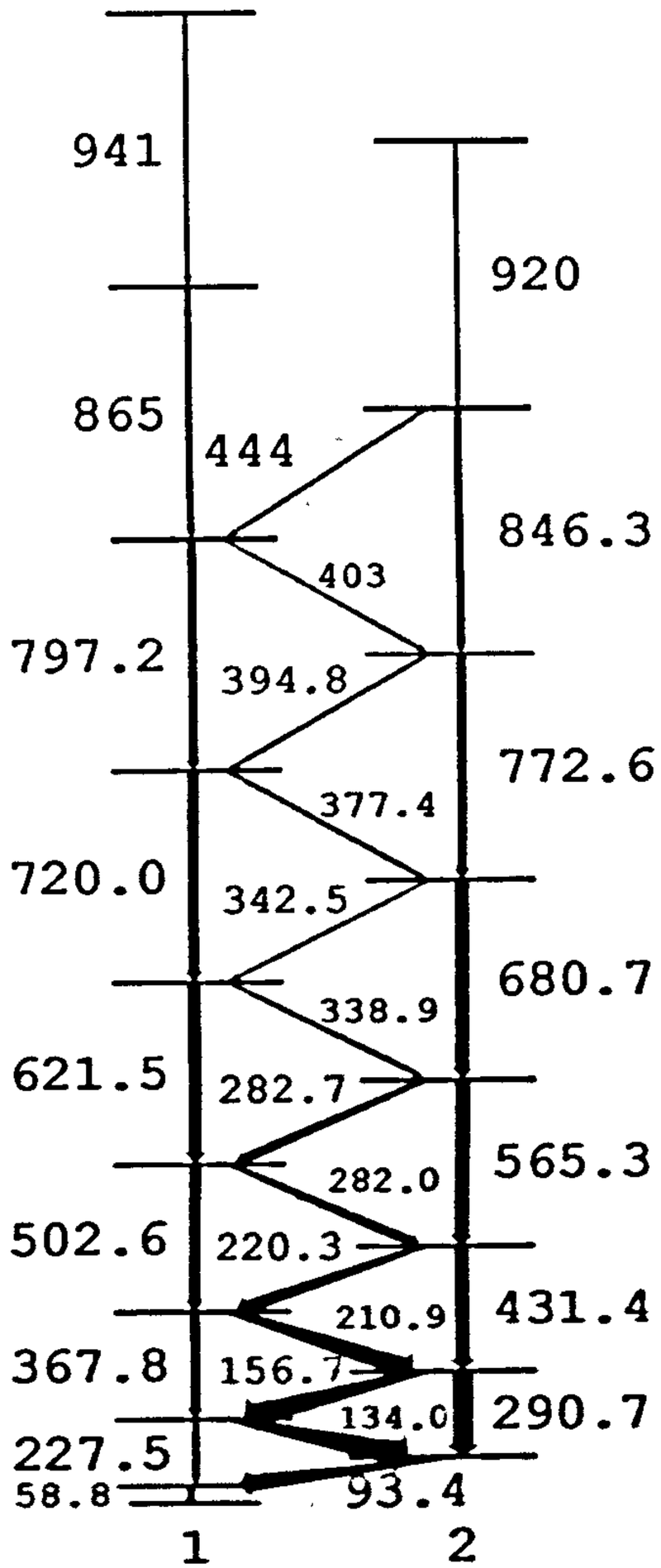

Figure 4.17: Decay Scheme for ^{128}Pr

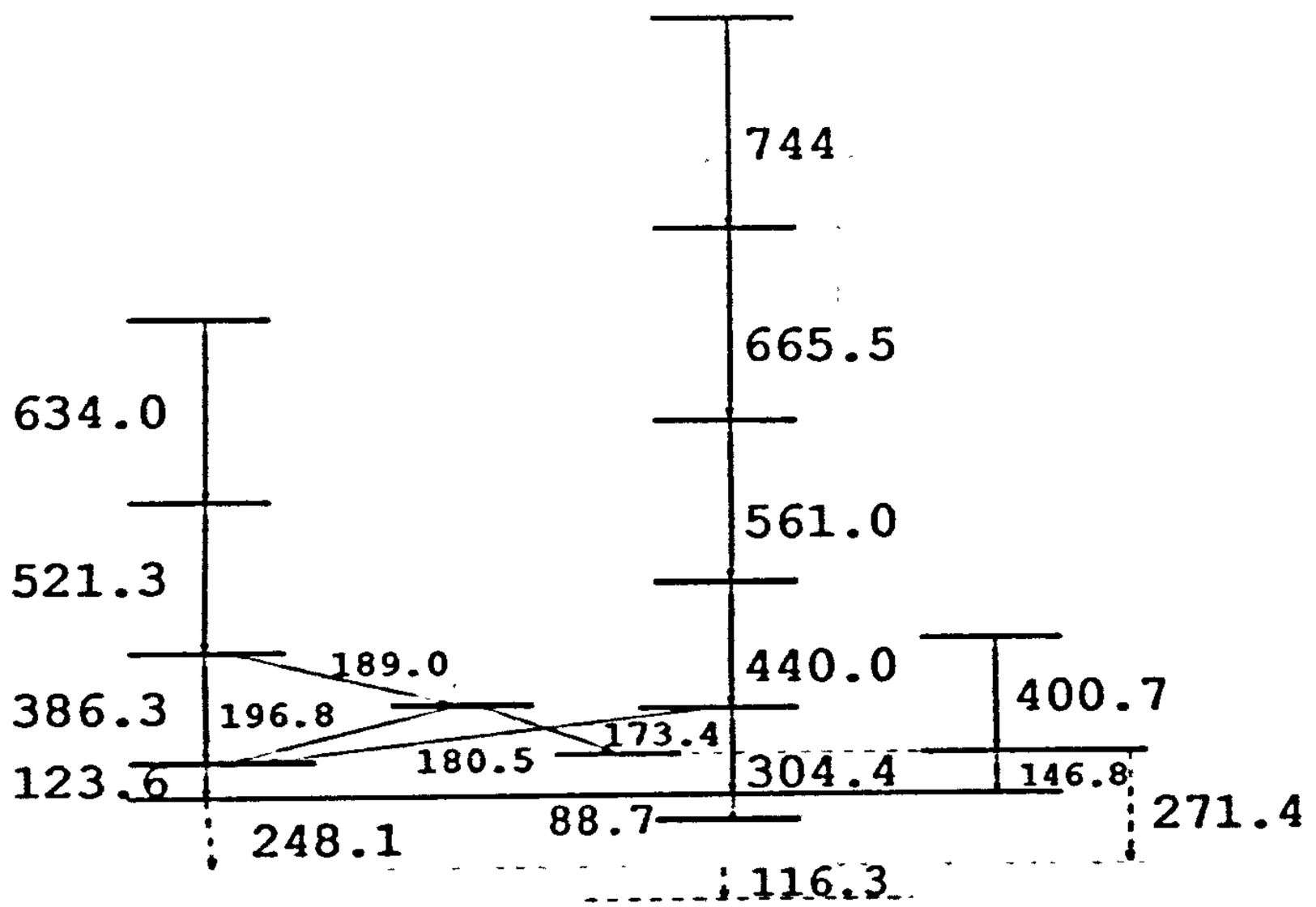

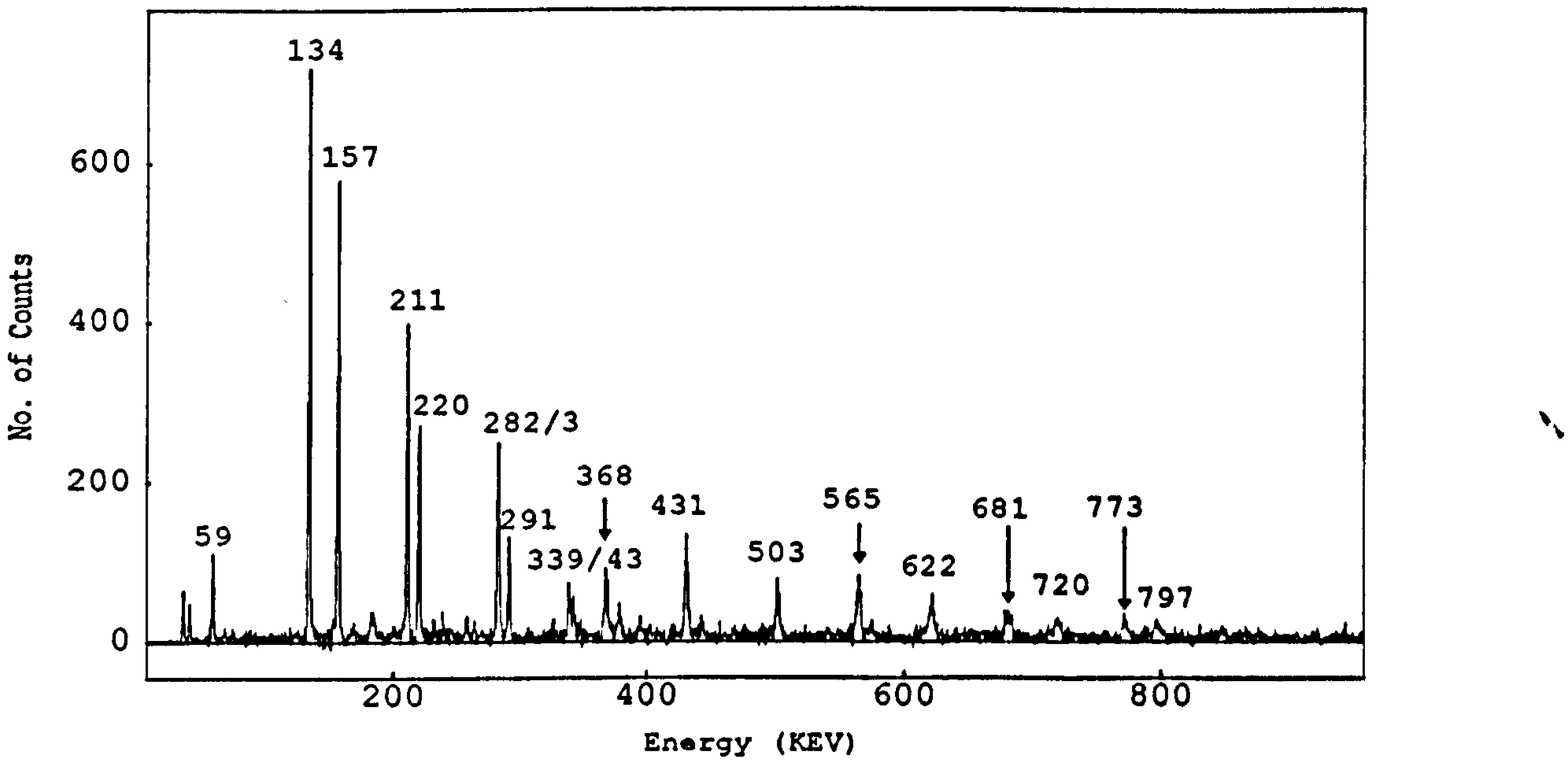

Figure 4.18: Spectrum from the RS data gated on the 93 keV transition between bands 1 and 2 as labelled in Figure 4.17. Note the large intensity of the 282/3 transition which supports the doublet within the decay scheme.

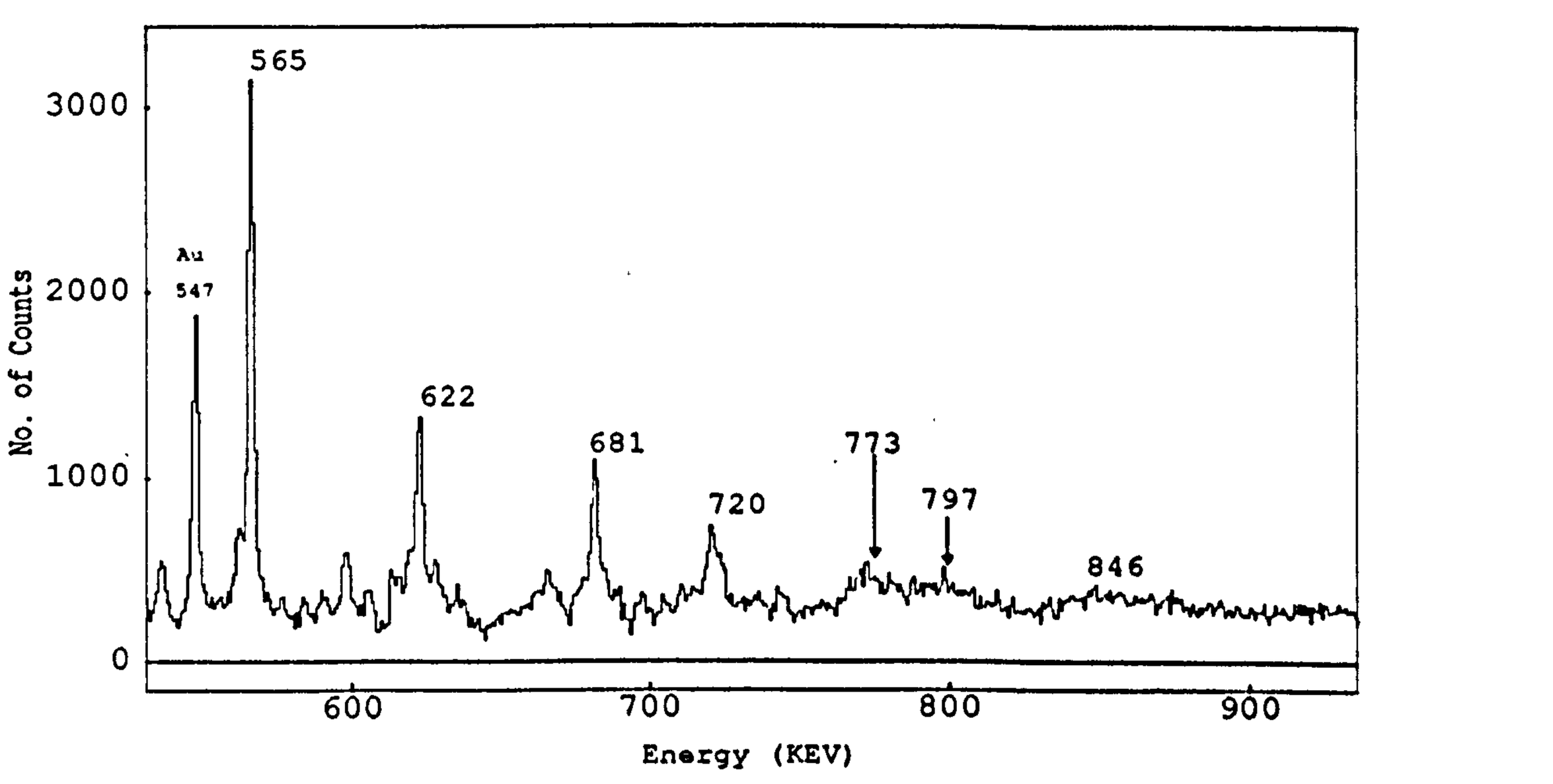

Figure 4.19: Partial spectrum from the ESSA-30 data gated on the 157 keV transition between Bands 1/ 2 showing that the top transitions visible in this data possess lineshapes indicative of states with short lifetimes.

E_{ex} (keV)	$E_\gamma(\Delta J = 1)$ (keV)	I_γ (%)	$E_\gamma(\Delta J = 2)$ (keV)	I_γ (%)	B(M1)/B(E2) $\mu_N^2(eb)^{-2}$
58.8	58.8(0.1)	20(1) ; 100	—	—	
152.2	93.4(0.1)	68(2) ; 197	—	—	
286.2	134.0(0.1)	100 ; 150 ;	227.5(0.2)	17(1) ; 19	1.09(3)[1], 1.20(2)[3], 1.03(3)[4]
442.3	156.7(0.1)	90(3) ; 119	290.7(0.2)	66(2) ; 70	0.87(1)[3], 0.99(2)[4]
653.8	210.9(0.1)	75(2) ; 88	367.8(0.2)	30(2) ; 31	1.24(3)[1], 0.84(2)[3], 1.24(3)[4]
874.1	220.3(0.1)	51(2) ; 59	431.4(0.1)	50(2)	1.03(3)[1], 0.95(2)[3]
1156	282.0(0.5)	69(3) ; 74	502.6(0.1)	34(2)	0.74(4)[3], 0.93(4)[4]
1439	282.7(0.3)	—	565.3(0.1)	49(3)	
1778	338.9(0.3)	15(1)	621.5(0.5)	39(3)	
2120	342.5(0.3)	7(1)	680.7(0.3)	41(2)	
2498	377.4(0.2)	13(2)	720.0(0.2)	33(5)	
2892	394.8(0.5)	10(1)	772.6(0.2)	26(2)	
3295	403(1)	7(1)	797.2(0.4)	25(2)	
3739	444(1)	10(1)	846.3(0.5)	16(2)	
4160			865(1)	15(2)	
—	—	—	920(1)	7(1)	
—	—	—	941(1)	8(1)	

Table 4.10: Energies and Intensities associated with bands 1 and 2 in ^{128}Pr as shown in Figure 4.17. The energies are taken from the cleanest gates. The relative intensities of transitions from below the 1778 keV level were measured from an efficiency corrected Z-selected spectrum and those above from an efficiency corrected 134 keV gate and normalised to the intensity of the 282 keV transition. The intensity of the 282 keV transition contains contributions from both elements of the doublet. The energies of the 282/283 doublet are taken from the 622/503 keV gates respectively and the errors reflect the strength and degree of contamination of these spectra. The 920 and 941 keV transitions are only truly seen in sums of gates so they have not been specifically assigned to either band. Intensities for these 2 transitions were assigned from this sum of gates.

the transitions with the nucleus. In particular the 110 and 116 keV transitions appear much enhanced in the backed target data.

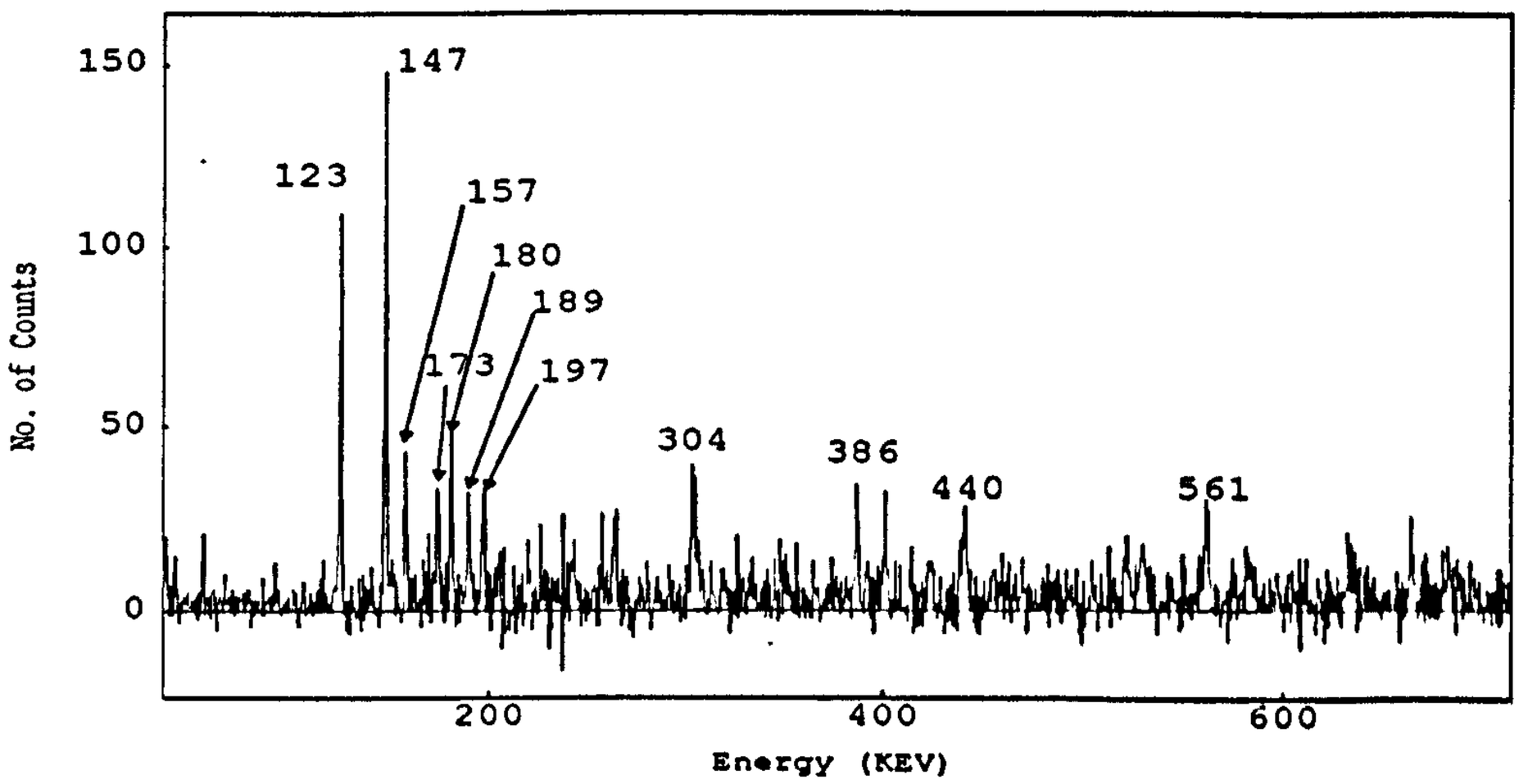

Figure 4.20: Gate on the 89 keV transition in ^{128}Pr.

4.4 ^{129}Nd

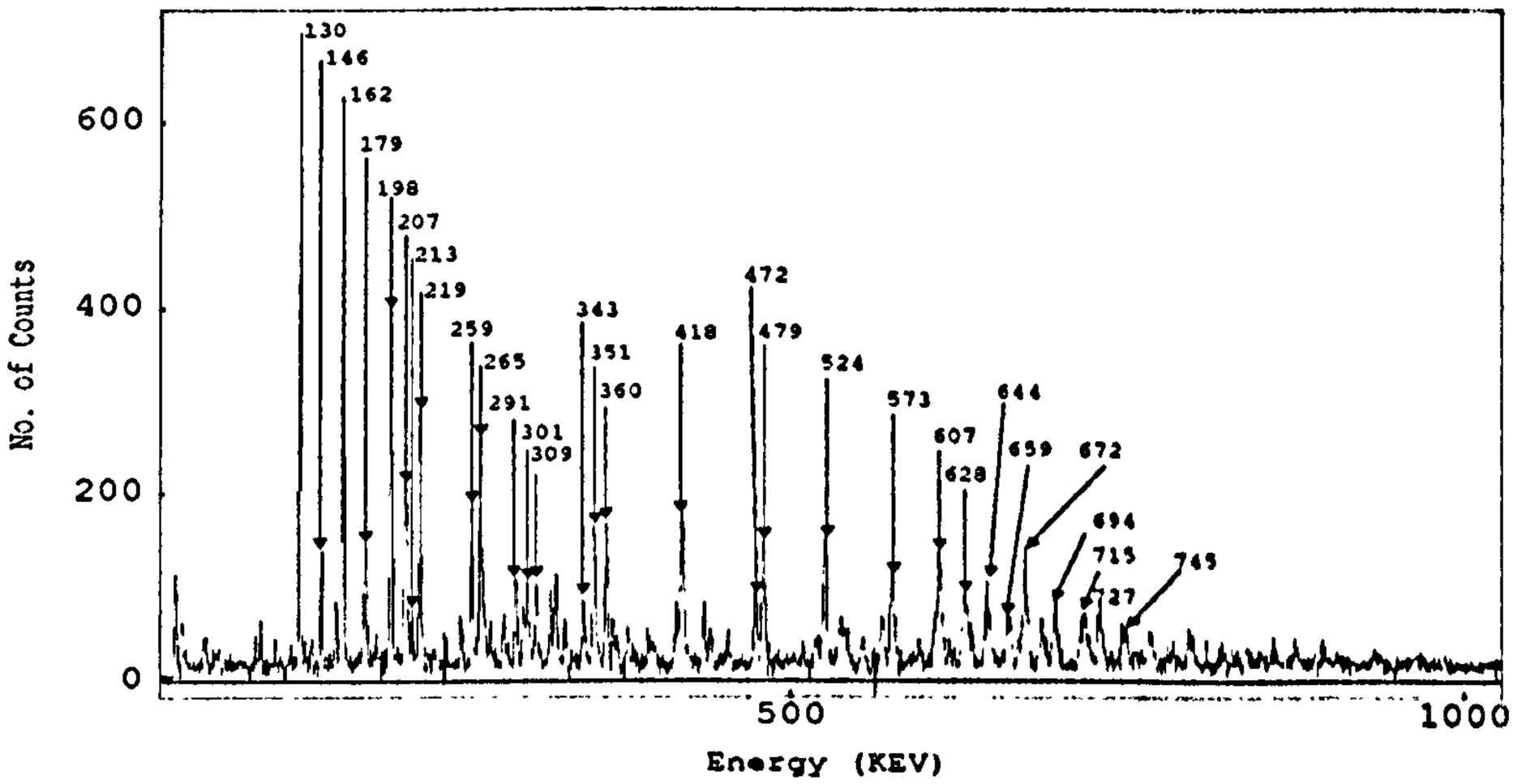

Figure 4.21: Z-selected spectrum of ^{129}Nd. Some of the principal γ transitions assigned to the following structures are indicated.

Four distinct decay sequences have been identified in ^{129}Nd. No linking transitions have been observed between them so their relative excitations remain unknown. It can be seen from Table 4.11 that the majority of transitions identified with the RS experiment have been identified. The ESSA-30 experiment did not yield any new information about this nucleus due to the lower cross section of formation of this channel and the poorer quality of the spectra obtained from it.

E_γ (keV)	I_γ(%)	I(143)/I(101)	Assignment
96.4	4(1)	—	
99.7	7(3)	1.41(0.63)	
130.1	100(4)	1.10(0.08)	2→1
138.4	5(2)	0.95(0.29)	5→
145.8	18(2)	1.17(0.21)	4→3
156.9	13(2)	1.10(0.16)	
162.1	90(3)	0.95(0.07)	1→2
178.3	30(3)	0.85(0.12)	3→4
187.2	5(2)	—	
198.1	67(3)	0.94(0.08)	2→1
208.8	48(5)	1.40(0.11)	5,6
213.3	13(4)	0.93(0.18)	4→3
219.8	51(5)	0.80(0.07)	1→2
239.9	2(1)	—	3→4
250.5	10(3)	1.24(0.19)	
258.8	31(3)	0.75(0.09)	2→1
265.8	54(5)	1.01(0.10)	1→2
268.9	13(2)		4→3
273.1	7(2)	2.26(0.95)	
283.2	12(3)	1.03(0.24)	3→4
291.8	20(4)	2.14(0.38)	1
297.8	16(4)	1.68(0.33)	
301.1	20(4)	0.86(0.12)	1→2
307.5	21(4)	0.66(0.09)	2→1
318.1	14(3)	1.39(0.32)	
322.0	24(5)	1.22(0.16)	6
328.4	11(3)	—	3,1→2
343.5	18(4)	0.93(0.15)	2→1
351.3	43(4)	1.24(0.13)	5,1→2
359.9	33(3)	1.57(0.22)	2
365.1	12(6)	0.70(0.13)	
368.6	7(3)	0.78(0.20)	2→1
376.7	7(3)	0.48(0.12)	
394.2	15(4)	1.23(0.20)	2
413.2	15(6)	—	
417.3	52(5)	—	1
433.3	16(4)	—	6
438.4	12(4)	1.96(0.26)	
451.2	8(4)	1.72(0.28)	3
472.0	23(2)	1.71(0.25)	5

E_γ	I_γ	I(143)/I(101)	Assignment
478.2	35(4)	1.65(0.18)	2
507.0	5(3)	1.35(0.31)	4
517.7	9(3)	1.04(0.14)	
523.6	39(4)	1.71(0.20)	1
538.2	25(5)	1.47(0.31)	6
550.8	7(3)	1.77(0.19)	3
565.7	16(4)	2.10(0.31)	5
572.8	30(1)	2.02(0.28)	2
607.1	51(5)	1.74(0.19)	1
627.7	41(5)	2.05(0.19)	5
643.3	29(4)	2.01(0.31)	2
658.7	21(5)	1.77(0.25)	5
670.9	45(4)	1.92(0.11)	1
683.7	17(4)	—	5
693.1	24(4)	2.01(0.29)	2
714.9	34(5)	1.86(0.27)	1
726.4	24(4)	2.00(0.27)	5
744.3	19(4)	1.82(0.37)	4
763.2	16(4)	2.23(0.33)	
792.6	16(4)	2.18(0.51)	
818.1	2(1)	2.00(0.26)	
870.3	7(3)	1.97(0.23)	

Table 4.11: Transitions observed in the Z-selected spectrum of ^{129}Nd. The intensities quoted are those from such a spectrum corrected for efficiency of the γ-ray detectors. The I(143)/I(101) ratios are taken from spectra recorded at the appropriate angle and selected on mass (129) only and therefore are contaminated in several cases by peaks in ^{129}Pr. The assignments refer to bands in ^{129}Nd as labelled in figure 4.22.

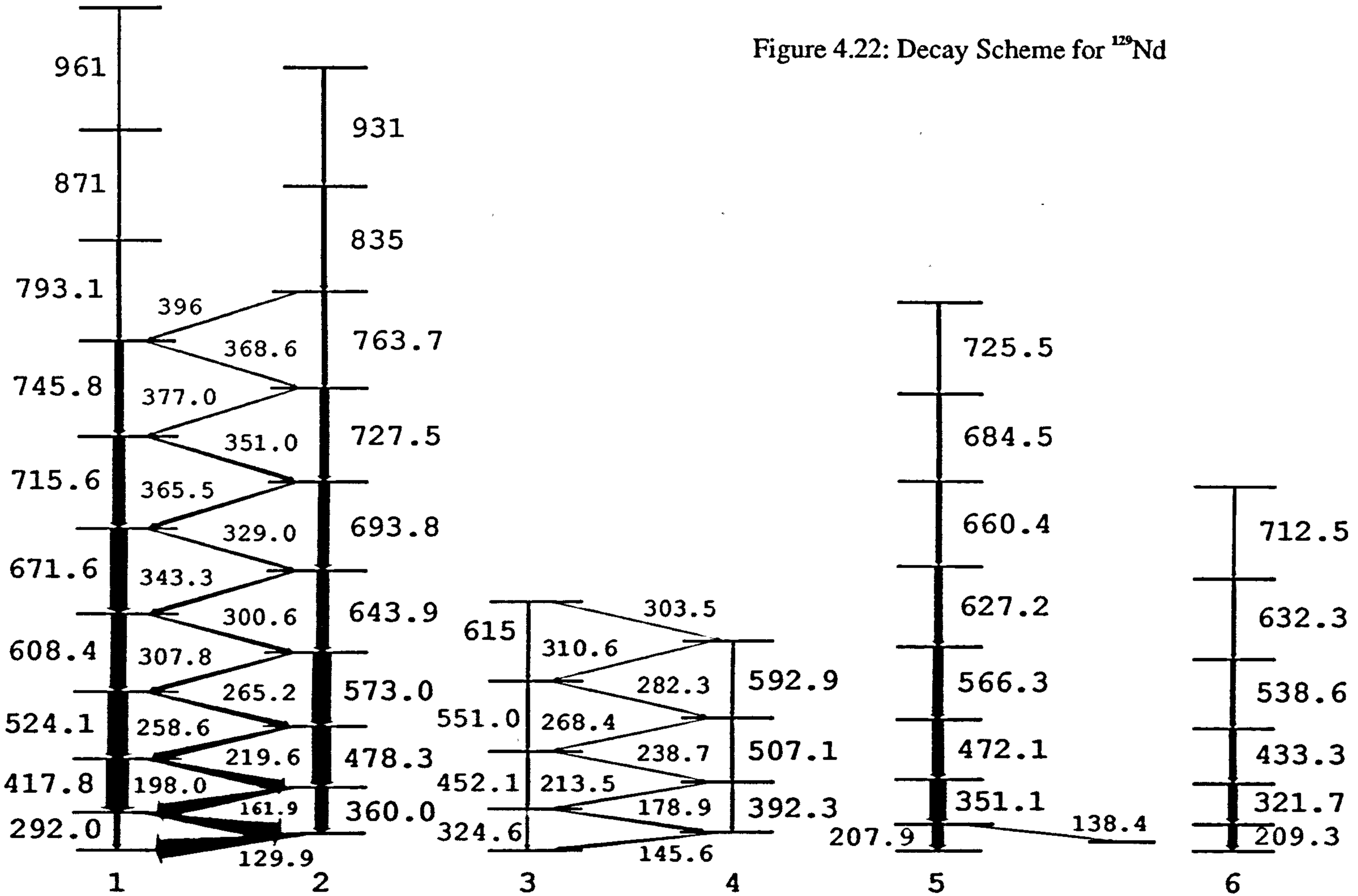

Figure 4.22: Decay Scheme for ^{129}Nd

4.4.1 Bands 1 and 2

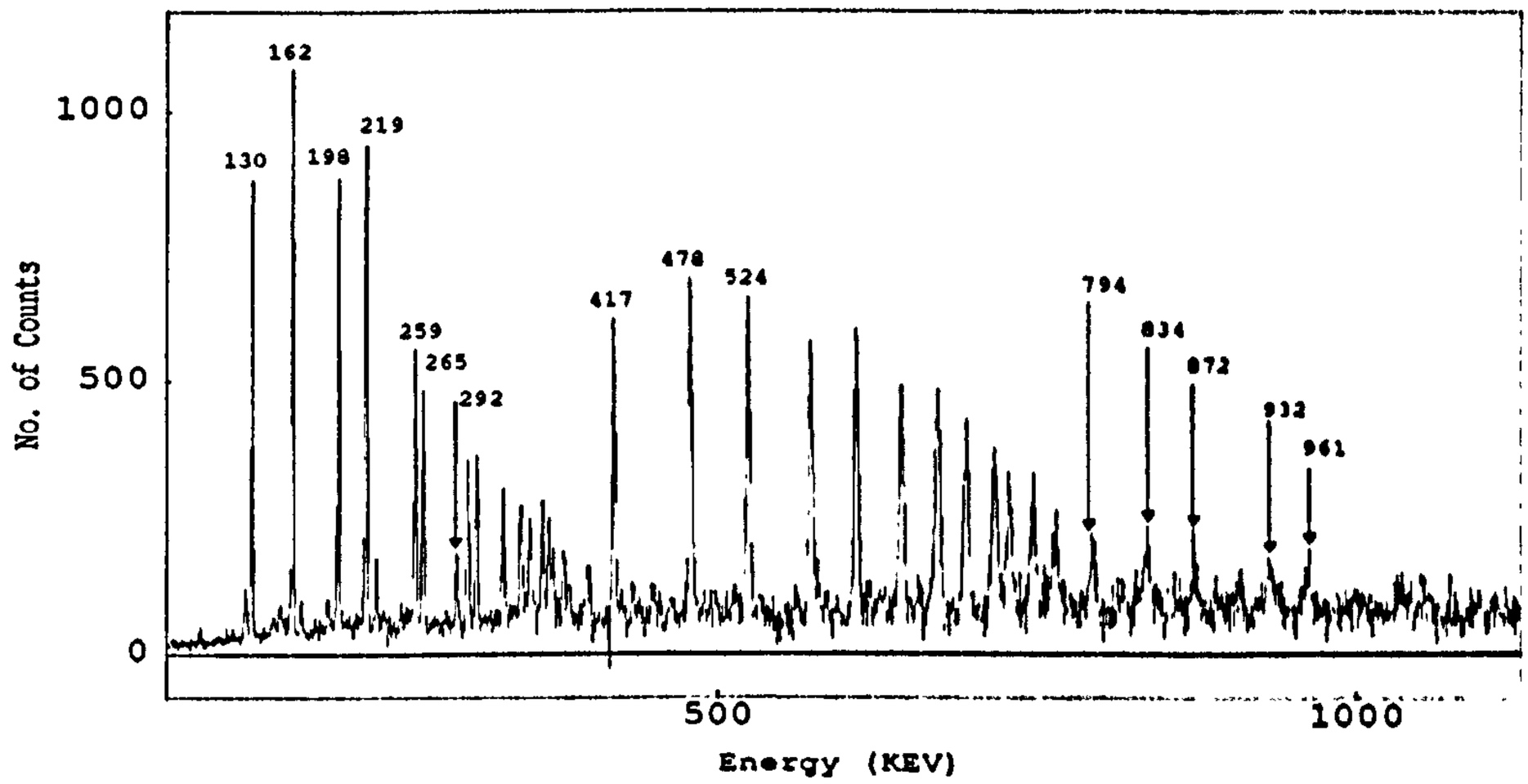

Figure 4.23: Sum of spectra in coincidence with the 130, 160 and 198 keV transitions linking Bands 1 and 2 from the RS data.

Bands 1 and 2 account for the majority of the decay intensity in ^{129}Nd and are strongly coupled by $\Delta J = 1$ transitions (see I(143)/I(101) ratios in Table 4.11). As can be seen in Figure 4.23 and Table 4.12 the band stretches to quite high excitation ($\sim$ 6 MeV) but the intensities of the higher transitions are too low to enable reliable placement.

E_{ex} (keV)	$E_\gamma(\Delta J=1)$ (keV)	I_γ (%)	$E_\gamma(\Delta J=2)$ (keV)	I_γ (%)	B(M1)/B(E2) $\mu_N^2(eb)^{-2}$
129.9	129.9(0.1)	100 ; 203			
191.8	161.9(0.1)	94(3) ; 147	292.0(0.2)	28(2) ; 30	1.25(6)[1], 1.00(2)[3]
389.8	198.0(0.1)	75(3) ; 91	360.0(0.1)	56(2)	0.76(2)[1], 0.77(3)[3]
609.4	219.6(0.2)	59(2) ; 68	417.8(0.1)	95(4)	0.57(2)[1], 0.59(2)[3]
868.0	258.6(0.2)	40(2) ; 44	478.3(0.1)	75(3)	0.55(2)[1], 0.64(3)[3]
1133.2	265.2(0.2)	30(2) ; 33	524.1(0.2)	84(4)	1.18(9)[1], 0.84(6)[3]
1441.0	307.8(0.3)	24(1) ; 25	573.0(0.2)	75(3)	0.52(4)[1], 0.62(4)[3]
1741.6	300.6(0.2)	21(1) ; 22	608.4(0.2)	64(3)	0.57(6)[1]
2084.9	343.3(0.3)	24(1)	643.9(0.4)	55(3)	0.65(4)[1], 0.8(1)
2413.9	329.0(0.2)	14(1)	671.6(0.5)	69(3)	0.35(3)[1]
2779.4	365.5(0.5)	20(4)	693.8(0.5)	50(3)	
3130	351.0(0.3)	20(1)	715.6(0.6)	51(3)	
3507	377.0(0.3)	10(1)	727.5(0.5)	42(3)	
3876	368.6(0.5)	8(2)	745.8(0.5)	35(2)	
4272	396(1)	10(2)	763.7(0.5)	22(2)	
5065			793.1(0.5)	18(2)	
—			835(1)	23(2)	
—			871(1)	8(1)	
—			931(1)	14(1)	
—			961(1)	>5	

Table 4.12: Energies and relative intensities for the transitions associated with bands 1 and 2 as shown in Figure 4.22. Energies are taken from the cleanest windows. Intensities were determined from efficiency corrected Z selected recoil-γ data where the peaks were distinct (ie below the 1441keV level) and from an efficiency corrected gate on the 130 keV transition in the RS data above this threshold normalised to the 162 keV intensity. The unassigned transition intensities were measured in a sum of gates. The 793 keV transition has been placed as it is by virtue of the broad appearance and 'higher than expected' intensity of the 396 keV transition pointing to the fact that it is probably a 395/398 doublet which would fit nicely with this placement of the 793 transition. The remaining higher energy transitions are too weak to be placed by coincidence requirements but would seem to be logical extensions to bands 1 and 2 as placed in the table. The large errors on the 366/369 energies are due to the non-separability of these transitions in any clean gate.

4.4.2 Bands 3 and 4

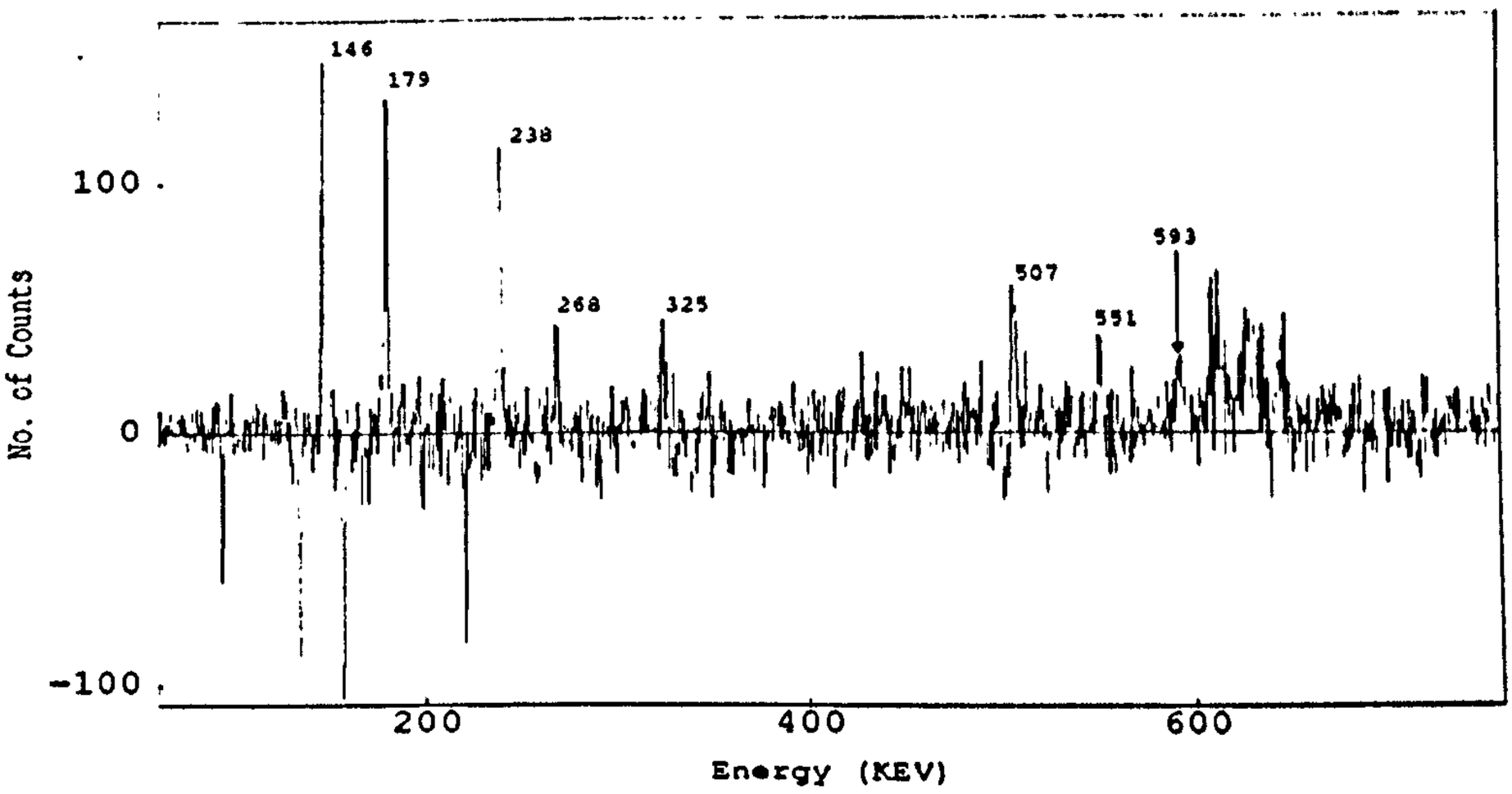

Figure 4.24: Spectrum from the RS data in coincidence with the 213 keV transition between Bands 3 and 4.

Bands 3 and 4 are, again strongly coupled but the intensity of the band is only 20% that of bands 1/2 as estimated from the Z-selected data. The only branching ratio estimable was that of the 325 keV level:

$$0.46(5)^{1} \quad 0.34(5)^{3} \quad \mu_N^2(eb)^{-2}$$

Due to the weakness of this band little else can be said.

E_{ex} (keV)	$E_\gamma(\Delta J = 1)$ (keV)	I_γ (%)	$E_\gamma(\Delta J = 2)$ (keV)	I_γ (%)
145.6	145.6(0.1)	—		
324.5	178.9(0.1)	100 ; 141	324.6(0.4)	—
538.0	213.5(0.2)	51(3) ; 60	392.3(0.2)	47(3)
776.7	238.7(0.3)	30(2) ; 34	452.1(0.2)	59(3)
1045.1	268.4(0.2)	26(2) ; 29	507.1(0.2)	51(4)
1327.4	282.3(0.3)	27(2)	551.0(0.3)	57(4)
1631	310.6(0.4)	13(1)	592.9(0.4)	48(3)
1942	303.5(0.5)	14(1)	615(1)	47(3)

Table 4.13: Energies and intensities for transitions associated with bands 3 and 4 as depicted in figure 4.22. Only the lower 3 transitions in the table are clearly visible in the Z-selected data. Of these, the 179 keV transition appears to be a doublet by virtue of its width so the only information this spectrum gives is that the 214 keV transition is seen at 70 % of the intensity of the 146 keV transition. The $\Delta J = 2$ transitions are visible as slight increases in the number of counts recorded at the appropriate energies, the 239 keV transition is seen but its intensity cannot be trusted due to the subtraction of the lowest transition in the intense yrast band of ^{129}Pr and the 268 keV is seen as a high energy shoulder on the 265 keV peak in Bands 1/2 in this nucleus. The association of this band with ^{129}Nd is thus not in doubt. The intensities given are those from the 146 keV gate in the RS data corrected for efficiency. They can be seen to be consistent with the structure deduced from these transitions.

4.4.3 Band 5

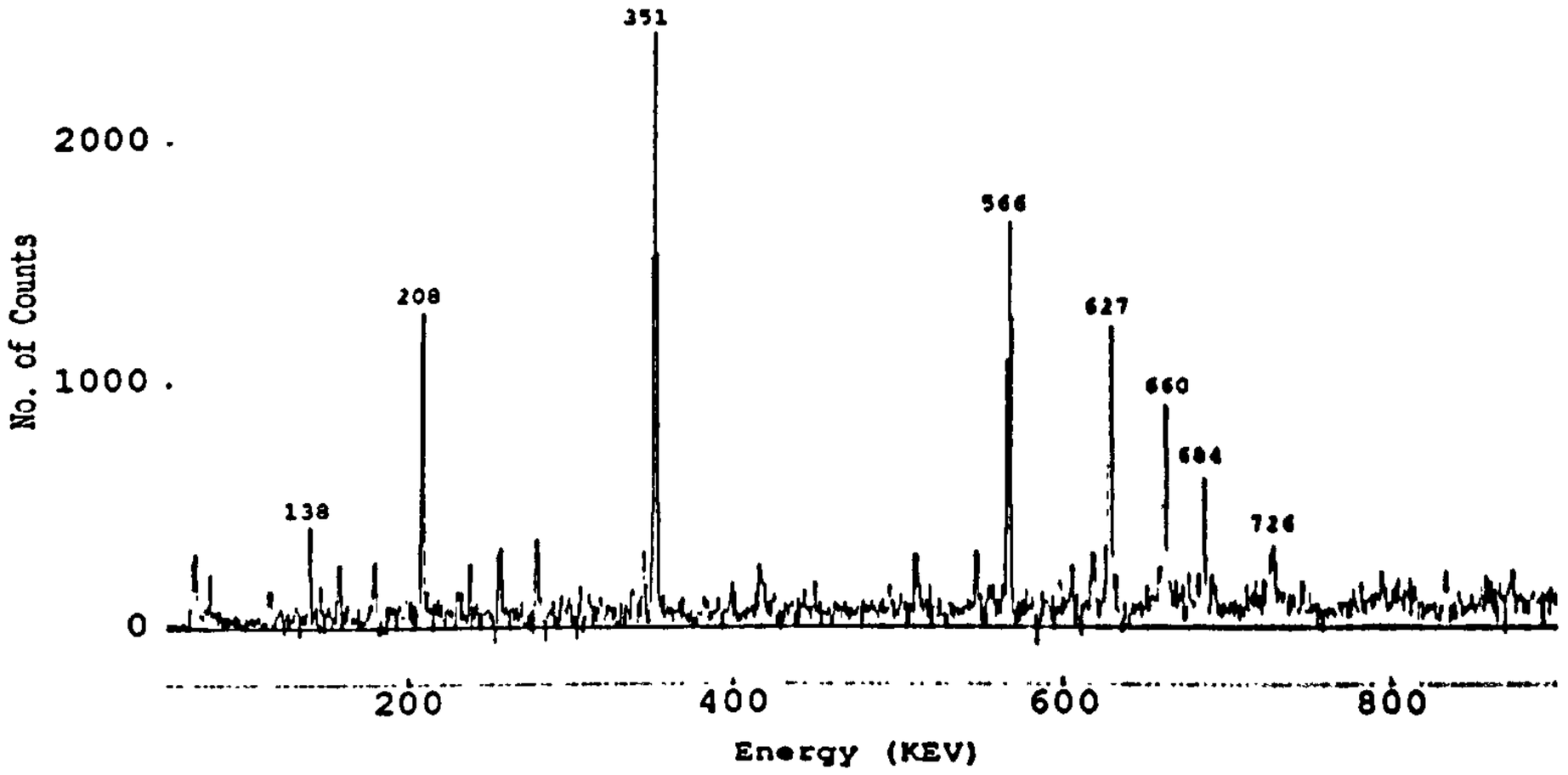

Figure 4.25: Efficiency corrected spectrum in coincidence with the 472 keV transition in Band 5.

Band 5 would appear to consist of a sequence of stretched $\Delta J = 2$ transitions and has an intensity of ~50% that of Bands 1/2 as seen in the RS data. The 208 keV transition is of lower intensity than the higher members of the band but can be placed at the base of the band by virtue of the smoothly decreasing intensities of the higher members in a spectrum in coincidence with this transition. The decreased intensity is explained, at least partially, by the 138 keV transition which depopulates the 208 keV level and exhibits the same intensity distribution as the 208 keV in its coincident spectrum.

E_{ex} (keV)	E_γ (keV)	I_γ %
207.9	138.4(0.1)	7(2) ; ~11
207.9	207.9(0.2)	71(4) ; 83
559.0	351.1(0.1)	100 ; 103
1031.1	472.1(0.1)	73(3)
1597.4	566.3(0.1)	64(3)
2224.6	627.2(0.2)	52(2)
2885.0	660.4(0.3)	33(2)
3570	684.5(0.5)	25(2)
4294	725.5(0.5)	19(2)

Table 4.14: Energies and relative intensities associated with band 5 in Figure 4.22. The relative intensities for the 138,351 and 472 keV transitions were determined from Z-selected RS data. The remaining intensities were measured from a spectrum in coincidence with the 351 keV transition from the ESSA-30 data and normalised to the intensity of the 472 keV transition. The intensity ratio between the 208 and 138 was found to be consistent in both the thin and backed target data. The 138 keV transition would be substantially converted but its multipolarity is dubious so no correction has been given, though for an E2 or M1 transition the total conversion coefficient would be of the order of 0.6. It would appear likely that the band is further extended by two further transitions with energies 793, 856 but the intensity of these transitions is too low to be certain.

4.4.4 Band 6

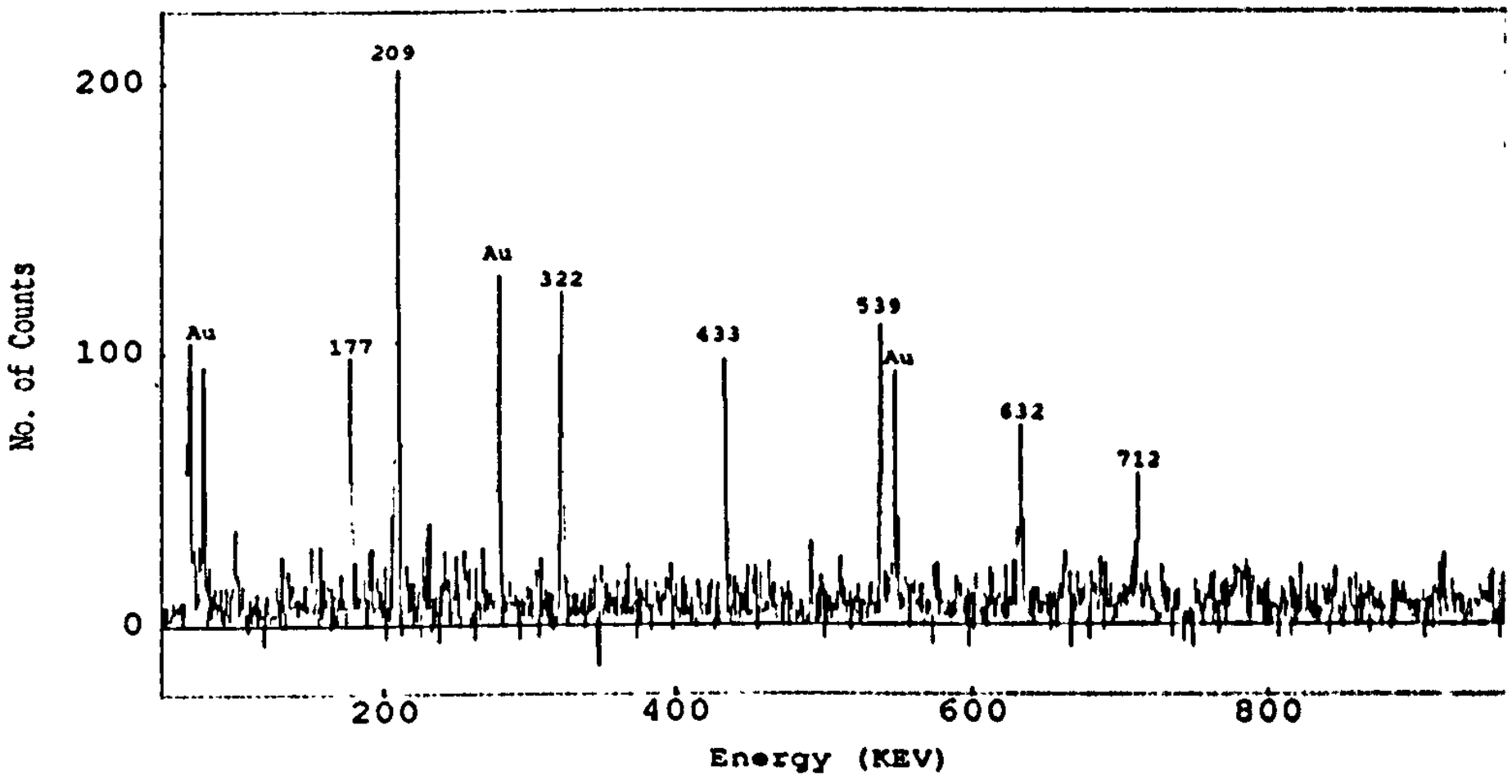

Figure 4.26: Summed spectra from ESSA-30 triples data in coincidence with transitions in Band 6. The spectra were projected from a matrix sorted with the requirement that the third transition satisfied windows on one of the 322, 433, 539 or 632 keV transitions. The strange intensity profile is due to this summation and sorting procedure. The 177 keV transition is consistently seen in all gates and is visible as a low energy tail on the 179 keV transition in the Z-selected spectrum.

Band 6 in ^{129}Nd has I(143)/I(101) ratios consistent with a series of $\Delta J = 2$ transitions. It is apparent that the bottom transition is of very similar energy tothat in Band 5. Distinction between the two transitions was further complicated by the fact that the 208 keV transition is the lowest member of the yrast band in ^{128}Ce and is present in ^{129}Pr. The transitions were finally and conclusively distinguished using triple events from the ESSA-30 data as detailed in Figure 4.26. There would appear to be a low energy (177 keV) transition associated with the band but its placement is uncertain.

E_{ex} (keV)	E_γ (keV)	I_γ %
209.3	209.3(0.1)	100 ; 118
531.0	321.7(0.2)	—
964.3	433.3(0.1)	79(2)
1502.9	538.6(0.1)	57(2)
2135.2	632.3(0.2)	40(2)
2845	712.5(0.5)	21(2)

Table 4.15: Energies and relative intensities associated with band 6 in Figure 4.22. As the 209,322 and 540 transitions all appear to be contaminated by doublets in the Z-selected data it was not possible to use this to measure the relative intensities. The intensities listed here are those observed in the 322 keV gate in an efficiency corrected gate from the ESSA-30 data.

4.5 ^{131}Nd

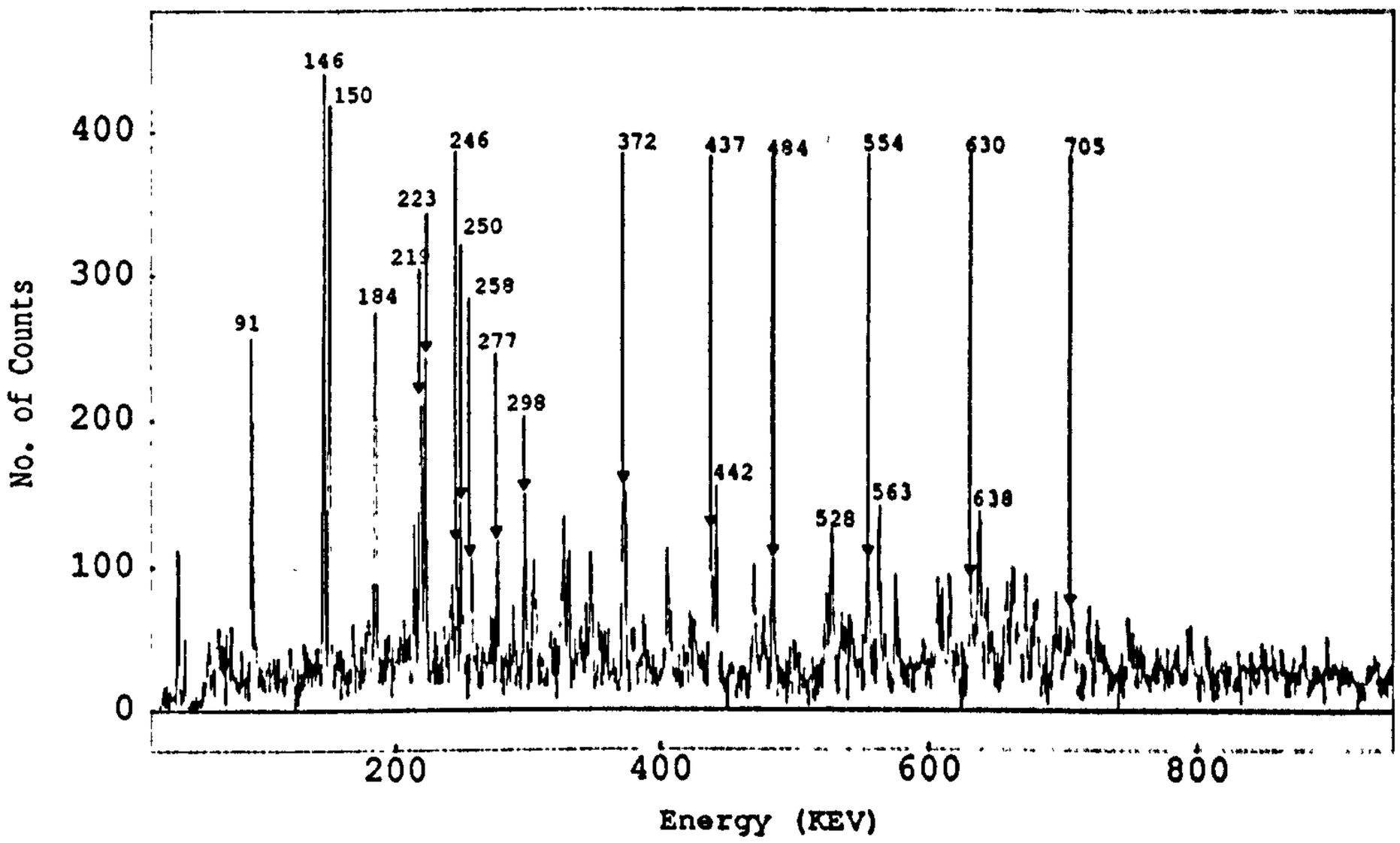

Figure 4.27: Z-selected spectrum of ^{131}Nd. Some of the principal γ transitions assigned to the following structures are indicated.

The mass 131 reactions were generally 'dirtier' than that producing the mass 129 products. The Z-selected spectrum for this nucleus is thus of poorer 'quality' so the assignment/existence of some of the weaker peaks to/in this nucleus is less certain. One of the main aims of the ESSA-30 experiment was to search for a possible super-deformed band. No evidence for such a band was found but, since the quality of the spectra was rather poor, it is not inconceivable that such a band was missed. If such a band does exist then it has an intensity <10% of the stronger structures.

E_γ (keV)	I_γ (%)	I(143)/I(101)	Assignment
92	53(5)	0.61(0.02)	2→1
95	12(8)		
146	100(5)	1.00(0.02)	4→3
150	100(5)	0.87(0.02)	1→2
167	9(2)		
179	20(4)		
185	63(3)	0.80(0.02)	3→4
214	28(4)		6
219	80(6)	0.75(0.02)	1→2,4→3
223	58(5)	0.74(0.02)	2→1
243	25(4)	1.24(0.05)	1
246	26(4)	1.53(0.06)	5
250	32(4)	0.89(0.02)	3→4
258	19(4)	0.70(0.03)	1→2
277	25(2)	0.79(0.03)	4→3
289	8(3)	0.75(0.04)	1→2
298	36(3)	1.04(0.03)	3→4
305	32(5)	0.68(0.02)	2→1
317	13(1)	0.79(0.04)	4→3
327	46(3)		3→4,6
331	31(2)	1.38(0.05)	3
348	30(2)	0.78(0.02)	2→1,1→2
373	63(6)	1.52(0.04)	5
380	17(2)		5→
387	14(2)		5→
406	42(4)	1.60(0.05)	4
427	34(3)		
438	46(4)	1.64(0.04)	5,6
442	44(4)	1.64(0.04)	1
470	40(3)	1.66(0.06)	3
478	25(3)		
485	31(3)	1.69(0.06)	5
524	29(3)	1.70(0.06)	
528	48(4)	1.80(0.05)	4
536	27(3)		
543	29(3)		6
555	35(3)	1.97(0.08)	5
563	45(4)	1.72(0.05)	1
576	30(3)	1.54(0.05)	3
607	31(3)	1.43(0.04)	2

E_γ(keV)	I_γ (%)	I(143)/I(101)	Assignment
610	27(3)		
616	32(3)	1.53(0.05)	4
632	40(4)	1.58(0.06)	5,6
638	62(6)	1.79(0.04)	1,2
643	43(4)	1.64(0.07)	3
658	34(4)		
663	48(5)	1.56(0.05)	4
673	24(4)	1.62(0.06)	1
679	35(6)	1.58(0.06)	2
696	38(8)		6
705	48(10)	1.98(0.09)	5
795	18(10)		6

Table 4.16: Transitions observed in a Z-selected spectrum for ^{131}Nd. The assignments refer to bands in ^{131}Nd as labelled in figure 4.28 and the intensities are not efficiency corrected.

Figure 4.28: Decay Scheme for ^{131}Nd

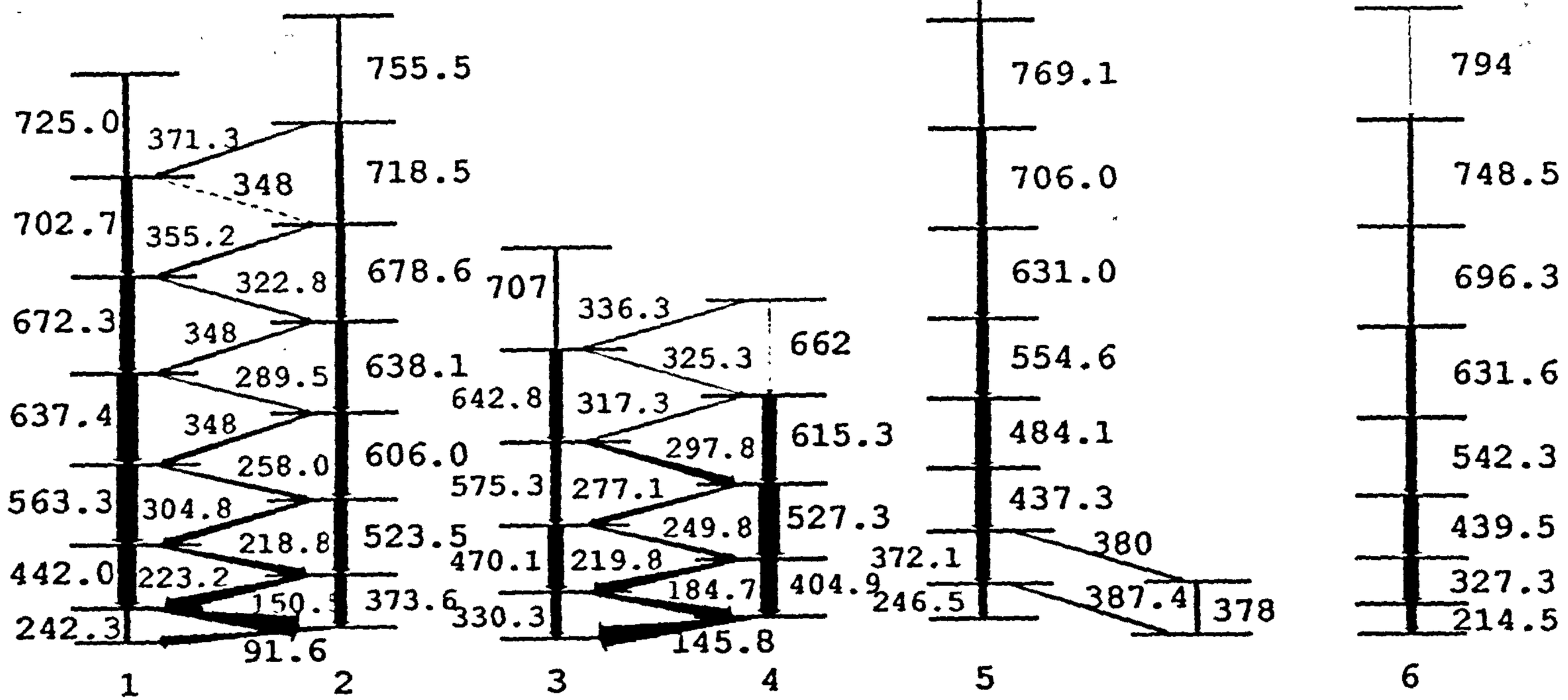

4.5.1 Bands 1 and 2

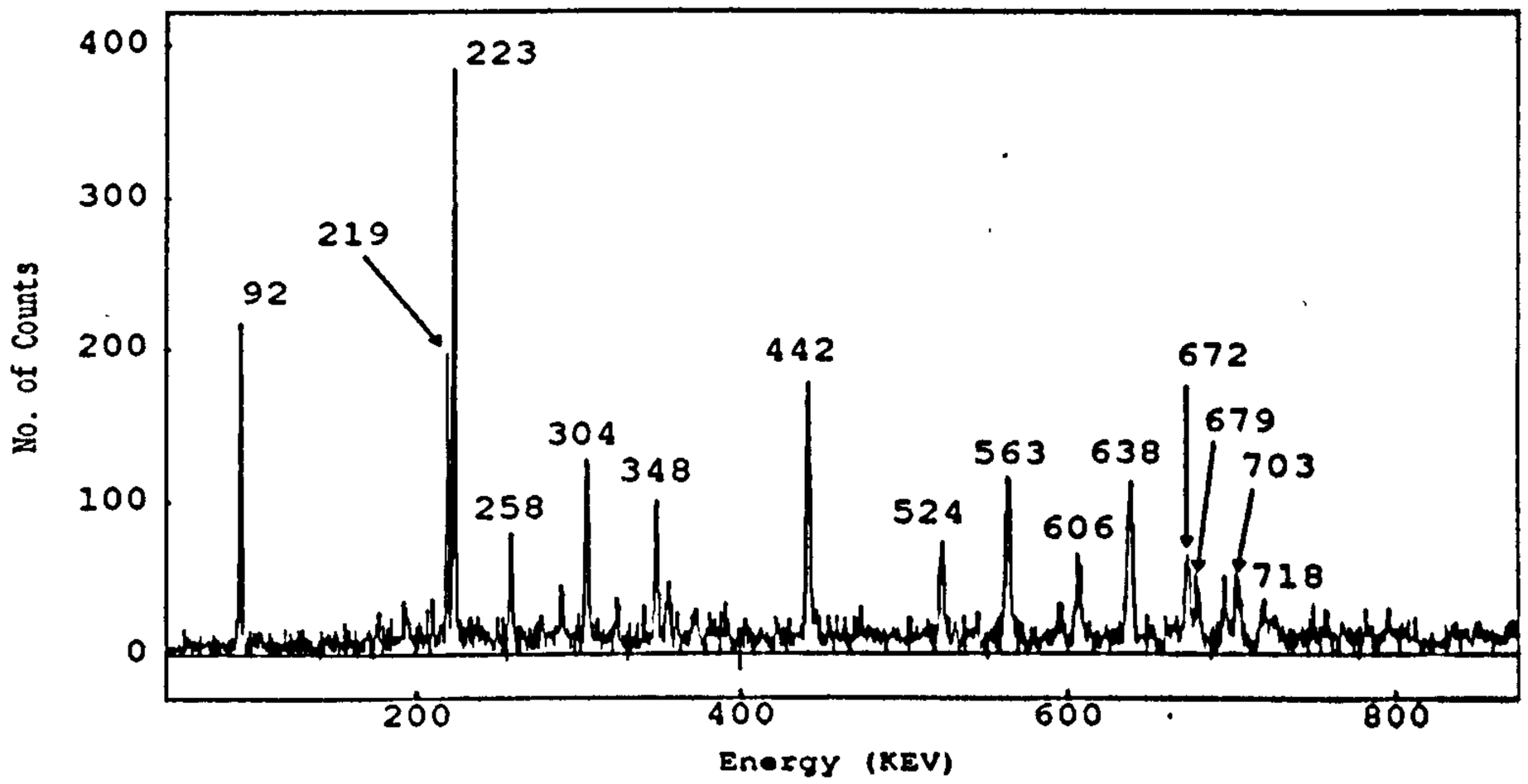

Figure 4.29: Spectrum in coincidence with the 151 keV transition between Bands 1/2. Note the strong appearance of the 348 and 638 keV transitions supporting the pair of doublets proposed in the decay scheme in Figure 4.28.The 696 keV transition mentioned in Table 4.17 can be seen as the unlabelled peak to the left of the 703 keV transition. The spectrum was taken from the RS data.

The decay scheme for Bands 1/2 in Figure 4.28 seems at first sight rather dubious due to the assumption of a doublet (638 keV) and a triplet (348 keV) of transitions. The intensity and coincidence relationships observed leave little doubt as to the correctness of the 637/8 keV doublet. There is insufficient data to confirm the existence of the 348 triplet although at least a doublet is required to explain the intensity of the peak. This quirk of the decay scheme meant that some of the branching ratios were inaccessible from this data.

E_{ex} (keV)	$E_\gamma(\Delta J = 1)$ (keV)	I_γ (%)	$E_\gamma(\Delta J = 2)$ (keV)	I_γ (%)	B(M1)/B(E2) $\mu_N^2(eb)^{-2}$
91.6	91.6(0.3)	45(2) ; 126			
242.1	150.5(0.1)	100 ; 150	242.3(0.3)	23(2) ; 26	0.81(6)[1], 0.93(6)[3], 0.86(6)[4]
465.3	223.2(0.2)	66(3) ; 77	373.6(0.2)	48(4)	0.63(3)[3], 0.84(2)[4]
684.1	218.8(0.1)	43(7) ; 50	442.0(0.1)	76(4)	0.64(3)[3], 0.98(3)[4]
988.8	304.8(0.2)	41(3) ; 44	523.5(0.1)	55(4)	0.45(3)[3], 0.69(3)[4]
1247.4	258.0(0.2)	21(2) ; 23	563.3(0.1)	89(5)	0.53(3)[1], 0.56(4)[3], 0.92(5)[4]
1594.8	348	*46 ; 48	606.0(0.3)	52(4)	
1884.8	289.5(0.3)	9(2)	637.4(0.4)	*135	0.62(9)[3], 0.91(9)
2232.9	348	*46	638.1(0.2)	*135	
2557.5	322.8(0.4)	9(2)	672.3(0.2)	56(5)	
2911.5	355.2(0.3)	17(3)	678.6(0.3)	35(4)	
3260	348	*46	702.7(0.3)	44(5)	
3630	371.3(0.5)	13(3)	718.5(0.3)	29(6)	
3985			725.0(0.5)	22(5)	
4386			755.5(0.5)	12(4)	
—			696		

Table 4.17: Energies and relative intensities for Bands 1 and 2 as shown in Figure 4.28. Energies are given relative to the lowest state observed. Intensities are taken from an efficiency corrected Z-selected spectrum for transitions feeding out from levels below the 2558 keV level. Above this the intensities are taken from a sum of gates on the 150 and 223 keV transitions normalised to the 305 keV intensity. The intensities of the 219 and 374 keV transitions were not obtainable from the Z-selected spectrum due to contamination from transitions in bands 3/4 and 5 respectively. Their intensities are thus estimated from the branching ratios of in-band/out-of-band transition strengths from transitions above. The intensities marked '*' are total intensities at that energy observed in the Z-selected data for which it is not possible to elucidate an estimate of the individual intensity due to the structure of the decay scheme. The 696 keV transition is included in this table as it would appear to be seen in coincidence with all the lower transitions in bands 1/2 but its placement is not clear.

4.5.2 Bands 3 and 4

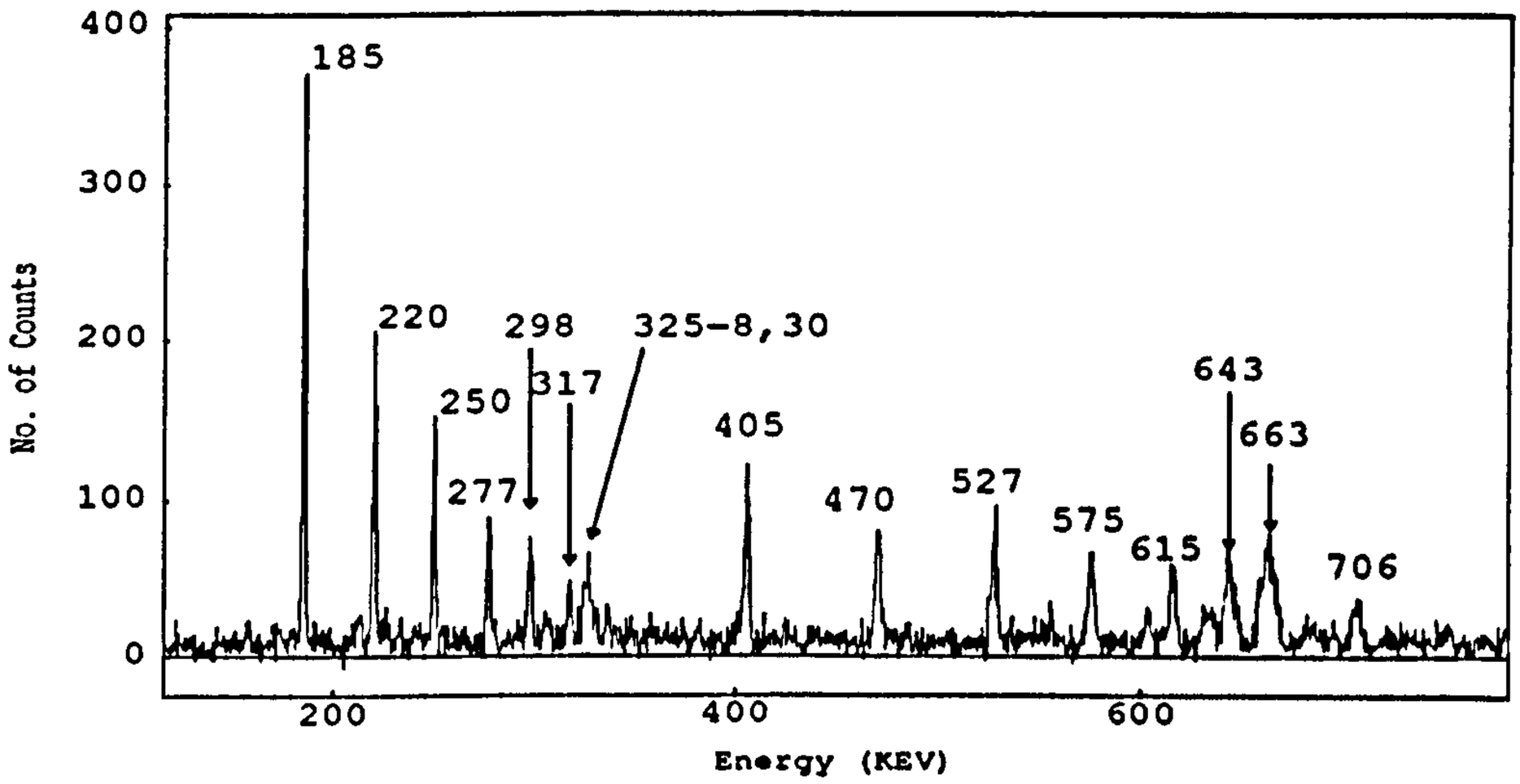

Figure 4.30: Spectrum in coincidence with the 146 keV transition between Bands 3 and 4 from the RS data. The width and strength of the 663 keV transition is apparent as is the confused doublet/triplet of transitions around 327 keV .

Bands 3/4 are strongly coupled via $\Delta J = 1$ transitions. The intensity of this structure is comparable to that of Bands 1/2 but the intensity appears to die out more rapidly with increasing spin. The precise structure at the highest excitations visible is uncertain but it does appear that there is a 663 keV doublet since both the 615 and 643 keV transitions are in coincidence with it. There is a weak 376 keV transition seen in some of the gates on higher members of the bands and as seen in Figure 4.29 there is a triplet 325-8 ,330 which could plausibly form a 325, 336, 328, 330, 376 keV sequence and both explain a 661/663 doublet and fit the 706 into Band 2. The 330 keV transition seen in the 146 keV gate is not that in Band 1 since it would not be in coincidence with this transition.

E_{ex} (keV)	$E_\gamma(\Delta J=1)$ (keV)	I_γ (%)	$E_\gamma(\Delta J=2)$ (keV)	I_γ (%)	B(M1)/B(E2) $\mu_N^2(eb)^{-2}$
145.8	145.8(0.1)	100 ; 172			
330.5	184.7(0.1)	63(3) ; 86	330.3(0.2)	—	0.65(5)[1], 0.90(6)[3]
550.3	219.8(0.1)	55(6) ; 64	404.9(0.2)	68(4)	0.58(3)[3]
800.1	249.8(0.1)	27(2) ; 30 ; 31	470.1(0.2)	63(4)	0.49(4)[1]
1077.2	277.1(0.2)	30(2)	527.3(0.3)	83(5)	0.44(4)[1], 0.27(2)[3]
1375.0	297.8(0.2)	44(3)	575.3(0.3)	44(3)	0.50(6)[3]
1692	317.3(0.3)	11(1)	615.3(0.3)	56(4)	0.42(6)[1]
2108	325.3(0.5)	—	642.8(0.5)	54(6)	
2355	336.3(0.5)	6(1)	663(1)	110(10)	
3056			706.5(0.5)	14(3)	

Table 4.18: Energies and relative intensities for Bands 3 and 4 as shown in Figure 4.28. Energies are given relative to the lowest state observed. Intensities are taken from an efficiency corrected Z-selected spectrum for transitions feeding from levels below the 2108 keV level and from a sum of gates on the 146,185 keV transitions for transitions above this. These latter intensities were normalised according to the intensity of the 250 keV transition. The 220 keV transition intensity was obtained from the 405 intensity and the observed branching ratio between the two γ-rays since the Z-selected peak was contaminated by one of similar energy in Bands 1/2. No intensity is given for the 325/330 transitions since they would appear to be part of an unresolved and complex multiplet.

4.5.3 Band 5

Band 5 is a sequence of $\Delta J = 2$ transitions stretching to the highest spins observed in this nucleus. The band de-populates at the bottom via two transitions but no connection between it or the states it feeds has been made with the other levels observed. The band is quite intense, being of the order of 60% of that seen in the lowest transitions seen in Bands 1/2 and 3/4.

E_{ex} (keV)	E_γ (keV)	$I_\gamma(246)$ (%)	$I_\gamma(484)$ (%)
387.4	246.5(0.2)	—	50(1)
759.5	372.1(0.1)	100	85(1)
1196.8	437.3(0.1)	81(5)	100
1680.9	484.1(0.1)	71(5)	—
2235.5	554.6(0.2)	58(4)	75(1)
2866.5	631.0(0.2)	57(4)	69(1)
3572.5	706.0(0.3)	48(4)	54(1)
4342	769.1(0.3)	21(3)	32(1)
—	791.5(0.5)		14(1)
—	818(1)		16(1)
—	852(1)		13(2)
387.4	387.4(0.1)	0	23(1)
759.5/378.3	378.3(0.5)	0	39
759.5/380.7	380.7(0.5)	0	39

Table 4.19: Energies and intensities of the transitions associated with Band 5 in Figure 4.28. The intensities were measured from the RS data (246) and ESSA-30 data (484) as in spectra gated by the transitions detailed in the table headings. The intensities measured in the 484 keV window are consistent with the feeding out of the bottom of band 6 via the 378/380 and 387 keV transitions listed at the end of the table. The energies of the 378 and 380 keV transitions were obtained by fitting two Gaussians to the doublet in spectra gated on transitions feeding into the 760 keV level. Neither set of data enabled the transitions in the doublet to be ordered. The transitions included without excitation energies appear consistently to be associated with Band 6 but are too weak to be placed by means of coincidence relationships. It would appear likely that the 818 keV transition is an extension to the band at least

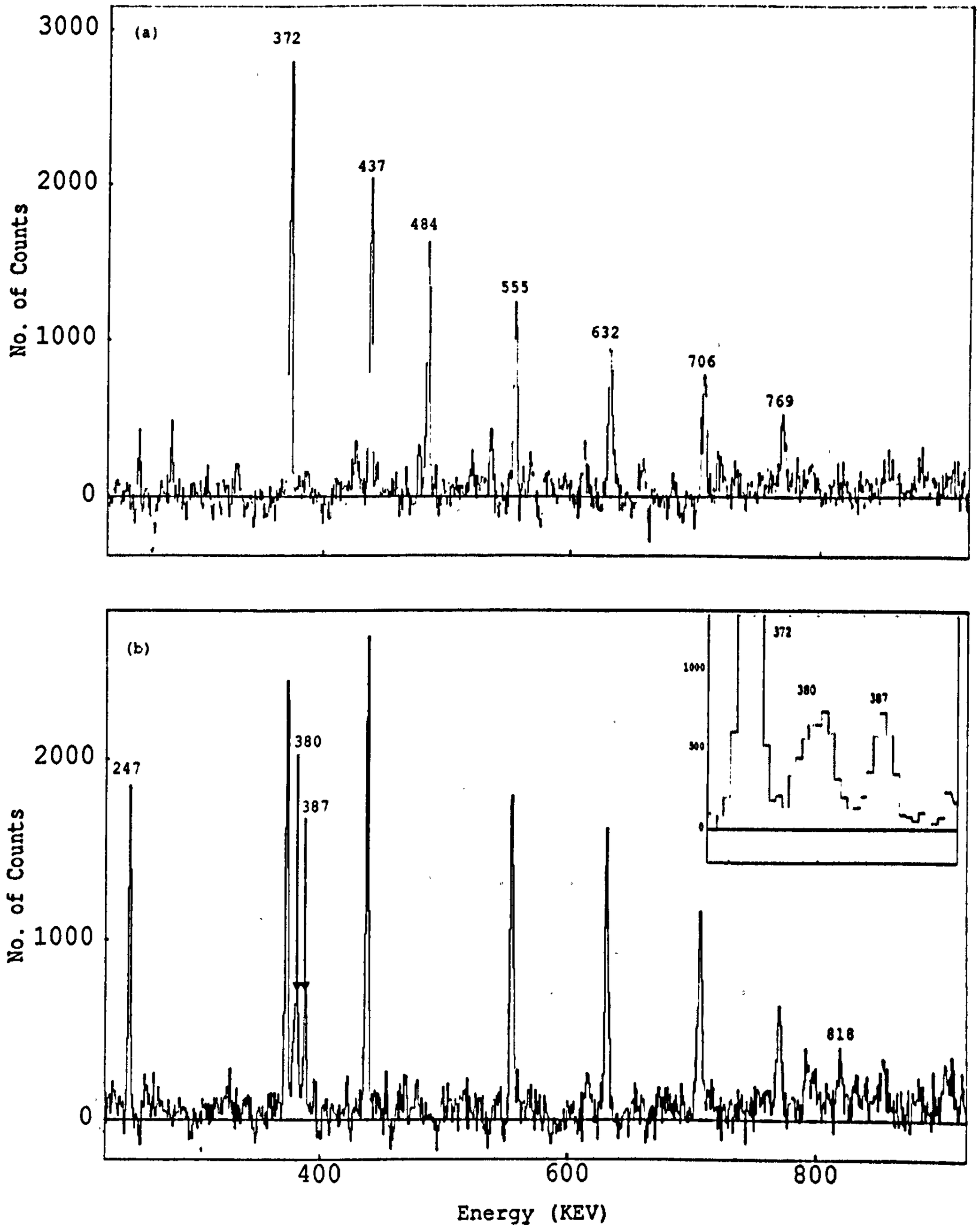

Figure 4.31: Efficiency corrected spectra taken from the ESSA-30 data in coincidence with the 246 (a) and 484 keV (b) transitions. The smooth decrease in intensity in (a) points to the fact that the transitions all belong to the same band. The drop in intensity observed for the lower transitions in (b) corresponds nicely with the 380 and 387 keV transitions depopulating Band 5 before the bandhead is reached. Note the broad appearance of the 380 keV peak (*see inset*) indicating that it is a doublet. A spectrum in coincidence with this peak does indeed show itself and the rest of Band 5 above the 372 keV transition but is highly contaminated.

4.5.4 Band 6

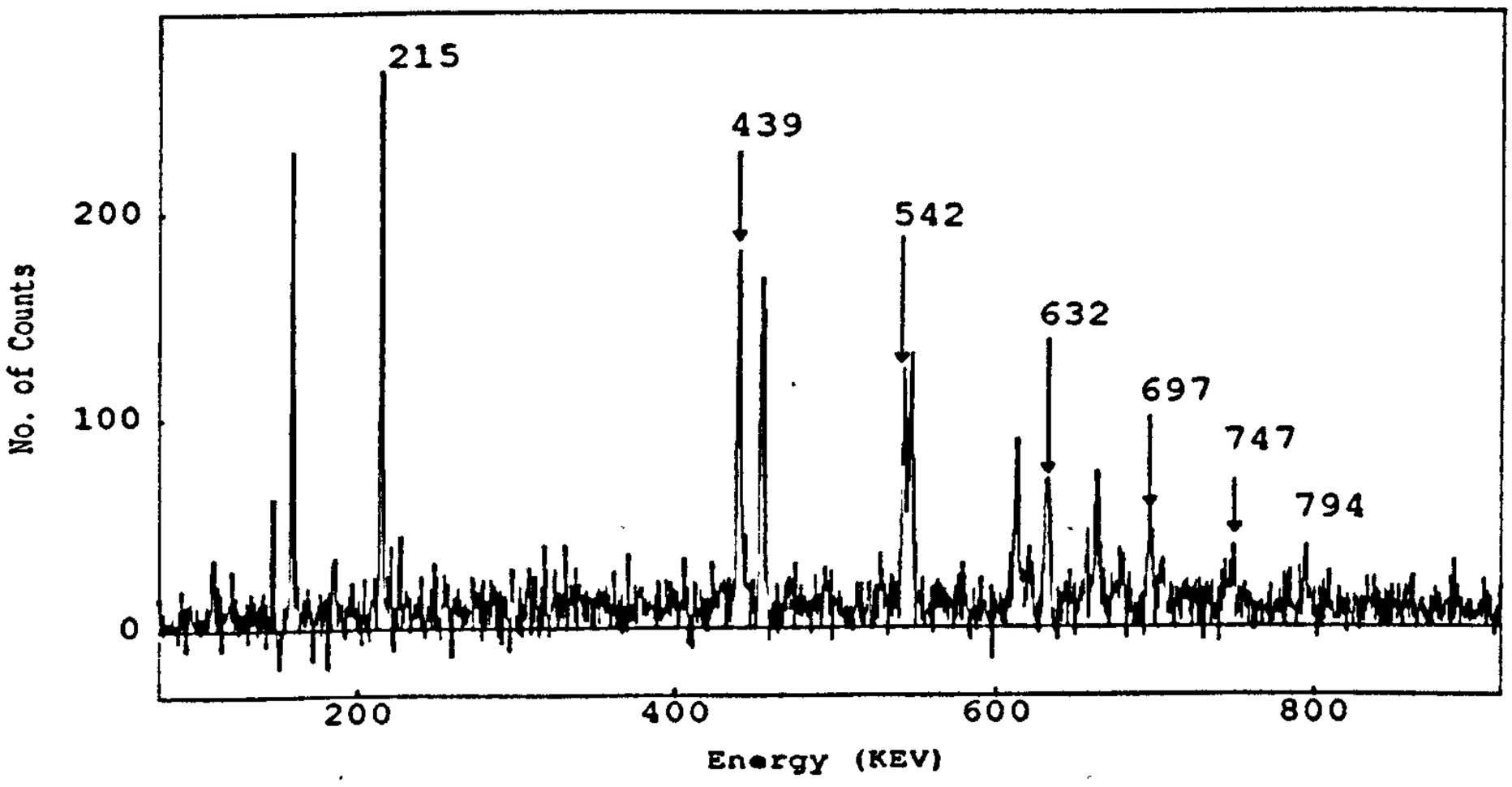

Figure 4.32: Spectrum in coincidence with the 327 keV transition identified with Band 6. The secondary band seen in this gate is the yrast band of ^{130}Nd which has a $4^+ \rightarrow 2^+$ transition of similar energy.

Band 6 is a sequence of $\Delta J = 2$ transitions of slightly lower intensity ($\sim 50\%$ compared to Bands 1/2 or 3/4) than Band 5. Again it has not been possible to establish any link between this and the other structures observed. The 214 keV transition is placed below the other transitions ascribed to the band despite its comparative weakness because it is in coincidence with the remaining transitions decrease in intensity up the band in a spectrum gated on the 214 keV transition as would be expected if the band as deduced feeds through this transition.

E_{ex} (keV)	E_γ (keV)	$I_\gamma(631)$ (%)	$I_\gamma(327)$ (%)
214.5	214.5(0.1)	40(3) ; 49	63(3)
541.8	327.3(0.1)	100	—
981.3	439.5(0.1)	*137(8)	100
1523.6	542.3(0.2)	95(7)	74(4)
2155.2	631.6(0.3)	—	61(3)
2851	696.3(0.5)	76(6)	36(3)
—	747(1)	52(5)	29(2)
—	794(1)	57(5)	—

Table 4.20: Energies and intensities of the transitions associated with Band 6 in Figure 4.28. The intensities were measured from the gates shown in the table headings in the RS data. The peaks in the Z-selected data were generally too contaminated to obtain any reliable estimates of relative intensity although this data does concur with the fact that the 214 keV transition is substantially weaker (54 %) than the 327 and that there must be some unobserved feeding from the 542 keV level. The intensity of the 440 keV transition in the 631 keV window is high but this is consistent with the 438/630 keV transitions proposed in band 5 and with the fact that the 438-440 keV peak in the Z-selected spectrum has twice the intensity of the 327 keV data. The positioning of the final two transitions is uncertain though it seems likely that they sit above the 2851 keV level in the order shown.

Chapter 5

Interpretation and Discussion

5.1 Comparison with CSM predictions

5.1.1 CSM calculations

In order to aid the interpretation of the data CSM calculations have been performed using the code QPLG [FM83]. The code generates quasiparticle levels as a function of ω for fixed field parameters or as a function of one of the field parameters at a fixed rotational frequency. This allows examination of the shape driving forces associated with the various orbitals. The strength of such forces varies with the position of the Fermi surface. Rules predicting the magnitude and direction of such forces have been extracted for the γ [LFM82] and the ϵ_2 degree of freedom [CL86].

In the calculations presented in Figure 5.1 the field parameter ϵ_2 was set according to the shapes predicted from the TRS calculations. These are parameterised in terms of β_2, β_4 so an exact match was not possible since the conversion between the two involves a power series expansion. The ϵ_4 parameter was set to $\epsilon_2^2/6$ which is the preferred liquid drop value and the triaxiality parameter γ was set at 0°, i.e. only prolate axial shapes were considered. This would seem reasonable since the experimental systematics and the TRS calculations indicate that the shapes are becoming increasingly rigid and axially deformed as nuclei depart from the valley of stability. The proton pair gap parameter was reduced from the 1.2 MeV used in the even Ce region in an attempt to reproduce the observed crossing frequencies. A decrease in ϵ_2 also decreases the crossing frequencies and could be used to explain the observed crossing frequencies but this would contradict the increase in deformation noted in section 5.2. Such calculations are useful for a qualitative explanation of the data but believable quantitative predictions are difficult to obtain due to the uncertainties as to the values of the field parameters and, indeed, the parameters determining the single particle levels. The calculations are thus expected to be appropriate but not directly predictive. The parameters were varied in order to ascertain the effects of each on the quasiparticle levels.

For the proton diagrams deformations much beyond $\epsilon_2 \sim 0.3$ required the

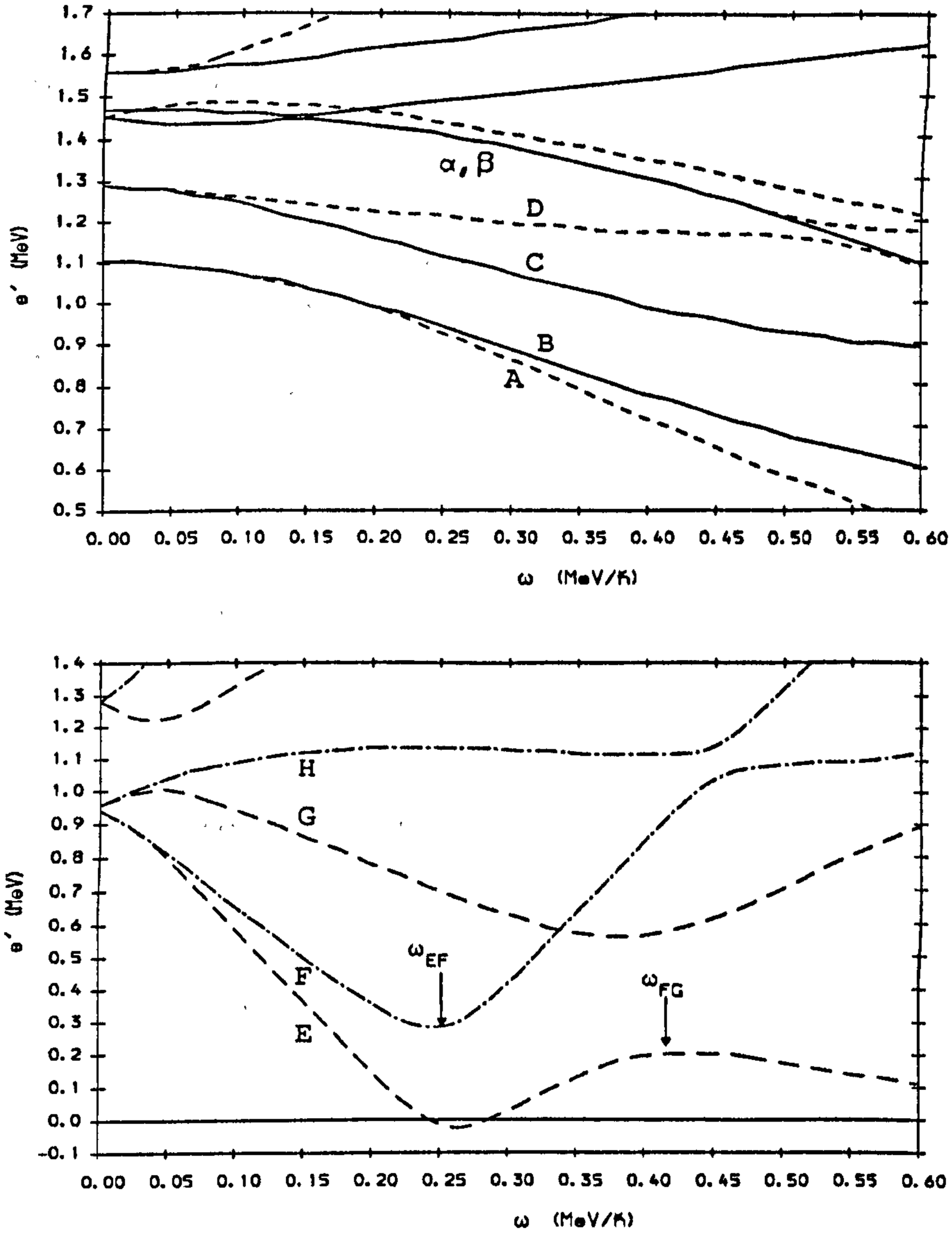

Figure 5.1: CSM predictions for the positve (*top*) and negative (*bottom*) parity proton levels in ^{129}Pr. The field parameters assumed were $\gamma = 0°$, $\epsilon_2 = 0.27$, $\epsilon_4 = 0.12$ and $\Delta = 0.8$ and the basis levels were calculated using the κ, μ values of[BR85] for shells 3 to 5. The signature/parity convention used in this and following diagrams is:

	(π, α)
solid	$(+,+)$
short dashed	$(+,-)$
dashed	$(-,-)$
chained	$(-,+)$

pairing parameter to be dropped to an unreasonably small value to achieve any degree of fit to the FG proton crossing frequency. The combined effect of reducing the pairing parameter and increasing the deformation is to increase the interaction at the FG crossing. A moderate variation in γ did little to change the negative parity proton levels.

A calculation of the neutron quasiparticle levels as a function of triaxiality at a fixed frequency is included in Figure 5.2. This illustrates the different shape driving forces possessed by different orbitals with respect to the triaxial degree of freedom. The ef orbital is observed to have a pronounced minimum at $\gamma \sim -50°$ and will thus tend to cause a polarisation of the nuclear core towards this deformation whilst the lowest (ab) positive parity orbitals are relatively insensitive to γ and thus exert little influence on the core in this degree of freedom. Note that this driving force is to be added to the core 'polarisability' in order to determine the equilibrium shape of the nucleus. Thus an upper mid-shell h11/2 neutron will not cause the field to possess significant triaxiality unless the core is soft with respect to such a deformation and the overall change in shape is energetically favourable.

It is also informative to look at the quasiparticle levels as a function of the quadrupole deformation. This is done in the diagrams presented in Figure 5.3. It is noted from the proton diagram that there is a positive parity orbital with a large equilibrium deformation which is caused by the g9/2 $\Omega = 9/2$ state which rises sharply from below the Fermi surface at Z~60 in the Nilsson diagram. The corresponding neutron diagram shows two orbitals descending rapidly at large deformations which can be associated with the i13/2 and h9/2 shells. The h9/2 level has a lower equilibrium deformation and approaches yrast behaviour for a deformation of around $\epsilon_2 \sim 0.3$. Again, the shape driving forces, must be balanced against the softness of the core with respect to quadrupole deformation.

5.1.2 The Reference Concept

The simplicity of the CSM is due to the adopted ideal of calculating all states with one set of field parameters $(\epsilon_2, \epsilon_4, \lambda, \Delta, \gamma)$. As with all shell models,the CSM does not calculate absolute excitations, only excitation spectra relative to a reference configuration. In order to compare experimental data with CSM predictions the reference behaviour must be subtracted from the data. The reference should attempt to satisfy the following three criteria [BFM86]

i the average field parameters and the collective rotational energy should be the same for reference and excited configurations since the addition of CSM quantities is only ensured if the average field is configuration independent and the collective rotational behaviour remains the same in excited states.

ii the reference should be yrast so as to ensure that the reference is well defined experimentally.

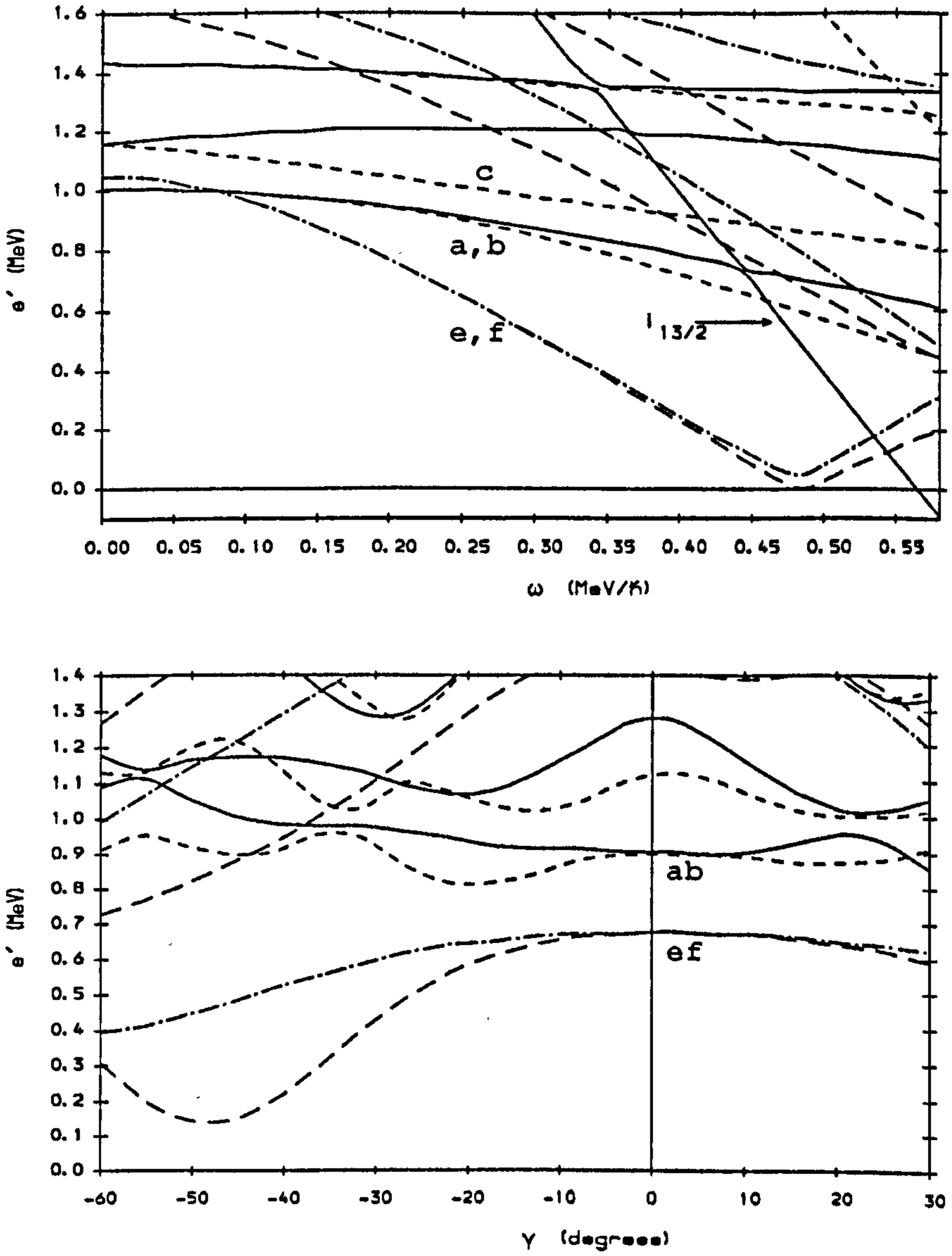

Figure 5.2: CSM predictions for the neutron levels in ^{129}Nd. The field parameters assumed for the calculation as a function of frequency (*top*) were the same as those for Figure 5.1 except that Δ was set to 1.0 MeV and the basis levels were calculated for shells 4 to 6. The calculation as a function of triaxiality (*bottom*) was performed at a frequency $\hbar\omega$ =0.2 MeV and the other paramaters held constant at the same values as above.

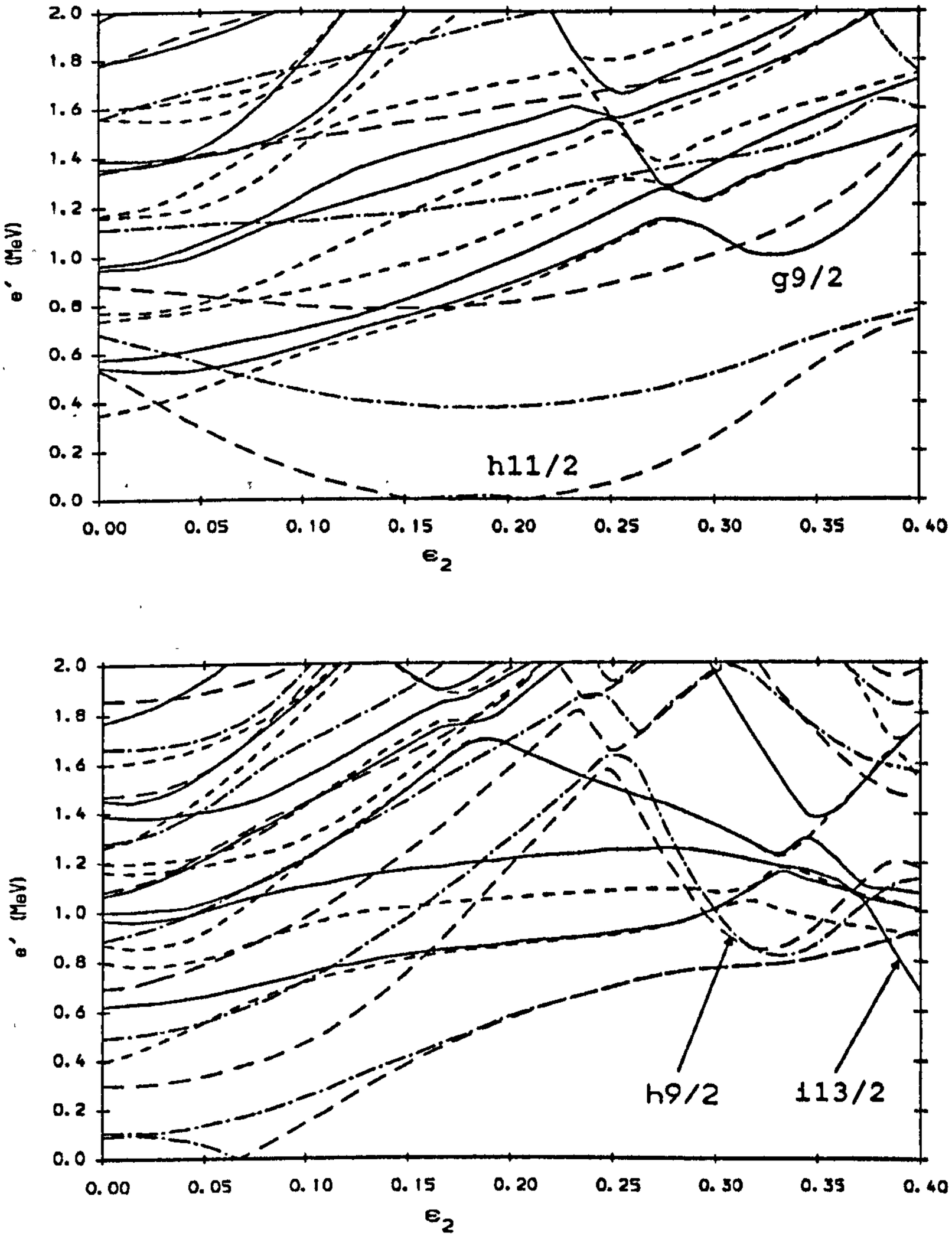

Figure 5.3: CSM predictions for the proton *top* and neutron *bottom* levels appropriate to ^{129}Pr and ^{131}Nd respectively as a function of the quadrupole deformation. The levels were calculated at a frequency $\hbar\omega$ =0.2 MeV with $\epsilon_4 = 0.015$ and $\gamma = 0.0$.

iii the reference should behave smoothly with ω. A rotational band is interpreted as a sequence of states where intrinsic structure varies slowly with ω and is associated with a quasiparticle configuration. It is desirable to refer all quantities to one band as a reference consisting of intersecting bands will cause irregularities at the intersection frequency in bands that are 'regular' at this frequency.

In real nuclei the extent to which (i) is fulfilled depends on the nucleus whilst (i) and (iii) to some extent conflict since the yrast line of deformed nuclei contains crossings and is hence irregular. The optimal reference tries to satisfy all three points to some extent. Some possibilities are enumerated below.

a Yrast reference - configuration with all quasiparticle levels with $e'(\omega) < 0$ occupied.

b G-reference - configuration with all diabatic quasiparticle levels $e'(\omega = 0) < 0$ filled.

c S-reference - configuration with the two diabatic quasiparticle levels which give rise to the S-band (above the first backbend) occupied.

d adapted G-reference - uses the G configuration as the zero quasiparticle state and bands with one or more excited quasiparticles to parameterise the reference functions.

By definition (a) fulfils criterion (ii) and is a good reference for nuclei with a gradually changing yrast line. For backbending nuclei references (b)- (d) are preferable though the yrast reference does produce a good general reference. The G-reference is a good reference up to the first backbend ($\omega < \omega_c$) and for strongly deformed nuclei ($\epsilon_2 \geq 0.23$). The S-reference is complementary to the G-reference for $\omega \geq \omega_c$ and is useful for analysing bands with strongly aligning quasiparticles. The adapted G-reference fit is favoured for strongly aligned configurations and low deformation. It is equivalent to the S-reference except that it does not include the contribution of the aligning particles in the reference function. It has been noted [Ki86] that the adapted G-reference produced more systematic behaviour of data than the G-reference in the ^{130}Ce region. This is probably due to the G-band being relatively 'soft' so that criterion (i) is violated; after the backbend the structure 'hardens' and this reference is preferred as it is more stable.

Within the CSM the vacuum configuration for an odd nucleus is found to be an admixture of wavefunctions from the (A+1) and (A-1) nuclei. This would tend to suggest that an appropriate reference for an odd nucleus would be some form of average between the neighbouring even-even nuclei. Thus for the nuclei discussed here we would use some averaged parameterization of the Nd and Ce isotones for odd-A Pr nuclei and an average of neighbouring Nd nuclei for the odd-Nd nuclei.

The even-even Nd nuclei are observed to exhibit strong interactions between the S and G bands. The G reference would thus violate criterion (iii) in that

the configuration is constantly changing. The S bands in these nuclei are not observed to high enough spins for the bands to attain a stable character so it was not possible to extract a meaningful reference for these nuclei. The yrast bands in the Ce nuclei, on the other hand, are known to spins above the first band crossing. In this work the adapted G-reference for the Ce isotone is thus used. The reference was obtained by fitting the observed alignment to a Harris [H65] type formula for the states above the first crossing:

$$i_x = i_o + \omega(\mathcal{J}_0 + \omega^2 \mathcal{J}_1)$$

The resulting references are given in Table 5.1.

Reference Nucleus	$\mathcal{J}_0$ $(\hbar^2 MeV^{-1})$	$\mathcal{J}_1$ $(\hbar^4 MeV^{-3})$
^{128}Ce	22.3	14.7
^{130}Ce	17.0	25.8
^{132}Ce	13.2	40.3

Table 5.1: Harris parameters used in references in this work. Note that the parameters obtained seem to concur with the $E_{4_1^+}/E_{2_1^+}$ ratios in that they imply the nuclei are becoming more rigid with decreasing neutron number as evidenced by the decreasing value of the $\mathcal{J}_1$ term.

5.1.3 Routhian Plots

In order to compare the experimental energy levels with the CSM predictions they must be transformed. The transformation applied is equivalent to the classical coordinate transformation into a system rotating at frequency ω. The classical transformed energies are termed Routhians and the terminology is carried over into CSM. The experimental Routhian is constructed from the experimental excitation energies (E_{ex}) as :

$$\begin{aligned} E' &= E_{ex} - \omega I_x \qquad (5.1) \\ &= \frac{1}{2}(E_i + E_f) - \omega(\bar{I}) I_x(\bar{I}); \end{aligned}$$

$$\bar{I} = \frac{1}{2}(I_i + I_f) \qquad (5.2)$$

The reference behaviour is then subtracted from this to give the excitation relative to the reference configuration which should be directly comparable to quasiparticle energy levels. If the reference is paramaterised using the Harris parameters for the moment of inertia the reference energy at a particular frequency

is:

$$E'_{REF} = -\int_0^{\omega} \omega' I_{x_{REF}}(\omega') d\omega' \qquad (5.3)$$
$$= -\frac{\omega^2}{2}\mathcal{J}_0 - \frac{\omega^4}{4}\mathcal{J}_1 + \frac{1}{8\mathcal{J}_0}$$

where the constant has been chosen to give the reference a zero energy at I=0 [BF79]. The final excitation energy obtained is thus:

$$e'(\omega) = E'(\omega) - E'_{REF}(\omega) \qquad (5.4)$$

As mentioned above, the CSM vacuum corresponds to a mixture of even particle number configurations. In order to directly compare nuclei the odd-even mass difference and different pair gap parameters for adjacent nuclei should be taken into account. Since the masses of these nuclei are unknown experimentally and the pair gap parameter is probably changing with increasing deformation such a comparison of absolute values between neighbouring nuclei is not attempted here.

5.1.4 Alignment Diagrams

Within the CSM alignment refers to the non-collective component of angular momentum of excited quasiparticles (denoted i) along the rotational axis. High spin data are often represented in terms of alignment diagrams in which the total angular momentum aligned along the x-axis (I_x) is plotted as a function of frequency with some reference function subtracted to account for the rotational angular momenta of the core ($I_{x_{ref}}$). Discontinuities in $I_x - I_{x_{ref}}$ are then interpreted as quasiparticles aligning and the alignment may be compared with predictions from quasiparticle diagrams. Odd nuclei already possess some aligned angular momentum since they are particle excitations so this must also be estimated from the configuration assigned to the band. The reference behaviour subtracted in such diagrams is

$$i_{x_{REF}}(\omega) = \omega(\mathcal{J}_0 + \omega^2\mathcal{J}_1)$$

so that the quantity actually plotted is

$$i_x(\omega(I)) = \sqrt{I(I+1) - K^2} - i_{x_{REF}}(\omega(I))$$

5.2 Systematics of neighbouring nuclei

Before discussing the data presented it is worthwhile to take a brief trip around some near neighbour nuclei to discover what trends one might expect to find in the most neutron deficient Nd and Pr nuclei. Although the following sections examine the nuclides in terms of changing N it must be realised that systematics

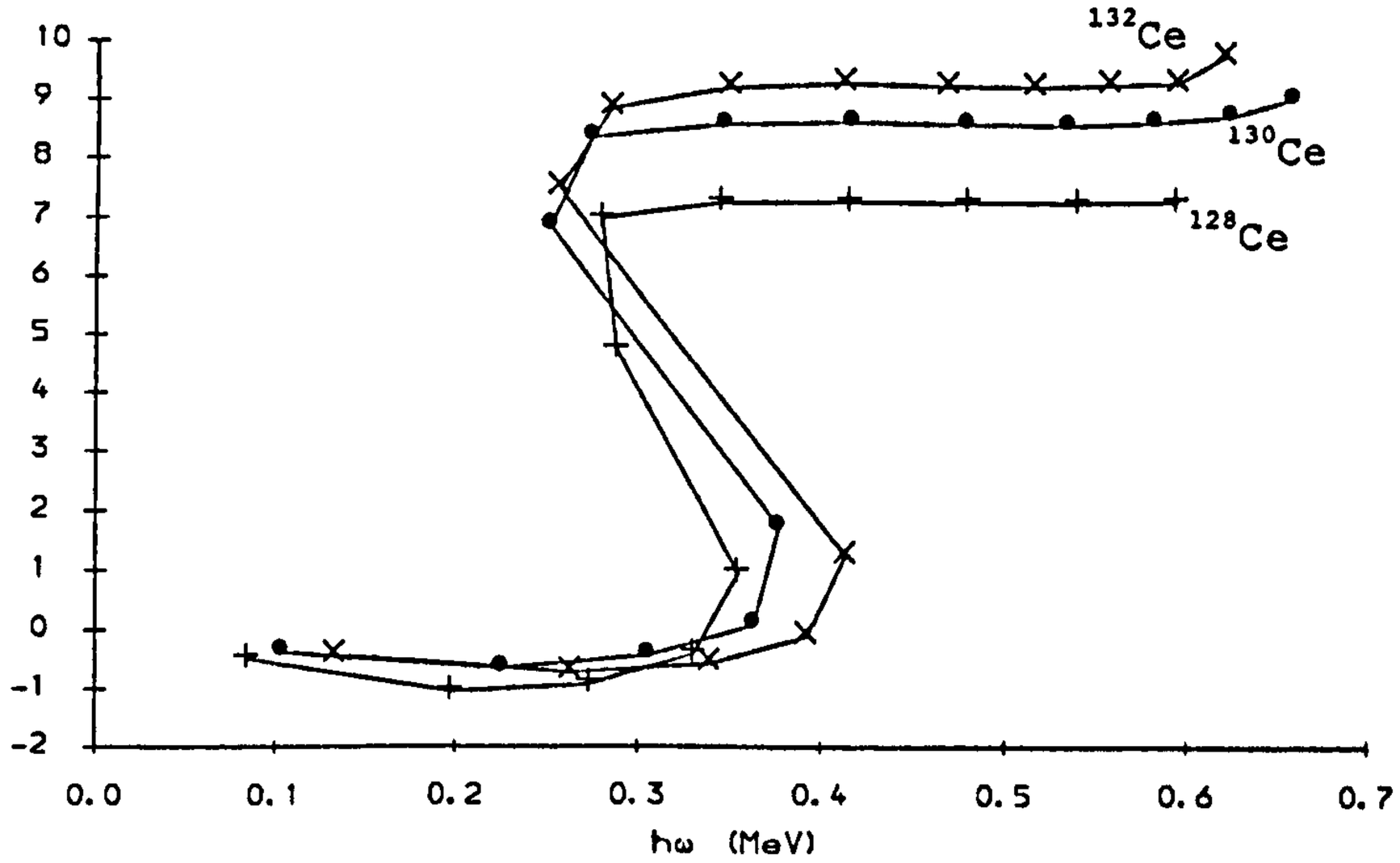

Figure 5.4: Alignment diagrams obtained for Ce nuclei which are subsequently used as references. The reference behaviour subtracted is that given by the Harris parameters in Table 5.1. The flatness of the curves above the backbend shows that the reference behaves well in the frequency regime discussed here.

for isotones as a function of Z are equally important. The references for the data discussed are given only once but relate to all the information detailed about each nucleus.

The main trend observed as isotopes become neutron deficient in this region is an increase in deformation (see e.g. [LVM85,LM82]). This is evidenced by the decreasing $E_{2_1^+}$ excitation energies in even nuclei which were observed [SDL72,G62] to be related to the deformation as:

$$E_{2_1^+} \approx \frac{1225}{A^{7/3}\beta^2} \quad MeV \tag{5.5}$$

The experimental ratio $E_{4_1^+}/E_{2_1^+}$ for even-even nuclei also provides useful information regarding the 'rigidity' of the nucleus as a rotor. The limiting values of this ratio corresponding to different classes of nuclear behaviour are:

2.0 quadrupole vibrator (SU(5) limit)

2.5 γ-soft rotor (O(6) limit)

3.33 symmetric rotor (SU(3) limit)

Thus nuclei with values of $E_{4_1^+}/E_{2_1^+}$ approaching 3.3 are expected to behave as good rotors. Nuclei with ratios between the limits 2.5 and 3.3 are termed

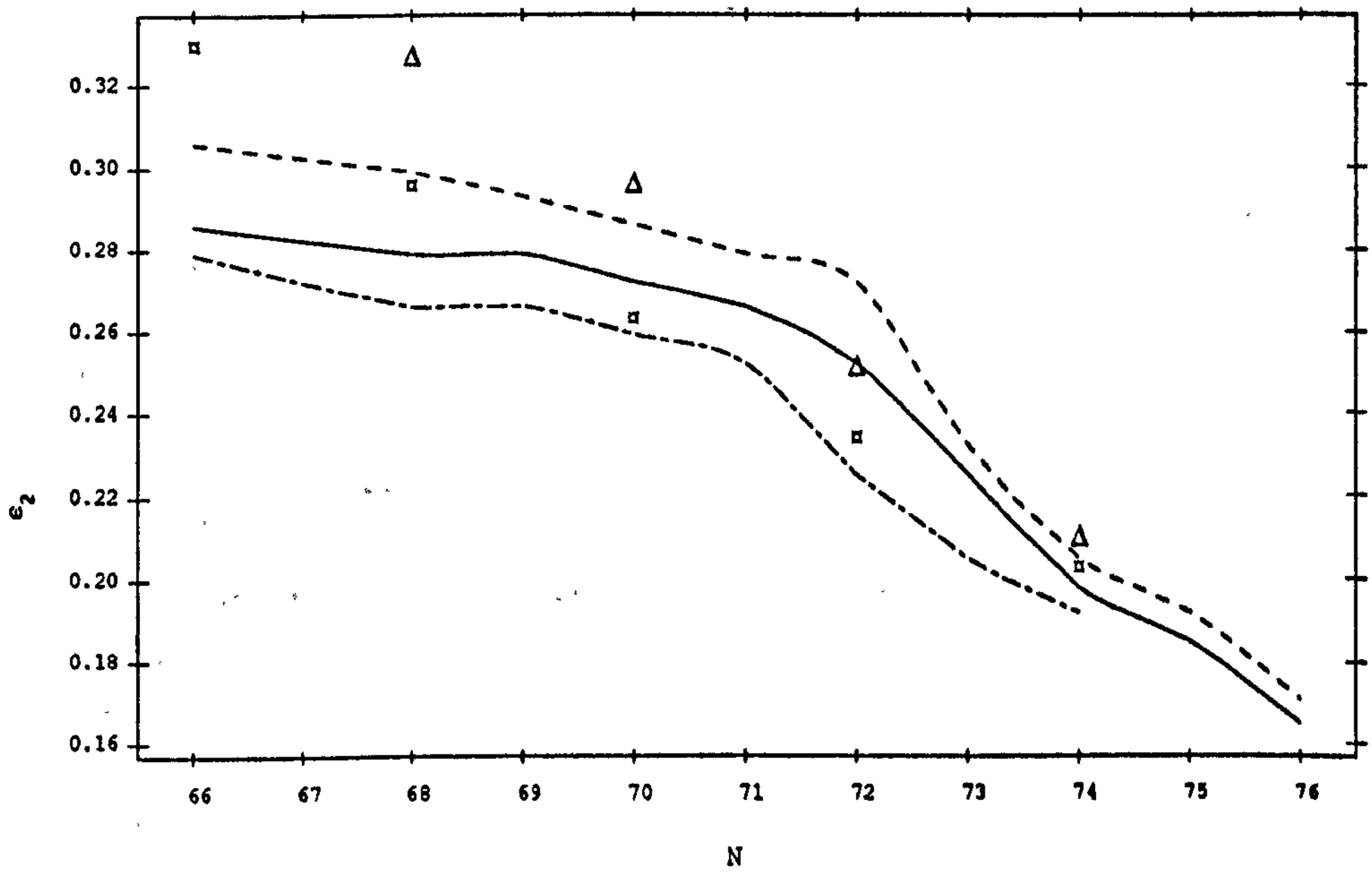

Figure 5.5: Quadrupole deformation predictions of [LM82] for the Nd (*dashed line*), Ce (*chained line*) and Pr (*solid line*) nuclei compared to experimental deformations extracted from $E_{2_1^+}$ [LVM85,YBJ86] using Equation 5.64. The points shown correspond to Ce nuclei (∘) and Nd nuclei (Δ).

transitional. Table 5.2 shows that this ratio and hence the rotational behaviour progressively approaches that of the symmetric rotor as N decreases and Z increases in this region.

N	Ce	Nd
68	3.06	3.15
70	2.93	3.06
72	2.80	2.87
74	2.64	2.68

Table 5.2: $E_{4_1^+}/E_{2_1^+}$ for Ce and Nd nuclei

5.2.1 Even-A Nd Nuclides (Z=60:$^{128-136}$Nd)

The Nd nuclei ground state bands show decreasing level spacing with decreasing N providing evidence for an increased deformation [LVM85,WOW88]. ^{132}Nd and

^{134}Nd show an upbend at a frequency $\hbar\omega_c \sim 0.32$ MeV which is attributed to a band crossing by the EF 2 quasiproton configuration. In ^{132}Nd this crossing is rapidly followed by that of the ef neutrons so the crossing is poorly defined. In both these nuclei two side bands are observed at an excitation of > 1.5 MeV and these can be attributed to the ae and af neutron configurations although this is not conclusive [WOW88]. If the Nd nuclei are compared with the corresponding Ce isotones then it is observed that the E_{2+} energies are lower for the Nd nuclide pointing towards greater deformation. A similar comparison of the alignment behaviour shows the Ce nuclei to back-bend quite sharply whilst the Nd nuclei exhibit upbends.

5.2.2 Odd-A Pr Nuclides (Z=59:$^{131-137}$Pr)

The spectroscopy of the deformed odd-A Pr nuclides is dominated by a decoupled band based on the π h11/2[541]3/2$^-$ configuration. At a rotational frequency $\omega_c \sim 0.46$ MeV $/\hbar$ the FG protons align and the band is crossed and the 3 quasi-proton (EFG) band becomes yrast. This crossing is manifested as an upbend in an alignment diagram. The 11/2$^-$ bandhead is isomeric ($\tau_{\frac{1}{2}} \geq 1\mu s$ ^{133}Pr [HBF88], $\tau_{\frac{1}{2}} = 105\mu$s ^{135}Pr [SSH86], $\tau_{\frac{1}{2}} \geq 2.7\mu s$ ^{137}Pr [XBM89]) and is to be found at a systematically decreasing excitation energy ($E_{ex} = 0.130$ MeV ^{133}Pr, $E_{ex} = 0.315$ MeV ^{135}Pr , $E_{ex} = 0.563$ MeV ^{137}Pr). The level spacing of the bands decreases as the neutron fermi surface drops progressively below the N=82 shell closure and is evidence for an increasing deformation. The unfavoured signature of this band has been observed in ^{137}Pr (where the band is more characteristic of a strongly perturbed coupled band and signature splitting is of the order of 350 keV), ^{135}Pr (splitting $\sim$ 410 keV) and possibly ^{133}Pr where two levels with spins 13/2$^-$ and 17/2$^-$ are observed with a splitting $\sim$ 440 keV). The unfavoured signature has not been identified in ^{131}Pr.

A weaker strongly coupled band based on the π g7/2[413]5/2$^+$ configuration is also systematically observed. In ^{137}Pr only the favoured signature is observed at low spins whilst in ^{135}Pr both signatures are seen to be linked by strong M1 transitions which drop off in intensity with increasing spin. In ^{133}Pr both signatures are identified but the M1 inter-band transitions are not seen. This band is crossed at a frequency $\omega_c \sim 0.3$ MeV $/\hbar$ which is due to an alignment of the EF protons and both signatures of the band continue with the configurations AEF and BEF. Above the backbend the M1 inter-band transitions become strong in ^{137}Pr and ^{135}Pr but are still absent in ^{133}Pr. The AEF/BEF bands feed strongly into the decoupled h11/2 band via high energy ($\sim$ 1 MeV) E1 transitions so the intensity below the crossing drops. The decay in the region of the crossing is observed to be fragmented in ^{135}Pr and ^{137}Pr and this is interpreted in [XBM89] to be due to a change in triaxiality from $\gamma \sim -30^0$ below the backbend to $\gamma \sim 0^0$ above the backbend. The transition between the bands appears to be smooth in ^{133}Pr and in ^{131}Pr only one signature of the 3 quasi-particle band is observed [GBK87].

The ground state in ^{137}Pr is known to be a 5/2$^+$ state and is associated with

the Nilsson orbital πg7/2[413]5/2$^+$ but in ^{135}Pr the ground state is a 3/2$^+$ state, corresponding to the Nilsson d5/2[411]3/2$^+$ orbital. In [GBSS88]it is argued that several unassigned positive parity states may belong to the two signatures of a coupled band based on this 3/2$^+$ state. The ground state in ^{133}Pr is observed to be a 5/2$^+$ state whilst in ^{131}Pr the lowest state observed is the 11/2$^-$ bandhead of the de-coupled band: it is not clear that this is indeed the ground state.

The results of calculations performed within the Wood-Saxon potential for various Pr nuclei are given in Table 5.3. The calculations predict the ground state of ^{135}Pr correctly but seem to bring the h11/2 states down too low in ^{133}Pr. Below this experimental data peters out. An interesting feature of the calculations for ^{131,129}Pr is the appearance of the g9/2 state giving rise to a structure of significantly greater deformation.

One final observation made in the odd-A Pr nuclei is the existence of bands of low energy $\Delta J = 1$ transitions without any $\Delta J = 2$ crossover transitions. Three such bands are seen in ^{133}Pr (at $\sim$ 2 MeV ,$\sim$ 3 MeV and unknown excitation energy) and one in ^{135}Pr (at $\sim$ 4 MeV excitation). The level spacings in these bands are typically of order 200 keV in ^{133}Pr and 400 keV in ^{135}Pr. In [HBF88] an argument is made that the lowest lying of these bands in ^{133}Pr is an oblate collective structure built on a $\pi h\frac{11}{2} \otimes (\nu h\frac{11}{2})^2$ configuration. The evidence presented for this is based on angular distribution coefficients, lack of signature splitting and a lower limit on the B(M1)/B(E2) ratio of $\sim$ 5.

5.2.3 Odd-A Nd Nuclides (Z=60:$^{133-137}$Nd)

The systematics of the odd-A Nd nuclides are somewhat less regular than their odd-A Pr counterparts since as the neutron Fermi level changes the orbital occupied by the single neutron varies.

^{137}Nd shows a rotationally perturbed coupled band based on an isomeric 11/2$^-$ state and feeding into a positive parity level sequence based on a 1/2$^+$ ground state. The levels in this nucleus are characteristic of a small prolate deformation [GGM74].

The Yrast band in ^{135}Nd at low spin is a strongly coupled band based on the single neutron configuration νh11/2[514]9/2$^-$ [PBF87]. The signature splitting in the band is $\sim$ 100 keV and increases with spin until the h11/2 protons align at $\hbar\omega \sim 0.32$MeV . This is a higher frequency than that expected and has been interpreted as a sign of a triaxial deformation ($\gamma \sim -20^0$) brought about by the oblate driving force of the upper mid-shell h11/2 neutron. Above the crossing the lower mid-shell h11/2 protons force a return to axiality as evidenced by the lack of signature splitting above the crossing. A second band at $\sim$2 MeV excitation and characterised by strong M1 inter-band transitions (the E2 crossover transitions have been seen in data presented in [BSB87])and zero signature splitting is also observed and an assignment of a $\nu h\frac{11}{2} \otimes \pi h\frac{11}{2} \otimes \pi g\frac{7}{2}$ 3 quasi-particle structure is argued in [PBF87]based on semi-classical considerations concerning the strength of the B(M1)/B(E2) ratios.

Nucleus	π	K	E	β_2	β_4
^{129}Pr	−	3/2	0	0.278	0.002
	+	1/2	0.12	0.276	−0.01
	+	3/2	0.25	0.262	−0.01
	−	5/2	0.43	0.282	−0.003
	+	9/2	0.44	0.317	0.001
	+	5/2	0.63	0.253	−0.021
	+	3/2	0.63	0.278	0.012
^{131}Pr	−	3/2	0	0.257	−0.004
	−	1/2	0.02	0.245	−0.013
	+	3/2	0.105	0.240	−0.016
	+	5/2	0.40	0.230	−0.0122
	−	5/2	0.43	0.257	−0.0112
	+	1/2	0.61	−0.283	0.0117
	+	9/2	0.64	0.308	0.0008
	+	3/2	0.64	0.251	0.0034
^{133}Pr	−	1/2	0	0.211	−0.0084
	+	3/2	0.02	0.205	−0.0134
	−	3/2	0.07	0.218	−0.005
	+	5/2	0.20	0.195	−0.02
	−	5/2	0.48	0.214	−0.012
	+	3/2	0.58	0.200	−0.0044
	+	1/2	0.63	−0.205	0.0078
	−	11/2	0.65	−0.204	0.0058
	+	1/2	0.69	0.191	−0.0232
	+	5/2	0.79	−0.226	0.0
^{135}Pr	+	3/2	0	0.164	−0.0118
	+	5/2	0.08	0.188	−0.0129
	−	1/2	0.08	0.173	−0.0039
	−	3/2	0.21	0.175	−0.0048
	+	1/2	0.31	−0.169	−0.0004
	+	3/2	0.31	−0.167	−0.003
	−	11/2	0.32	−0.170	−0.0008
	+	5/2	0.35	−0.159	−0.0104
	+	1/2	0.54	0.151	−0.0104
	−	5/2	0.56	0.170	−0.0129

Table 5.3: Bandhead calculations for the odd-A Pr nuclei performed by the Lund/Warsaw collaboration courtesy of Dr. R. Wyss (Lund). The calculations were performed at $\omega = 0.0$ and restricted to the axially symmetric case $\gamma = 0$. This latter restriction would seem to be increasingly valid as the neutron number is decreased since the minima in the TRS surface calculations and the systematics for the region indicate that the nuclei become progressively more deformed and more rigidly prolate. Each single particle level was then separately blocked and the energy minimised with respect to the parameters β_2, β_4. The single particle levels were generated within the Wood-Saxon potential and pairing was treated by the Lipkin method outlined in section 2.3.6.

Two apparently coupled structures are observed in ^{133}Nd [M89] at undetermined relative excitation. The structure with lowest signature splitting is thought to be based on the $\nu g\frac{7}{2}[404]\frac{7}{2}^+$ orbital. The second structure, for which the decay sequence is mostly unobserved for one of the signatures, is probably based upon the $\nu h\frac{11}{2}[523]\frac{7}{2}^-$ configuration although the $\nu h\frac{11}{2}[514]\frac{9}{2}^-$ is a possibility and is in fact observed to be the bandhead of a similar structure in ^{131}Ce.

Calculations of the same type as those listed in 5.2.2 are detailed in Table 5.4. Unfortunately, there is no data regarding the relative excitations of the structures observed in the nuclei listed so the quality of the calculations cannot be compared. However, it is interesting to note that a low lying $1/2^-$ state (presumably the h9/2 neutron) is predicted with a significantly larger deformation. The most

Nucleus	π	K	E_{ex}	β_2	$\beta 4$
^{131}Nd	+	5/2	0	0.273	-0.0084
	-	7/2	0.174	0.272	-0.0006
	-	1/2	0.239	0.306	0.0076
	-	9/2	0.454	0.270	-0.0158
	+	1/2	0.478	0.281	0.0046
	+	7/2	0.609	0.250	-0.001
	-	3/2	0.969	-0.284	0.0105
^{133}Nd	-	9/2	0	0.240	-0.0222
	+	7/2	0.025	0.228	-0.013
	+	5/2	0.097	0.257	-0.015
	-	1/2	0.154	0.285	0.0004
	-	7/2	0.338	0.225	-0.0038

Table 5.4: Bandhead calculations for some light Nd nuclei performed in the same manner as those of Table 5.3.

exciting systematic observation amongst all the Nd nuclides is that of highly deformed ($\beta \sim 0.4 - 0.5$) bands [WKL87] in which it seems likely that the $i\frac{13}{2}$ orbital plays a significant role. These bands have been observed in all Nd nuclei from ^{133}Nd to ^{137}Nd, most strongly in ^{133}Nd. The band appears to be significantly more strongly populated in the odd-A nuclides, a feature which is thus far not understood.

5.2.4 Even Pr Nuclides (Z=59:$^{130-134}$Pr)

The odd-odd Pr nuclei would be expected to show properties that are representative of the unpaired valence nucleons and the manner in which these nucleons couple their angular momenta.

The yrast band in ^{134}Pr [BHP87] is strongly coupled and characterised by a high B(M1)/(BE2) ratio (probably in excess of 10 $(\mu_N/eb)^2$ at I $\sim$ 10) and a small

signature splitting. The structure proposed for this band is πh11/2[541]3/2$^-$ $\otimes$ νh11/2[514]9/2$^-$ where the angular momenta couple perpendicularly to give a bandhead spin and parity of $\sim 7^+$ and K $\sim$ 6 so as to account for the strong M1 transitions. A second band in which only M1 transitions are seen is found at an excitation of $\sim$ 2.5 MeV and is thought to be the band based on the $\pi g\frac{7}{2}[413]\frac{5}{2}^+ \otimes \nu h\frac{11}{2}[514]\frac{9}{2}^-$ configuration after the alignment of the h11/2 protons i.e. the two signatures of the band are the eAFG and fAFG 4 quasi-particle configurations.

In moving to ^{132}Pr [SBF88] the neutron fermi level drops and two strongly coupled bands are seen separated by only 283 keV . In both of these structures the proton occupies the [541]9/2$^-$ orbital. The lower lying negative parity band is formed by coupling this to the $g\frac{7}{2}[404]\frac{7}{2}^+$ neutron orbital with the spins coupled anti-parallel to give a bandhead with I=7 and a K of about 2 which fits the observed B(M1)/B(E2) ratio of around 3.5 $(\mu_N/eb)^2$. The higher lying positive parity band can be formed by coupling this proton to an h 11/2 neutron (either [523]7/2$^-$ or [514]9/2$^-$) orbital giving a bandhead of spin 8 and K of around 4 which fits the B(M1)/B(E2) ratios of about 0.8$(\mu_N/eb)^2$. A series of weak $\Delta J = 2$ transitions are observed and explained as a doubly de-coupled νi13/2$\otimes\pi$h11/2 band.

The decay of ^{130}Pr [MPS88] is very similar to that of ^{132}Pr except that the postive parity bandhead is now only 110 keV above the negative parity bandhead and the B(M1)/B(E2) ratios have dropped to around 2 and 1 $(\mu_N/eb)^2$ respectively for the positive and negative parity bands. This is explained by the lowering of the neutron fermi level so that the orbitals coupled to the proton are now the $\nu g\frac{7}{2}[402]\frac{5}{2}^+$ and $\nu h\frac{11}{2}[523]\frac{7}{2}^-$.

5.3 ^{129}Pr

Band 1 in ^{129}Pr is easily identified as the de-coupled proton band based on the [541]3/2 Nilsson orbital and systematically observed in all the neutron deficient odd-A Pr nuclei. A comparison of the alignment behaviour of Band 1 with de-coupled bands from other Pr nuclei shows that the alignment at the band crossing and the crossing frequency decrease as the neutron number decreases. The de-coupled h11/2 bands have been identified in a large number of nuclei now, ranging from the I (Z=53) nuclei up to the Pm (Z=61) nuclei. This enables systematic trends to be observed. One such trend, first noted in [SGG82], but concerned with a more limited sample of nuclear species, is the ratio of the transition energies of the lowest transitions in the decoupled band to that of the $2^+ \rightarrow 0^+$ in the Z$-$1 core nucleus (Figure 5.7). A ratio of 1.0 corresponds to the weak/de-coupled limit which can be seen to be applicable to the La nuclei at moderate deformations (i.e. N<72) and is explicable within the particle rotor model by the rotational alignment of the odd proton as a result of the strong Coriolis interaction expected for a high j low K orbital. The low values of the ratio exhibited in the I and Cs nuclei have been attributed to the πh11/2 orbital

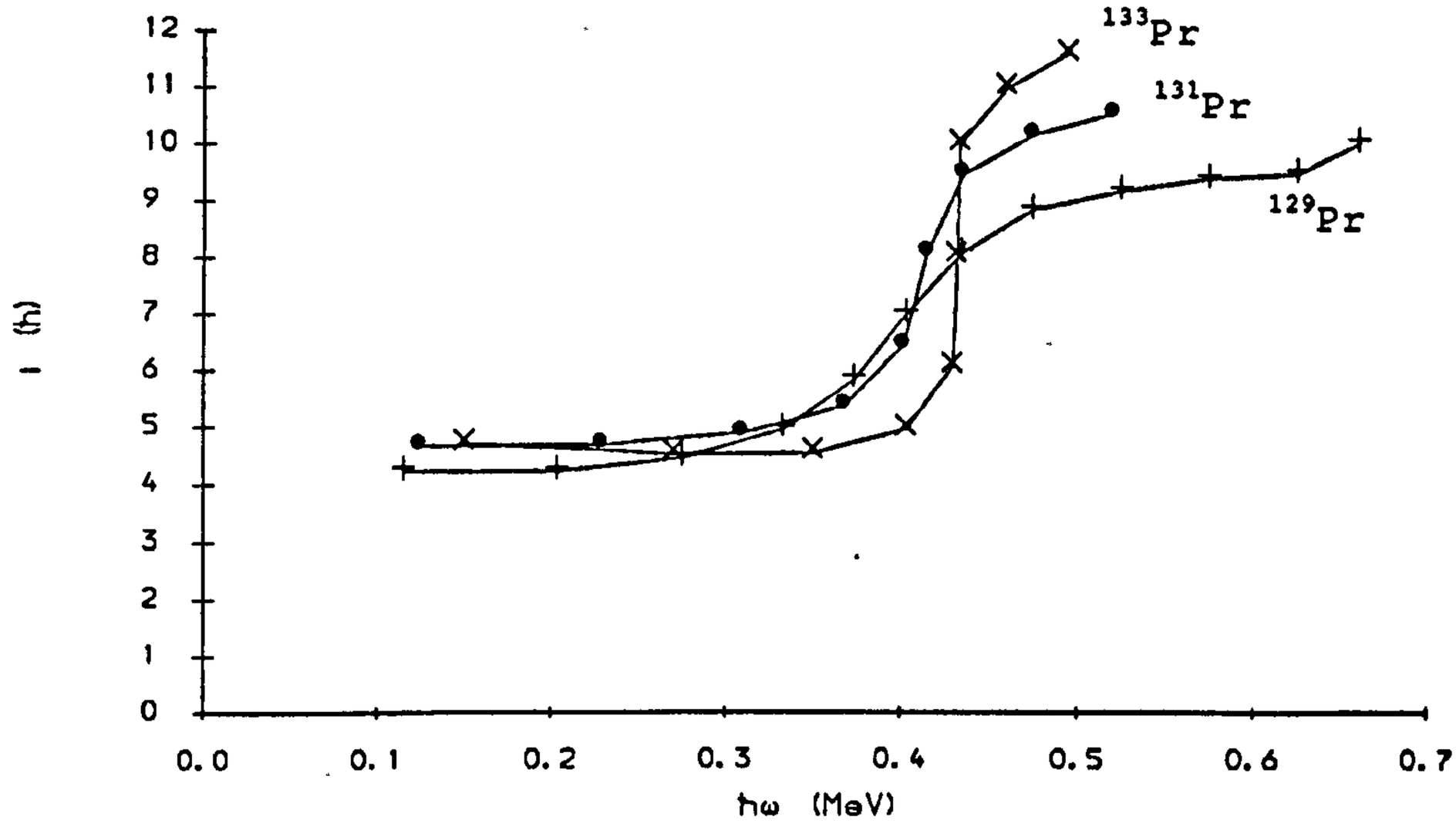

Figure 5.6: Comparison of the alignment behaviour of de-coupled bands in the odd Pr nuclei. The K value assumed for the bands was 3/2 as is consistent with the [541]3/2 Nilsson level and all the levels in ^{129}Pr were assumed to be of stretched E2 character as implied by the I(143)/I(101) ratios in Table 4.4. The reference subtracted for each nucleus was the adapted g-reference from the corresponding Ce isotone as described in Section 5.1.4.

driving the core to greater deformations in the odd-A case compared to the even-even nucleus [BB78] thus increasing the moment of inertia of the band in the odd case. The converse argument would require that the lower mid-shell πh11/2 orbital has an opposite effect in the case of Pr and Pm which show increasingly large ratios. This is clearly untenable. A plausible explanation is provided by the particle-rotor model. The model predicts (Figure 5.8) that the excitation of the $15/2^-$ state relative to the $11/2^-$ begins to rise above the core E_{2_1} as the deformation exceeds $\beta \sim 0.25$ and that the magnitude of this increase increases as the Fermi surface rises above the $\Omega = 1/2$ level in the shell. The calculations shown in Figure 5.8 are taken from [S72] and are slightly inappropriate in that the Fermi surface is too low in the calculations on the left and the deformation too small in the calculations on the right but the diagrams do exhibit the requisite features. The effect is thus simply a manifestation of the increasing core deformation and the rising proton Fermi surface. The core is no longer completely de-coupled from the odd nucleon and thus the de-coupled scheme proposed in [LNM73] is no longer valid. It was noted in [LVM85] that the Pm isotopes did not show the sudden increase in deformation expected from

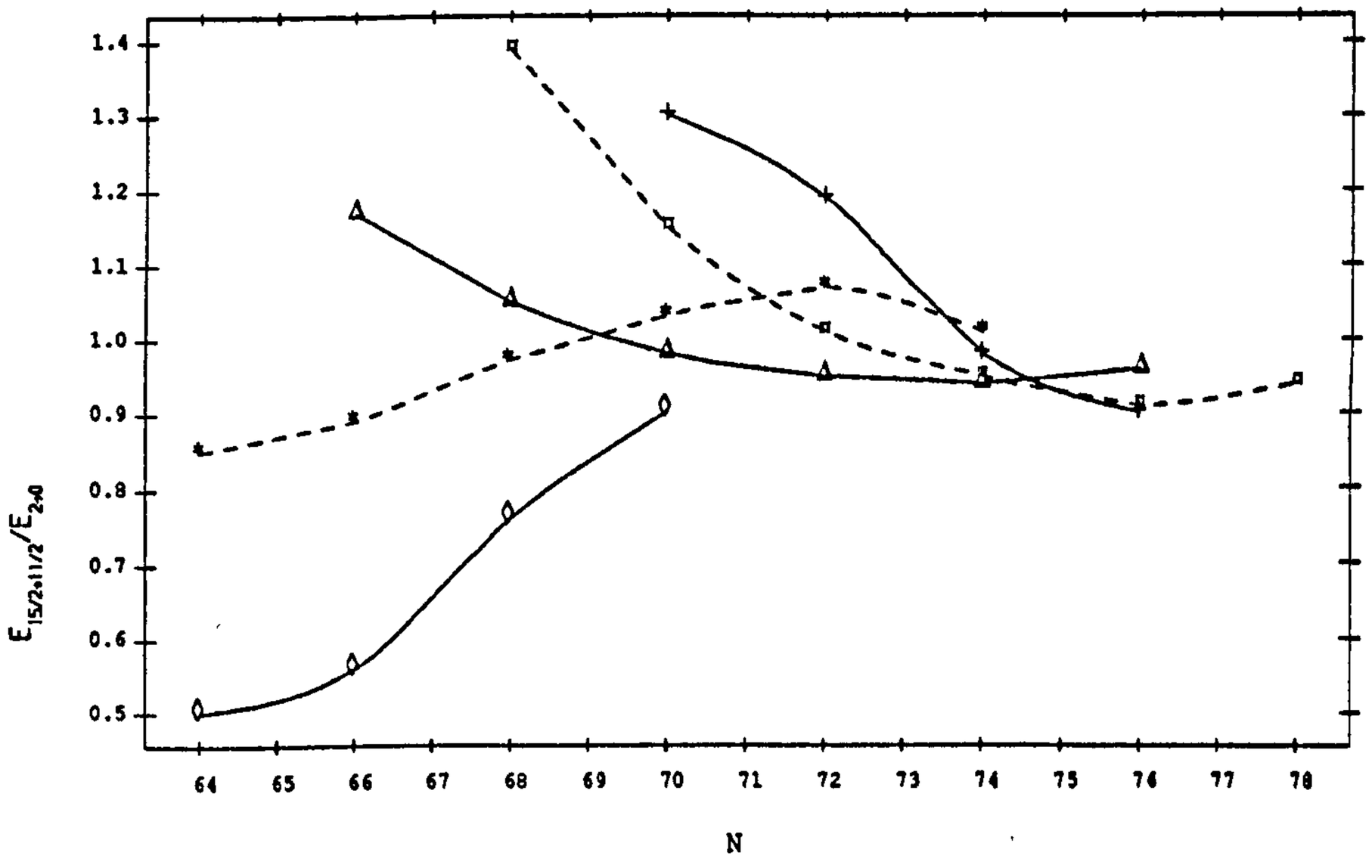

Figure 5.7: Comparison of $E_{15/2-\to11/2-}$ in de-coupled h11/2 bands with $E_{2+\to0+}$ for the corresponding even-even core nucleus as a function of N and Z. The curves refer to Te/I (Z=52/53,$\diamond$), Xe/Cs (Z=54/55,$*$), Ba/La (Z=56/57,Δ), Ce/Pr (Z=58/59,$\circ$) and Nd/Pm (Z=60/61,+). The last points for ^{131}Pm and ^{127}Pr use energies taken from RS Z-selected data. It was possible to confirm the energies in the RS data from the ESSA-30 mass 131 experiment in the case of ^{131}Pm.

the calculations of [LM82] when the deformations were extracted from the h11/2 bands using Equation 5.64 under the assumption of complete decoupling. It is also noted in [B88] that the deformations extracted from lifetimes for the Pm nuclei are significantly greater than those from the simple estimate of Equation 5.64 under the assumption that the odd nucleus behaviour accurately mimics the core. This apparent discrepancy in the deformations from the two methods is resolved when it is realised that the premise upon which the latter estimate was made is false.

Bands 2 and 3 can be interpreted as a $\pi \otimes \pi$FG band by analogy with similar bands in ^{133}Pr and ^{135}Pr. This seems reasonable since the level spacings of the bands and the excitation relative to and decay into the h11/2 band via high energy transitions are similar. The odd proton occupies the [413]5/2 orbital in the heavier isotopes but the trend towards greater deformation as the neutron number decreases opens up the possibility that the single proton possesses significant [420]1/2 and/or [422]3/2 character as these orbitals are close to the Fermi surface at a deformation $\epsilon_2 \sim 0.3$. The assignment of a specific configuration to

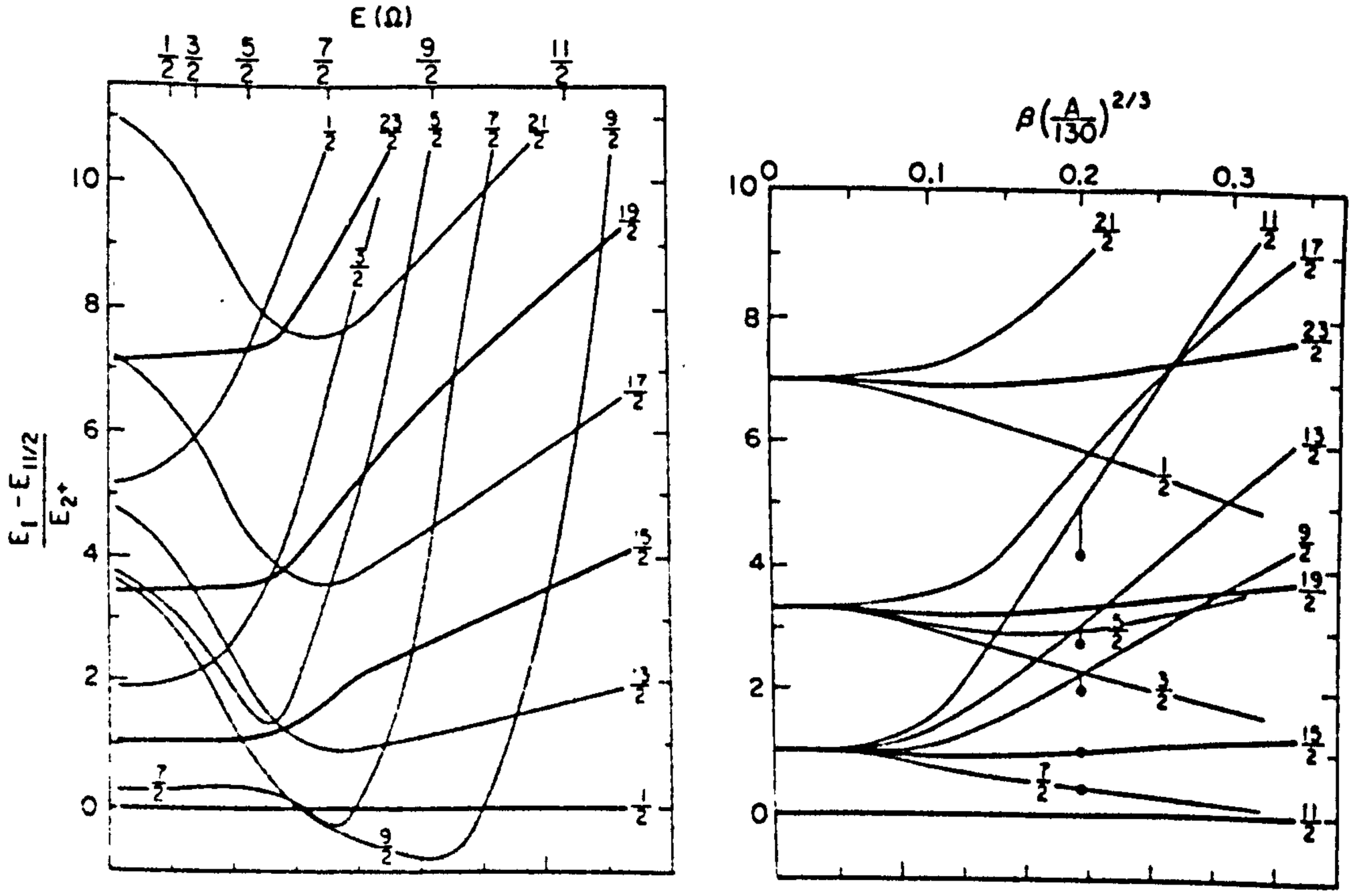

Figure 5.8: Particle-rotor calculations for an h11/2 proton
Right: as a function of deformation with the Fermi surface held at the $\Omega = 1/2$ level. The calculation shown was appropriate for the nucleus ^{127}La and the ^{126}Ba core behaviour was fitted by an empirical expansion in rotational angular momentum up to order 6. The dots show the effects of diagonalising a more realistic Hamiltonian.
Left: as a function of the Fermi level λ at a fixed deformation (β=0.25). The approximate locations of the various h11/2 orbitals are shown at the top of the diagram. $\Omega = 3/2$ is pertinent for the Pr nuclei and $\Omega = 5/2$ for the Pm nuclei.

this band is thus left open.

If the 567 keV transition were confirmed and Bands 6/7 firmly tied to Bands 2/3 then the backbending behaviour would be very similar to that observed in ^{133}Pr and ^{135}Pr as can be seen in Figure 5.9, the crossing occurring at a frequency

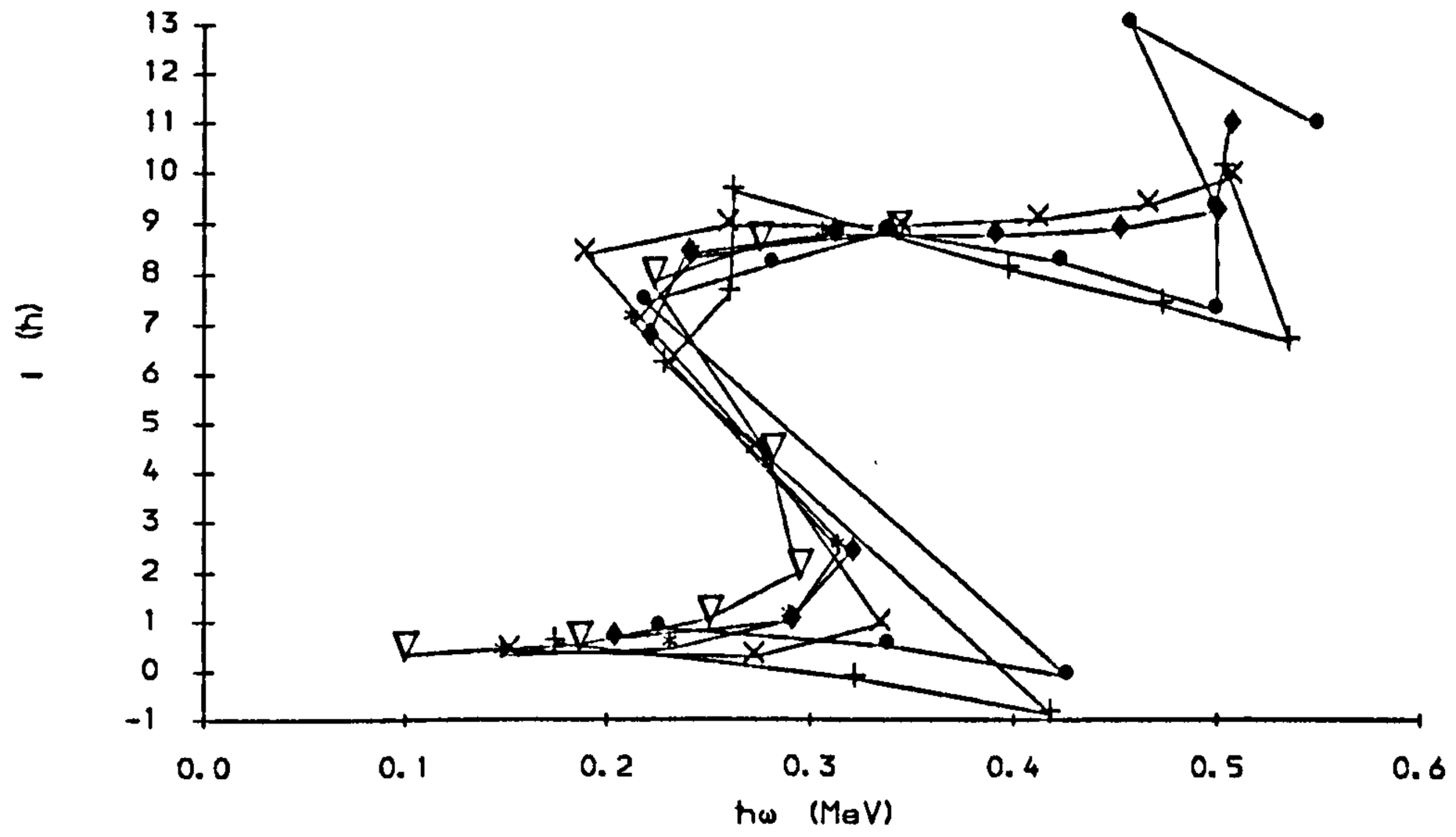

Figure 5.9: Comparison of the alignment behaviour of coupled bands systematically observed in the odd Pr nuclei. The K values used for the bands were K=5/2 for ^{135}Pr (+, •) and ^{133}Pr (×, ◇), and K=3/2 for ^{129}Pr (∗, ∇). The reference subtracted for each nucleus was the adapted g-reference from the corresponding Ce isotone as described in Section 5.1.4. This would seem to be slightly inappropriate for ^{133}Pr from the negative alignment seen at low frequency and decreasing alignment at high frequency.

$\hbar\omega_c \sim$0.27 MeV . The existence of a link is supported by the increasing signature splitting of Bands 6/7 towards the observed signature splitting between Bands 2 and 3 (Figure 5.10). The backbend may also be compared with that observed in ^{128}Ce (see Figure 5.4) which has been attributed to the AB protons. The alignment gained in the two cases is $\Delta i_x \approx 8\hbar$ though the crossing frequency is higher by $\sim$ 0.03 MeV /$\hbar$. The reduction in frequency of the crossing in the odd proton nucleus is a systematic observation in ^{133}Pr, ^{135}Pr and now, tentatively, ^{129}Pr, and can be ascribed to a reduction in the pairing correlation parameter Δ_p due to blocking of an orbital near the Fermi surface. A similar systematic decrease in Δ_n is observed in the odd neutron rare earths [GAG81]. It did not prove possible to produce a set of quasiproton levels which correctly predicted both the EF and FG crossing frequencies. This could be an indication that the

pair field is dependant on the single proton level occupied and that occupation of a single g7/2 level reduces the pairing strength more significantly than occupation of an h11/2 level since the reduced pairing in Figure 5.1 pushes the first crossing far too low in frequency.

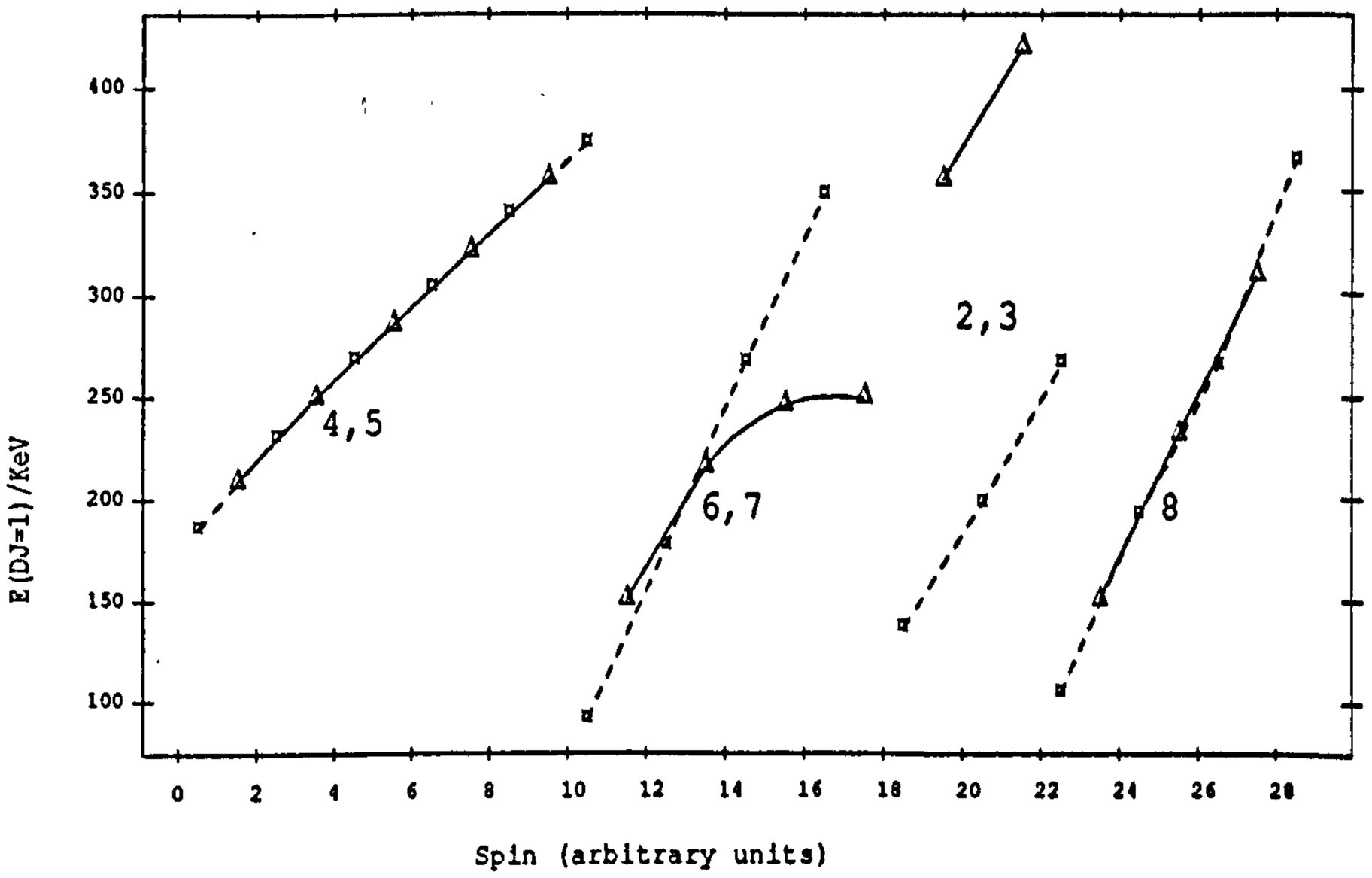

Figure 5.10: Plot of $\Delta J = 1$ energies versus arbitrary spin to show the signature splitting in the various bands in ^{129}Pr. Where no such transitions exist, as in the case of Bands 2/3, the $\Delta J = 1$ energies have been calculated from the staggering of the levels.

Again, *if* the 567 keV is established then the excitation of the h11/2 band is fixed relative to that of bands 6/7 and is contrary to the calculations illustrated in Table 5.3 which place the $3/2^-$ orbital at the lowest energy. The calculations also predict the negative parity states to lie too low in ^{133}Pr and this could mean that the potential used does not give the correct relative energies to the h11/2 orbitals compared to the positive parity d5/2, g7/2 levels. Bands 4/5 and 6/7 can then be associated with the lowest lying positive parity proton Nilsson orbitals. Assuming the high energy transitions feeding from Bands 2 and 3 to be of unstretched and stretched character respectively would give the 1770 and 1949 keV levels spin/parity assignments of $19/2^+$ and $21/2^+$ respectively. The E1 character for these transitions is based upon the multipolarity observed for similar transitions in ^{133}Pr and ^{135}Pr and the fact that any other multipolarity of transition would be very unlikely to be observed. The choice of stretched and unstretched transitions is forced to be as stated if the 567 keV transition is of stretched E2 character as would be expected for an in-band transition otherwise

the bandhead would have a negative spin! The bandhead spin and parity can thus be assigned as $1/2^+$ and associated with the [420]1/2 Nilsson orbital. The presence of the coupling transitions and lack of signature splitting in these bands would suggest strong admixtures of higher K orbitals in the structure.

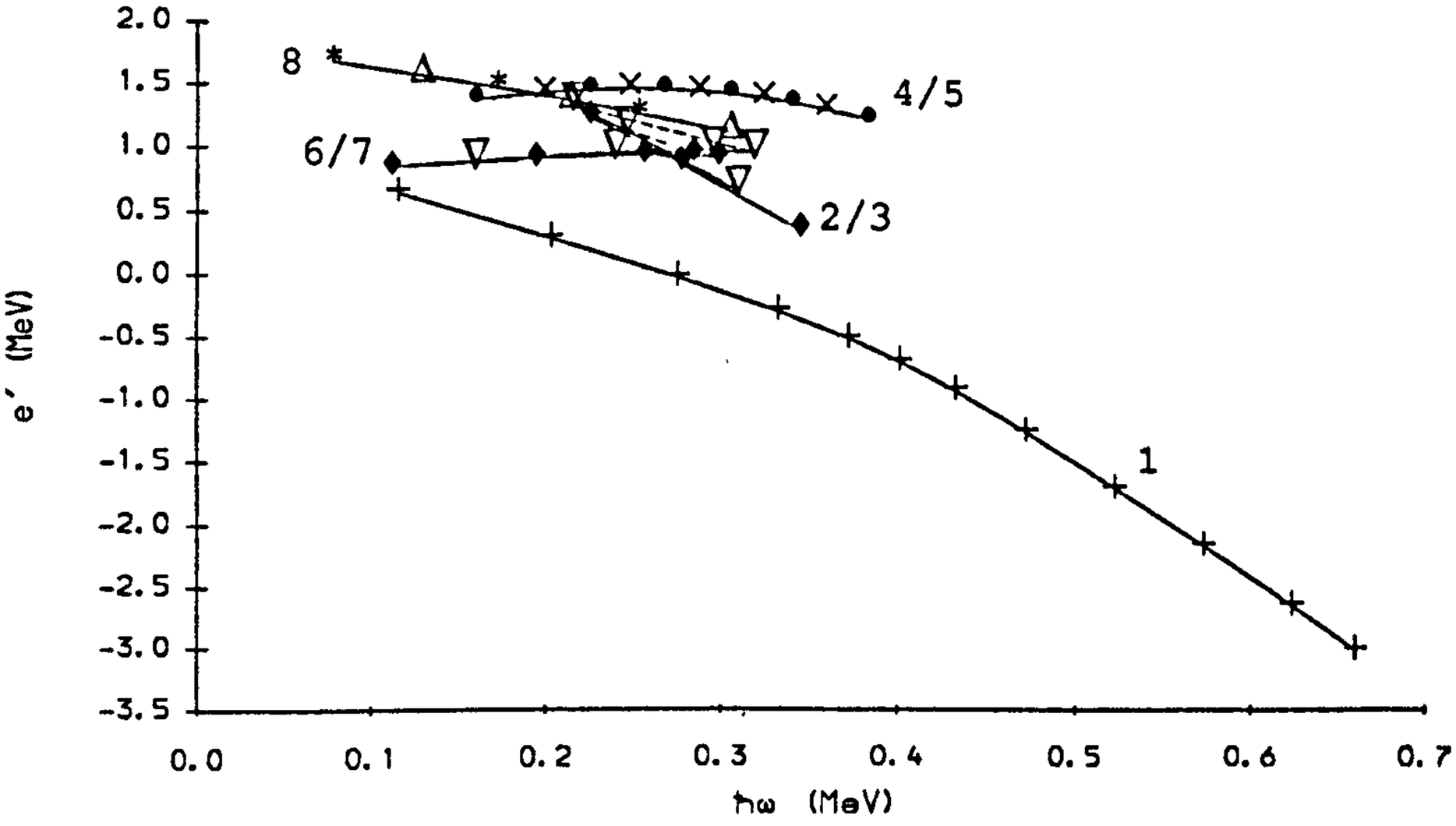

Figure 5.11: Plot of the Routhians constructed for the bands in ^{129}Pr using the prescription described in Section 5.1.3. The K values are as described in the text and the reference subtracted is detailed in Table 5.1

The bandheads of Bands 4/5 may now be assigned to the [422]3/2 Nilsson level which lies very close to the [420]1/2. The transition feeding from Band 4 into Band 6 would thus most likely be an M1 transition involving an increase in K and angular momentum and hence be likely to be hindered as observed by the long lifetime of the bottom state in Band 4. This assignment would also fit well with the bandhead calculations of Table 5.3 and the hinderance of the decay from bands 4/5 to 6/7 could be understood in terms of the increase in deformation required to decay from the K=3/2 to the K=1/2 structure. The high B(M1)/B(E2) ratios for this band also suggest admixtures from other orbitals. The fact that the branching ratios in bands 4/5 are significantly higher than those of 6/7 lends weight to the assumption of a higher K value for these bands. It is also interesting to note that Bands 4/5 do not backbend sharply in the manner of Bands 6/7 but may show a strong interaction at around the same frequency as can be observed in Figure 5.11. This fact is rather difficult to interpret. This interaction is reflected in the $\mathcal{J}^{(2)}$ moment of inertia for the band which has a

magnitude $\sim 50\ \hbar^2\mathrm{MeV}^{-1}$, around twice that of the other bands in the nucleus.

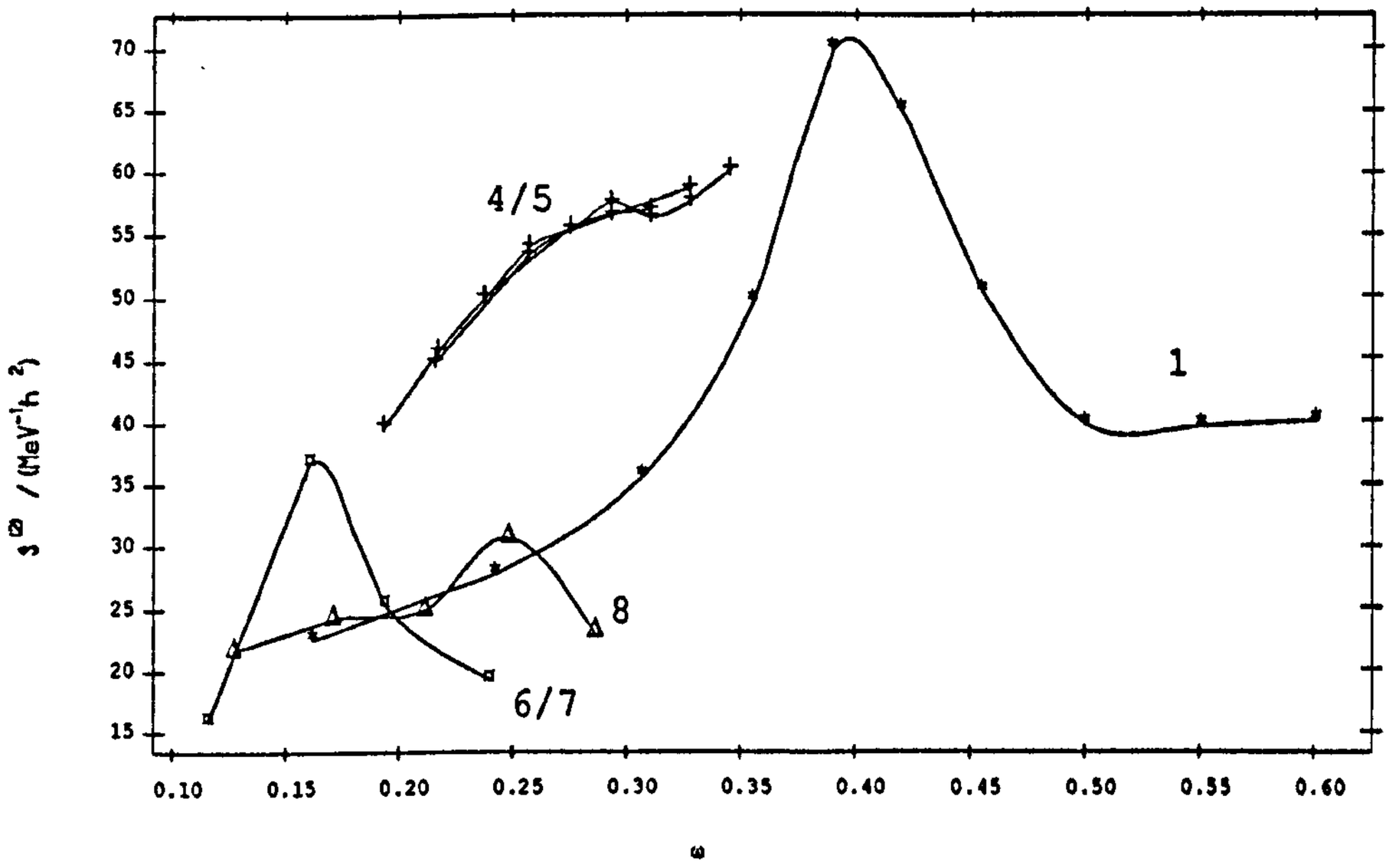

Figure 5.12: Dynamic moments of inertia for the bands observed in ^{129}Pr. The moments were calculated according to equation 1.8 in the case of Band 1 and from an equivalent formula for $\Delta J = 1$ transitions for the remaining bands. Values obtained by both methods are plotted for bands 4/5 to show that they are equivalent. This is only true if there is no signature splitting between the bands.

It is tempting to interpret the remaining structure in ^{129}Pr as an oblate structure since several such structures have recently been proposed in the A$\sim$130 region for strongly coupled structures in the La's and Pr's. The fact that all the rest of the evidence in the region points towards increasingly rigid deformed prolate behaviour suggests that another explanation would be more attractive. A glance at the Nilsson diagram shows the $\pi g9/2[404]9/2^+$ orbital rapidly approaching the Fermi surface until at a deformation $\epsilon_2 \sim 0.3$ it is of comparable excitation to the g7/2 and d5/2 orbitals already mentioned. Band 8 is thus assigned as a K=9/2 band based on the g9/2 orbital. Extensive systematics exist on bands based on the g9/2 proton hole states in the odd-A I [SGG82], Sb [SGS79], Cs [GSF79] and extending up to ^{125}La [SGG82]. Such bands are characterised by high B(M1)/B(E2) ratios ($\geq$ 3.7, in many cases the $\Delta J = 2$ transitions are not seen), zero signature splitting and isomeric ($\sim$few ns in the case of I nuclei) bandheads. The N=68 isotones exhibit a series of g9/2 bands of decreasing level spacing with increasing Z. Evidence that the influence of the

g9/2 orbital disappears in the doubly odd nuclei ^{126}La, ^{122}Cs and ^{128}La is presented in [QBC86]. It is possible that the increased deformation of the Pr nuclei relative to the corresponding La nuclei lowers the energy of the g9/2 hole-like state sufficiently to be observed again.

5.4 ^{131}Nd

A major obstacle to the interpretation of the structures observed in ^{131}Nd is the lack of any knowledge of their relative excitations. The comparable intensities of the bands suggest that they may all lie relatively low in energy. The Nilsson orbitals close to the Fermi surface for a deformation 0.2-0.4 and neutron number 71 are the [404]7/2, [402]5/2 and [523]7/2 and the configurations of the strongest bands will be based upon these orbitals.

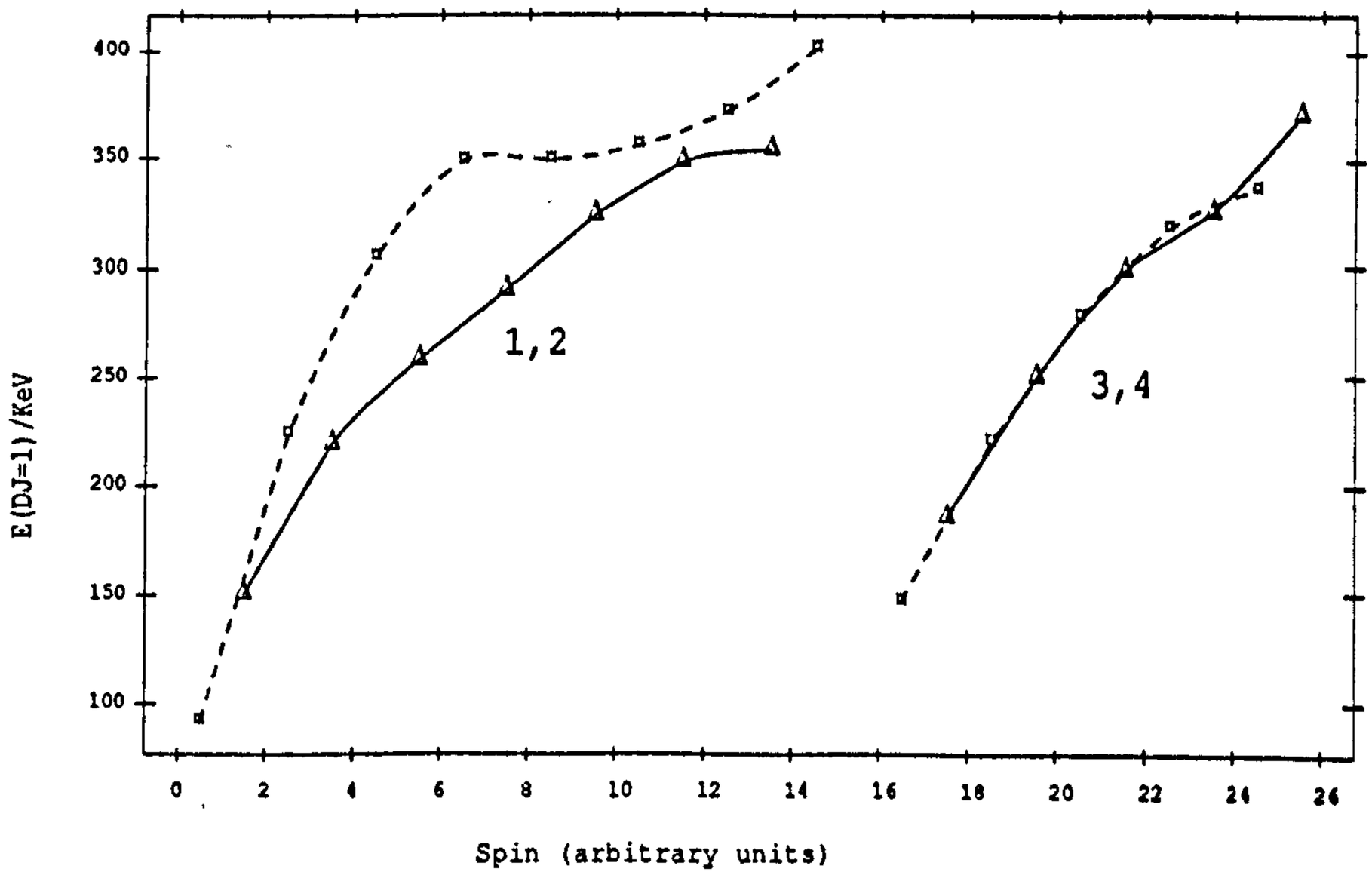

Figure 5.13: Plot of $\Delta J = 1$ energies versus arbitrary spin to show the signature splitting in the various bands in ^{131}Nd.

Bands 1/2 would appear to be based on the h11/2 [523]7/2$^-$ orbital since this orbital has the higher K value and would be expected to show stronger M1 transitions. This is reflected in the higher B(M1)/B(E2) ratio for Bands 1/2 as compared to Bands 3/4. The different signatures of this structure are split by approximately 50 keV as opposed to the zero signature splitting observed in Bands 3/4. Such splitting has been interpreted as indicative of a triaxial structure with a negative γ in the heavier Nd nuclei. This would support the assignment

since the upper mid-shell h11/2 neutron would tend to exert a polarizing effect towards negative γ whereas there is little shape preference in the g7/2 orbital (see Figure 5.2). The signature splitting would also appear to exhibit itself in a splitting of the B(M1)/B(E2) ratios which is a direct result of the signature

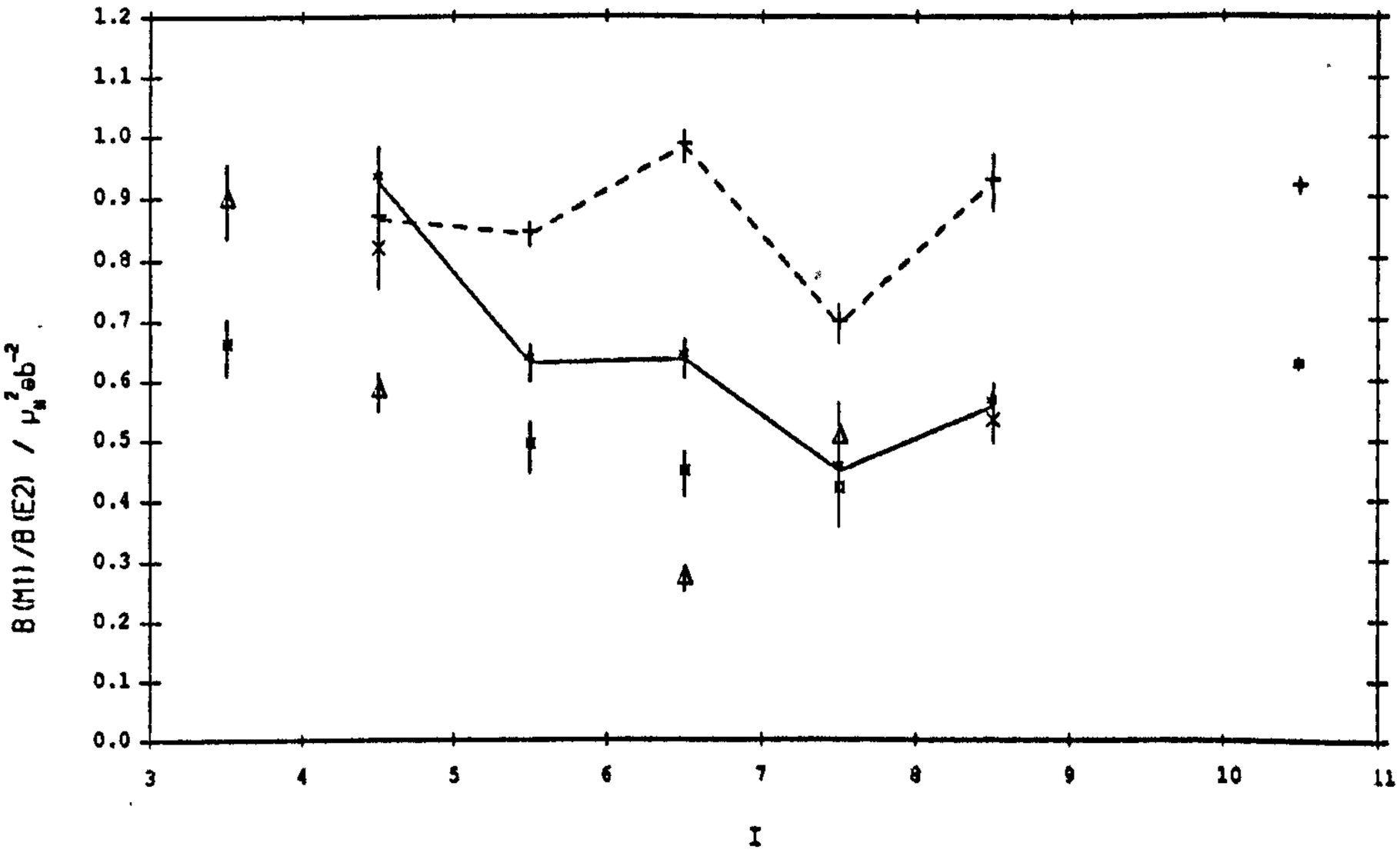

Figure 5.14: B(M1)/B(E2) ratios for Bands 1/2 and 3/4 in ^{131}Nd. The points corresponding to Bands 1/2 are joined to show the staggering more clearly. The values displayed are from both the ESSA-30 data (Band 1/2 +, Band 3/4 Δ) and the RS data (Band 1/2 $*$, $\times$, Band 3/4 $\circ$).

splitting of the levels in the simple semi-classical geometrical model of Donau and Frauendorf [DF82]. The magnitude of the splitting seen is comparable to that of the semi-classical estimate discussed in Section 1.8.

The second coupled structure is assigned as the g7/2 [402]5/2 band for the complimentary reasons to the assignment for Bands 1/2. An estimate of the the B(M1)/B(E2) ratios expected for various single particle levels as a function of spin is shown in Figure 5.15. The calculations assumed Schmidt values for the g-factors and particles aligned according to the DAL coupling scheme. The ratio obtained for the h11/2 neutron is in agreement with experiment but that of the g7/2 neutron is an order of magnitude too low. The magnitude of the ratio in the case of Bands 3/4 is better described by the estimate for the d5/2[413]5/2 particle. This is to be expected since an examination of the Nilsson diagram 2.2 indicates a strong interaction between the two 5/2 levels at a relatively low deformation. At higher deformations the levels will have exchanged character to

a great extent. That this is so is indicated by the labelling of these two levels in Figure 2.2.

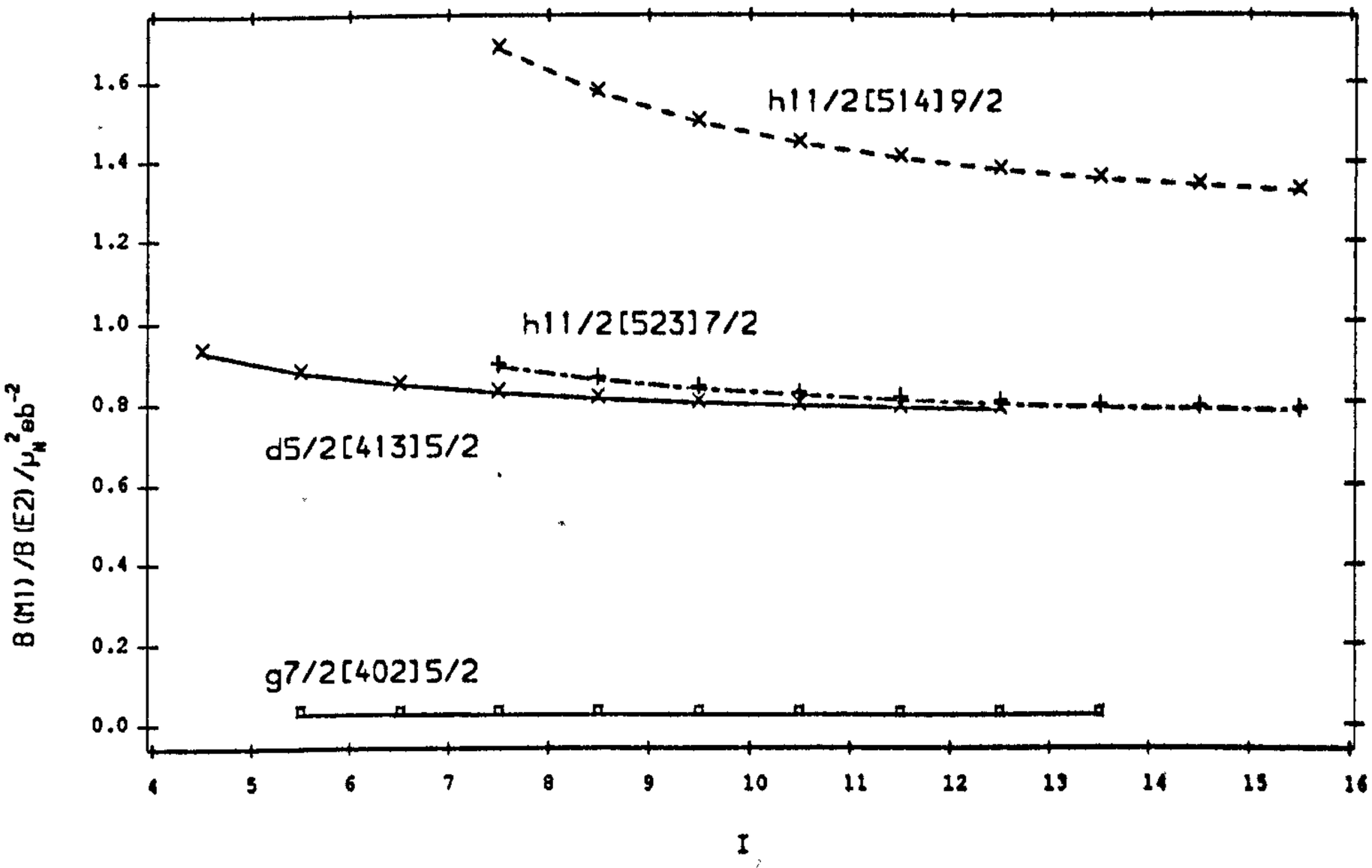

Figure 5.15: B(M1)/B(E2) ratios calculated according to the formalism of [DF82] for different single neutron configurations close to the Fermi surface of ^{131}Nd. The quadrupole moment was chosen rather arbitrarily to correspond to a deformation of about $\beta_2 \sim 0.3$ and thus probably overestimates the B(E2). Only the relative values thus have any significance. The Ω=9/2 h11/2 level looks a less likely candidate for the bandhead of Bands 1/2 since it would predict a larger ratio. The estimates would be expected to be better for the h11/2 configurations since these are intruder states and therefore do not mix significantly with other nearby levels.

The remaining Bands in ^{131}Nd are of a de-coupled nature indicating the involvement of a low Ω orbital. A plot of the $\mathcal{J}^{(2)}$ moment of inertia reveals that Band 5 has a significantly higher moment at frequencies in excess of 0.25 MeV . The value is comparable to that of the super-deformed bands in the heavier Nd nuclei when scaled by $A^{5/3}$. It is interesting to observe that the moment of inertia for Band 5 does not seem to show any discontinuity at around $\hbar\omega \sim$0.3 where the alignment of the EF protons is expected. Indeed, in this region the moment is practically constant whereas the other bands in the nucleus all show some deviation. This may point to a multi-quasiparticle configuration for this band. The large anomaly in the $\mathcal{J}^{(2)}$ at $\hbar\omega \sim$0.39 may be the FG proton crossing although the frequency is a little low. However, a multiproton configuration would be expected to show reduced pairing. The high moment of inertia for this

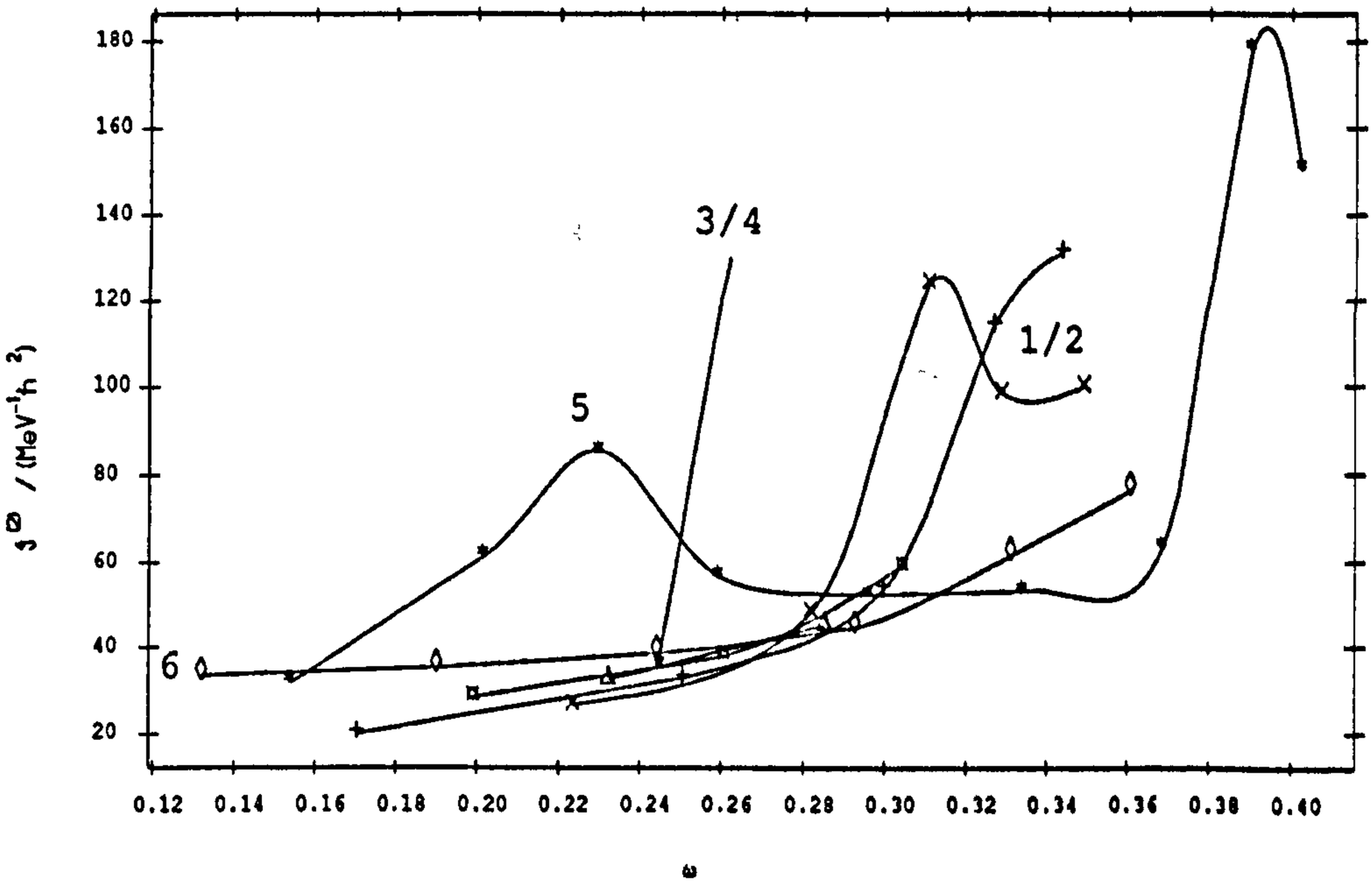

Figure 5.16: Dynamic moments of inertia for the bands observed in ^{131}Nd as a function of rotational frequency.

band may herald the appearance of the h9/2 neutron, as yet unobserved in this region, which would be expected to be strongly deformation driving and thus increase the moment of inertia. In the Nilsson (or Woods-Saxon) single particle level diagrams (Figures 2.2 and 2.3) both the f7/2 and h9/2 $\Omega = 1/2$ levels can be seen to descend rapidly with increasing deformation. The cranking model would predict the h9/2 band to drop most rapidly with increasing frequency since the expectation for the aligned angular momentum for these states would be larger. The CSM calculations performed do not show any negative parity orbitals descending rapidly from above which may mean that the single particle parameters input should be changed to bring these orbitals down more rapidly or alter the relative excitations of the h9/2 and h11/2 shells. The (perhaps more realistic) Woods-Saxon single particle level diagram shows the h9/2 orbital lying at the Fermi surface for a deformation of $\beta_2 \sim 0.3$ (Figure 2.3) and neutron number 71.

Band 6 is possibly based upon the s1/2 [411]1/2 orbital which can be seen in the CSM calculations (Figure 5.2) to give rise to a pair of levels with the large signature splitting indicative of a RAL aligned state. This possibility is made unnattractive by the the assignment of the s1/2 orbital to the ground state in ^{133}Ce [MPB89] where the band is observed to be strongly coupled. However, this must be due to strong admixtures in the wavefunction as the s1/2 orbital would be expected to give rise to strong signature splitting via a large decoupling

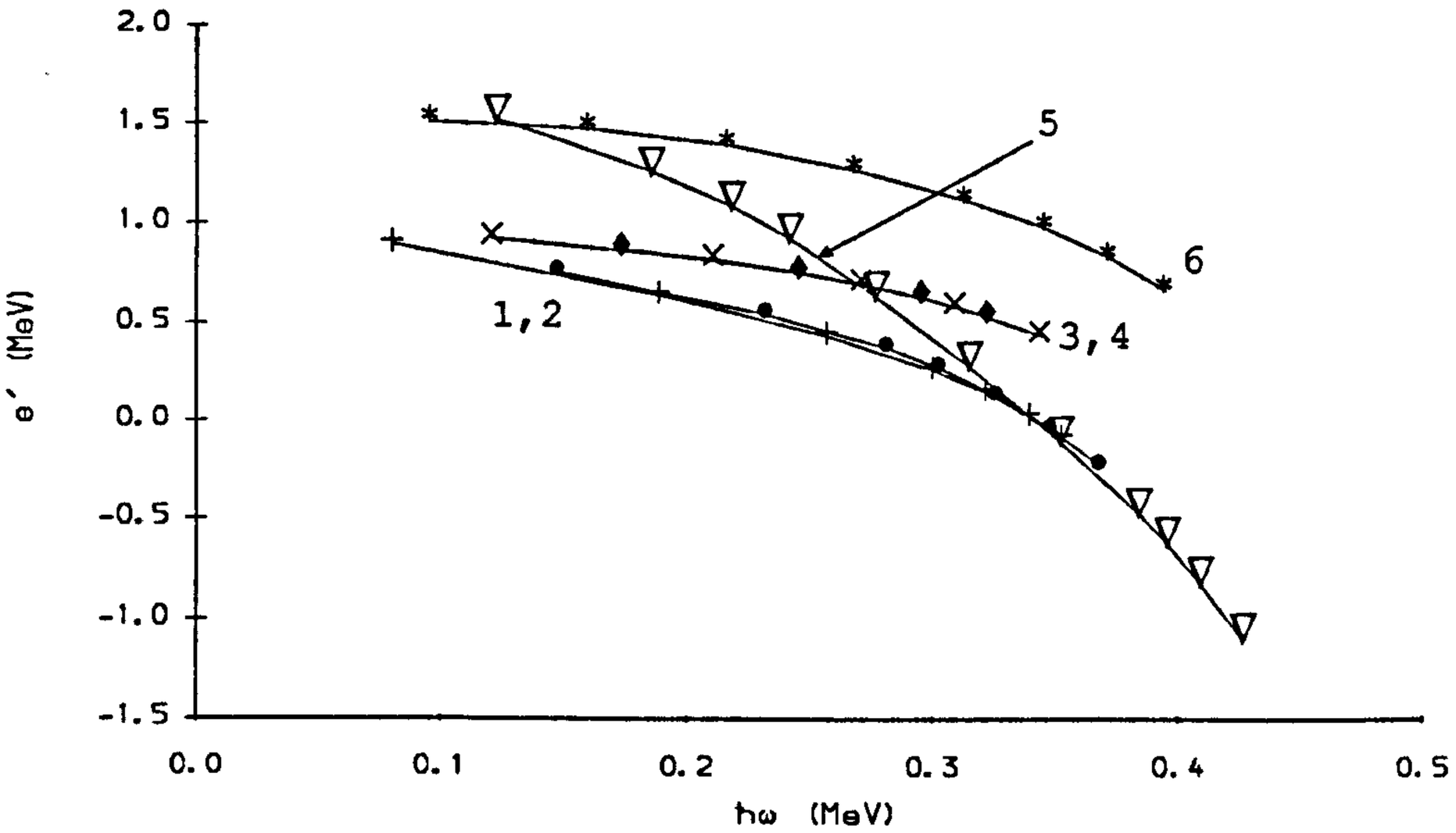

Figure 5.17: Routhians for the bands observed in ^{131}Nd. The reference subtracted is that of ^{128}Ce and the K values for Bands 1/2 and 3/4 are as detailed in the text. Bands 5 and 6 have been assigned a K value of 1/2 and spins 9/2 and 1/2 as appropriate for h9/2 and s1/2 bands respectively. The behaviour is swapped over if these assumptions are reversed. The relative excitations are arbitrary and the pair gap has been set to 1.0 MeV .

parameter. Alternative explanations for the decoupled bands could involve the f7/2 orbital which would also be expected to drop rapidly with increasing deformation and frequency or the h9/2 orbital in combination with a different proton configuration or even the i13/2 orbital. None of these seem very plausible since the moment of inertia of Band 6 is more comparable to that of Bands 1/2 and 3/4 indicating a similar configuration. It is interesting to note that two unplaced $\Delta J = 2$ sequences of similar energies exist in the nucleus ^{135}Sm [M89] where a third such sequence is interpreted as a direct observation of the i13/2 orbital. The non-observation of any super-deformed band may indicate the importance of the N=72 gap apparent in the single particle diagrams for the appearance of the superdeformed bands.

5.5 ^{129}Nd

The band structures in ^{129}Nd are remarkably similar to those observed in ^{131}Nd. The same problem with undetermined relative excitations of the different se-

quences is encountered. The signature splitting observed in Bands 1/2 is reduced compared to that seen in the analogous structure in ^{131}Nd (see Figure 5.18). The signature splitting seen in the corresponding structure in ^{133}Nd is >150 keV . The smaller splitting may be interpreted as a sign that the nucleus is closer to axial symmetry and that the macroscopic deformation effects have become stronger than the shape polarisation due to the unpaired neutron.

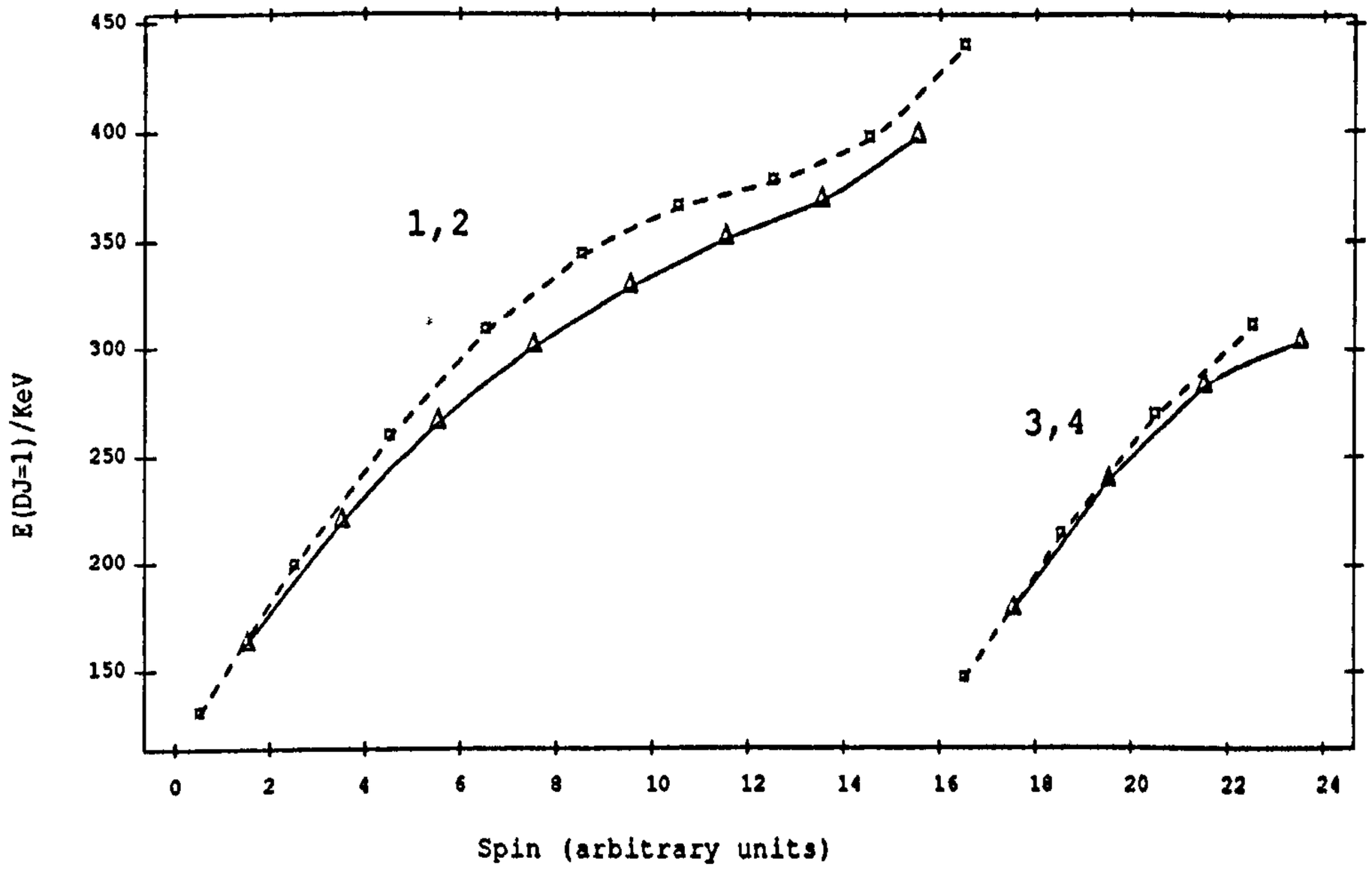

Figure 5.18: Plot of $\Delta J = 1$ energies versus arbitrary spin to show the signature splitting in the various bands in ^{129}Nd.

The branching ratio data for Bands 3/4 is limited but it would appear that the M1 transition strengths are greater for Bands 1/2. It is thus proposed that Bands 1/2 are based upon the ν h11/2 [523]7/2 configuration and Bands 3/4 on the ν g7/2 [402]5/2 configuration. It is noted that the relative strength of the positive parity band to the negative parity band is reduced in this nucleus as compared to the equivalent bands in ^{131}Nd where both are of approximately the same intensity. From the Nilsson diagram one may expect the h11/2 neutron to be closer to the Fermi surface at a deformation of $\epsilon_2 \geq 0.3$ so this may be a pointer towards a larger deformation in this nucleus. The B(M1)/B(E2) ratios are also generally reduced in this nucleus compared to those of ^{131}Nd which would be explained by an increase in deformation relative to that of ^{131}Nd.

The $\Delta J = 2$ bands seen in ^{131}Nd are also echoed in ^{129}Nd. The relative intensity of the bands is changed when compared to ^{131}Nd. Band 5 is reduced in intensity compared to the strongest structure and is significantly stronger than Band 6 as opposed to the roughly equal and greater strengths observed for Bands

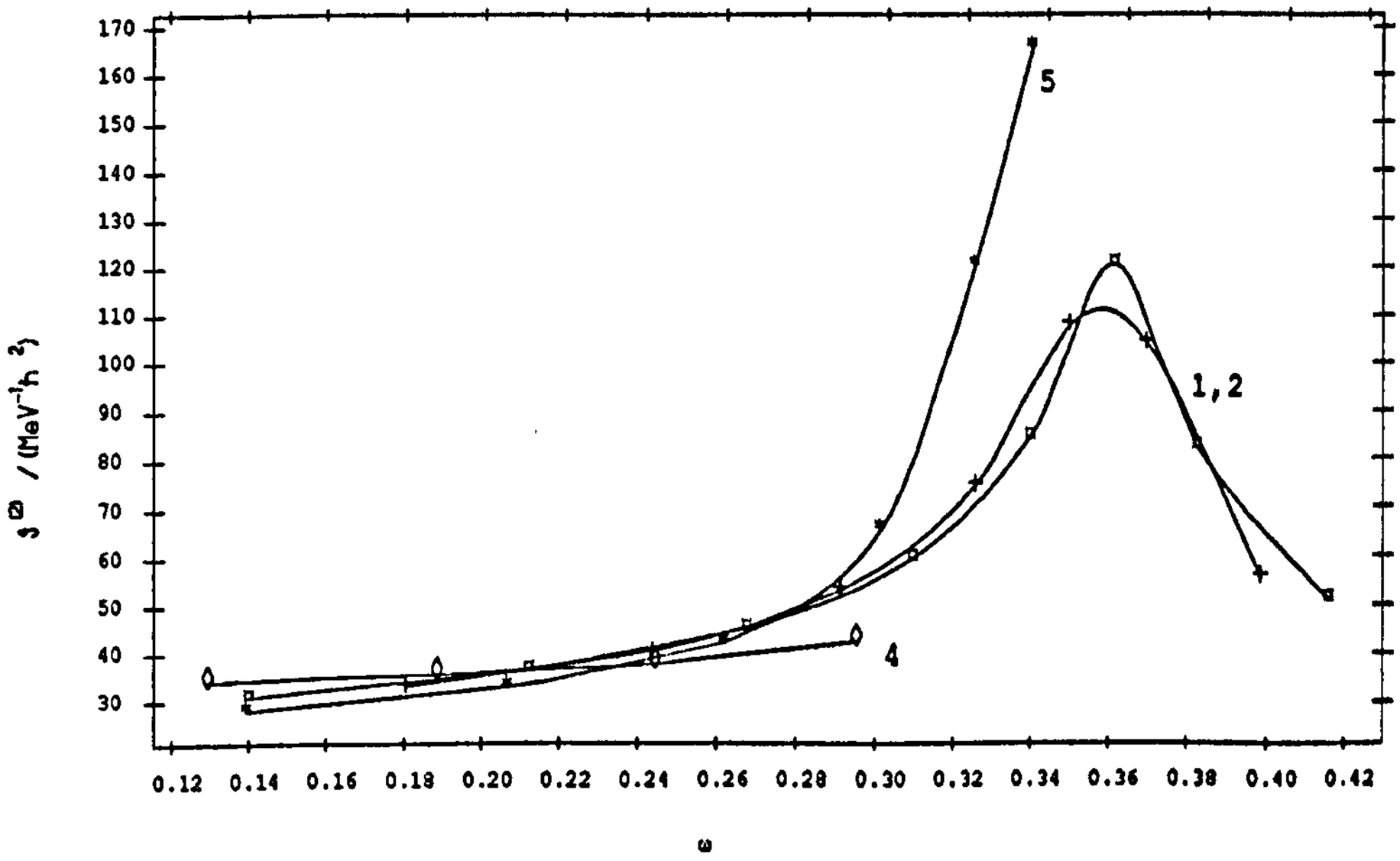

Figure 5.19: Dynamic moments of inertia for the various bands observed in ^{129}Nd.

5 and 6 in ^{131}Nd. The moments of inertia for the de-coupled bands in ^{129}Nd are rather similar and neither show the low frequency interaction of Band 5 in ^{131}Nd.

5.6 ^{128}Pr

The coupled Bands 1/2 in ^{128}Pr can be interpreted as the two signatures of a rotational band based on a state with J,K determined by a coupling of the single particle angular momenta. From the discussion of the neighbouring odd A nuclei ^{129}Pr and ^{129}Nd it would seem that a de-coupled h11/2 proton should be seen coupled to a DAL neutron from either the g7/2 or h11/2 shells. From the signature splitting observed ($\sim$ 25 keV) it would seem likely that the neutron in fact occupies the h11/2 orbital since there is no signature splitting associated with the g7/2 configuration. This also concurs with the systematic observation of $\pi h11/2 \otimes \nu g7/2$ bands with zero signature splitting and $\pi h11/2 \otimes \nu h11/2$ bands with moderate splitting ($\sim 30-50$ keV) amongst the odd-odd La and Pr nuclei. The occupation of the E quasiproton state associated with the $\pi h11/2$ orbital is confirmed by the lack of any backbending in the structure below a frequency $\hbar\omega \sim 0.4$ MeV . The start of an upbend which would correspond to the FG crossing seen in ^{129}Pr is beginning to show at the highest frequencies observed. It is interesting to note the inversion of the signature splitting as the upbend

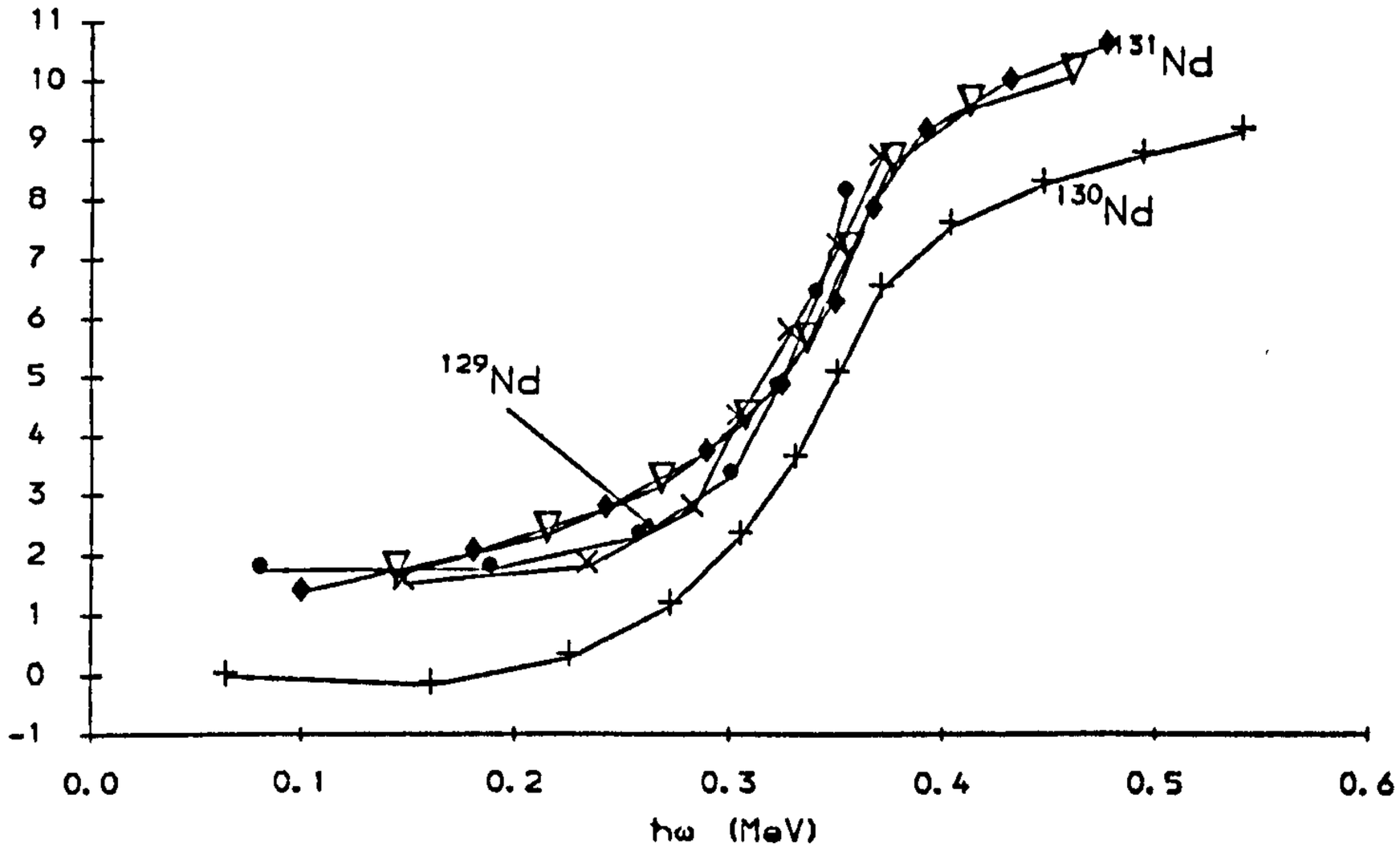

Figure 5.20: Alignment diagram for Bands 1/2 in ^{129}Nd, ^{130}Nd and ^{131}Nd. The reference subtracted is that of ^{128}Ce. The bands all appear to behave in a similar fashion although this would not be the case in different references were used.

forms.

The K of the band can be predicted according to the 'weak' Gallagher-Moskowski rule (Equation 1.2) as $K=\Omega_p + \Omega_n$ resulting in a $K^\pi=5^+$ bandhead assuming occupation of the Nilsson orbitals $\nu[523]7/2^-$ and $\pi[541]3/2^-$ as argued for the corresponding odd-A nuclide. A perpendicular coupling of the angular momenta following [MPS88] gives rise to a spin of ~7 for the bandhead. These are the parameters assumed in the alignment plot Figure 5.22. The low energy 58 keV transition has been assumed not to be part of the band structure as the corresponding $\Delta J = 2$ transition is not seen and the positive parity band is systematically seen to de-populate via a low energy E1 transition.

The B(M1)/B(E2) ratios are reduced with respect to those observed in the heavier Pr nuclei. This is to be expected due to the systematically increasing deformation (and hence increasing quadrupole moment) and the falling Fermi level in the h11/2 shell which corresponds to a decreasing K value and hence reduced M1 transition strengths.

The remaining levels are rather confused. It is likely that the extended sequences of transitions observed are the h11/2 proton coupled to the positive parity g7/2 neutron but it is impossible to pick out the signatures of the bands from the data. There would also seem to be other structures present, as is seen in

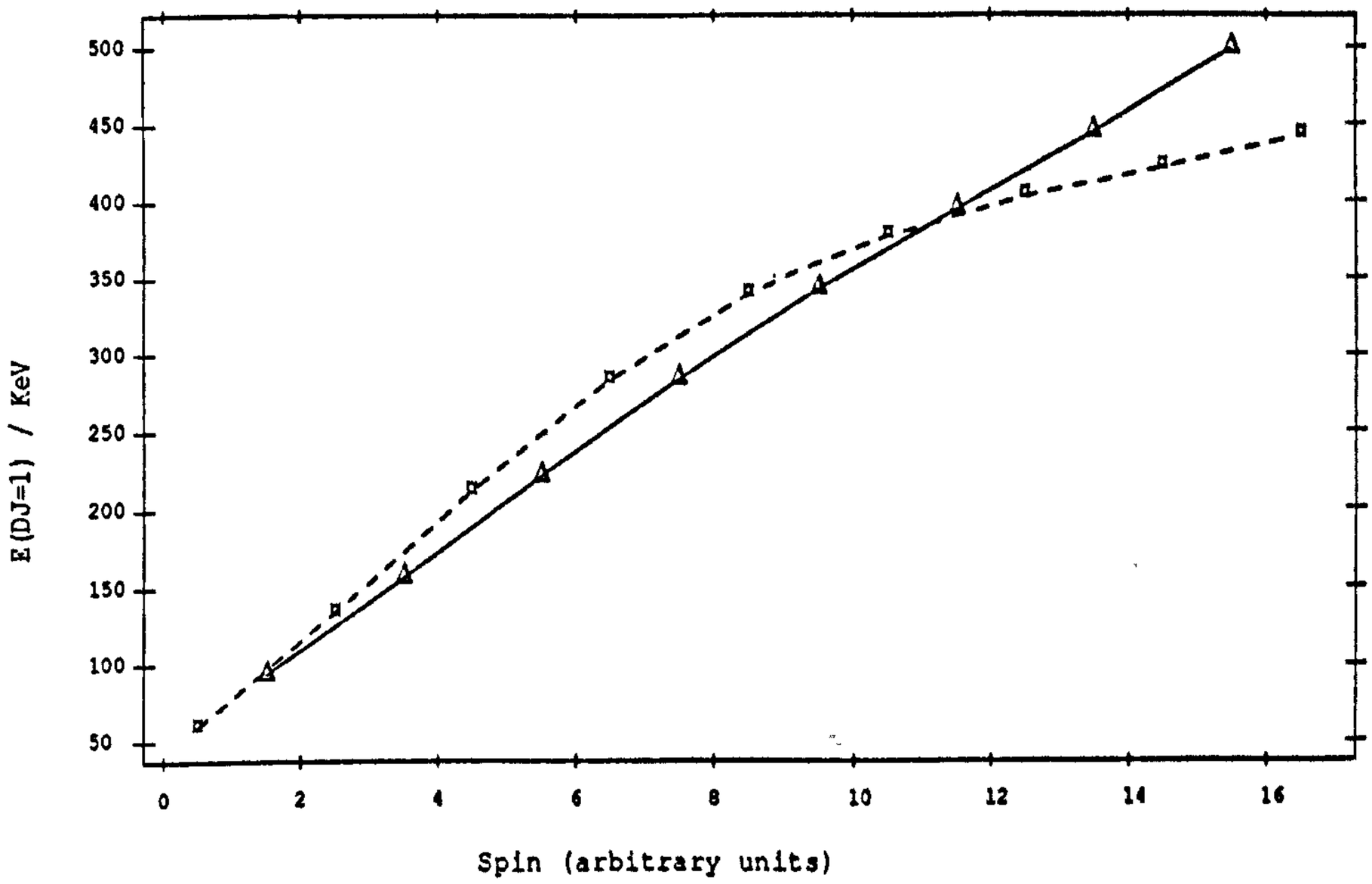

Figure 5.21: Plot of $\Delta J = 1$ energies versus arbitrary spin to show the signature splitting of Bands 1/2 in ^{128}Pr.

^{132}Pr. The fact that only one band is seen in this nucleus and that its properties are most consistent with the occupation of the νh11/2 orbital lends weight to the argument that the more weakly populated Bands 3/4 in ^{129}Nd are indeed based upon the g7/2 rather than the h11/2 configuration.

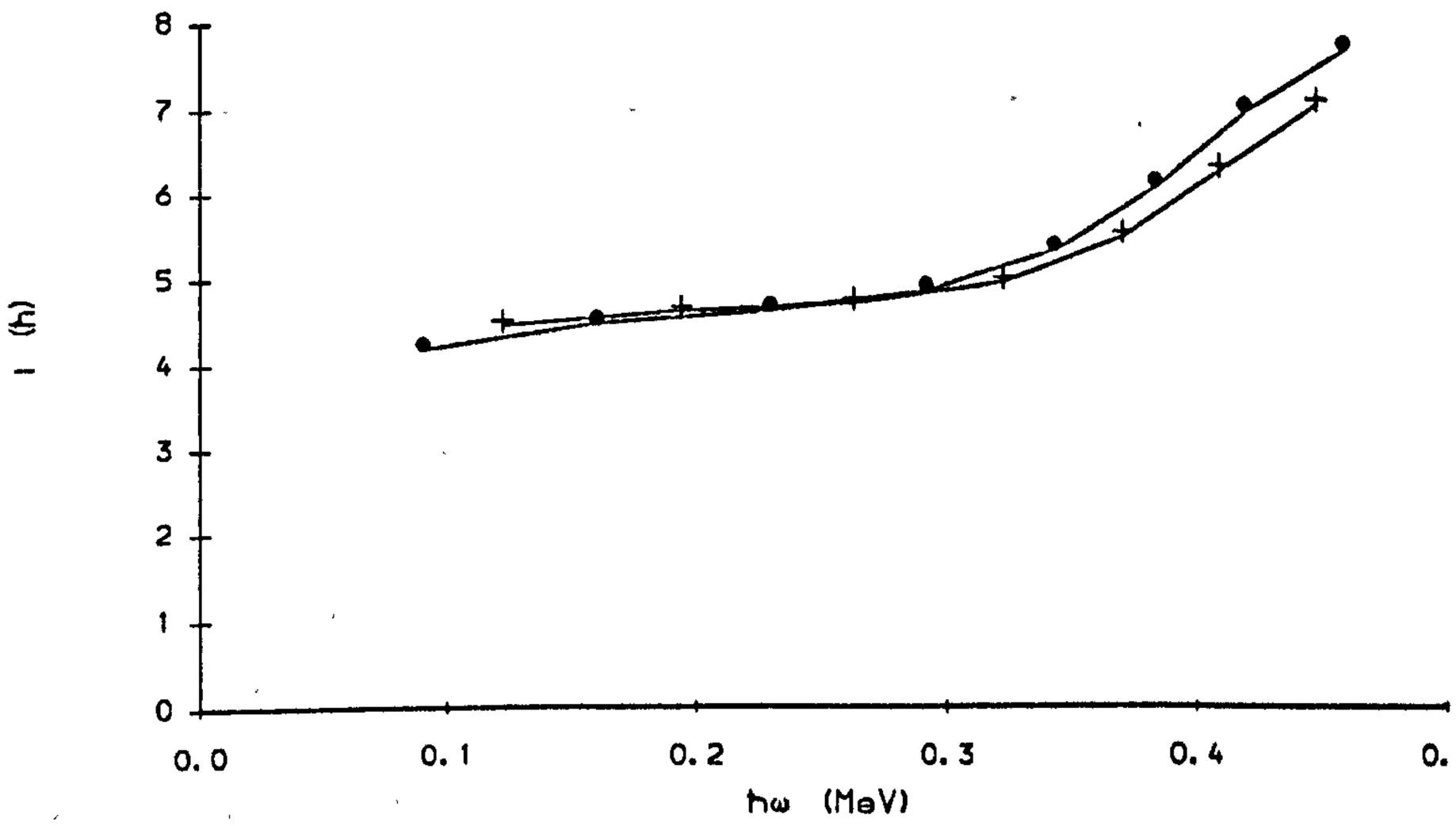

Figure 5.22: Alignment diagram for Bands 1/2 in ^{128}Pr. The reference subtracted was $\mathcal{J}_0 = 29, \mathcal{J}_1 = 10$ which was obtained by extrapolation of the parameters in Table 5.1 to ^{126}Ce. This was done as the ^{128}Ce reference did not appear appropriate, indicating that the band was constantly aligning.

Chapter 6

Summary

The data presented in this work are consistent with increased deformation as the neutron Fermi surface is lowered as expected from previous data and theoretical PES calculations. This is manifested in the postulated observation of νh9/2 and πg9/2 structures in ^{129,131}Nd and ^{129}Pr respectively and in the departure of the decoupled proton band in ^{129}Pr from the even-even core. The decreasing signature splitting as the Nd nuclides become increasingly neutron deficient implies a hardening of the minimum in the β, γ PES towards axiality in accordance with the TRS surfaces in the Figure 2.4.

The difficulty in obtaining a coherent picture of these nuclei in terms of the simplistic CSM calculations may imply that configuration dependent field parameters are of importance. The bandhead calculations presented in Sections 5.2.2 and 5.2.3 certainly support this. The adoption of such configuration dependent parameters is contrary to the CSM rationale. The second problem with interpretation of results in this region in terms of the CSM is the reliability of the reference used. For the Ce nuclei this is quite well defined in terms of the adapted g-reference. It is not clear that this reference is still appropriate for higher Z, especially in light of the stronger interaction seen in the Nd nuclei. It would be useful to extend the yrast bands of the even-even Nd nuclei beyond the upbend so that the reference behaviour of the Pr nuclei may be interpolated. Current data do not extend to high enough spins to extract a reference from the Nd nuclei. It would also be useful to see mass measurements for the nuclei in this region as this would give a direct indication of the pair gap parameters. Accurate lifetime measurements would give an estimate of the quadrupole moment and hence some better idea of the deformation of these nuclei. Such measurements would be particularly useful in establishing the πg9/2 and νh9/2 structures which are expected to be significantly deformed. The former of these would be an exceedingly difficult experiment but a DSAM experiment would suffice in the latter case.

Perhaps the most significant barrier to interpretation of this and other data in this region is the lack of knowledge about the relative excitations of the various structures. This may be due to isomerism as evidenced by the decay of Band 4 in ^{129}Pr. An experiment to investigate the decay of isomeric states in the A$\sim$129

Nd/Pr nuclides is currently under analysis by Dr. A.N.James.

The use of the RS for the identification of transitions with particular nuclides proved very successful. The simple γ-γ data without any channel selectivity was inconclusive in some cases, notably the confirmation of the 567 keV transition in ^{129}Pr. The confirmation of this transition would be useful as it would fix the relative excitations of several single particle levels at an extreme deformation. It would also be in contradiction with the bandhead calculations in Section 5.2.2 but these are only as good as the parameterisation of the levels! There is a need for Recoil-γ-γ spectroscopy but this would require at least and order of magnitude improvement in efficiency. Hopefully the next round of improvements to the RS and the next generation of γ spectrometers will be capable of providing such data. RS Recoil-γ data shows the existence of low energy transitions in ^{131}Pr which probably belong to bands analogous to those seen in ^{129}Pr but the γ-γ data was not of sufficient quality to decipher the structures.

Angular distribution/correlation experiments would access the spins of the observed levels and mixing ratios of the transitions between them. This would be of particular value in determining the configurations in ^{129}Pr and would provide a sensitive test bed for any calculation of transition strengths performed for this nucleus.

It is hoped that these nuclei will be further studied and that the low spin structure will be given as much attention as the exciting discoveries made in the high spin/excitation regime in this region.

Bibliography

[ALL76] G.Andersson *et.al.* Nucl.Phys. A268 (1976) 205

[B88] P.J.Bishop Ph.D. Thesis, Liverpool University (1988)

[BB78] M.Beckerman and M.Blann Phys.Rev. C 17 (1978) 1615

[BCS57] J.Bardeen, L.N.Cooper, and J.R.Schrieffer Phys.Rev. 108 (1957) 1175

[BF79] R.Bengtsson and S.Frauendorf Nucl. Phys. A327 (1979) 139

[BFM86] R.Bengtsson, S.Frauendorf and F.R.May At. Dat. and Nuc.Data Tables 35 (1986) 15

[BG85] R.Bengtsson and J.D.Garrett International Review of Nuclear Physics Vol 1 (World Scientific Publishers, Singapore)

[BHP87] C.W.Beausang, L.Hildingsson, E.S.Paul, W.F.Piel, Jr., N.Xu, and D.B.Fossan Phys.Rev. C 36 (1987) 1810

[BM75] A.Bohr and B.R.Mottelson Nuclear Structure (Benjamin 1975 Reading, Mass)

[BMP58] A.Bohr, B.R.Mottelson, and D.Pines Phys.Rev. 110 (1958) 936

[BQ81] M.Brack and P.Quentin Nucl.Phys. A361 (1981) 35

[BR85] T.Bengtsson and I.Ragnarsson Nucl.Phys. A436 (1985) 14

[BSB87] E.M.Beck, F.S.Stephens, J.C.Bacelar, M.A.Delaplanque, R.M.Diamond, J.E.Draper, C.Duyar and R.J.McDonald Phys.Rev.Lett 58 (1987) 2182

[BV58] N.N.Bogoluibov Nuovo Cimento 7 (1958) and J.G.Valatin in the same journal

[Be59] S.T.Belyaev Mat.Fys.Medd.Dan.Vid.Selsk 31 (1959) 11

[Bo52] A.Bohr Mat.Fys.Medd.Dan.Vid.Selsk 26 (1952)

[Br67] K.L.Brown Advances in Particle Physics Vol 1 (1967) 71

[CBH87] R.F.Casten, D.S.Brenner, and P.E.Haustein Phys.Rev.Lett. 58 (1987) 658

[CL86] Y.S.Chen and G.A.Leander, Physics division progress report, ORNL DWG 86-17476 Oak Ridge National Laboratory (1986)

[CP82] K.A.Connell and M.M.Przybylski Daresbury Technical Memorandum 57E (1982)

[CPS74] S.Cohen, F.Plasil, and W.J.Swiatecki Ann.Phys. 82 (1974) 557

[dV83] M.J.A.de Voight, J.Dudek, and Z.Szymański. Rev.Mod.Phys. 55 (1983) 4

[DF82] F.Donau and S.Frauendorf Invited Seminary, Brasow Summer School; Proc. Conf. on High Angular Momentum properties of Nuclei, Oak Ridge (1982)

[DNSW88] J.Dobaczewski, W.Nazarewicz, J.Skalski, and T.Werner Warsaw preprint IFT/1/88 (1988)

[Dr81] G.D.Dracoulis Nucl.Inst.Meth. 187 (1981) 413

[FM83] S.Frauendorf and F.R. May Phys. Lett. 125B (1983) 245

[FP77] P.Federman and S.Pittel Phys.Lett. 69B 4 (1977) 385

[G62] L.Grodzins Phys.Lett. 2 (1962) 88

[GAG81] J.D.Garrett *et.al.* Phys.Rev.Lett 47 (1981) 75

[GBK87] M.J.Godfrey, P.J.Bishop, A.Kirwan, P.J.Nolan, D.J.Thornley, D.J.Unwin, D.J.G.Love and A.H.Nelson J.Phys.G: Nucl.Phys. 13 (1987) 1165

[GBSS88] A.Goswami, S.Bhattacharyu, M.Saha and S.Sen Phys.Rev. C37 (1988) 370

[GG67] J.R.Gover and J.Gilat Phys.Rev. 157 (1967) 814

[GGM74] J.Gizon, A.Gizon, M.R.Maier, R.M.Diamond and F.S.Stephens Nucl.Phys. A222 (1974) 557

[GM58] C.J.Gallagher.Jr. and S.A.Moskowski Phys.Rev. 111 (1958) 1282

[GSF79] U.Garg, T.P.Sorjeen, and D.B.Fossan Phys.Rev. C 19 (1979) 207

[H65] S.M. Harris Phys.Rev. 138 (1965) B509

[HBF88] L.Hildingsson, C.Beausang, D.B.Fossan and W.F.Piel, Jr.Phys.Rev C 37 (1988) 985

[HS68] R.S.Hagar and E.C.Seltzer Nucl.Data.Tables 4 (1968) 1

[In54] D.R.Inglis Phys.Rev. 96 (1954) 1059

[JBM83] A.N.James, P.A.Butler, T.P.Morrison , J.Simpson andK.A.Connell Nuc.Inst. and Meth. 212 (1983) 545

[JMY88] A.N.James, T.P.Morrison, K.L.Ying, K.A.Connell, H.G.Price and J.Simpson Nucl.Instr. and Meth. in Phys. Research A267 (1988) 144

[Ja87] A.N.James Proc. 19^{th} Mikalajki Summer School on Nuclear Physics (1987)

[Ki86] A. Kirwan PhD. Thesis University of Liverpool (1986)

[LF61] A.E.Litherland and A.J.Ferguson Can.J.Phys. 39 (1961) 788

[LFM82] G.A.Leander, S.Frauendorf, and F.R.May. Proc. Conf. on High Angular Momentum Properties of Nuclei , Oak Ridge, Tennessee (1982)

[LM82] G.A.Leander and P.Moller Phys.Lett. 110B (1982) 17

[LNM73] J.R.Leigh, K.Nakai, K.H.Maier, F.Puhlhofer, F.S.Stephens, and R.M.Diamond Nucl. Phys. A213 (1973) 1

[LVH70] K.E.G.Lobner, M.Vetter, and V.Honig Nucl.Dat.Tables A7(1970) 495

[LVM85] C.J.Lister *et.al.* Phys.Rev.Lett 55(1985) 810

[Li60] H.J. Lipkin Ann. of Phys. 31 (1960) 525

[M89] S.M.Mullins private communication (1989)

[MCC87] J.H.McNiell, M.Campbell, A.A.Chisti, W.Gelletly, C.J.Lister and B.J.Varley Nuclear Physics Ann. Rep., Manchester University (1987) 96

[MN81] P.Möller and J.R.Nix At.Dat. and Nucl.Dat. Tables26 (1981) 2

[MPB89] R. Ma, E.S. Paul, C.W. Beausang, S. Shi, N. Xu and D.B. Fossan Stony Brook preprint (1989)

[MPS63] E.Marshalek, L.W.Person, R.K.Sheline Rev.Mod.Phys 35(1963) 1

[MPS88] R.Ma, *et.al.* Phys.Rev.C 37 (1988) 1926

[MS69] W.D.Myers and W.J.Swiatecki Ann.Phys. 55 (1969) 395

[Ma49] M.G.Mayer. Phys.Rev. 75 (1949) 1969

[Ma50] M.G.Mayer. Phys.Rev. 78 (1950) 16

[Mo62] B.R.Motteslon from a lecture series, Copenhagen, Autumn 1962

[Mo86] T.P.Morrison Nuc.Inst.Meth. A251 (1986) 337

[ND68] V.S.Nikolaev and I.S.Dmitriev Phys.Lett. 28A (1968) 277

[ND85] W.Nazarewicz. *et.al.* Nucl.Phys. A435 (1985) 397

[NGT85] P.J.Nolan, D.W.Gifford, and P.J.Twin Nuc.Inst.Meth. A236 (1985) 95

[NR81] W.Nazarewicz and P.Rozamej Nucl.Phys. A369 (1981) 390

[NS-S79] P.J.Nolan and J.F.Sharpey-Schafer Rep.Prog.Phys 42 (1979) 1

[NS70] L.C.Northcliffe and R.F.Schilling Nuc.Dat.Tables A7 (1970) 23

[NTS69] S.G.Nilsson. *et.al.* Nucl.Phys. A131 (1969) 1

[Na86] W.Nazarewicz. Contribution to International Conference on Nuclear Structure, Reactions and Symmetries. Dubrovnik (1986)

[Ni55] S.G.Nilsson. Mat.Fys.Medd.Dan.Vid.Selsk. 29 (1955) 16

[No64] Y.Nogami Phys.Rev B313 (1964) 134

[PBF87] W.F.Piel, Jr., C.W.Beausang, D.B.Fossan, L.Hildingsson and E.S.Paul Phys.Rev. C 35 (1987) 959

[Pu77] F. Pulhofer Nucl. Phys. A280 (1977) 267

[QBC86] M.A.Quader , C.W.Beausang, P.Chowdhury, U.Garg and D.B.Fossan Phys.Rev. C 33 (1986) 1109

[RB67] H.J.Rose and D.M.Brink Rev.Mod.Phys. 39 (1967) 306

[RS80] P.Ring and P.Schuck The Nuclear Many-Body Problem (Springer 1980 New York)

[RT52] G.Racah and I.Talmi Physica 18 (1952) 1097

[Ra50] J.Rainwater Phys.Rev. 79 (1950) 432

[Re72] J.M.Reid The Atomic Nucleus (1972) Manchester University Press

[Ro70] D.J.Rowe Nuclear Collective Motion (Methuen 1970 London)

[S72] F.S.Stephens Lectures from the 5th Nuclear Physics Summer School Rudziska, Poland (1972)

[SBF88] S.Shi, C.W.Beausang, D.B.Fossan, R.Ma, E.S.Paul, N.Xu and A.J.Kreiner Phys.Rev. C 37 (1988) 1478

[SDL72] F.S.Stephens, R.M.Diamond, J.R.Leigh, T.Kammuri, and K.Nakai Phys.Rev.Lett 29 (1972) 438

[SGG82] R.E.Shroy, D.M.Gordon, M.Gai, D.B.Fossan and A.K.Gaigalas Phys.Rev. C 26 (1982) 1101

[SGS79] R.E.Shroy, A.K.Gaiglas, G.Schatz, and D.B.Fossan Phys.Rev. C 19 (1979) 1324

[SH78] H.Schmidt-Bocking and H.Hornung Z.Physik A286 (1978) 253

[SS88] J.F.Sharpey-Shafer and J.Simpson Article to be published in Progress in Particle and Nuclear Physics (1988)

[SSH86] T.M.Semkow *et.al.* Phys.Rev. C 34 (1986) 523

[St66] V.M.Strutinsky Nucl.Phys. A95 (1967) 420

[Sz83] Z.Szymański Fast Nuclear Rotation Clarendon Press Oxford(1983)

[TNA83] P.J.Twin, P.J.Nolan, R.Aryaeinejad, D.J.G.Love, A.H.Nelson, and A.Kirwan Nucl.Phys. A409 (1983) 343c

[VLM84] B.J.Varley, C.J.Lister, and R.Moscrop Proc. Conf. on Instrumentation for Heavy-Ion Nuclear research, Oak Ridge, Tennessee (1984)

[WBF87] P.J.Woods *et.al.* Nuclear Structure Appendix to theDaresbury Annual Report (1987) 127

[WNJ87] R.Wyss *et.al.* Lund preprint Lund-MPh-87/16 (1987)

[WKL87] R.Wadsworth *et.al.* J.Phys.G: Nucl.Phys. 13 (1987) 1207

[WOW88] R.Wadsworth *et.al.* J.Phys.G: Nucl.Phys. 14 (1988) 239

[We35] C.F.von Weizsäcker Z.Physik 96 (1935) 431

[XBM89] N.Xu, C.W.Beausang, R.Ma, E.S.Paul, W.F.Piel,Jr., D.B.Fossan and L.Hildingsson Phys.Rev. C 39 (1989) 1799

[YBJ86] K.L.Ying *et.al.* J. Phys. G Nucl. Phys 12 (1986) L211

[Yi86] K.L.Ying Liverpool University Thesis (1986)

[ZX88] J-y.Zhang. *et.al.* Stony Brook preprint (1988)